



**University of  
Nottingham**  
UK | CHINA | MALAYSIA

# Towards the Automated Synthesis of Artemisinin at Low Temperature

James John Herron, MSci

Thesis submitted to The University of Nottingham

for the degree of Doctor of Philosophy

Supervisors: Prof. Michael W. George & Prof. Sir Martyn Poliakoff

March 2023

## Abstract

According to the World Health Organisation (WHO) there were an estimated 228 million cases of malaria worldwide in 2018, resulting in 405,000 deaths, the majority of which occur in the most underdeveloped regions in the world.<sup>1</sup> Since 2002, Artemisinin-based combination therapies (ACTs) have been designated as the first-line antimalarial treatment by the WHO, and despite the development of the first-generation RTS,S/AS01 vaccine in 2021, ACTs remain the most viable treatment of malaria.<sup>2-4</sup> There is, therefore, a great necessity for a substantial and reliable delivery of affordable artemisinin.<sup>1</sup>

Since industrial production of artemisinin was developed by Sanofi in 2013, investigations have been made to improve the synthesis, with the ultimate aim of reducing the cost of this crucial drug.<sup>5</sup> A crucial step in this synthesis is the reaction of the precursor, dihydroartemisinic acid (DHAA), with singlet oxygen ( ${}^1\text{O}_2$ ). The reaction can be conducted using photochemically generated  ${}^1\text{O}_2$  to produce several hydroperoxide intermediates, of which it is generally accepted that only one can form artemisinin.<sup>5-9</sup> The reduction of the photo-oxidative temperature can lead to increased selectivity towards the desired hydroperoxide.<sup>8</sup>

Herein, this Thesis describes the development of a continuous flow reactor capable of conducting reactions at  $-80^\circ\text{C}$ , to further exploit increases in selectivity of the photo-oxidation. The reactor was then adapted to perform the continuous synthesis of artemisinin which was simultaneously developed with ‘On-line’ HPLC-UV and -ELSD (evaporative light scattering detector) analysis to produce an automated flow reactor.

Chapter 2 details modifications to a prototype photochemical reactor previously built at Nottingham. Ultimately, a minimum interior reactor temperature of  $-46^\circ\text{C}$  was achieved, resulting in improvements to the selectivity of the photo-oxidation of DHAA.

Chapter 3 presents the further development of a second reactor capable of conducting reactions down to  $-80^\circ\text{C}$ , resulting in further improvements in photo-oxidative selectivity. The reactor was then employed to perform the semi-synthesis of artemisinin using continuous ‘one-pot’ and semi-continuous ‘two-pot’ regimes. Through simultaneous reactor and reaction development, the enhancements at low temperature were found to translate to improved yields of artemisinin at  $-80^\circ\text{C}$ , achieving a highest yield of 68 %.

Chapter 4 explores further adaptations to facilitate automated reactions. This required establishing a method for ‘On-line’ analysis that exhibits high accuracy, precision and sufficient dynamic range. Modifications to the reactor were also needed to implement a reliable sampling of the liquid-gas mixture. HPLC-UV and -ELSD were selected as the methods of analysis. The use of the dual ‘On-line’ detection combined with automatic sampling provided valuable data verification and insights into the formation of artemisinin; showing that the conversion of the hydroperoxide to artemisinin occur slowly and required adaptation to the reactor, including the addition of a Vortex reactor, to improve the formation of artemisinin.

The implementation of a low temperature, biphasic, multi-step synthesis into an automated system, provided numerous challenges. However, through iterative reactor development the automated syntheses of artemisinin and rose oxide were performed, showcasing the ability of the system and the self-optimisation framework to conduct computer controlled reactions. These experiments highlighted the potential for further advancements, both in reactor design and the self-optimisation framework, to enable the efficient implementation of fully self-optimised systems.

Chapter 5 outlines the experimental work carried out within this Thesis, including HPLC method development for the quantification of photochemically synthesised artemisinin and rose oxide. Many challenges were encountered in the development of the method for artemisinin detection, primarily due to large fluctuations in the sensitivity of the ELSD. Eventually, HPLC-UV was made the primary method for quantitative analysis, while ELSD was used to gather additional information into the composition of the photoproduct.

Finally, Chapter 6 summarises the work described in this Thesis and examines the success of the approaches with respect to the initial aims. A summary of future works is also presented.

## **Acknowledgements**

Firstly, I would like to thank my supervisors, Professor Sir. Martyn Poliakoff and Professor Michael George for their support and guidance. I would also like to thank PhotoElectro and the University of Nottingham for enabling this research to take place. For technical support, thanks go to Richard Wilson, David Litchfield, Martin Dellar, Mark Guyler, Clive Dixon and Connor Howell-Bennett.

My sincerest thanks go to all of the Post-docs and PhD students that have provided valuable advice, and helped relieve many stresses throughout the past few years. In particular, for their advice and fundamental work that allowed for this research to take place, I would like to thank Dr. Rowena Howie and Dr. Jie Ke. For more general help and for creating an enjoyable working environment, during particularly difficult times, I would like to thank: Dr. Hamza Boufroura, Dr. Jonathan Moore, Dr. Darren Lee, Dr. Marcos Veguillas, Dr. Samantha Tang, Bryan Tambosco, Toby Waldron-Clarke, Taranvir Bedi, Wagma Ayub, Hamza Ali, Adam Lee, Amy Flinn, and the rest of the George/Poliakoff group who have all played a part in getting me to this point.

Thank you to my parents, David and Paula. The help with finishing this chapter of my life has been invaluable and I don't think I could have done it without them. The same goes for my partner Laurie, whose support has been required countless times and for which I am forever grateful.

## **Declaration**

I declare that the work presented in this Thesis is a record of my own work for the period of October 2018 to March 2023. Where any work has been carried out in collaboration, the relevant researcher has been acknowledged. This Thesis has not been accepted in partial or complete fulfilment of any other degree or personal qualification.

James John Herron, 31<sup>st</sup> March 2023

## Abbreviations

UV	ultra-violet
ISC	inter-system crossing
HOMO	highest occupied molecular orbital
LUMO	lowest unoccupied molecular orbital
d <sup>6</sup> -DMSO	deuterated dimethyl sulfoxide
ϕ	quantum yield
τ	singlet oxygen lifetime
<sup>1</sup> O <sub>2</sub>	singlet oxygen
<sup>3</sup> O <sub>2</sub>	triplet oxygen
ISC	intersystem crossing
PS	photosensitiser
ACT	artemisinin combination therapy
PTFE	polytetrafluoroethylene
FEP	fluorinated ethylene propylene
PEEK	polyether ether ketone
PFA	perfluoroalkoxyalkane
S <sub>0</sub>	electronic ground state
S <sub>1</sub>	first singlet excited state
T <sub>1</sub>	first triplet excited state
LED	light emitting diode
HPR	high pressure reactor
GLS	gas-liquid separator
HPLC	high pressure liquid chromatography

## Numbered Compounds

1	-	Maleimide
2	-	1-hexyne
3	-	1+2 product: 6-butyl-3-azabicyclo[3.2.0]hept-6-ene-2,4-dione
4	-	tetrahydropthalic acid anhydride (THPA)
5	-	propargyl alcohol
6	-	3 + 4 bridged product
7	-	3 + 4 minor product
8	-	citronellol
9	-	7-hydroperoxy-3,7-dimethyloct-5-en-1-ol
10	-	6-hydroperoxy-3,7-dimethyloct-5-en-1-ol
11	-	secondary diol
12	-	tertiary diol
13	-	rose oxide
14	-	DHAA (Dihydroartemisinic acid)
15	-	DHAA Tertiary hydroperoxide
16	-	DHAA secondary hydroperoxide A
17	-	DHAA secondary hydroperoxide B
18	-	artemisinin
19	-	6-lactone
20	-	dihydro- <i>epi</i> -deoxyarteannuin
21	-	DHA ethylcarbonate
22	-	Arteannuin H

# Table of Contents

Abstract.....	2
Acknowledgements.....	4
Declaration.....	5
Abbreviations.....	6
Numbered Compounds .....	7
Chapter 1. Introduction.....	11
1.1. The Principles of Photochemistry .....	11
1.1.1. The First Law of Photochemistry .....	12
1.1.2. The Second Law of Photochemistry.....	13
1.1.3. Kinetic Rate Dependence on Temperature versus Photons .....	13
1.2. Singlet Oxygen.....	15
1.2.1. Oxidations with ${}^1\text{O}_2$ .....	16
1.2.2. Lifetime and Quenching of ${}^1\text{O}_2$ .....	17
1.2.3. Photosensitisers for ${}^1\text{O}_2$ Generation .....	18
1.3. Photo-Oxidations with Singlet Oxygen.....	19
1.3.1. Schenck-ene Photo-Oxidation .....	20
1.4. Reactor Design Considerations .....	23
1.4.1. Light Sources for Photochemistry .....	23
1.4.2. Continuous-Flow Photochemistry .....	25
1.5. Continuous Flow Photo-Oxidation.....	27
1.6. Reactors for Continuous Photo-Oxidations.....	29
1.6.1. Taylor Flow Reactor.....	30
1.6.2. Vortex Reactor .....	31
1.6.3. Rotor-Stator Spinning Disk Reactor.....	31
1.6.4. Nebuliser-Based Continuous Flow Reactor.....	32
1.7. Rose Oxide.....	33
1.8. Artemisinin and Malaria .....	35
1.8.1. Mechanism for the formation of Artemisinin .....	36
1.8.2. Photochemical Synthesis of Artemisinin.....	42
1.8.3. Continuous Flow Synthesis of Artemisinin .....	45
1.8.4. Reaction Optimisation.....	46
1.9. Photo-oxidation at Low Temperature.....	47
1.10. Thesis Aims .....	48
Chapter 2. Development of a Low Temperature Continuous-Flow Photoreactor .....	49
2.1. High Temperature, High Pressure Photoreactor.....	50
2.1.1. Description of Reactor Systems .....	50
2.2. Description of the PhotoLED .....	54
2.3. Testing the Capabilities of the HPR .....	57
2.4. [2+2] Cycloaddition of THPA and Propargyl Alcohol .....	60
2.5. Limitations of the High-Pressure Reactor .....	62
2.6. Testing the Spiral Reactor .....	63
2.7. HPR Development for Low Temperature Photochemistry.....	64
2.7.1. Initial Set-up for Low Temperatures .....	64
2.7.2. Adaptations to the Reactor .....	65
2.8. Low-Temperature Photo-Oxidations in the HPR .....	72
2.8.1. Rig Modifications needed to permit Photo-Oxidations .....	73
2.9. Photo-Oxidation of Citronellol in the HPR .....	74
2.10. Photo-Oxidations of DHAA in the HPR .....	76
2.11. Summary .....	81
Chapter 3. Development of a Continuous-Flow Reactor for Low Temperature Photo-Oxidations.....	84
3.1. Reactor Design.....	85
3.2. Temperature Testing .....	88
3.3. Photo-Oxidations in the Low Temperature FEP Coil Reactor .....	90
3.3.1. Photo-Oxidation of DHAA .....	90
3.4. Investigating the Photo-Oxidative Synthesis of Artemisinin .....	91
3.4.1. Initial Semi-Continuous Synthesis of Artemisinin .....	92
3.4.2. Continuous ‘One-Pot’ Synthesis of Artemisinin .....	93
3.4.3. Semi-Continuous ‘Two-Pot’ Synthesis using DCA in DCM .....	96
3.4.4. Effect of TPP Concentration .....	97
3.4.5. ‘One-Pot’ Synthesis of Artemisinin with TPP in DCM.....	98
3.5. Pressure Issues Encountered with the ‘Thin-Walled’ FEP Reactor.....	99
3.6. Alternative Photoreactor Materials .....	100
3.6.1. PFA Photoreactor .....	100
3.6.2. ‘Thick Wall’ FEP .....	100

3.6.3. Issues with the ‘Thick-Walled’ FEP Reactor.....	104
3.7. ‘Near-micro’ FEP reactor.....	105
3.7.1. Initial Reactor Testing .....	105
3.7.2. Adaptations and Pressure Testing.....	106
3.7.3. Double-Layer FEP .....	107
3.7.4. Comparison of TFA and TCA .....	109
3.7.5. Reactions with TCA .....	110
3.8. Investigation into the formation of 6-lactone, 19.....	113
3.8.1. Synthesis of Artemisinin using DHA Ethylcarbonate.....	118
3.9. Summary .....	119
Chapter 4. Development Towards a Self-Optimising Reactor for Photo-Oxidative Reactions .....	121
4.1. Background .....	122
4.1.1. Self-Optimisation.....	122
4.1.1. Design of Experiment .....	123
4.1.2. Process Analytical Technology.....	124
4.1.3. Online-Process Analytical Technology for the Detection of Artemisinin.....	127
4.1.4. HPLC.....	128
4.1.5. Evaporative Light Scattering Detection (ELSD) .....	128
4.2. HPLC Method Development for the Quantification of Artemisinin.....	130
4.3. Synthesis of 18 to Test the HPLC Methods.....	133
4.4. Assessing the Product Composition at the Time of Sampling .....	139
4.5. Modifications to Increase the Formation of Artemisinin .....	142
4.5.1. Heated Secondary Coils.....	142
4.5.2. Adaptation of the Reactor to Facilitate Continuous ‘Two-Pot’ Synthesis of Artemisinin ..	142
4.5.3. Varying Acid Concentration .....	146
4.5.4. Reactions in Toluene .....	147
4.5.5. Addition of the Vortex Reactor.....	153
4.6. Implementation of On-line Detection into the Automated Synthesis of 18 .....	158
4.6.1. Automated ‘One-Pot’ Reactions .....	159
4.7. Issues with the Automated Synthesis of 18 .....	164
4.8. Continuous Synthesis of Rose Oxide.....	165
4.8.1. Semi-Continuous Synthesis of 13 .....	166
4.8.2. Continuous Synthesis of 13 .....	167
4.8.3. Development of the Automated System for the Continuous Synthesis of 13 .....	170
4.8.4. Computer Controlled List Run to Test Calibration .....	171
4.8.5. CCF DoE for the Synthesis of Rose Oxide .....	174
4.9. Summary .....	178
Chapter 5. Experimental.....	180
5.1. Materials.....	180
5.2. General Analysis .....	180
5.2.1. NMR Analysis .....	180
5.2.2. Statistical Analysis .....	181
5.3. Development of a Low Temperature Continuous-Flow Photoreactor .....	181
5.3.1. UV Initiated [2+2]-cycloadditions .....	182
5.3.2. [2+2] Photo-cycloadditions of THPA and propargyl alcohol .....	183
5.3.3. Photo-Oxidations in the HPR .....	184
5.4. Development of a Continuous-Flow Reactor for Low Temperature Photo-Oxidations.....	188
5.4.1. <sup>1</sup> H NMR Analysis .....	188
5.4.2. General Reaction Procedures .....	190
5.5. Development towards a Self-Optimising Reactor for the Synthesis of 18.....	194
5.5.1. Description of the Automated Reactor .....	194
5.5.2. Issues with RS232 Connection to FP89-ME Control Unit .....	207
5.5.3. HPLC Method Development for the Quantification of 18 .....	208
5.5.4. ELSD Parameter Optimisation .....	212
5.5.5. External Artemisinin Calibration 1 .....	214
5.5.6. External Artemisinin Calibration 2 .....	220
5.5.7. Issues with ELSD Detection .....	224
5.5.8. External Standard Calibration 3 .....	230
5.5.9. Gradient Mobile Phase to Aid the Elution of DHAA .....	233
5.5.10. Internal Standard Calibration of DHAA and Artemisinin in Toluene .....	234
5.5.11. Internal Standard Calibration of 14 and 18 in DCM .....	241
5.5.12. Investigations into the Source of the Unknown Peak in UV .....	243
5.5.13. Internal Standard Calibration in DCM using ELSD .....	248
5.5.14. Internal Standard Calibration in Toluene .....	250
5.5.15. Alternative Column for the Separation of 18 and Toluene .....	254
5.5.16. Internal Standard Calibration in Toluene using UV.....	254
5.5.17. General Procedures for the Synthesis of 18 .....	258

5.6. Developing the Automated Synthesis of Rose Oxide, 13.....	263
5.6.1. HPLC Method Development.....	263
5.6.2. Internal Standard Calibration of Citronellol, trans- and cis-rose oxide .....	268
5.6.3. Reactions Conducted during the Development of the Automated Synthesis of 13 .....	273
5.6.4. Continuous Synthesis of the Citronellol Diols .....	275
Chapter 6. Thesis Conclusions and Future Directions .....	279
6.1. Aim 1 .....	279
Rationale .....	279
Progress.....	279
6.1. Aim 2 .....	280
Rationale .....	280
Progress.....	281
6.2. Aim 3 .....	282
Rationale .....	282
Progress.....	282
6.3. Future Directions .....	283
Bibliography .....	286

# Chapter 1. Introduction

Photochemistry has a long history stretching back to the 19<sup>th</sup> century and has the potential to contribute to the sustainability of the chemical manufacturing industries in the 21<sup>st</sup> century.<sup>10-15</sup> Recent advancements, in light and reactor technology, have allowed for the beginnings of a renaissance for photochemical synthesis.<sup>16-18</sup> In an era where environmental awareness is being pushed to the forefront of societal consciousness, industries, in particular chemical, are being increasingly required to develop more sustainable and energy-efficient processes that see reductions in waste generation and overall environmental impact.<sup>19</sup> Light can be regarded as a renewable, traceless reagent, therefore photochemistry has the potential to form the foundations for the transition to more sustainable chemical synthesis, that adhere to the 12 principles of green chemistry.<sup>15,20,21</sup>

However, there are a number of technical challenges which still need to be addressed before chemical manufacture powered by light or even sunlight can become widespread.<sup>18,22-25</sup> This Chapter explains the principles of photochemistry and outlines these challenges, particularly through the example of the semi-synthetic anti-malarial drug artemisinin which highlights some of the technical problems and how previous research has tried to address them. The Chapter ends with the overall aims of this Thesis and the strategy which has been developed to achieve them.

## 1.1. The Principles of Photochemistry

Photochemistry encompasses chemical reactions that are driven through the absorption of light, this can either be through the direct excitation of the molecule, or through the use of photocatalysts to facilitate electron transfer, generating reactive intermediates under mild conditions.<sup>26-29</sup> The absorption of a photon of appropriate energy generally results in the transition of an electron from the highest occupied molecular orbital (HOMO) to the lowest unoccupied molecular orbital (LUMO).<sup>30</sup> The high energy intermediates formed possess different electronic properties to their ground state analogues, thus, providing novel reactivity and enabling access to previously unobtainable synthetic pathways.<sup>31-35</sup>

Photochemical processes are governed by two fundamental principles: (i) the Grothüs-Draper law; and (ii) the Einstein-Stark law.

### 1.1.1. The First Law of Photochemistry

The first law of photochemistry, the Grotthüs-Draper law, states that only light that is absorbed is effective in producing chemical change.<sup>14</sup> Upon absorption of an incident photon of sufficient energy, an electron from the molecule's ground state ( $S_0$ ) undergoes a vertical 'vibronic' transition to a higher-energy excited singlet state ( $S_1$ ). For organic molecules, the energy required for these transitions is typically high and requires UV light. The excited states are usually short-lived and can be deactivated *via* physical or chemical processes. One such process is inter-system crossing (ISC), an intramolecular spin-forbidden transition between isoenergetic states of different multiplicities, such as, a transition from the first excited singlet state,  $S_1$ , to the first triplet state,  $T_1$ , as shown in Figure 1.1.<sup>36</sup> The relaxation from  $T_1$  to the ground state,  $S_0$ , referred to as phosphorescence, is spin-forbidden and, therefore, typically occurs on a longer timescale than the relaxation from a singlet excited state, such as  $S_1$ . Photochemical reactions of an excited state molecule will, according to Kasha's rule, usually originate from the lowest vibrational level of  $S_1$  or  $T_1$ .<sup>37</sup>

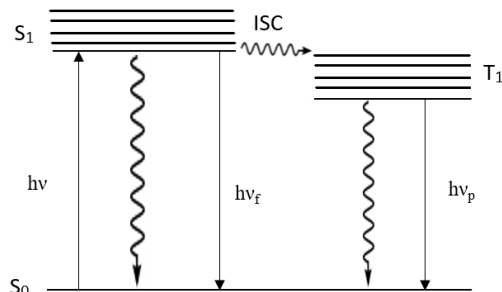


Figure 1.1: Simplified Jablonski diagram indicating excitation from the ground state ( $S_0$ ) to the first singlet excited state ( $S_1$ ) with the possibility of decay back to the ground state as fluorescence ( $h\nu_f$ ) or via intersystem crossing (ISC) to the longer-lived triplet state ( $T_1$ ). From  $T_1$  the excited molecule may decay back to the ground state via phosphorescence ( $h\nu_p$ ). Non-radiative decay in the form of vibrational relaxation may also occur from the excited states to reform the ground singlet state, depicted by the wavy arrows.

The excitation of an electron leads to the population of an anti-bonding orbital, lengthening and, hence, weakening the corresponding bond, resulting in the increased reactivity of the excited molecule. From the higher energy excited states, there is the potential for new synthetic pathways that cannot be pursued from the ground state. Processes that may be thermodynamically unfavourable in the ground state could be favourable when the molecule resides in an 'energy-rich' excited state.<sup>30</sup>

The redox properties between excited state and ground state molecules also differ. Excited state species are simultaneously both superior oxidising and reducing agents

compared to their ground states, allowing for labile photo-induced electron transfer (PET) processes to occur.<sup>30</sup>

### 1.1.2. The Second Law of Photochemistry

The second law, which is governed by the Einstein-Stark law of photochemical equivalence, states that the absorption of light is a quantum process involving one quantum per absorbing molecule (or atom).<sup>14</sup>

The efficiency of a photochemical process is described by its quantum yield,  $\phi$ , as shown in (1.1).<sup>38</sup> In an ideal situation, all absorbed photons result in a chemical transformation in which case  $\phi = 1$ . However, the quantum yield is rarely at unity and a yield above 0.3 is considered to be an efficient process.<sup>39</sup>

(1.1)

$$\phi = \frac{\text{number of molecules formed}}{\text{number of photons absorbed}}$$

### 1.1.3. Kinetic Rate Dependence on Temperature versus Photons

The Arrhenius equation (1.2), one of the fundamental equations in reaction kinetics, indicates the relationship between temperature and rate of reaction.<sup>40,41</sup> Where  $k$  is the rate constant,  $T$  is the absolute temperature (K),  $A$  is the pre-exponential factor related to the frequency of collisions between reactant molecules,  $E_a$  is the activation energy (J·mol<sup>-1</sup>), and  $R$  is the universal molar gas constant (8.314 JK<sup>-1</sup>mol<sup>-1</sup>).

$$k = A e^{(-\frac{E_a}{RT})} \quad (1.2)$$

To overcome the activation energy,  $E_a$ , and accelerate the reaction rate, heat is often employed. However, the temperature required to facilitate the reaction often causes decomposition of the reagents.<sup>42</sup> Therefore, strategies have been developed to lower the activation energy using additional reagents, such as, catalysts, acids/bases or, reductants/oxidants. These can be aggressive reagents, resulting in a detrimental effect on the green credentials of the processes.<sup>20,35,43</sup> An alternative is the use of light to generate highly reactive intermediates under mild, essentially reagent-less conditions.<sup>15,44</sup> The kinetics of photochemical reactions are strongly dependent on the photon flux, the number of photons absorbed per unit time, as shown in equation (1.3),

where  $k$  is the rate constant,  $\alpha$  is a constant dependent on the type of photochemistry,  $I$  is the light intensity ( $\text{W}\cdot\text{m}^{-2}$ ), and  $\beta$  is a constant dependent on the photon flux.<sup>45</sup>

$$k = \alpha I^\beta \quad (1.3)$$

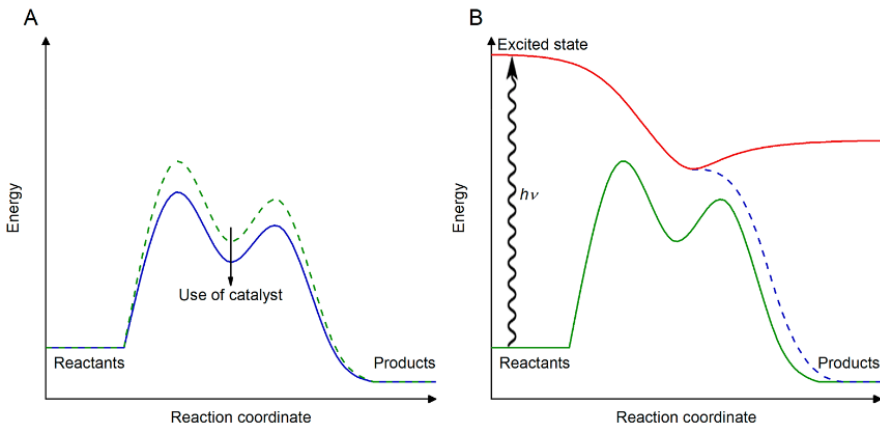


Figure 1.2: Reaction energy diagrams depicting, Left: typical profile of a thermal reaction with a stable intermediate, the use of a catalyst lowers the activation energy and, hence, increases the rate of the reaction. Right: photochemical activation. Upon absorption of a photon the substrate enters an excited state, from which the energy barrier to thermal transition has been avoided. Taken from Buglioni et al.<sup>35</sup>

For low light intensities ( $< 250 \text{ W}\cdot\text{m}^{-2}$ ),  $\beta$  is equal to 1, indicating a linear response between reaction rate and light intensity.<sup>45</sup> Upon increasing the light intensity to saturation,  $\beta = 0$ , the rate of reaction becomes independent of the photon flux. Additional photons will not be productively absorbed after this point. The linear part of this correlation can be extended by increasing the concentration of the photon absorbing species, be that substrate or photocatalyst. In terms of efficiency it is therefore important to balance the catalyst/substrate concentrations with the light intensity.<sup>35</sup> Since there is no thermal component to equation (1.3), photochemical reactions can be carried out at room temperature and below. Photochemical reactions can be rapidly quenched through the removal of light, greatly enhancing the safety aspects of these approaches.

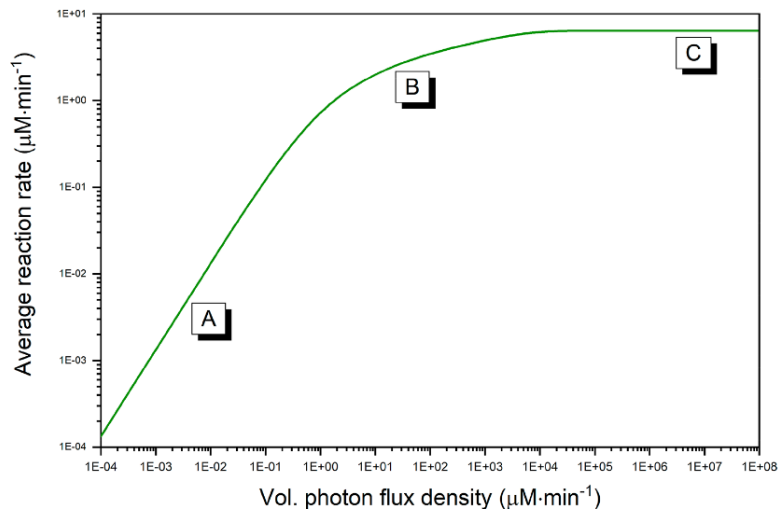


Figure 1.3: Average reaction rate versus photon flux. (A) Linear regime where  $\beta$  is 1.0 can be observed at lower light intensities. The reaction is photon limited in the entire reaction. The linear part can be extended by increasing the photocatalyst loading. (B) For intermediate light intensities,  $\beta$  is around 0.5 and kinetic limitations are apparent in some parts of the reactor. (C) For high photon flux,  $\beta$  become 0, and thus, the reaction rate is independent of the light intensity. Kinetic limitations are observed in the entire reactor. Taken from Buglioni et al.<sup>35</sup>

## 1.2. Singlet Oxygen

The physical, chemical and biological properties of singlet oxygen,  ${}^1\text{O}_2$ , have gathered ever increasing attention since the work done by Khan and Kasha in 1963.<sup>46</sup> The photosensitised production of singlet oxygen, has significant applications within photooxidation, photodynamic therapy (PDT) and in polymer science.<sup>47</sup>

The ground state of  $\text{O}_2$  is a triplet state,  ${}^3\text{O}_2$ , with the molecular term symbol  ${}^3\Sigma_g$ , this is the most stable and abundant form.  $\text{O}_2$  has two low-lying singlet excited states,  ${}^1\Delta_g$  and  ${}^1\Sigma_g$ , which are 95  $\text{kJ mol}^{-1}$  and 158  $\text{kJ mol}^{-1}$  above the ground state, respectively.<sup>48</sup> The  ${}^1\Sigma_g$  state is short-lived, rapidly decaying via a spin-allowed transition to  ${}^1\Delta_g$ . The relaxation of  ${}^1\Delta_g$  to  ${}^3\Sigma_g$  is spin-forbidden, resulting in a relatively long lifetime of the highly reactive  ${}^1\Delta_g$  state. The radiative lifetimes of the species highlights the difference in their stabilities with lifetimes for  ${}^1\Delta_g$  of 45 minutes in the gas phase and  $10^{-6}$ -  $10^{-3}$  s

in solution, compared to 7-12 s in the gas phase and  $10^{-11}$ -  $10^{-12}$  in solution for  ${}^1\Sigma_g$ .  ${}^1\Delta_g$  is therefore generally referred to as ‘singlet oxygen’ or  ${}^1\text{O}_2$ .

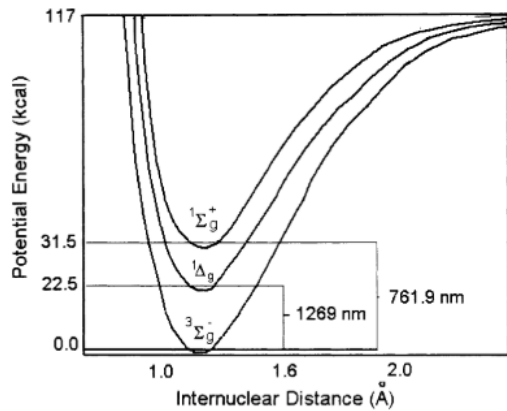


Figure 1.4. Potential energy plot of the ground state and excited states of oxygen, indicating that the  ${}^1\Delta_g$  state is the lowest lying excited state. Taken from DeRosa *et al.*<sup>47</sup>

### 1.2.1. Oxidations with ${}^1\text{O}_2$

Singlet oxygen can be generated chemically or photochemically, the latter being relevant to the research presented in this thesis.<sup>47</sup> The spin-forbidden direct excitation from  ${}^3\text{O}_2$  into  ${}^1\text{O}_2$  is a highly inefficient process, rendering it unsuitable for applications in synthesis. Therefore, a photosensitiser is required to facilitate the generation of  ${}^1\text{O}_2$ . Photosensitised oxidations with  ${}^1\text{O}_2$  occur via two mechanisms: Type I and Type II.

Type I photosensitised oxidation involve hydrogen abstraction or electron transfer between the excited photosensitiser, residing in its  $T_1$  state, and an organic substrate, yielding reactive oxygen species (ROS) that reacts with  ${}^3\text{O}_2$  forming an active oxygen species such as the superoxide radical anion,  $\text{O}_2^{\cdot-}$ .<sup>47</sup>

Type II photo-oxidations occur via the relaxation of the photosensitiser from the excited singlet,  $S_1$ , or most prominently from the triplet state  $T_1$  to the ground state  $S_0$ ; during this process, sufficient energy is transferred to  ${}^3\text{O}_2$  to promote it directly into the lowest lying excited state  ${}^1\text{O}_2$ . This pathway is preferred as the photosensitiser is not consumed during the process.<sup>47</sup>

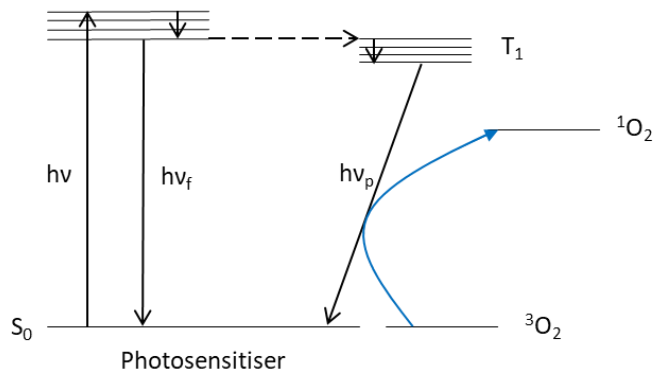


Figure 1.5. Generation of singlet oxygen via Type II photosensitisation. Excitation of the photosensitiser into the  $S_1$  excited state followed by ISC to a  $T_1$  state, energy transfer from this state results in the promotion of  $^3O_2$  into its lowest singlet excited state.

### 1.2.2. Lifetime and Quenching of $^1O_2$

The deactivation of  $^1O_2$  can proceed via radiative and non-radiative decay.<sup>49</sup> Radiative decay results in the emission of infrared light, while nonradiative decay occurs through the conversion of excitation energy to thermal energy.<sup>49,50</sup> Nonradiative decay is most prevalent while  $^1O_2$  is in solution, and the lifetime of  $^1O_2$  exhibits a strong dependence on the solvent, varying from microseconds in water to milliseconds in halogenated solvents.<sup>51-54</sup>

Table 1.1: The lifetime of  $^1O_2$  in different air-saturated solvents. Increased lifetimes can be observed when standard solvents have been deuterated, the highest lifetimes are observed in halogenated solvents.<sup>51-54</sup>

Solvent	Lifetime ( $\mu s$ )
carbon tetrachloride	59000
hexafluorobenzene	21000
chloroform-d	7000
acetone- $d_6$	992
benzene- $d_6$	681
chloroform	229
dichloromethane	99
acetonitrile	77
deuterium oxide	68
acetone	51
ethyl acetate	45
benzene	30
toluene	29
methanol	10
water	3

### 1.2.3. Photosensitisers for ${}^1\text{O}_2$ Generation

There are a number of photophysical parameters that determine the ability of a photosensitiser to produce  ${}^1\text{O}_2$ ; the singlet oxygen yield ( $\phi_\Delta$ ), the triplet-state yield ( $\phi_t$ ), the parameter  $S_\Delta$ , the triplet-state lifetime ( $\tau_t$ ), the triplet-state energy ( $\Delta E_t$ ) and the rate constant  $k_t^h$ .<sup>55</sup> The singlet oxygen yield,  $\phi_\Delta$ , is the probability that after absorbing a quantum of light, a photosensitiser populates its  $T_1$  triplet-state and then *via* energy transfer, promotes ground state oxygen,  ${}^3\text{O}_2$ , into its singlet state,  ${}^1\text{O}_2$ . The probability of the photosensitiser first populating the  $T_1$  state is represented by  $\phi_t$ . The triplet-state energy,  $\Delta E_t$ , is defined as the energy difference between  $T_1$  and the ground state,  $S_0$ . For singlet oxygen generation to occur,  $\Delta E_t$  must be higher in energy than singlet oxygen. The energy of singlet oxygen,  ${}^1\Delta_g$ , ( $\Delta E_\Delta$ ) is found to be 94.2 kJ mol<sup>-1</sup>.<sup>56</sup>

An ideal photosensitiser for singlet oxygen generation must therefore possess several properties:<sup>47</sup>

- Triplet state energy of  $E_t > 94.2$  kJ mol<sup>-1</sup>
- High absorption coefficient,  $\epsilon$ , in the spectral region overlapping with the incident light
- High triplet-state quantum yield ( $\phi_t > 0.4$ ) with a long  $T_1$  lifetime ( $\tau_t > 1\mu\text{s}$ )
- High photostability

There are several commercially available visible light absorbing photosensitisers that possess ideal attributes for  ${}^1\text{O}_2$  generation.<sup>57-60</sup> The photosensitisers of relevance in the following research are: rose bengal, ruthenium trisbipyridine  $[\text{Ru}(\text{bpy})_3]^{2+}$ , 9,10-dicyanoanthracene (DCA), and 5,10,15,20-Tetr phenylporphyrin (TPP), shown in Figure 1.6.

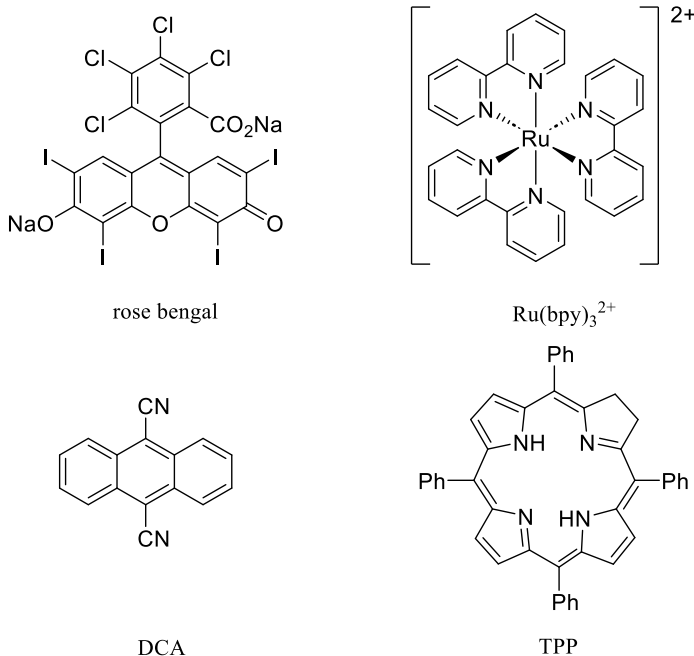


Figure 1.6: Commonly used photosensitisers for  ${}^1\text{O}_2$  generation, rose bengal,  $\text{Ru}(\text{bpy})_3^{2+}$ , DCA and TPP.

### 1.3. Photo-Oxidations with Singlet Oxygen

The  ${}^1\text{O}_2$  excited state can be deactivated via two main pathways: physical and chemical quenching. The process for physical quenching involves the interaction between  ${}^1\text{O}_2$  with a substrate in which only the deactivation of  ${}^1\text{O}_2$  to  ${}^3\text{O}_2$  occurs, with no product formation. Chemical quenching on the other hand involves the reaction of  ${}^1\text{O}_2$  with a substrate to produce a new product.<sup>47</sup>

Due to the vacant  $\pi^*$  molecular orbital,  ${}^1\text{O}_2$  is a strong electrophile, reacting rapidly with unsaturated carbon-carbon bonds.<sup>47</sup> The majority of the  ${}^1\text{O}_2$  reactions with unsaturated compounds can be divided into three distinct groups according to their pathways: cycloadditions: [4+2] and [2+2]; and the Schenck-ene reaction, shown in Figure 1.7.

[4+2] cycloadditions form endoperoxides, and are favoured by conjugated dienes, in a mechanism analogous to the [4+2] Diels-Alder cycloaddition. Electron-rich alkenes preferably react *via* a [2+2] mechanism to give 1,2-dioxetanes. Unactivated olefins, with allylic hydrogen atoms, undergo Schenck-ene type reactions to give allylhydroperoxides.<sup>61,62</sup>

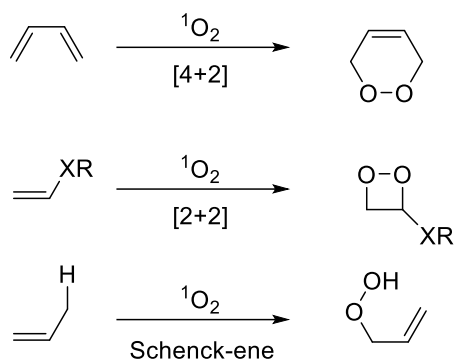


Figure 1.7. Potential reaction modes of singlet oxygen with olefinic substrates, from top to bottom: [4+2] cycloaddition to form an endoperoxide, [2+2] cycloaddition to form a dioxetane, Schenck-ene to produce a hydroperoxide.

### 1.3.1. Schenck-ene Photo-Oxidation

The Schenck-ene reaction of singlet oxygen and appropriate olefins was first discovered by Günther Schenck in 1943.<sup>61,63,64</sup> The reaction of singlet oxygen with unactivated alkenes has been studied extensively, providing a regioselective, and often stereoselective route to allylic hydroperoxides. The hydroperoxide products are synthetically useful: reduction leads to allylic alcohols; reaction with  $\text{Ti}^{\text{IV}}$  complexes produces epoxy alcohols; dehydration provides access to synthetically useful functionalised enones, as shown in Figure 1.8.<sup>65–69</sup>

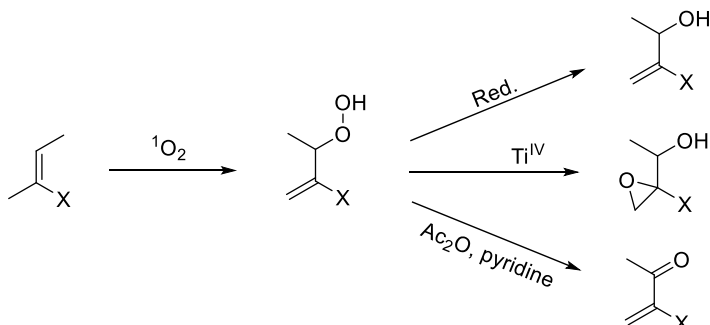


Figure 1.8. The reaction of  $^1\text{O}_2$  with a substrate possessing allylic hydrogens has the potential to form a hydroperoxide product, from which several synthetically useful products may be produced.

The mechanism of the ene-reaction has been heavily debated; several pathways, intermediates and transition states have been proposed.<sup>70–72</sup> The main point of contention is whether the reaction is concerted through a six-membered transition state, or stepwise.<sup>73–75</sup> A number of stepwise mechanisms involving several intermediates such as: an open biradical/dipolar;<sup>76,77</sup> a perepoxide;<sup>78</sup> an exciplex,<sup>79,80</sup> intermediate, or a 1,2-dioxetane have been proposed.<sup>81</sup>

Kinetic isotope effects (KIE) measurements on deuterium labelled tetramethylethylenes have provided the deepest understanding of the ene-reaction mechanism.<sup>73</sup> These measurements have ruled out the concerted mechanism along with the open biradical/dipolar intermediates.<sup>73</sup> Experimental data suggests a three-step pathway via an exciplex and a perepoxide is a viable mechanism for  ${}^1\text{O}_2$  addition to simple alkenes.<sup>73,82-84</sup> The most generally supported mechanism is via a three-step pathway, involving both a perepoxide and an exciplex intermediate, shown in Figure 1.9.<sup>85</sup>

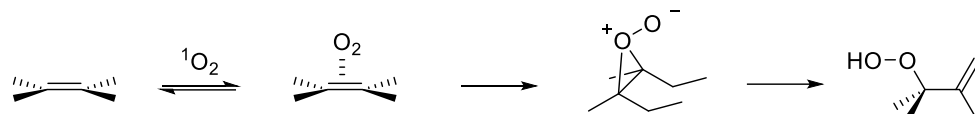


Figure 1.9. Stepwise mechanism for the ene-reaction, initiated with a reversible exciplex formation followed by a perepoxide and finally allylic hydrogen abstraction.<sup>85</sup>

The ene-reaction is in competition with the two other modes of photo-oxidation, 1,2- and 1,4- cycloadditions. The successful use of the ene-reaction, therefore, requires an understanding of the factors that favour this mechanism. These factors can be divided into three categories: conformational, steric, and electronic effects.

Conformational control occurs due to the nature of product forming step which requires a correctly aligned allylic hydrogen, depicted in Figure 1.10.<sup>61</sup> These effects are crucial in cyclic systems, in which the allylic hydrogens are only accessible from one  $\pi$  face of the substrate.

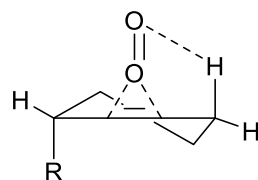


Figure 1.10. Diagram showing conformational control within a cyclic compound, abstraction of the correctly aligned allylic hydrogen occurs. Adapted from Prein *et al.*<sup>61</sup>

Even though  ${}^1\text{O}_2$  is a small electrophile, steric effects can still impact the facial selectivity of the reaction. Non-bonding repulsion between the substrate and  ${}^1\text{O}_2$  resulting in one  $\pi$  face of the double bond being more susceptible to  ${}^1\text{O}_2$  attack than the other.<sup>61</sup>

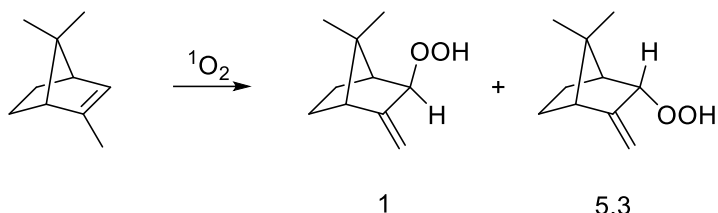


Figure 1.11. Steric control exhibited by the photo-oxidation of the dimethyl derivative of norbornene, attack from the top face is hindered.<sup>86</sup>

Electronic effects have been further divided into stereoelectronic and electronic control by Prein et al.<sup>61</sup> Stereoelectronic control describes the preference of  ${}^1\text{O}_2$  to attack the face of highest  $\pi$  electron density, this can occur in structures that exhibit orbital distortion. Electronic control describes through space interactions between the substrate and  ${}^1\text{O}_2$ , such as attractive hydrogen bonding as well as electrostatic attractions and repulsions.<sup>33,61</sup>



Figure 1.12. Left: 'stereochemical' control indicating differences in the electron density of the two faces of the alkene. Right: electronic control, interaction between the substituent  $X$  and singlet oxygen directs the electrophilic attack. Adapted from Prein et al.<sup>61</sup>

Control of selectivity is crucial for synthetic utility. Since  ${}^1\text{O}_2$  is a small, highly reactive reagent, control of its regioselectivity is non-trivial.<sup>61</sup> If a substrate has several allylic hydrogens, abstraction can take place from these various sites, leading to a complex mixture of isomeric products.<sup>61</sup> Several empirical rules have been established that allow for the determination of the regioselectivity of reactions with various substrates, these are depicted in Figure 1.13.

The *cis* effect, also referred to as side selectivity, states that hydrogen abstraction is most likely to occur at the most substituted side of the double bond; this is due to increased stabilisation of the negative charge of the perepoxide intermediate by H-bonding motifs.<sup>87</sup> The *gem* effect, also end selectivity, applies to the germinal-substituted alkenes, for which regioselectivity is induced by hyperconjugation between the  $n(O)$  and  $\sigma^*$  (C-EWG) orbitals; abstraction at the germinal position predominates.<sup>88,89</sup> The “Large group non-bonding effect” describes the site of preferred hydrogen abstraction for highly substituted alkenes.<sup>90,91</sup>

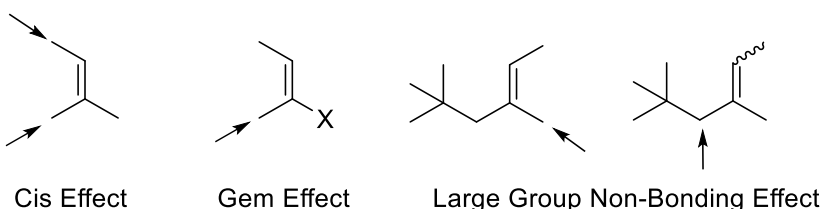


Figure 1.13. Indication of the sites of highest probability for hydrogen abstraction during the ene-reaction. Adapted from Prein *et al.*<sup>61</sup>

## 1.4. Reactor Design Considerations

### 1.4.1. Light Sources for Photochemistry

Light sources are classified according to their mode of light generation. The three most prominent types of light generation are incandescence, electric discharge and (electro)luminescence.<sup>92</sup> More useful for photochemical synthesis is the distinction between the type of light emitted, such as: a continuous polychromatic spectrum (type A); a discrete, polychromatic spectrum (type B); or a narrow-band monochromatic spectrum (type C).

Type A sources are typically incandescence-, halogen-, xenon arc- and fluorescence-lamps. These emit over a wide spectral range; to ensure reaction control, optical filters are used. Mercury arc lamps, depending on the pressure used, can vary between type A and type B. The Hg arc lamp is a commonly used light source in synthetic photochemistry often used in tandem with an immersion-well reactor.<sup>22</sup> The immersion-well has been the most dependable apparatus for laboratory scale photochemistry for over half a century.<sup>22</sup> The lamp is contained in a double-jacketed water-cooled immersion well, which is then placed into a reaction flask containing the substrate solution. The most common light source used in this set-up is a medium pressure Hg arc lamp, typically of powers 125-400 W for laboratory purposes. These lamps are type B with the most intense output being in the UV region. The polychromatic emission of UV, visible and IR regions means they are highly inefficient, with the latter emission spectra resulting in exceptionally high operating temperatures, up to 160°C on the surface.<sup>22,93</sup> A wide emission spectrum without sufficient filtration has the potential to influence detrimental side reactions.<sup>94</sup> Therefore, the choice of glassware is particularly important, functioning as an optical filter – quartz, Vycor®, Pyrex® and uranium glass have been used, which exhibit UV cut-off points of 200, 240, 300 and 350 nm respectively.<sup>22</sup>

Under the bracket of type C light sources fall: lasers, excimer lamps, light emitting diodes (LEDs), and organic light-emitting diodes (OLEDs). A significant factor in enabling the resurgence in photochemistry is the continual improvements in the development of LEDs, which, despite having broader emissions than lasers or excimers, allow for the facile use of near-monochromatic light. Furthermore, LEDs are energy efficient, durable, and produce high intensity light, reducing the effective cost of photons.<sup>92,95</sup> Since photochemistry is chromoselective, it is essential to maximise the overlap between the emission wavelength of the light source and absorption characteristics of the photon-absorbing molecule. Therefore, a light source is selected to have the optimum overlap with the maximum absorbance,  $\lambda_{\max}$ , of the molecule, or to overlap within a region whereby no competing photochemically induced side reactions occur.<sup>96</sup> LEDs emit through electroluminescence, this technology provides a wide selection for near-monochromatic spectra, minimising side-reactions and energy waste while increasing selectivity.<sup>95,97</sup> Due to the low intensity of a single LED, they are combined into arrays to provide higher overall intensities.

Maximising the available photon flux within a reactor is key for an intensification of the process - the position of the light source is therefore an important consideration. Light intensity is inversely proportional to the square of the distance, according to the inverse-square law of light (1.4). Clearly, the greater the distance between the light source and the reactor, the lower the light intensity within the reaction medium, resulting in reduced reaction capacity. It is, therefore, important to minimise this distance.

$$I = \frac{S}{4\pi r^2} \quad (1.4)$$

A key limitation with this style of “batch” photochemistry is described by the Bouguer-Beer-Lambert law equation (1.5) for light absorbance of a solution, where  $A$  is the light absorbance,  $T$  is the transmittance,  $\varepsilon$  is the molar absorption coefficient,  $c$  is the concentration of the solution,  $l$  is the path length through solution,  $I$  is the intensity of light after passing through sample, and  $I_o$  is the intensity of incident light.<sup>98</sup> The attenuation of light occurs exponentially with distance from the light source, leading to areas of significantly decreased irradiation within the reactor. For example, a strongly absorbing  $\pi, \pi^*$  transition with a molar extinction coefficient of  $20,000 \text{ M}^{-1} \text{ cm}^{-1}$  in a solution of concentration  $0.05 \text{ M}$ , will absorb 90% of the incident light at a distance of  $0.01 \text{ mm}$ .<sup>22</sup>

$$A = -\log_{10} T = -\log_{10} \frac{I}{I_0} = \epsilon cl \quad (1.5)$$

In a typical batch photochemical set-up, the area of solution furthest from the light source will be significantly under-irradiated when compared to the areas closest to the source. The problem is exacerbated upon scale up as the diameter of the vessels increases, a greater proportion of solution is under-irradiated, thereby greatly affecting conversion rates, yields and potential by-product formation.<sup>99</sup>

#### 1.4.2. Continuous-Flow Photochemistry

Continuous-flow methodology offers an elegant solution to the inherent problem of light attenuation. The use of narrow, transparent tubing results in only a small proportion of the total solution being irradiated at any one time, while the reduced path length allows for more efficient, uniform irradiation, thus, allowing the use of increased reaction concentrations, as shown in Figure 1.14.<sup>22,100,101</sup>

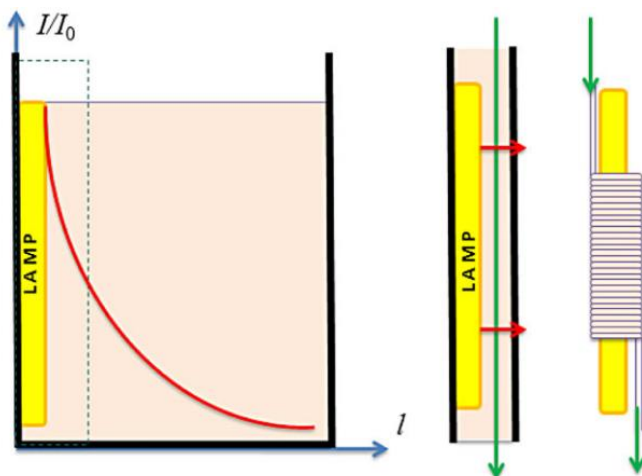


Figure 1.14. The intensity of light decreases rapidly with respect to the path length, flow systems with short path lengths are far more efficient. Taken from Gilmore *et al.*<sup>100</sup>

Continuous flow systems are becoming ever more popular within organic synthesis since their first introduction; due to enhanced reaction control.<sup>102,103</sup> Furthermore, flow systems are intrinsically safer than batch processes, as minimal volumes of solvent are in proximity to a potential ignition source at any one time.<sup>22</sup> They are also superior to conventional reactors in terms of mass and heat transfer, due to their high interfacial areas.<sup>104</sup> Heat transfer out of solution is more efficient as a greater proportion of the solution is in contact with the reactor walls, this effect can be enhanced by using materials and heat-exchange fluids with high conductivities. The improved heat management, in conjunction with low reactor temperatures can result in improved yields and selectivity.

Microflow ‘lab-on-a-chip’ photochemical reactors have gained significant interest as alternatives to batch processes.<sup>24,105–107</sup> Micro-structured reactors consist of a solid support with channels of only several micrometres in thickness, up to 1 mm, and are typically used with flow rates up to 1 mL min<sup>-1</sup>.<sup>105</sup> The reduction of channel size to, in some cases, only a few microns, allows for excellent light penetration of the reaction solution together with good heat and mass transport, permitting close control over reaction conditions including irradiation time, temperature, pressure and mixing.<sup>106</sup> There are, however, some disadvantages with these systems. Clearly, the throughput of a single microreactor is not sufficient, this can be addressed through a numbering up strategy.<sup>108</sup> This strategy can, however, lead to a number of challenges including: higher pressure drops, the need for multiple autonomous reaction systems and issues with inefficient flow distribution.<sup>108–110</sup> Therefore, numbering-up strategies are typically restricted to low throughput production.<sup>111–113</sup> Furthermore, microflow reactors are usually lithographically etched or moulded onto a planar surface and are, therefore, inefficient at fully capturing radial emission resulting in poor productivity.<sup>22</sup>

The most efficient method of maximising photon capture is to construct the reactor around the light source, the so-called annular reactor. The first example of this design was produced by Booker-Milburn by coiling UV transparent FEP tubing around an immersion well with the light source placed down the centre of the apparatus.<sup>114</sup> This design not only maximised photon capture but also utilised low cost, non-specialised equipment, therefore, bringing continuous flow photochemistry into the macroscale. The large surface area and proximity of the reactant solution to the light source ensured efficient irradiation of relatively large volumes of solution. These factors, along with the precise control of conditions, resulted in the production of 20–500 g of photochemical products in 24 hours.<sup>101,114</sup>

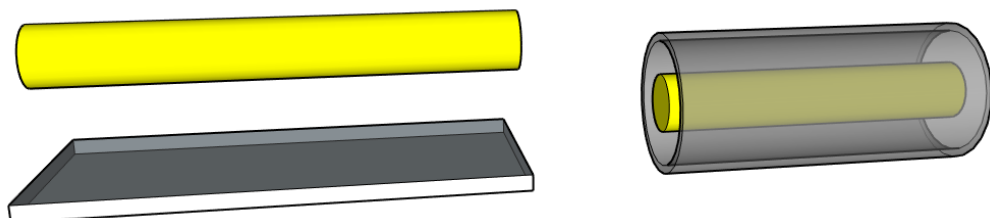


Figure 1.15. Models of a planar microfluidic reactor and light source (left) and an annular reactor with light source in the centre (right), the annular reactor can capture the radial emission of the light source far more efficiently than the planar microfluidic reactor.

## 1.5. Continuous Flow Photo-Oxidation

Liquid phase oxidations, which combine highly reactive species with organic solvents with the risk of combustion, have been shown to be safer at lower temperatures.<sup>115-117</sup> The intermediates and products formed, such as peroxides, are typically thermally unstable and may undergo vigorous decomposition at elevated temperatures.<sup>118</sup> These reactions are often highly exothermic; inefficient removal of heat from the reactor will affect the reaction thermodynamics and kinetics leading to reduced levels of selectivity and yield.<sup>104</sup> One of the most significant limiting factors is establishing the required stoichiometry by solubilising sufficient quantities of the gas into the reaction media.<sup>119</sup> Due to the often low solubility of gases, high pressures are required. As Henry's Law states, when a reaction temperature is elevated an increase in pressure is needed to maintain the same concentration of dissolved gas. The reverse is true for low temperatures.

Liquid phase oxidations are typically complicated to carry out in batch.<sup>119</sup> The reaction rate and the selectivity are greatly influenced by the mass transfer rate, which in turn is significantly improved by increasing the interfacial area.<sup>120,121</sup> Traditional reactors such as, bubble columns, trickle-bed reactors and stirred round bottom flasks, result in low interfacial areas. The scale-up of such reactors is non-trivial considering the safety hazards associated with these reactions.<sup>122-124</sup> In the case of a round bottom flask, the interfacial area decreases with increasing size, resulting in increasingly insufficient heat and mass transfer, further complicating scalability.<sup>119</sup>

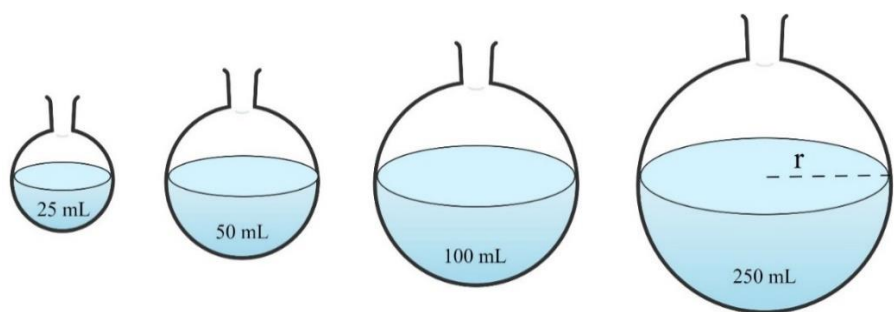


Figure 1.16 Schematic indicating the reduction in interfacial area between the liquid and the gas phase upon increasing the radius of a round-bottom flask. Adapted from C. Mallia et al.<sup>119</sup>

Due to the low solubility of oxygen in typical reaction solvents, low rates of diffusion occur resulting in slow reaction kinetics, and lengthy reaction times.<sup>125</sup> Moreover, oxygen at high concentrations will preferentially reside in the reactor headspace combining with reaction fumes, potentially leading to explosive conditions.<sup>126</sup> This is further exacerbated by the increased reaction length. To reduce these safety concerns in

batch oxidations, pure oxygen or oxygen enriched air is rarely used, adversely affecting the reaction kinetics and the selectivity.<sup>104</sup>

Continuous-flow systems are superior to conventional reactors in terms of mass and heat transfer, due to their potentially high interfacial areas.<sup>104</sup> Heat transfer out of solution is more efficient as a greater proportion of the solution is in contact with the reactor walls, this effect can be enhanced by using construction materials and heat-exchange fluids with high conductivities. The improved heat management, in turn with low reactor temperatures will lead to improved yields and selectivity. A common continuous-flow regime is the formation of Taylor flow (slug or segmented flow). Taylor flow is a highly uniform flow pattern characterised by gas bubbles separated by liquid ‘slugs’ and a thin film of solution coats the channel walls.<sup>104</sup> Internal circulations form in both the gas and liquid phases, give rise to homogeneous mixing and facilitates a fast mass transfer between the two phases.<sup>127–129</sup> Taylor flow can be initiated by simply combining a flow of gas with a flow of liquid at a junction.<sup>114</sup>

Taylor flow improves reactor safety. Only small proportions of potentially flammable solvents and substrates are in contact with oxygen at any time. Hazardous intermediates are generated *in situ*, which can be rapidly reacted in down-stream reactions, minimising the total amount of hazardous material being held in the laboratory.<sup>104</sup> It has been found that the explosion region was reduced under continuous-flow conditions when compared to batch processing.<sup>130–132</sup> High gaseous flow rates allow for higher oxygen concentrations to be used, avoiding the occurrence of ‘dead zones’ which are typically the cause of an explosion. An increase in the flow rate and a decrease in the pressure or temperature will increase the minimum critical oxygen concentration above which flame propagation becomes possible. Flow processing therefore widens the operational zone for these oxidation processes with higher reliability than batch processing.<sup>130</sup> In general, gases are easier to use in flow, their delivery can be regulated by dosing controlled volumes, and additionally the increased back-pressure due to the use of narrow tubing will aid the dissolution of oxygen, however, the use of narrow channels may also increase the risk of blockages.<sup>22</sup>

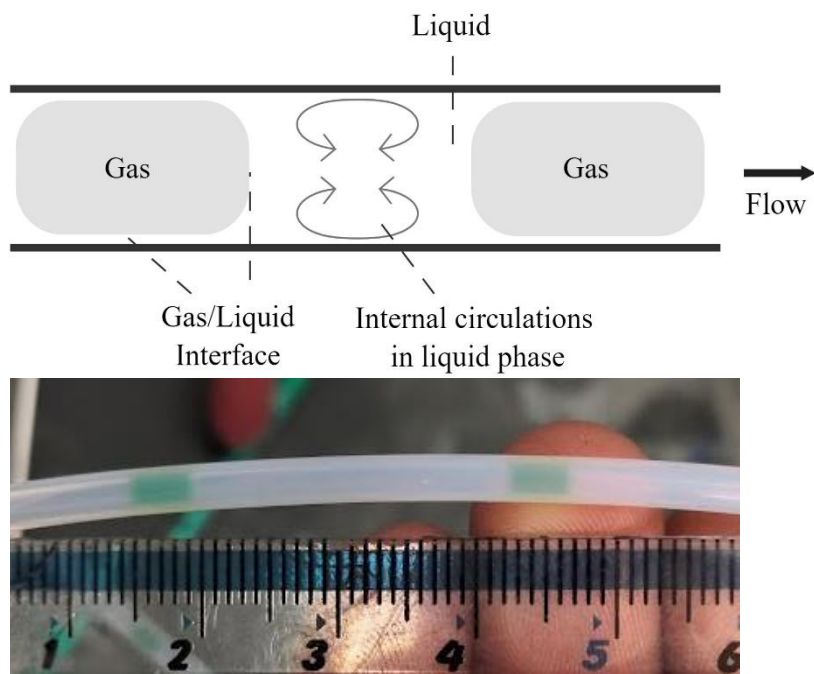


Figure 1.17: Top: Schematic of Taylor flow formation in a continuous-flow reactor, the arrows indicate the internal circulations within the liquid plug. Bottom: Photo of a Taylor flow in an FEP coil photoreactor.

## 1.6. Reactors for Continuous Photo-Oxidations

The first continuous-flow photo-oxidation, the [4+2] oxidation of  $\alpha$ -terpinene to produce ascaridole, was reported by *Wootton et al.* in 2002, using a lab-on-a-chip ‘nanoreactor’.<sup>133</sup> The reaction produced an ascaridole yield of 85% and an overall productivity of  $0.18 \mu\text{mol min}^{-1}$ .<sup>133</sup>

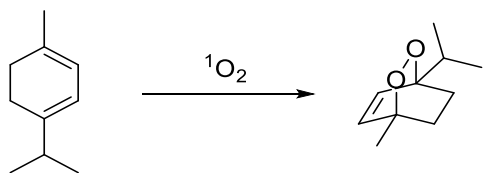


Figure 1.18. [4+2] oxidation of  $\alpha$ -terpinene with singlet oxygen to produce ascaridole.

This research opened the door for continuous-flow photo-oxidations, however, due to the low-throughput, this technology remained limited to laboratory scale investigations. The increase in attention on synthetic photochemistry for the production of important molecules, has caused an increase in the demand of novel reactor designs that improve reaction outcomes, and crucially, facilitate scale-up. The use of biphasic systems for

photo-oxidations presents significant design challenges and has, therefore, resulted in a diverse set of reactor designs have been to perform these reactions safely and efficiently. These reactors include, but are not limited to: falling film,<sup>134,135</sup> bubble column,<sup>136</sup> spinning disk,<sup>137–139</sup> Taylor flow,<sup>9,134,140</sup> Vortex,<sup>141–143</sup> high-pressure,<sup>144,145</sup> and nebulisation.<sup>146</sup>

### 1.6.1. Taylor Flow Reactor

The simple annular FEP reactor discussed in Section 1.4.2 has been regularly employed for performing photo-oxidative reactions. The generation of Taylor flow results in a high interfacial surface area, efficient mixing between the gaseous and liquid phases and therefore, high levels of mass transfer.<sup>140</sup> The first example of this reactor being used to perform photo-oxidations was reported by Lévesque *et al.* in 2011.<sup>140</sup> The reactor used FEP tubing coiled around an immersion-well photo-reactor containing a 450 W medium pressure mercury arc lamp.<sup>114,140</sup> The substrate and oxygen flows were combined and mixed using a polytetrafluoroethylene (PTFE) T-mixer. The researchers achieved high levels of conversion and reasonable productivities, on the mmol min<sup>-1</sup> scale, for the photo-oxidations of citronellol,  $\alpha$ -pinene and  $\alpha$ -terpinene. In later research, Lévesque also used this style of reactor to perform the photo-oxidation of dihydroartemisinic acid, **14**, and subsequent reaction to yield artemisinin, **18**, with an impressive productivity of 200 g day<sup>-1</sup>.<sup>9</sup>

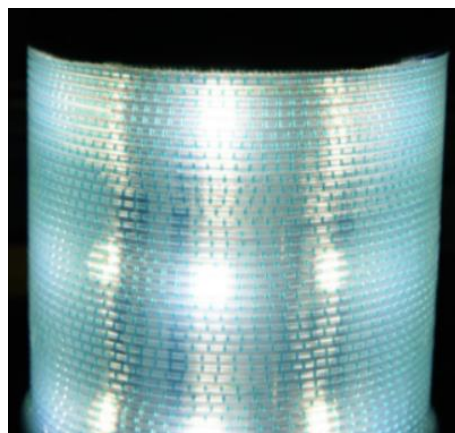


Figure 1.19: Photograph of a microfluidic FEP reactor performing the photo-oxidation of *N*-methyl-1,2,3,6-tetrahydropthalimide in acetonitrile using methylene blue as the photosensitiser. The individual substrate and oxygen slugs can be clearly seen in a periodic pattern. Photo taken from Schachtner *et al.*<sup>147</sup>

### 1.6.2. Vortex Reactor

The Vortex encompasses a group of reactors, developed in our group. They use a rapidly rotating stainless steel cylinder (50 - 4000 rpm) to generate Taylor vortices for continuous flow thermal and photochemical reactions, primarily photo-oxidations.<sup>79</sup> The generation of vortices enhances mixing and enables rapid mass transfer between the gas and liquid phase, allowing for a high efficiency dissolution of gasses.<sup>141</sup> The first design of the Vortex reactor, reported in 2017, is capable of efficiently drawing air from the laboratory without the need to use pressurised oxygen. This reactor possessed a volume of 8 cm<sup>3</sup>, and was used to perform the photo-oxidative syntheses of ascaridole and artemisinin, exhibiting productivities of 2.73 mmol h<sup>-1</sup> and 0.75 mmol h<sup>-1</sup> respectively.

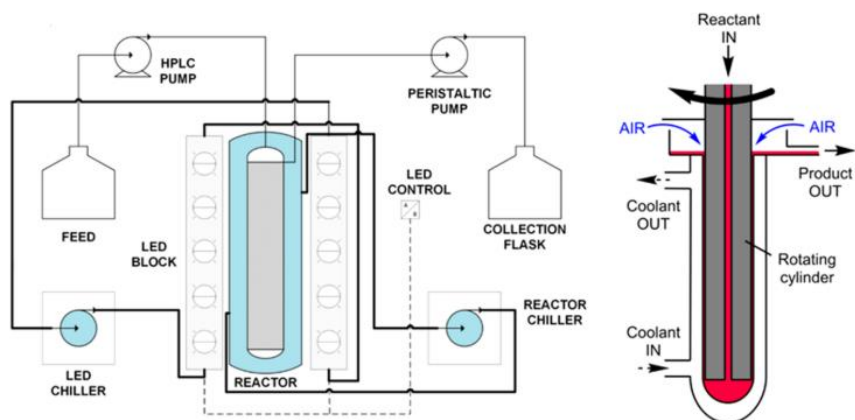


Figure 1.20: Left: Diagram of the Vortex reactor setup showing the tubing connected to the reactor, and the position of the LED blocks. Right: Cross-section of the reactor showing the delivery and removal of reagents and of the intake of air.

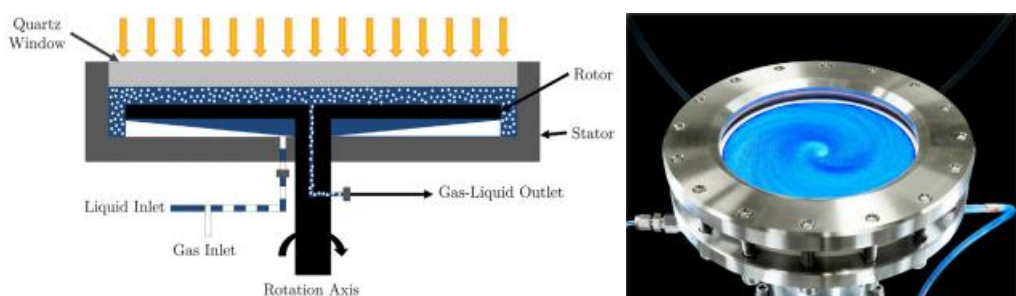
Subsequent design adaptations have facilitated the scale up of the reactor to a volume of 280 mL.<sup>142</sup> This Vortex was used for the photo-oxidation of citronellol, giving a high level of productivity, measured to be 2 kg day<sup>-1</sup>, a significant increase on 6.4 g day<sup>-1</sup> achieved with the original reactor.

### 1.6.3. Rotor-Stator Spinning Disk Reactor

The Rotor-Stator Spinning Disk Reactor (RS-SDR) was first reported by Chaudhuri *et al.* in 2020, in which it was reported that this reactor possessed high throughput capabilities, performing the photo-oxidative synthesis of ascaridole on a 1.1 kg day<sup>-1</sup> scale.<sup>139</sup> Furthermore, when compared to other reactors capable of performing this photo-oxidation such as the batch immersion well, microflow, falling film, thin film

and Vortex reactors, the RS-SDR was found to have higher productivity as well as higher productivity per volume.

The RS-SDR consists of a fast-rotating disk, the rotor, which is encased between two stators positioned at short distance from the rotor (1-2 mm). At high RPM, the fluids are highly turbulent due to the velocity difference between the spinning disk and the stator, resulting in efficient and rapid mixing, consequently leading to high mass and heat transfer rates.<sup>139,148,149</sup>



#### 1.6.4. Nebuliser-Based Continuous Flow Reactor

The Nebuliser-Based Continuous Flow Reactor uses a highly innovative approach for undertaking large-scale photo-oxidations.<sup>146</sup> The reactor addresses the two major drawbacks of photo-oxidations; the effect of poor oxygen solubility on the rate of biphasic gas-liquid reactions and, the high level of light attenuation by solutions. The reactor operates by nebulising the photo-oxidation solution inside a low-energy energy strip. Thus, greatly increasing the interfacial area, improving light penetration and, consequently, leading to improved reaction rates.<sup>146</sup> This reactor has been employed to perform the photo-oxidations of citronellol,  $\alpha$ -terpinene, and (5-methylfuran-2-yl)methanol, achieving high levels of conversion and productivities on a  $\text{mmol min}^{-1}$  scale.

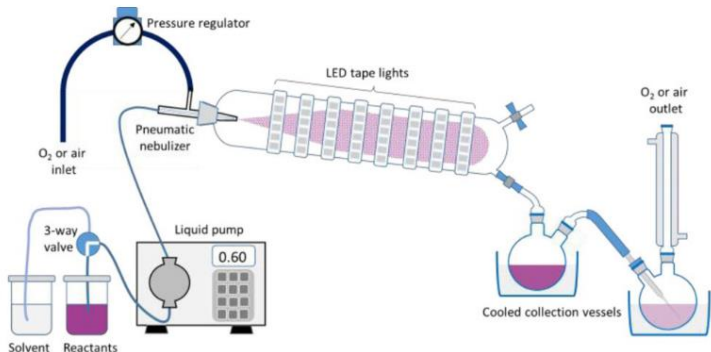


Figure 1.21: Schematic of the Nebulizer-Based Photo-oxygenation Reactor (NebPhotOX). Image taken from Ioannou et al.<sup>146</sup>

## 1.7. Rose Oxide

Rose oxide, **13** in Figure 1.23, is the common name of the four diastereoisomers of *cis*- and *trans*-4-methyl-2-(2-methylprop-1-enyl)tetrahydro-2H-pyran. Rose oxide was first isolated from Bulgarian rose oil in 1959, since then each of the four isomers have been identified in many plants, flowers and fruits.<sup>150,151</sup> However, it is (-)-*cis*-rose oxide ( (2S, 4R)-4-Methyl-2-(2-methylprop-1-enyl) tetrahydro-2H-pyran form that is the main olfactory contributor and, hence, the most desired and expensive. The extraction process of rose oxide is expensive with approximately 3000 kg of rose blossoms required to produce 1 kg of rose oil, hence, this process is limited to the preparation of high value perfumes.<sup>152,153</sup>

A number of routes for the synthesis of rose oxide have been developed utilising both traditional and photochemical techniques;<sup>151,152,154,155</sup> the most significant of which is the photochemical route developed by Dragoco (now Symrise) and described in their patent.<sup>156</sup> The chemical synthesis of rose oxide is one of the very few examples of photochemistry being used industrially for the production of a fine chemical.<sup>157</sup> Synthetic rose oxide, however, contains a mixture of the four stereoisomers, shown in Figure 1.22, and is largely used in lower value cosmetics and scents.

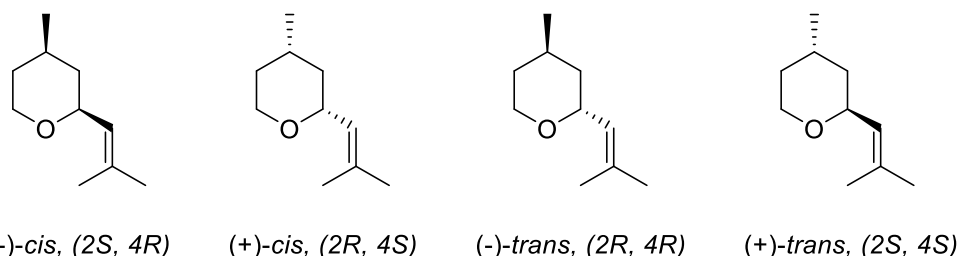


Figure 1.22. The four stereoisomers of rose oxide. (-)-cis-rose oxide and (-)-trans have both been described to have a floral green odour with detection thresholds of 0.5 and 160 ppb respectively. While the two (+)-forms have both been described to possess a herbal green odour with thresholds of 50 ppb for the cis- and 80 ppb for the trans-form.

The Dragoco protocol is based on the rose bengal photosensitised oxidation of citronellol, **8**, in methanol. The first step is the Schenck-ene photo-oxidation, producing two hydroperoxides intermediates, **9** and **10**, which are subsequently reduced *via* the addition of sodium sulphite,  $\text{Na}_2\text{SO}_3$ , to the corresponding diols - 3,7-diemthyl-5-octen-1,7-diol, **11**, and 3,7-diemthyl-5-octen-1,6-diol, **12**. The 1,7-diol then undergoes a sulphuric acid catalysed cyclisation to afford rose oxide. The 1,6-diol is considered unable to be synthesised into rose oxide and is therefore a by-product. Increasing the selectivity of the photo-oxidation will in turn increase the yield of the 1,7-diol and hence, after cyclisation, the overall yield of rose oxide.

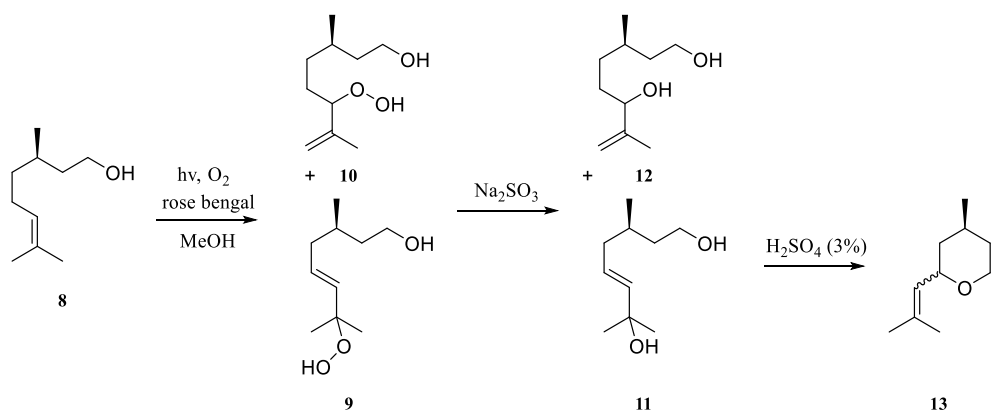


Figure 1.23: Dragoco synthesis of rose oxide. The photo-oxidation of citronellol, **8**, using rose bengal,  $\text{Hg}$  arc lamp, in methanol produces two hydroperoxides, **9** and **10**, these are subsequently reduced to the corresponding diols, **11** and **12**, from which on **11** cyclises to afford rose oxide, **13**.

Building on from the Dragoco protocol, Meyer *et al.* utilised the beneficial properties of a microreactor equipped with LEDs to develop the synthesis of rose oxide in flow. Their work reported an increase in the space-time-yield of an order of magnitude of the microreactor compared to a traditional batch immersion well.<sup>154</sup>

The reported procedure focusses on the photo-oxidation of (S)-(-)- $\beta$ -citronellol, while using the same conditions as the Dragoco protocol for the subsequent reduction and

cyclisation to yield *cis*- and *trans*-(-)-rose oxide. The researchers selected as the photosensitiser, tris(4,4'-*tert*-butyl-2,2'-dipyridyl)-ruthenium(II)-dichloride, Ru(<sup>t</sup>bpy)<sub>3</sub>Cl<sub>2</sub>, which possess a greater quantum yield of singlet oxygen generation,  $\Phi_{\Delta}$ , than rose bengal, while also possessing higher stability towards quenching by  $^1\text{O}_2$ .<sup>158</sup> The reaction was carried out in ethanol, a more benign solvent than methanol. The photosensitiser and solvent combination gives a  $\lambda_{\text{max}}$  around 460 nm which overlaps well with the blue LED  $\lambda_{\text{max}}$  of 468 nm. Their work found that rose bengal was approximately twice as efficient in the conversion of citronellol as the ruthenium complex, explained by the latter's significantly larger molar absorption coefficient.<sup>58,159</sup>

## 1.8. Artemisinin and Malaria

According to the World Health Organisation's (WHO) Malaria report from 2019, there were an estimated 228,000,000 cases and a subsequent 405,000 deaths caused by malaria worldwide in 2018.<sup>1</sup> Malaria, caused by the *Plasmodium* parasite and transmitted most commonly by female mosquitos, continues to be one of the most deadly infectious diseases in the world.<sup>160-162</sup> Malaria has devastated vast areas of the globe, primarily in tropical and sub-tropical regions. These regions contain some of the most underdeveloped nations in the world. The ultimate goal for the treatment of malaria is the development of a vaccine. This has been a challenge due to the complex, multi-stage life cycles of the *Plasmodium* parasites. However, this goal was achieved in 2021 success through the development of the RTS,S/AS01 vaccine.<sup>163</sup> The vaccine is 50% effective in preventing clinical cases of malaria in children aged 5 to 17 months.<sup>164</sup> The modest efficacy combined with the logistical complexities of the widespread roll-out, have prevented the vaccine from being the panacea that is desired.<sup>3</sup> Therefore, the continued development of effective chemotherapeutics remains the most viable method for the treatment of malaria.<sup>165,166</sup>

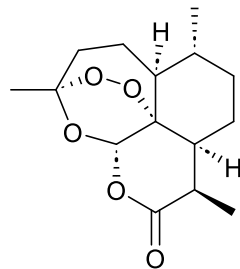


Figure 1.24: Artemisinin

Artemisinin is a sesquiterpene endoperoxide, that is active against both chloroquine-sensitive and quinine-resistant strains of *Plasmodium falciparum*, the most virulent

species of the malaria parasite.<sup>167,168</sup> Artemisinin combination therapy (ACT) has been successfully used for the treatment of severe cerebral malaria.<sup>168,165</sup> ACT is the combination of artemisinin or derivatives with a secondary antimalarial drug, was designated as the first-line antimalarial treatment by the World Health Organisation (WHO) in 2002.<sup>2,169</sup> The mechanism of action of artemisinin is not fully understood, however it is accepted that the 1,2,4-trioxane endoperoxide moiety is necessary for its antimalarial properties.<sup>165,170,171</sup>

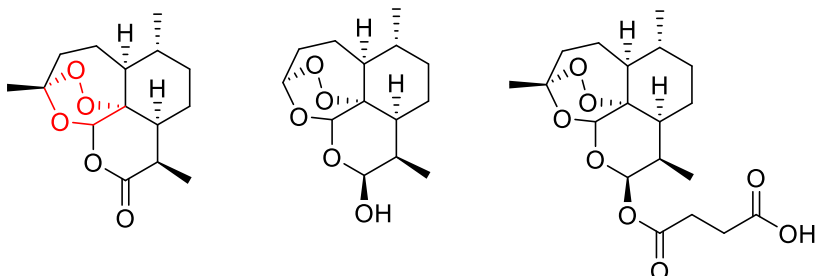


Figure 1.25. Left to right: the structures of artemisinin, highlighting in red the 1,2,4-trioxane endoperoxide moiety, dihydroartemisinin and artesunate.

A single adult ACT treatment course costs approximately US \$1, around 10 times more than treatment with chloroquine, which is itself unaffordable for the majority of impacted people. Furthermore, chloroquine is becoming increasingly ineffective.<sup>171</sup> The relatively high cost of ACT treatment reflects the cost in growing large amounts of the plant, *Artemisia annua*, from which artemisinin is extracted. High costs are also involved in the reduction of artemisinin to dihydroartemisinin, a step that allows for the synthesis of the artemisinin derivatives; this process is labour, energy and cost intensive, all of which are reflected in the price of the final product.<sup>171,172</sup> It is, therefore, of great importance to find an alternative, non-plant derived method to produce artemisinin, such that it may be produced on a sufficiently large scale and importantly, at an affordable price so that those most in need can have the access to ACT treatment.

### 1.8.1. Mechanism for the formation of Artemisinin

The total synthesis of artemisinin was first reported by Schmid and Hofheinz in 1983; this method is, however, complex and expensive.<sup>173</sup> The semi-synthesis of artemisinin is a far more attractive and realistic prospect for reliable production on a large and affordable scale.<sup>174</sup> Keasling and co-workers, reported the bio-synthesis of artemisinic acid in engineered yeast and bacteria in 2006 and 2009 respectively.<sup>174,175</sup> Artemisinic acid is reduced to form dihydroartemisinic acid (DHAA), compound **14** in Figure 1.26, a biosynthetic precursor to artemisinin, **18**.<sup>176</sup>

Wallaart *et al.* isolated DHAA from *Artemisia Annua* in a 29 % yield, along with the tertiary allylic hydroperoxide, **15**, shown in Figure 1.26, hence, determining that the biosynthetic pathway proceeds *via* this intermediate. **15** is also the major hydroperoxide formed through the photo-oxidation of **14**, thus, providing evidence for a non-enzymatic photochemical conversion of **14** to **18**, *in vivo*, in the plant.<sup>7,176–178</sup> It has been known for some time that the 1,2,4-trioxane (endoperoxide) ring is responsible for the antimalarial efficacy of artemisinin.<sup>179</sup> The formation of this moiety has, therefore, been a topic of interest for decades, with investigations into the potential enzymatic,<sup>180–182</sup> and non-enzymatic pathways.<sup>7,176–178,183,184</sup>

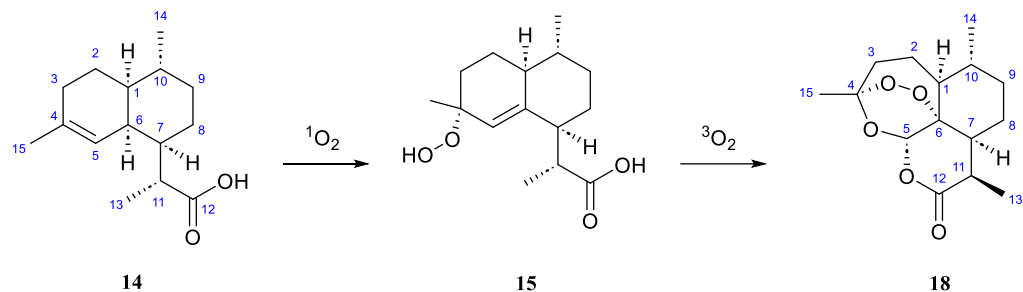


Figure 1.26 Formation of artemisinin, **18**, from dihydroartemisinic acid, **14**, through the tertiary allylic hydroperoxide intermediate, **15**.

The mechanism is accepted to first involve a Schenck-ene oxidation of **14** with  $^1\text{O}_2$  to form three allylic hydroperoxide products, **15**, **16** and **17** shown in Figure 1.27. Hock Cleavage of the C4-C5 bond of **15**, followed by oxidation with  $^3\text{O}_2$  and subsequent cyclisation forms the endoperoxide bridge of **18**.<sup>5,184</sup>

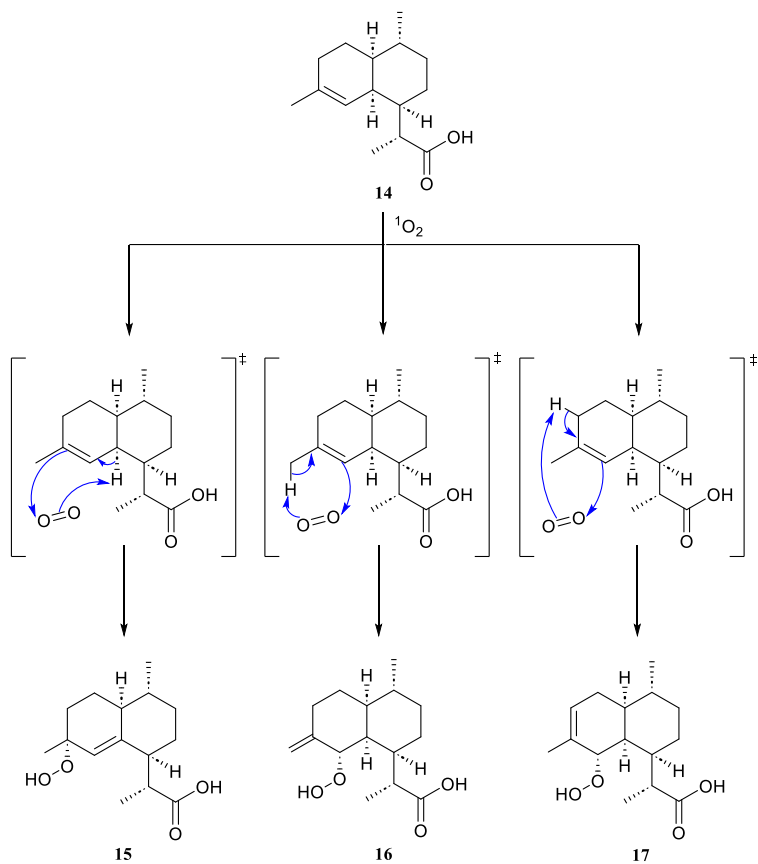


Figure 1.27: Mechanism of the formation of the three hydroperoxides proceeding via the Schenck-ene oxidation of **14**.

In a study that involved the reaction of the DHAA hydroperoxide and  $^{18}\text{O}_2$  gas in the presence of acid in  $\text{Et}_2\text{O}$ , conducted by Acton *et al.* it was confirmed that the endoperoxide oxygen originates from molecular oxygen reacting with the hydroperoxide intermediate.<sup>7</sup> The resulting artemisinin synthesised in this study had a distribution of non-labelled, mono-labelled, and di-labelled products in a ratio of 53:100:43 as determined by mass spectrometry and 65:100:48 through  $^{13}\text{C}$  NMR.<sup>6</sup> These observations, provided evidence that **18** is formed through a complex mixed mechanism.<sup>7,184</sup> Further studies by Varela *et al.* measured **18** with isotopic composition of 1.0:7.2:14 for  $^{18}\text{O}_2$ : $^{18}\text{O}_3$ : $^{18}\text{O}_4$ ; these findings corroborating the proposal of a complex mixed mechanism.<sup>183,184</sup>

Despite extensive studies, the actual biosynthetic mechanism from **14** to **18** is still a point of contention.<sup>184</sup> There is, however, significant evidence of the direct conversion of **14** to **18**.<sup>177,178,184-186</sup> In a 2002 study, G. Brown and L. Sy investigated the mechanism of the auto-oxidation of **14** to **18** and other products; **14**, stored in deuterated chloroform

over several weeks, was found to produce, **18**, **15**, dihydro-*epi*-deoxyarteannuin B, **20**, and arteannuin H. <sup>1</sup>H NMR signals belonging to **15** appeared early on and then declined, **18** formed steadily, indicating that **15** is an intermediate in the spontaneous conversion of **14** to **18**. To confirm this, a purified sample of **15** was left in a solution of CDCl<sub>3</sub> for several days, the formation of **18** and **20** was observed, along with a gradual decline in **15**. Next, the researchers added trifluoroacetic acid (TFA) to a petroleum ether solution of **15**, they noted that the transformations were ‘rapid and simplified (in comparison to the auto-oxidation product mixture)’ with two products being isolated, **18** and **20**.

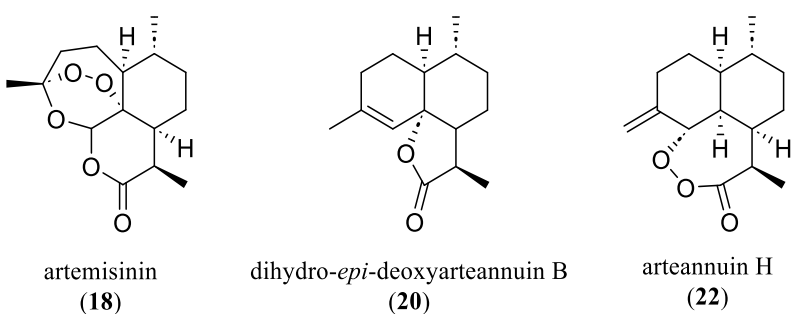


Figure 1.28: Common products found from the spontaneous auto-oxidation of DHHA, **14**, as determine by Brown and Sy.<sup>178</sup>

In efforts to investigate the mechanism for the C4-C5 cleavage the researchers attempted to prevent the oxidation of **15**, by preparing the compound in a solution of CDCl<sub>3</sub> under an atmosphere of N<sub>2</sub>. In total, 12 compounds were separated by HPLC and characterised by 2D NMR. The most prominent compound measured was the aldehyde formed through the tautomerisation of the enol intermediate, as shown in Figure 1.29. Addition of TFA resulted in almost immediate conversion into the 6-lactone, **19**. This was repeated at 233 K with continual monitoring by 2D NMR, allowing for the structure of the enol to be confirmed. Increasing the temperature to 298 K while maintaining an atmosphere of nitrogen, caused the enol to be predominantly converted into **19**. In comparison, when the temperature was raised and oxygen introduced, almost quantitative conversion of the enol into **18** was measured.

Arteannuin H is thought to derive from the secondary allylic DHAA hydroperoxide, **16** in Figure 1.27.<sup>187</sup> Small <sup>1</sup>H NMR peaks were detected that correspond to the primary allylic hydroperoxide which has been reported as a product from the 3,2-allylic rearrangement of **16** which competes with the lactonisation reaction involved in the formation of arteannuin H, Figure 1.30.<sup>185,187</sup>

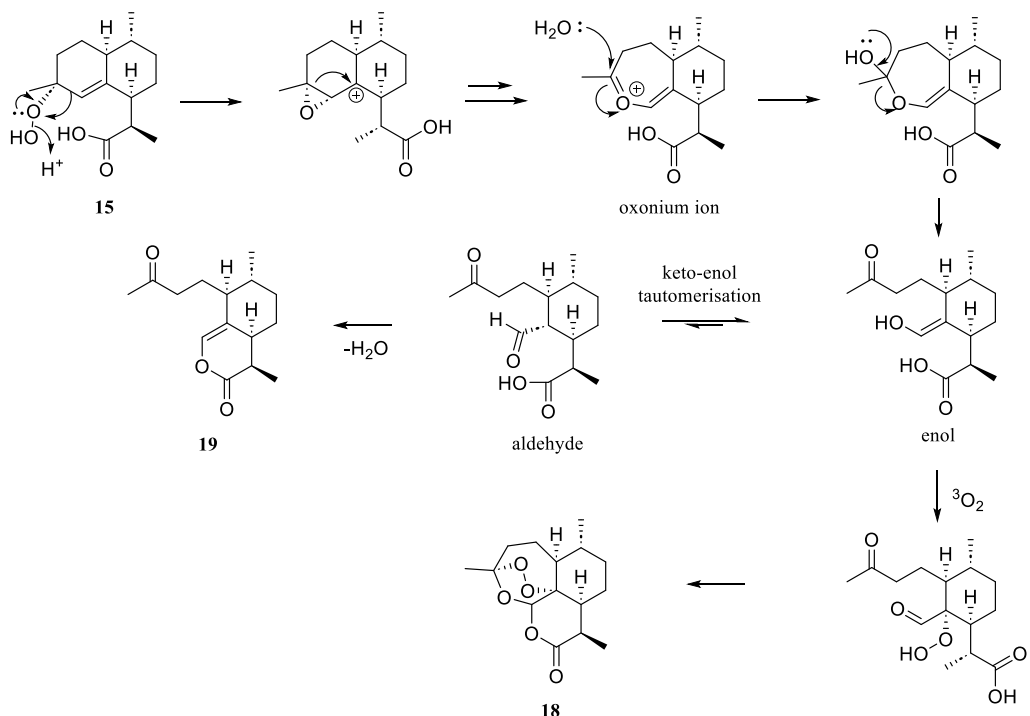


Figure 1.29: Mechanism for the synthesis of **18** from hydroperoxide **15**. Addition of acid to the **15** catalyses the Hock Cleavage to form the oxonium ion which subsequently opens to form the enol intermediate. Addition of ground state oxygen,  $^3O_2$ , forms another hydroperoxide which eventually cyclises through a series of cascade reactions to form the endoperoxide bridge and afford **18**. The enol, in the absence of  $O_2$ , will tautomerise to the aldehyde, addition of acid then cyclises the aldehyde to the 6-lactone, **19**, as shown. Adapted from Lee *et al.* and Kopetzki *et al.*<sup>8,141</sup>

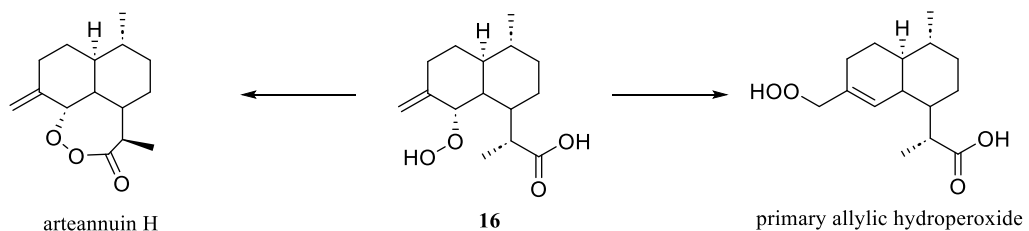


Figure 1.30: The competing reactions of the secondary DHAA hydroperoxide, **16**. The primary allylic hydroperoxide is formed through a 3,2-allylic rearrangement, while arteannuin H is formed through the lactonisation of **16**. Adapted from Sy *et al.*<sup>178</sup>

In 2004 Brown and Sy also reported the formation of **18** in a sample of solid **14** stored at  $-20^{\circ}\text{C}$  in the absence of light for six months.<sup>177</sup> Varela *et al.* confirmed the formation of **18** from **14** stored in glass vials left open to the air, in both light and dark conditions, albeit with a far slower rate of conversion for the latter.<sup>184</sup> They reported a potential NMR signal corresponding to **15** after 10 days, however the signal at  $\delta$  5.24 is slightly upfield of the expected value of  $\delta$  5.26, and the area of the peak was found to be insignificant relative to that of **18** ( $\delta$  5.87).<sup>176</sup> A signal with a chemical shift of  $\delta$  5.64 appeared after 7 days, corresponding to **20**, a natural product that has been isolated from

*A. Annua* and was also found by Brown and Sy.<sup>178,184,188</sup> The formation of **20** follows an intramolecular S<sub>N</sub>2' displacement of hydrogen peroxide by the carboxylic acid moiety in **15**.<sup>178</sup>

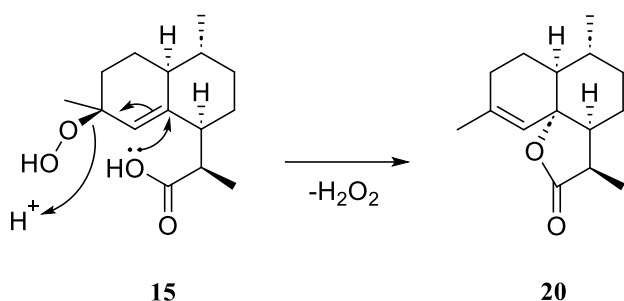


Figure 1.31: Formation of **20** through the intramolecular  $Sn2'$  displacement of hydrogen peroxide to form the 5-membered lactone. Adapted from K. Varela et al.<sup>184</sup>

Recently, Varela *et al.* conducted further research to try to elucidate the pathways in this complex cascade reaction; proposing that all the allylic hydroperoxides, **15–17**, convert to the same oxonium ion (shown in Figure 1.29) which then reacts with oxygen to afford **18**, as shown in Figure 1.34.<sup>183</sup> This mechanism however, does not agree with the generally accepted mechanism in which only **15** is considered capable of forming **18**. Moreover, the mechanism contradicts the observations that the secondary hydroperoxides, **16** and **17**, are stable under the conditions of the acid catalysed Hock Cleavage and thermal oxidation cascade.<sup>8,9,183,184,189</sup>

Varela and co-workers also investigated the effect of irradiating **14** with UV-C light - forming **18** after 2.5 hours.<sup>183</sup> **18** was then irradiated with UV-C light for 8 days, the material was purified and a rearranged product that lacked the endoperoxide bridge was identified, shown in Figure 1.32. This compound was previously detected when **18** was left under ambient light for 64 days, however was not present after sample of **18** was left in the dark for the same length of time.<sup>184</sup> This suggests that although light accelerates the conversion of **14** to **18**, prolonged exposure to excessively strong radiation will result in decomposition.<sup>183</sup> The decomposition product was also previously identified when artemisinin was heated to 190°C.<sup>190</sup> Along with irradiation with UV-C, **14** was irradiated with IR radiation and at 80°C, neither of these conditions produced **18**.

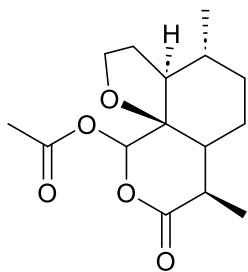


Figure 1.32: Structure of the compound isolated from the irradiation of **18** with UV-C light.<sup>184</sup>

Figure 1.33

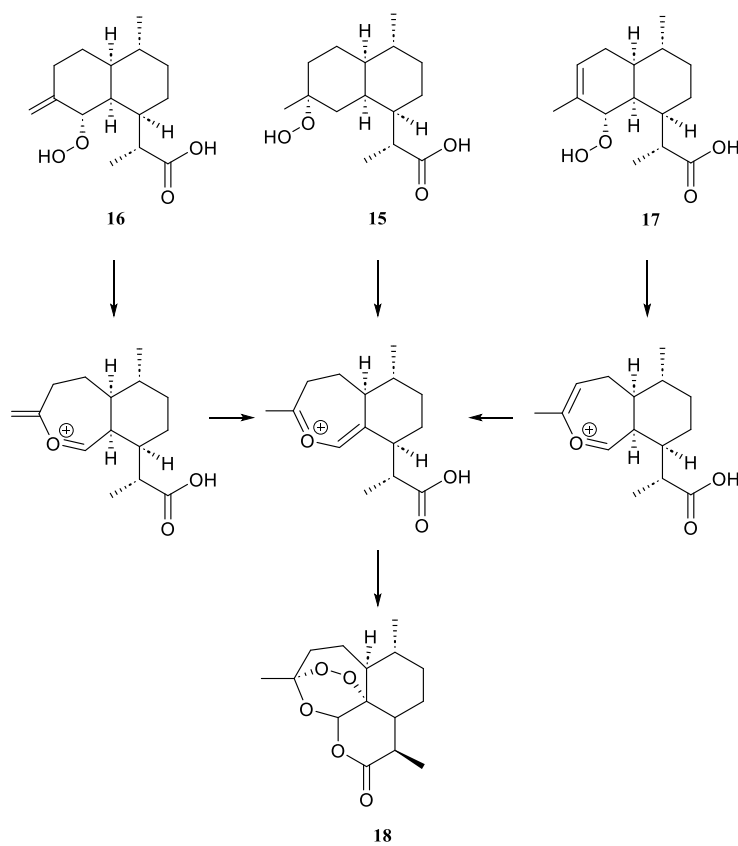


Figure 1.34: proposed mechanism for the conversion of the three DHAA hydroperoxides, **15-17** to their corresponding oxonium ions, which each rearrange to form the common oxonium primarily formed through **15**. From this oxonium ion the subsequent formation of **18** can occur.

### 1.8.2. Photochemical Synthesis of Artemisinin

The first partial synthesis of artemisinin was carried out by Roth and Acton in 1989, their method started with a nickel boride reduction of artemisinic acid to give a 5:1 (R:S) mixture of **14**, of which only the R-isomer can form **18**.<sup>6</sup> **14** was then photo-oxidised at -78°C in dichloromethane, using methylene blue as the photocatalyst. The

resulting solution was then left to stand in petroleum ether at room temperature for 4 days, giving a 17 % yield of **18**.<sup>6</sup>

The first semi-synthetic method that had scale-up potential was developed by the team at Amyris.<sup>191</sup> Their method first involved the use of Wilkinson's catalyst for the asymmetric catalytic hydrogenation of artemisinic acid to give a 9:1 (R:S) ratio of **14**. To avoid the significant cost associated with using specialised photochemical equipment on an industrial scale, Amyris decided to generate  $^1\text{O}_2$  chemically, giving a 40% yield of **18**. This technology was then transferred to the biopharmaceutical company, Sanofi, in 2008, where it became apparent that the route had reached its performance limits and would not be cost-effective enough for commercial production.<sup>192</sup>

Sanofi revisited the photochemical production of  $^1\text{O}_2$ . Photochemical reactions are rarely practiced within industry, with even less precedence for large scale photo-oxidations.<sup>193</sup> Upon initiating a photochemical strategy, solvents, coolants, light-sources, glassware must be consciously selected. Photo-oxidations add further complexity. Solvents require sufficient transparency to the wavelength of incident light, while having suitable solubility towards the substrates, photosensitiser and to oxygen. Moreover, non-radiative deactivation of  $^1\text{O}_2$  shows a strong dependence to the solvent used (*vide supra* Table 1.1). Furthermore, the products generated are often unstable compounds such as peroxides and dioxetanes, presenting imposing safety challenges; while achieving efficient mixing, high interfacial areas and sufficient light transfer become more problematic upon scale-up.<sup>5</sup> In the case of the synthesis of **18**, these challenges are even further complicated as the photo-oxidation of **14** is the first step of a complex reaction sequence.<sup>183,184,194</sup>

Nevertheless, in 2014, Sanofi reported an isolated yield of **18** of 55 % from artemisinic acid.<sup>5</sup> Their approach firstly involved the diastereoselective hydrogenation of artemisinic acid to **14**; achieving near quantitative yields with high selectivity of 95:5 (R:S). The photo-oxidation of **14** was completed in dichloromethane using meso-tetraphenylporphyrin (TPP) as the photosensitiser. DCM, being non-flammable, was primarily selected to address the inherent safety concerns of such a reaction. Sanofi ensured complete containment and, implemented recycling capabilities to minimise the environmental impact. Further safety fears over the accumulation of the hydroperoxides led to the use of a 'one-pot' regime - all reagents including the acid were added to the

starting reaction vessel, this way the Hock Cleavage and endoperoxide ring formation would occur immediately after the formation of the hydroperoxides.

Optimisation of the crucial photo-oxidation step was investigated by Burgard and co-workers.<sup>194</sup> The process developed by Sanofi irradiated TPP with a medium pressure mercury arc lamp. Irradiation of the Soret band of TPP at 419 nm (in DCM) is the major contributor to the generation of singlet oxygen, for protonated TPP ( $\text{H}_4\text{TPP}^{2+}$ ) the maxima of this absorption shifts to 436 nm.<sup>194</sup> The overlap between the Hg lamp emission spectra and the absorbance maxima of TPP is poor, as shown in Figure 1.35, although it is sufficient for the reaction to proceed. The poor spectral overlap results in a highly inefficient process. Furthermore, Hg lamps have strong emissions in the infrared region, causing the lamp to operate at high temperatures, resulting in not only significant energy loss, but also high complexities and costs associated with cooling the lamp.<sup>22</sup>

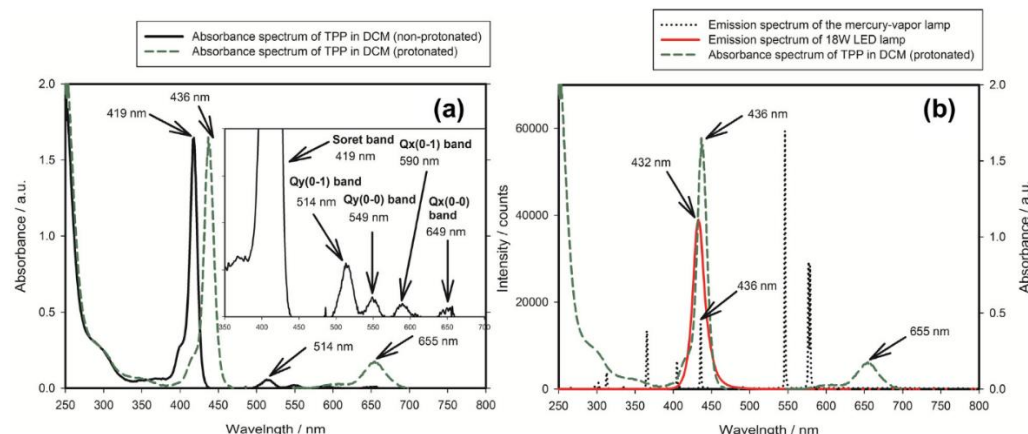


Figure 1.35. UV/Vis absorption spectra of TPP in DCM, free base  $\text{H}_2\text{TPP}$  (solid line) vs protonated form  $\text{H}_4\text{TPP}^{2+}$  (dashed line) and b) emission spectra of 18 W LED (red solid line) and TQ150-Hg vapour lamp (black dotted line) in comparison with the absorption spectrum of protonated TPP (green-dashed line). Taken from Burgard *et al.*<sup>194</sup>

Noting the inefficiency of using mercury lamps for the excitation of TPP, attention was turned to the use of light emitting diodes (LEDs). LEDs are an ideal choice for photochemical reactions as they emit near monochromatic light, thus, allowing for selective excitation of the target molecule. LEDs also have several other benefits, such as, low power consumption, long lifetime, rapid response time, compact physical size, and physical robustness.<sup>194</sup>

Figure 1.35 highlights the good overlap between protonated TPP and the 18W LED used by Burgard. A comparison of the 18W LED and the Hg arc lamp for the conversion of **14** into **18** exhibited a yield of 46 % over 8 hours for the LED, whereas the Hg setup

yielded 45 % in 14 hours.<sup>194</sup> The LED clearly outperformed the Hg lamp, replacement of which leads to significant energy savings. However, LED technology does require development before it can be readily used on an industrial scale. High-efficiency LEDs convert up to 25% of electrical power to visible light, the energy loss results in heat generation, which if not sufficiently removed from the system, can affect efficiency, emission wavelengths and decrease lifetimes.<sup>194</sup>

Burgard and co-workers also observed photobleaching of TPP, while using both light sources.  $^1\text{O}_2$  can oxidise TPP, cleaving the conjugated ring system and hence disrupt the photophysical properties of the compound.<sup>194</sup> Photosensitiser quenching is negated by reducing its concentration. This in turn reduces the concentration of  $^1\text{O}_2$ , therefore the vast majority of the  $^1\text{O}_2$  molecules react with DHAA, with very few TPP molecules being affected by bleaching.<sup>194</sup>

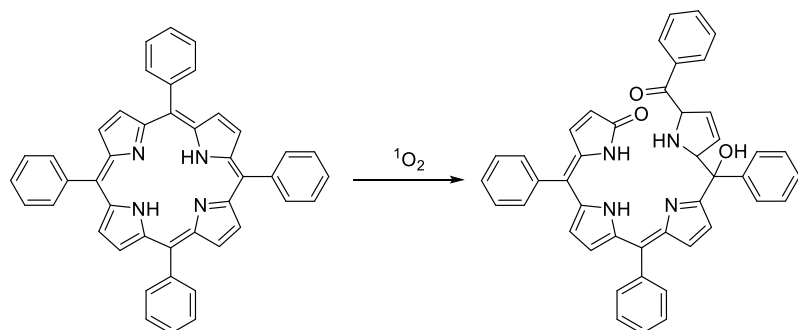


Figure 1.36. Photobleaching of TPP by singlet oxygen, adapted from Bonnett *et al.*<sup>195</sup>

### 1.8.3. Continuous Flow Synthesis of Artemisinin

The benefits of continuous flow technology for photochemical and in particular photo-oxidative synthesis have been highlighted in 1.5. To improve upon the syntheses previously outlined, the implementation of continuous flow technology is key.

Seeberger and co-workers were the first to investigate the continuous flow synthesis, producing a yield of 39% from **14**.<sup>9</sup> They utilised a ‘one-pot’ regime, mixing together **14**, TPP and TFA in DCM before combining with a stream of  $\text{O}_2$ . The reactor was constructed from FEP tubing wrapped around a Schenk immersion well with a 450 W medium pressure Hg lamp placed down the centre. Improvements were made in later research switching to microchannel photoreactor using two LED block arrays of  $\lambda_{\text{max}}$

420 nm. It was highlighted that the photo-oxidation is the key step in the reaction, improvements made here could lead to significant positive end results.<sup>8</sup>

The effect of the reactor temperature on the selectivity of the photo-oxidation was investigated. Seeberger *et al.* found that decreasing the temperature led to increased selectivity for **15**, the crucial hydroperoxide for the subsequent synthesis of **18**.<sup>8</sup> The lowest temperature reached during the photo-oxidation stage was -20°C. At this temperature the three hydroperoxides were produced in yields of 84 %, 10 %, and 3 % for **15**, **16** and **17** respectively, while other by-products made up the remaining mass.<sup>8</sup>

#### 1.8.4. Reaction Optimisation

Further optimisation of the process was investigated by Seeberger and co-workers, with attention being turned towards the nature of the photosensitiser and the acid used to catalyse the Hock Cleavage. As previously discussed in section 1.8.1, the free base form of TPP ( $\text{H}_2\text{TPP}$ ) can be protonated at two sites to form  $\text{H}_4\text{TPP}^{2+}$ , this shifts the  $\lambda_{\text{max}}$  from 418 nm to 436 nm, and lowers the quantum yield of triplet-state formation resulting in a reduced quantum yield for singlet oxygen formation,  $\phi_{\Delta}$ .<sup>194,8,196</sup> Therefore, the researchers investigated the use of dicyanoanthracene, DCA, which remains unprotonated in acidic conditions. The acid can, therefore, be added to the starting solution without having a detrimental impact of the photo-oxidation step. Furthermore, DCA possesses a higher singlet oxygen quantum yield ( $\phi_{\Delta} = 0.86$  in benzene and 0.76 in acetonitrile) than TPP ( $\phi_{\Delta} = 0.63$  in benzene and  $\phi_{\Delta} = 0.60$  in DCM and toluene), indicating that DCA may be a superior alternative for the photo-oxidation of **14**.<sup>47,57,197</sup> However, due to the low molar absorption coefficient of DCA compared to TPP, higher concentrations were required.

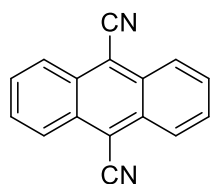


Figure 1.37. The photosensitiser 9,10-dicyanoanthracene (DCA)

The choice of the acid was also found to be crucial; finding that trifluoroacetic acid, TFA, at 0.5 equivalents, best induced the Hock Cleavage; higher concentrations

resulted in reduced selectivity, while lower required heating for full conversion to take place.<sup>6,8,9</sup> TFA with a pKa of -0.25 appears to reside in a ‘Goldilocks region’; the use of weaker acids such as acetic (pKa = 4.76) led to reduced conversion and increased by-product formation, while, strong acids such as sulfuric (pKa = -3.0) led to the formation of mostly the 6-lactone, **19**. The formation of **19** indicated that the tautomerisation of the enol intermediate to the aldehyde, under highly acidic conditions, is too fast to allow for the subsequent oxidation to form **18**.<sup>8</sup>

The choice of solvent did not influence the extent of the conversion of **14**, however, it was found that lower yields of **18** were produced when polar aprotic solvents were used, with the **19** being a major by-product, indicating the shift of the tautomerisation equilibrium to the aldehyde.<sup>8</sup> Solvents of low polarity and perfluorinated solvents reduced the by-product formation. Toluene was selected as the ideal choice as it gave high selectivity and is more affordable and environmentally benign in comparison to the perfluorinated solvents. The temperature dependence of the acid-catalysed step in toluene was investigated. The highest yield of **18** was produced at 25°C; at lower and higher temperatures there was substantial by-product formation and, hence, low yields of **18**. It was also found that increasing the reaction time at low temperatures would not improve the overall yield.<sup>8</sup> Therefore, it was clear that while the photo-oxidation should be carried out at low temperature, the subsequent steps would require the system temperature to be increased. The group were able to construct a continuous-flow system, that allowed for the photo-oxidation to take place at -20°C followed by two reaction lines at 10°C and 25°C to carry out the subsequent acid catalysed cascade reactions. The set-up led to the successful synthesis of artemisinin of up to 69 % yield.<sup>8</sup>

## 1.9. Photo-oxidation at Low Temperature

Seeberger’s work outlined above underlines the value of conducting photo-oxidations at low temperatures. Firstly liquid phase oxidations can be safer at lower temperature because of the reduced vapour pressure of organic solvents and, as previously discussed in section 1.5, liquid phase oxidations combine highly reactive species with organic solvents which can lead to combustion and potential explosions. Furthermore, the intermediates and products that are often formed are highly thermally unstable and can undergo vigorous decomposition at elevated temperatures.<sup>118</sup> Decreasing the reaction temperature increases the minimum critical oxygen concentration above which flame propagation becomes possible.<sup>104</sup> Liquid phase oxidations are often highly exothermic,

reducing the reaction temperature may therefore shift the equilibrium towards product formation.

Secondly, dissolving a gas into a liquid has a negative effect on the systems entropy,  $\Delta S_{sol} < 0$ , therefore according to the Gibbs free energy of solution as expressed in equation (1.6) a reduction in the system temperature will reduce the size of the  $T\Delta S_{sol}$  term and correspondingly reduce the overall free energy. Hence, a reduction in the system temperature leads to an increase in the solubility of the gas in the liquid.<sup>198</sup>

$$\Delta G_{sol} = \Delta H_{sol} - T\Delta S_{sol} \quad (1.6)$$

## 1.10. Thesis Aims

It is clear from the descriptions above that continuous-flow systems have great potential for carrying out low temperature photo-oxidations because (i) flow systems are superior to conventional reactors in terms of mass and heat transfer;<sup>104</sup> (ii) heat transfer out of the solution is also more efficient in flow systems as a greater surface area of the solution is in contact with the reactor walls. It should also be clear that most of the flow photoreactors described have limitations which present problems for operation at temperatures well below ambient. Therefore, the primary aims of this Thesis are:

1. To develop robust design(s) of flow reactors that can be used at low temperature; overcoming the problems of dissipating the heat from the light sources without compromising the low temperature operation of the reactor.
2. To apply the photoreactor to the examples outlined in this chapter namely the photo-oxidations of DHAA and citronellol by  ${}^1\text{O}_2$  where in both cases the yields of the desired photo-products are favoured by low temperatures.
3. To interface the photoreactor with modern self-optimisation techniques so that process development can be accelerated, particularly for reactions with costly starting materials.

## Chapter 2. Development of a Low Temperature Continuous-Flow Photoreactor

This Chapter will present the design and testing of a high-pressure continuous-flow reactor, shown in Figure 2.2, and the adaptations made finally to achieve an internal reactor temperature of -46°C.

The aims of developing continuous flow photochemistry at high pressure and low temperature are to (i) exploit enhancements of the selectivity, yield and safety of photochemical reactions at low temperature, focussing on – particularly photo-oxidations, and (ii) facilitate the photochemistry in atypical media such as liquid CO<sub>2</sub> or liquid NH<sub>3</sub> that require reduced temperature and increased pressure and would enable reactions under new conditions. Specifically, this Chapter aims to develop and exploit a robust continuous flow reactor to be used at low temperatures. We have used the following strategy to address these aims:

- To initially explore the low temperature capability of an untested reactor that had been designed and developed by Dr. Rowena Howie, and Richard Wilson for carrying out photochemistry at high temperature and pressure.
- To assess the reactor's performance, initially examining UV initiated [2+2] photocyclisations, and to make necessary adaptations to enhance the reactor performance, and determine the ultimate level of performance of the first generation reactor.
- To modify the design to reach as low a temperature as possible, and for these modifications to be tested and iteratively adjusted to optimise the reactor's low temperature capabilities.

Once a suitably low internal temperature has been achieved, studies will begin on the effect of the reduced temperature on the photo-oxidations of citronellol and dihydroartemisinic acid, key steps in the syntheses of two commercially important molecules, rose oxide and artemisinin.

## 2.1. High Temperature, High Pressure Photoreactor

### 2.1.1. Description of Reactor Systems

The first-generation reactor was developed to undertake photochemical reactions at high temperatures and pressures in superheated/near-critical water, the critical point of water being 647 K (374°C) and 22.1 MPa (221 bar).<sup>199</sup> The corresponding reactor will be abbreviated to HTPR (High Temperature Pressure Reactor) throughout this Thesis. The interest in this research stems from the differing properties of superheated, subcritical and critical water as they change with temperature and density.<sup>200</sup> The ionisation constant of near-critical water is ca. three orders of magnitude above that of ambient water, providing a source of hydroxide and hydronium ions, so that near-critical and supercritical water can act simultaneously as a solvent, reagent and catalyst.<sup>200</sup>

Batch and continuous flow reactors for the use of supercritical water have been developed previously, however, these often do not facilitate the transmission of light.<sup>201,202</sup> The sapphire tube reactor, Figure 2.1, is an example of high-pressure continuous-flow photochemical reactor has previously been developed in our group, and used in the work described by Dr. Xue Han and Dr. Richard A. Bourne and adapted by Dr. Jessica Bellamy.<sup>145,189,203,204</sup> The main component of the reactor is a sapphire tube held in place by a pair of EPDM O-rings and connected to the flow system using 1/8" Autoclave Engineer fittings.<sup>203</sup> A portion of the sapphire tube is exposed and is irradiated by LED blocks placed on the periphery of the reactor. The design allows for the internal reactor temperature to be controlled via the circulation of coolant fluid through a Lexan™ tube that surrounds the sapphire tube.

This design allows for moderate cooling and heating via the flow of a heat transfer fluid around the sapphire tube, but is inadequate for achieving very high or very low temperatures. Furthermore, the use of LED blocks on the periphery of the reactor does not maximise photon capture.

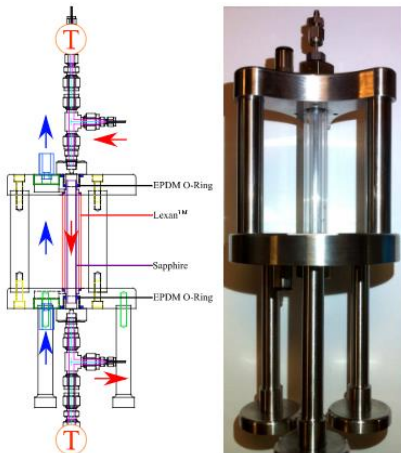


Figure 2.1 The sapphire tube reactor designed and developed by Dr. Xue Han, Dr. Richard Bourne, Dr. Jessica Bellamy and Richard Wilson. The sapphire tube reactor (Saint-Goban Crystals, 10 mm o.d, 1 mm wall thickness, 120 mm long) is sealed to the high pressure fluid system via two EPDM O-rings. A Lexan™ tube surrounds the sapphire to improve the safety of the reactor, and also as a transparent material beneath which coolant is circulated to control the internal reactor temperature. In the case of the arrows, red represents the flow of the high pressure fluid, and blue indicated the coolant flow. T represents the fitting holding a K-type thermocouple into both the top and bottom of the sapphire tube. The LED units are held in place by grooves cut into the stainless steel base of the reactor. Adapted from Jessica Bellamy's Thesis.<sup>203</sup>

The aim of reaching high pressures and temperatures with the added complication of access to light is clearly non-trivial. Robust materials with high thermal conducting capacities have to be used in conjunction with powerful heating elements which must be used around the main portion of the reactor to ensure control of the internal temperature. Irradiation therefore has to originate from the centre of the reactor. Therefore, the HTPR is an annular photoreactor, maximising photon capture. The light source is housed in a closed end borosilicate tube, placed within an open ended quartz tube (30 mm o.d, 2 mm wall thickness). A key difference from the sapphire reactor is that the pressure is compressive rather than tensile, consequently, the quartz can be relatively thin. The quartz and borosilicate tubes are held a Bohlender® (PTFE) T-piece with silicone seals at the top of the reactor and a similar L-shaped block at the bottom of the reactor. The perpendicular joints allow a heat transfer fluid to flow vertically up through the centre of the quartz tube and out the side arm of the top T-piece. The borosilicate tube is therefore necessary to protect the light source from this fluid. The reactor is sealed at the top and bottom between the internal steel wall and the quartz tube with an FEP encapsulated silicone O-ring (temperature rated from -20 to +200 °C) followed by a PEEK back up ring.

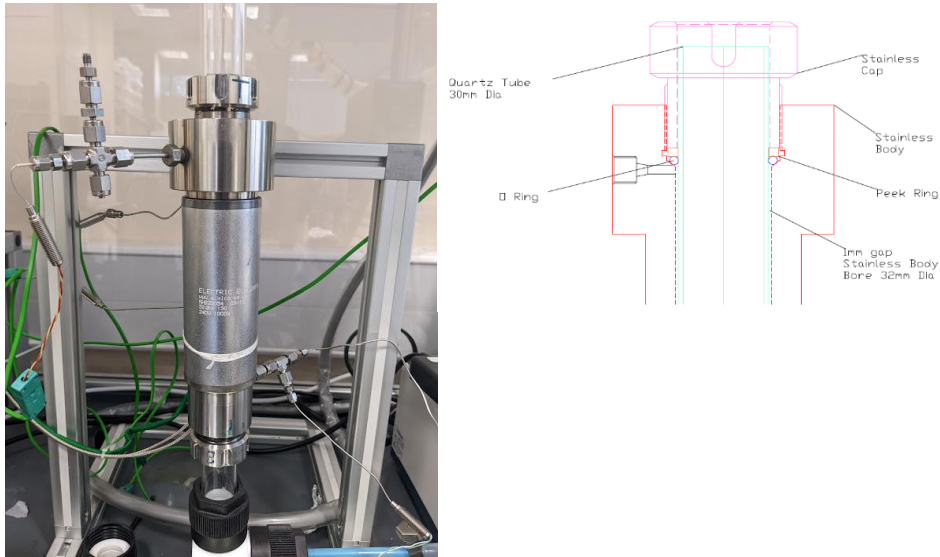


Figure 2.2: Left: Photo of the high temperature, high pressure reactor developed by Dr. Rowena Howie and Richard Wilson. The external electric heating jacket (Electric Elements, 240 v, 1000 W) around the centre of the reactor is controlled by a Eurotherm 216 PID temperature controller, while a Jasco BP-2080 back-pressure regulator is used to control the pressure within the system. Thermocouples placed in the interior and the outlet of the reactor are monitored by a Eurotherm 2132i temperature indicator. Pressure transducers are placed prior to and post of the reactor. Right: Schematic of the top section of the reactor. The stainless steel cap is tightened to compress the PEEK back-up ring onto the FEP encapsulated silicone O-ring to seal the reactor above the outlet. There is a 1mm gap between the quartz tube and the reactor wall, and hence a 1 mm path length.

The remainder of the reactor is mostly constructed from 316 stainless steel. An external electric heating jacket (Electric Elements, 240 v, 1000 W) around the centre of the reactor is used to heat the reactor and is controlled by a Eurotherm® 216 PID temperature controller. K-type thermocouples are placed at the inlet, outlet and within the interior of the reactor and are monitored by Eurotherm 2132i temperature indicators. Solution flow rates are controlled by Jasco® PU-980 HPLC pumps while the system pressure is controlled and applied using a Jasco® BP-2080 back-pressure regulator. The pressure is measured by transducers placed before and after the photoreactor. The pressure transducers and temperature monitors are connected to a trip box, in the event that the pressure or temperature within the system exceeds designated levels, the trip will trigger, the HPLC pumps and the temperature controller. The trip box also possesses an emergency stop button, allowing for the operator to manually trip the system. This may be necessary in the case of reactor malfunction where the trip levels have not been exceeded.

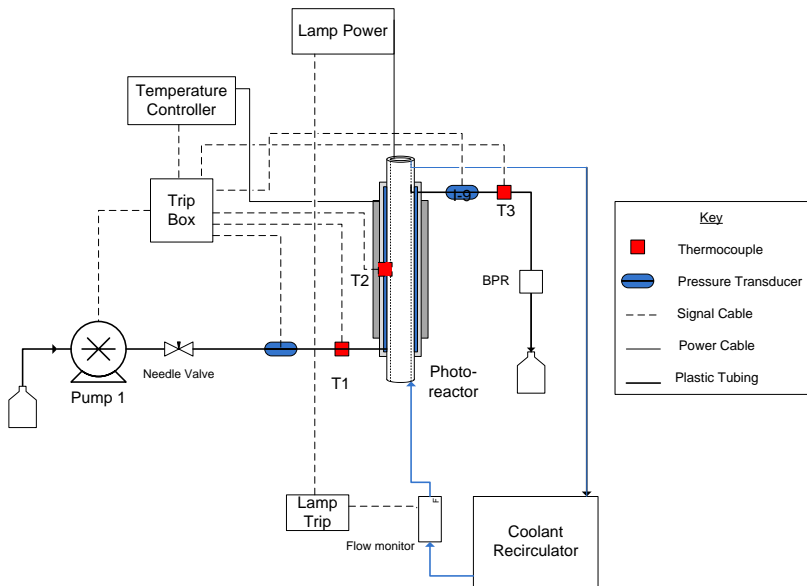


Figure 2.3 Diagram of the reactor set-up for high temperature, high pressure, UV initiated photoreactions.

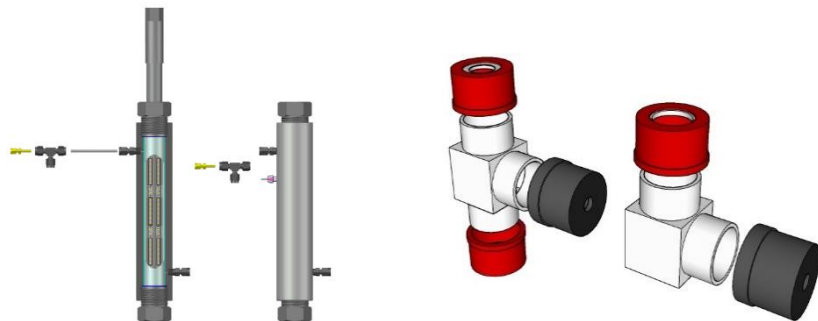


Figure 2.4 Left: CAD model of the reactor, a cross-section showing the positioning of the light source in relation to the inlet and outlet. Right: CAD models of the T- and L-joints fittings supplied by Bohlender®.

Reaction solution is pumped towards the inlet at the bottom of the reactor and upon entering, travels vertically upwards between the inner wall of the stainless steel body and the quartz tube. Quartz has desirable optical properties with a UV cut-off below 200 nm making it ideally suited for UV and visible photochemistry.<sup>205</sup>

The reactions first investigated in the HTPR are initiated by UV light around 300 nm, due to the length of the reactor and the positioning of the Bola T-piece an extra-long medium pressure Hg arc lamp (Photochemical Reactors LTD) is required to irradiate the reactor from the centre.<sup>206</sup> Hg arc lamps require external cooling, this is provided by a recirculating chiller that flows coolant up through the centre of the quartz tube. To prevent the lamp overheating and malfunctioning, a flow monitor connected to a second

trip box connected to the lamp power source, is incorporated into the set-up, as shown in Figure 2.3.

A second generation of the HTPR was also produced. The electrical heating jacket was replaced by a bored aluminium block with an external copper coil, shown in Figure 2.5. The reactor possessed the same pressure rating as the original, but the temperature was now controlled *via* the use of heat transfer fluid through the copper coil, allowing for either moderate heating or cooling of the reactor. This reactor is referred to as the HPR (high pressure reactor). The reactor has the same dimensions as the first generation with a solution path length of 1 mm and an internal volume of 19.5 cm<sup>3</sup>. It is the capabilities of this second-generation reactor that will be the focus of this Chapter.

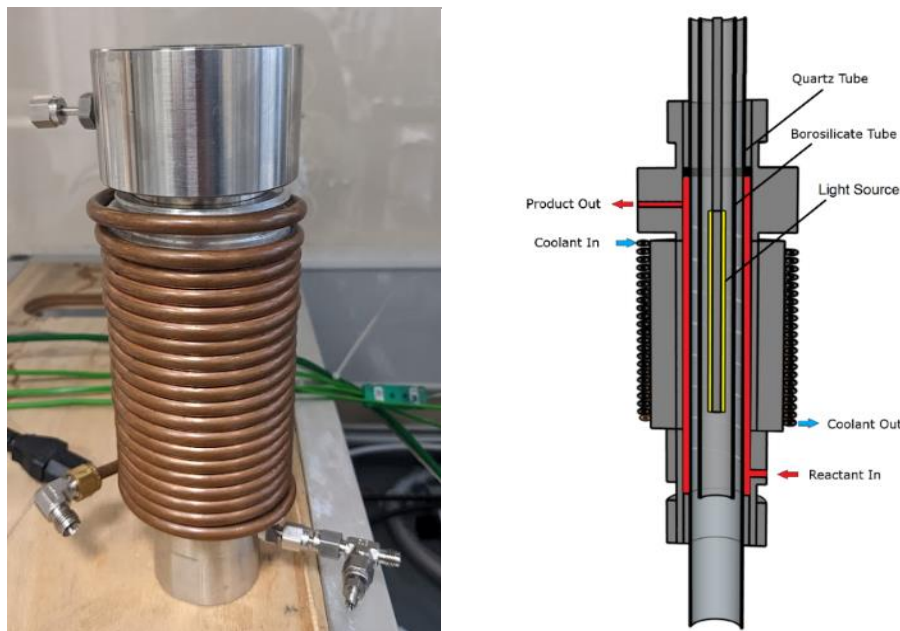


Figure 2.5: The second generation high pressure photoreactor, HPR, the electrical heating jacket of the first generation has been replaced by an external copper coil, allowing for moderate heating or cooling via the use of a heat transfer fluid and recirculator. Right: 3D cross-sectional schematic of the reactor highlighting the positions of the borosilicate and quartz tubes and the light source. The reactant fluid stream is indicated in red and shows how the solution enters the reactor through the inlet at the bottom and travels vertically upwards within the 1 mm gap between the quartz and the steel wall. The blue arrows indicate the coolant stream through the external copper coil.

## 2.2. Description of the PhotoLED

Due to the narrow range of emission of a particular LED in the visible region combined with the ease of manufacture of the LEDs, these light sources can be easily tuned to

closely match the absorption profile of a photosensitiser, improving reaction efficiency when compared to the traditional light sources used in photochemistry. Furthermore, their low-power consumption, high luminous efficiency, and more environmentally benign characteristics further increase the attractiveness of LEDs.<sup>207</sup>

The PhotoLED was the colloquial name given to a group of LED light sources designed and developed in our group. Six LED strips are fixed onto the external surface of a stainless steel cold finger. The LEDS developed include (i) blue light, with typical  $\lambda_{\max}$  emissions around 420 nm, (ii) phosphor converted white LEDs which are manufactured from blue LEDs coated with a yellow phosphor, these LEDs therefore have a strong emission in the blue region, with a lower intensity broadband emission, (iii) near-UV with a  $\lambda_{\max}$  of 365 nm.

The coldfinger allows the PhotoLED to be cooled internally via a recirculating chiller. This reduces the likelihood of the LEDs overheating and negates the use of exterior cooling add a layer of complexity to the reactor set up, especially when considering low reactor temperatures.

The first-generation PhotoLED had 6 blue LED strips with an emission maximum of 424 nm. The second-generation blue PhotoLED has a shorter wavelength emission maximum of 411 nm and newer LED strips than the original and due to the rapid advance in LED technology, which have a greater emission intensity than the original, as can be seen in Figure 2.6. The white LED (also second-generation) exhibits a maximum emission around 440 nm due to the underlying blue LED strips. Due to the absorption of the blue light by the phosphor coating and the subsequent re-emission of white light, the intensity is far lower than either of the blue LEDs.

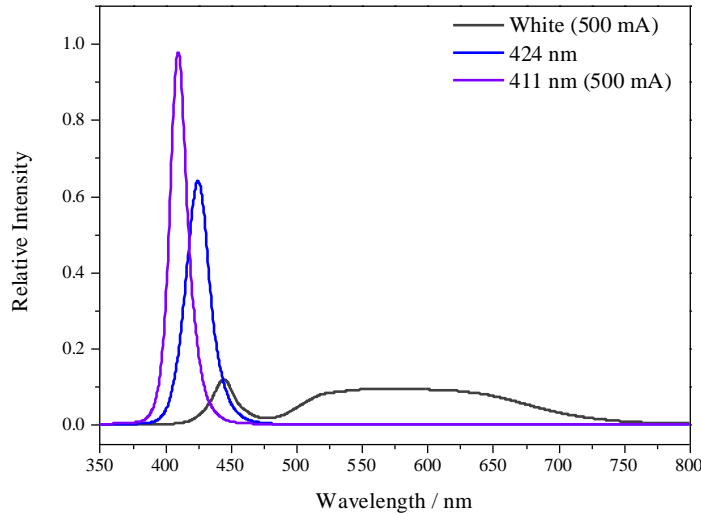


Figure 2.6: Emission spectra of the first-generation 424 nm PhotoLED, and the second-generation - 411 nm, and white PhotoLEDs. The second generation blue LED produces light of a slightly lower wavelength and greater intensity than the first generation. The emission of the white LED shows the  $\lambda_{\text{max}}$  around 440 nm of the underlying blue LED strips. Due to the absorption of the blue light by the phosphor coating and the subsequent re-emission of white light, the intensity is far lower than either of the blue LEDs. Measurements were taken in a black-box with the emission detector placed 10 cm away from the light source. The second generation LEDs were operated at their maximum current of 500 mA.



Figure 2.7: Left two images: First-generation PhotoLED with a  $\lambda_{\text{max}}$  emission of 424 nm. Right two images: Second-generation PhotoLED, white light emission is generated through the use of blue LED strips coated in yellow phosphor. The two red tubes at the top of the housing are the inlet and outlet for the interior cooling.

Further advantages of the second-generation LED and its control box include i) the addition of an inbuilt thermocouple, placed on the end of the housing, with an inbuilt power trip if the temperature exceeds 50°C, ii) the ability to measure individually the current running through each of the six LED strips, thereby allowing for faulty LED

strips to be easily identified and replaced, and iii) control of the maximum current, between 50 and 500 mA, delivered to the LED strips.



Figure 2.8. Second generation control box for the PhotoLED. In normal display mode the LED current can be set ( $I_s$ ) up to 500 mA. The LEDs turn on once a current of 50 mA has been set. The actual current ( $I_a$ , highest current through an individual strip) can be observed, along with the temperature of the PhotoLED.

### 2.3. Testing the Capabilities of the HPR

The original HTPR had previously been temperature and pressure tested, and photochemical reactions carried out by Dr. Rowena Howie. The HPR that is the focus of this chapter had only been pressure tested, with no photochemical reactions being performed before the author took over the work on its development. As such, the performance of the HPR was compared to two commonly used photochemical reactors – the batch immersion well and a continuous-flow FEP coil.<sup>22,60,101,114</sup>

The tests were first accomplished by conducting the reaction of maleimide (**1**) and 1-hexyne (**2**) to produce compound **3**, shown in Figure 2.9. **1** and **2** undergo a UV initiated [2+2] photocycloaddition in the absence of a photo-initiator to form 6-butyl-3-azabicyclo[3.2.0]hept-6-ene-2,4-dione (**3**).<sup>208</sup> **1** absorbs within the UV region,  $\lambda_{\text{max}} \sim 273$  nm therefore high energy UV irradiation is required, and as such a standard medium pressure 125 W Hg arc lamp was used. Initial investigations into the reaction of **1** and **2** highlighted limitations of the HPR when compared to the reactions in the FEP coil.

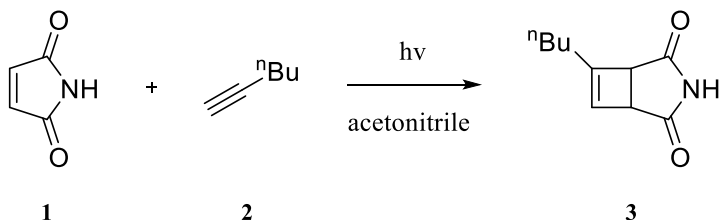


Figure 2.9: Reaction scheme of the [2+2] photocycloaddition of maleimide (**1**) and 1-hexyne (**2**) in acetonitrile.<sup>101</sup>

To obtain the first benchmark, the reaction of **1** and **2** was investigated using a traditional borosilicate immersion well set-up. Aliquots were taken every 15 minutes for a total of 90 minutes, and analysed by  $^1\text{H}$  NMR. Under these conditions full conversion was achieved after 75 minutes with a corresponding yield of 74%.

Following on from the reaction in the immersion well reactor, the photocycloaddition of **1** and **2** was carried out in an FEP coil flow reactor. This reactor was constructed from thin-walled FEP (1/8" o.d, 0.01" wall thickness, length 25 ft (ca 7.6 m), volume 22 cm<sup>3</sup>) wrapped around an immersion well in a single layer coil. The highest levels of conversion and yield were obtained at the lowest flow rate and, hence, longest residence time. A residence time of 22 minutes resulted in a yield of 74%, equal to highest value during the batch reaction but with a significantly reduced reaction time. During this experiment, a white precipitate was formed which was insoluble in  $\text{CDCl}_3$ . The material was subsequently analysed by NMR in  $d_6$ -DMSO and identified as the product of the dimerization of maleimide, Figure 2.10, the formation of which explains the less than quantitative yields despite full conversion.

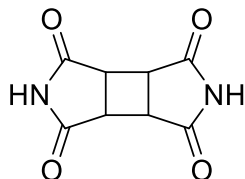


Figure 2.10 Maleimide dimer formed via an intermolecular [2+2] photocycloaddition of two maleimide molecules Literature NMR values match well with the experiment:<sup>209,210</sup> Literature:  $^1\text{H}$  NMR (600 MHz,  $d_6$ -DMSO);  $\delta$  3.29 (s, 4H), 11.67 (s, 2H); Experimental:  $^1\text{H}$  NMR (400 MHz,  $d_6$ -DMSO);  $\delta$  3.29 (s, 4H), 11.63 (s, 2H).

The HPR was subsequently tested under similar conditions to the FEP reactor, albeit with a lower initial flow rate of 0.50 mL min<sup>-1</sup>, corresponding to a residence time of 39 minutes. Despite the longer residence time only a poor yield of 37% was achieved. These results are presented in Table 2.1.

Table 2.1. A comparison of the efficiency of the HPR reactor compared to an FEP coil and batch immersion well reactor for the [2+2] photocycloaddition of **1** and **2**.

Flow Rate / mL min <sup>-1</sup>	Residence time / min	<b>3</b> (FEP) / %	Residence time / min	<b>3</b> (HPR) / %
0.5	-	--	39	37 ± 4
1.0	22	74 ± 13	20	31 ± 3
1.5	15	56 ± 6	13	30 ± 5
2.0	11	51 ± 2	10	26 ± 1
3.0	8	39 ± 2	7	24 ± 2

The reaction temperature and pressure were not measured. The flow rates have been converted into residence time to allow for appropriate comparison between the reactors. Aliquots were taken in triplicate to allow for the margin of error (95 % confidence interval) to be calculated.

The results from these experiments highlight limitations of the HPR. Two simple changes were made in an attempt to improve these results, i) the thickness of the quartz tube was reduced from 2.0 mm to 1.5 mm ii) The length of the Hg arc lamp was increased to better irradiate the centre of the reactor.

The [2+2] cycloaddition of **1** and **2** was then repeated. The yield for the residence time of 39 minutes increased from 37 % to 83 %; however this is marred by a considerable error value of 17%. The associated errors were found to decrease at higher flow rates, the results between the two reactors are more appropriately compared at the flow rates of 2 and 3 mL min<sup>-1</sup> where the errors in the HPR are to a level that correspond to those previously found. At these flow rates it is clear that the adaptations have led to improvements. It was thought that a low fluid velocity led to ineffective mixing, resulting in non-uniform irradiation and reduced reactant-reactant interactions. However, the discrepancy between the level of conversion and the corresponding yield is indicative of by-product formation.

Table 2.2. Results for the [2+2] cycloaddition of **1** and **2** in the HPR using 1.5 mm thick quartz and the long Hg arc lamp.

Flow Rate / mL min <sup>-1</sup>	Residence Time / min	Conversion / %	<b>3</b> / %
0.50	40	96 ± 3	83 ± 17
1.00	20	86 ± 6	73 ± 21
2.00	10	67 ± 3	52 ± 3
3.00	6.5	54 ± 12	33 ± 2

To improve mixing and reduce the optical path length, glass beads were added to the interior of the reactor. In the first investigation, the reactor was fully packed with glass beads of sizes 212-300 µm. This considerably reduced the internal volume of the reactor from 19.5 cm<sup>3</sup> to 1.5 cm<sup>3</sup>. To avoid removal of the glass beads through either the outlet or inlet during the reaction, fine mesh filters were added into the joints of these two

areas. The glass beads were expected to have no detrimental impact on the absorbance of the solution, high energy UV light was already filtered out by the borosilicate sheath before reaching the solution.

The reaction of **1** and **2** in the HPR packed with 212-300  $\mu\text{m}$  glass beads led to a considerable improvement in the level of error associated with the yields and conversion. A highest yield of  $68 \pm 12\%$  was achieved within in a residence time of 6 minutes, comparable to the 6.5 minute residence time within the empty HPR which resulted in a yield of 33 %. The reaction was then repeated with larger glass beads of sizes 400-625  $\mu\text{m}$ , reducing the original reactor volume to 10.0  $\text{cm}^3$ . In comparison to the 212-300  $\mu\text{m}$  results, the larger beads produced lower conversions and yields but improved the associated error.

*Table 2.3 Results from the [2+2] photocycloaddition of **1** and **2** in the HPR reactor filled with 212-300  $\mu\text{m}$  and 425-600  $\mu\text{m}$  glass beads.*

Flow Rate / $\text{mL min}^{-1}$	212-300 $\mu\text{m}$			425-600 $\mu\text{m}$		
	Residence Time / min	Conversion / %	<b>3</b> / %	Residence Time / min	Conversion / %	<b>3</b> / %
0.25	6.0	95 $\pm$ 2	68 $\pm$ 12	40.0	87 $\pm$ 4	59 $\pm$ 3
0.5	3.0	87 $\pm$ 1	62 $\pm$ 3	20.0	69 $\pm$ 12	42 $\pm$ 2
1	1.5	68 $\pm$ 2	49 $\pm$ 3	10.0	34 $\pm$ 4	20 $\pm$ 2

The results presented good yields up to 68 % and with relatively low errors when compared to the previous experiments containing no beads. The conversion and yields using the 212-300  $\mu\text{m}$  beads are superior to the 425-600  $\mu\text{m}$  despite the significantly shorter residence times.

## 2.4. [2+2] Cycloaddition of THPA and Propargyl Alcohol

The similarly well studied [2+2] cycloaddition of tetrahydropthalic acid anhydride (THPA, **4**) and propargyl alcohol (**5**) was selected to further investigate the performance of the reactor and to exhibit that the effects shown above are not limited to a single particular reaction. This reaction differs slightly from the [2+2] cycloaddition of **1** and **2** due to the formation of a secondary product (**7**). The formation of this by-product has been previously shown to occur through a distinct reaction pathway via a biradical intermediate that also forms the main ring closure product (**6**), and not a secondary photoproduct derived from the main product.<sup>206</sup>

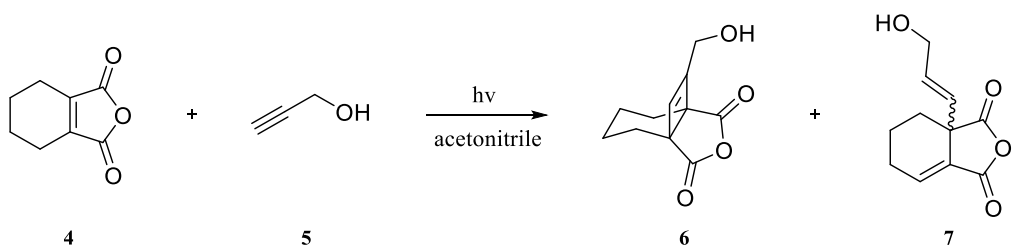


Figure 2.11. Reaction scheme of the [2+2] cycloaddition of THPA and propargyl alcohol forming the major bridged product and the minor product. Adapted from Booker-Milburn *et al.*<sup>206</sup>

The cycloaddition of **4** and **5** was carried out with a number of reactor packing scenarios. 212-300  $\mu\text{m}$  glass beads were either fully packed (volume 1.5  $\text{cm}^3$ ), partially packed (volume 13.5  $\text{cm}^3$ ) or empty (volume 19.5  $\text{cm}^3$ ). A partially filled reactor was investigated as it would be beneficial for the reaction productivity to achieve high levels of mixing, without a large reduction in the reactor volume.

Table 2.4: Results of the photocyclisation of **4** and **5**.

Fully Packed				
Flow Rate / $\text{mL min}^{-1}$	Retention time / min	Conversion / %	<b>6</b> / %	<b>7</b> / %
0.25	6.0	96 $\pm$ 1	70 $\pm$ 14	16 $\pm$ 5
0.5	3.0	96 $\pm$ 2	67 $\pm$ 8	17 $\pm$ 4
1.0	1.5	94 $\pm$ 4	65 $\pm$ 5	18 $\pm$ 3
2.0	0.8	91 $\pm$ 1	63 $\pm$ 3	17 $\pm$ 1
3.0	0.5	91 $\pm$ 1	58 $\pm$ 4	16 $\pm$ 3
4.0	0.4	84 $\pm$ 3	54 $\pm$ 4	16 $\pm$ 4
5.0	0.3	71 $\pm$ 3	42 $\pm$ 1	12 $\pm$ 1
Partially Packed				
Flow Rate / $\text{mL min}^{-1}$	Retention time / min	Conversion / %	<b>6</b> / %	<b>7</b> / %
0.25	54	95 $\pm$ 1	64 $\pm$ 4	15 $\pm$ 6
0.5	27	94 $\pm$ 1	65 $\pm$ 3	16 $\pm$ 2
1.0	13.5	91 $\pm$ 2	65 $\pm$ 4	17 $\pm$ 3
2.0	6.8	84 $\pm$ 1	59 $\pm$ 5	17 $\pm$ 4
3.0	4.5	71 $\pm$ 3	50 $\pm$ 3	15 $\pm$ 1
4.0	3.4	62 $\pm$ 3	43 $\pm$ 4	13 $\pm$ 2
5.0	2.7	58 $\pm$ 3	35 $\pm$ 1	11 $\pm$ 3
Empty				
Flow Rate / $\text{mL min}^{-1}$	Retention time / min	Conversion / %	<b>6</b> / %	<b>7</b> / %
0.5	40	93 $\pm$ 2	74 $\pm$ 25	18 $\pm$ 2
1.0	20	91 $\pm$ 3	66 $\pm$ 8	17 $\pm$ 4
2.0	10	80 $\pm$ 3	58 $\pm$ 3	17 $\pm$ 1
3.0	6.5	66 $\pm$ 2	49 $\pm$ 4	13 $\pm$ 1
4.0	5.0	55 $\pm$ 2	42 $\pm$ 2	12 $\pm$ 4
5.0	4.0	56 $\pm$ 11	35 $\pm$ 1	11 $\pm$ 4

Samples were made in triplicate after an equilibrium time equal to two reactor volumes. The margin of error was calculated to the 95 % confidence interval.

As expected the trend observed in the cycloaddition of **4** and **5** followed on from that found in the reaction of **1** and **2**, with yields increasing with residence time. However, the measured error also increased, again posing questions about the effect of mixing within the system. Table 2.4 allows for a comparison to be made between the three reactor setups. The addition of the glass beads, both in for the fully packed and partially packed reactor has led to general increases in conversion, compared to the empty reactor. The comparison of yield improvements, however, is difficult. There appears to be no significant increase in yield for the packed reactors at the lowest flow rates, in part due to the relatively large errors observed, likely due to reduced levels of mixing at these lower velocities. The superiority of the fully-packed reactor only becomes statistically significant at a flow rate of  $3.0 \text{ mL min}^{-1}$  at which point a conversion of  $91 \pm 1\%$  and a yield of **6** of  $58 \pm 4\%$  is achieved compared to  $71 \pm 3\% / 50 \pm 3\%$  and  $66 \pm 2\%$  and  $49 \pm 4\%$ , for the partially packed and empty reactors respectively. These results indicate that the effect of the beads is not significant when the velocity of the solution is low, resulting in low levels of mixing that are not enhanced by the beads.

## 2.5. Limitations of the High-Pressure Reactor

Practical difficulties were found with the use of the glass beads. Firstly, their addition through the top of the reactor, between the quartz tube and the reactor's interior wall, often resulted in accidentally overfilling the interior, with the beads getting stuck in the threads of the top screw joint and in close proximity to the O-rings; insufficient removal of the beads would result in damage to the reactor and prevent proper sealing, a major issue if high pressures were to be used. Moreover, the presence of the beads is expected to create localised areas of increased pressure upon the quartz, creating a stress gradient and reducing the pressure to which it can maintain. This rudimentary packing method was also not reproducible, the amount of beads and hence the reactor volume varied each time it is packed.

During each experiment, the solution flow caused the beads to pack closely together, hindering the removal of both the quartz tube and the beads. Removal of the inlet and outlet filters and flushing the reactor with water did allow the majority but not all of the beads to be removed, with enough remaining to provide significant friction during removal of the quartz tube, with fears of shattering it in the process. Therefore, it became apparent that a more robust design that would allow for greater reproducibility and ease of use was needed.

The idea of ‘rifling’ the interior of the reactor like a gun barrel was suggested. Rifling the interior walls of the reactor would potentially force the solution to spiral up the reactor, increasing turbulence and hence the level of mixing. However, carrying out this procedure would be permanent and would diminish the pressure rating of the reactor. Therefore, an alternative method was investigated, involving an interior spiral that would fit tightly between the quartz and the steel inner wall, introducing lateral motion in the flow. The spiral prototype was made by coiling PTFE tape around the quartz tube.

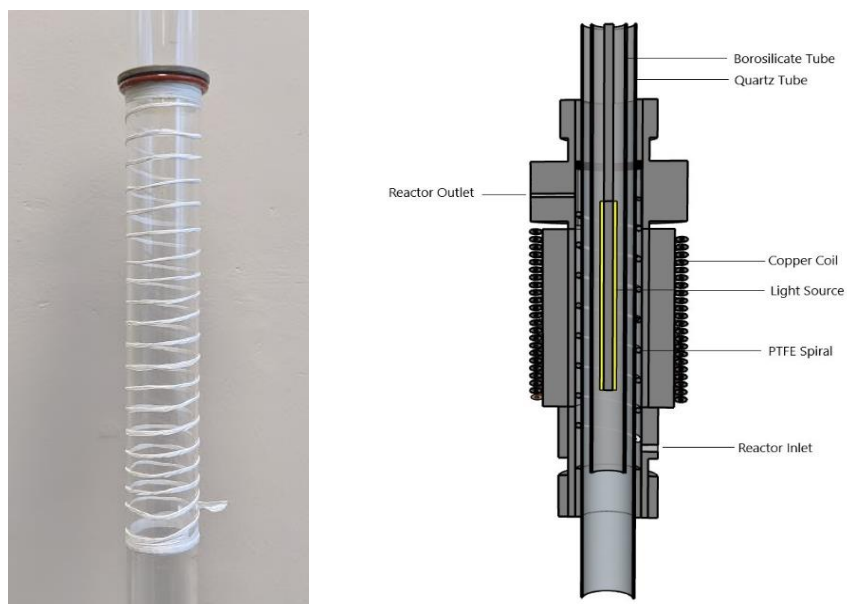


Figure 2.12: Left: PTFE tape spiralled around the quartz tube, the FEP encapsulated silicone O-ring and the back-up PEEK o-ring can also be seen. Right: CAD model of the HPR indicating the position of the PTFE spiral between the quartz tube and the interior reactor wall

## 2.6. Testing the Spiral Reactor

Preliminary tests of the spiral design were carried out by placing a borescope down the centre of the quartz tube and pumping a coloured solution up the reactor. The spiralled path of the solution can be observed in Figure 2.13. To test and compare the ability of the spiralled reactor against the glass bead-filled reactor the [2+2] cycloadditions of i) **1** and **2** and ii) **4** and **5** were carried out. The increased velocity of the solution around the spiral is likely to increase the level of mixing, hence improving the homogeneity of the solution and thus the uniformity of irradiation and rate of reaction.<sup>211</sup> For the synthesis of **3**, the use of the spiral has slightly reduced the yields at the lowest flow rates in comparison to the fully packed reactor but the uncertainties are encouragingly

low. For the synthesis of **6** and **7**, it is clear that the spiral outperforms the beads in terms of yields, while the uncertainties remain relatively similar. These results indicate that along with the improved practicability of the spiralled tube, the chemical productivity is not hampered and may even be improved.

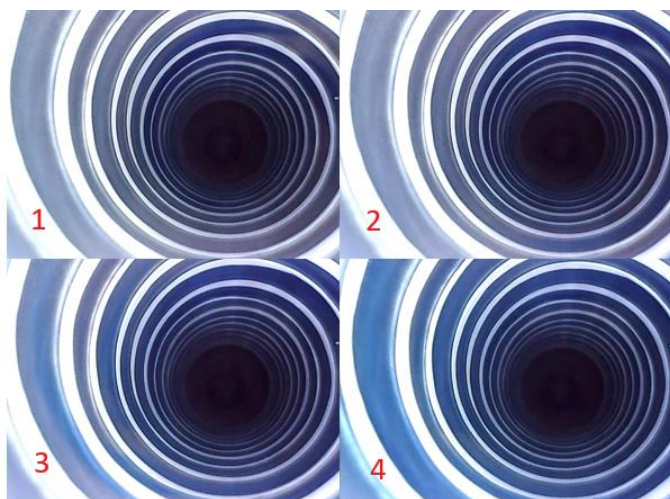


Figure 2.13. Photos taken from the borescope at regular intervals during the preliminary test with a coloured solution spiralling up the reactor.

Table 2.5. Results for the reaction of **1** with **2** and **4** with **5** in the spiralled reactor.

Retention time / min	Conversion / %	<b>3</b> / %	Conversion / %	<b>6</b> / %	<b>7</b> / %
80.0	$96 \pm 1$	$56 \pm 3$	-	-	-
40.0	$89 \pm 2$	$54 \pm 3$	-	-	-
20.0	$80 \pm 6$	$50 \pm 3$	$97 \pm 2$	$70 \pm 5$	$17 \pm 2$
10.0	$65 \pm 8$	$43 \pm 4$	$95 \pm 1$	$64 \pm 11$	$16 \pm 4$
6.5	$54 \pm 22$	$33 \pm 3$	$92 \pm 1$	$65 \pm 2$	$17 \pm 2$
5.0	-	-	$90 \pm 1$	$64 \pm 2$	$19 \pm 1$
4.0	-	-	$86 \pm 2$	$61 \pm 5$	$17 \pm 3$

Good levels of conversion and yield were achieved with low levels of error.

## 2.7. HPR Development for Low Temperature Photochemistry

The external copper coil allows a heat transfer fluid to be used to control the reaction temperature. By splitting the path of this fluid it can be directed both through the coil and the centre of the quartz tube. Therefore the use of an ultra-low temperature refrigerated circulator with an appropriate bath fluid would allow photochemical reactions to be performed at low temperature.

### 2.7.1. Initial Set-up for Low Temperatures

Initial temperature testing used a similar set-up to that for the previous [2+2] cycloadditions. The custom made Hg arc lamp remained as the light source. A Haake®

F-3 recirculating chiller was used in conjunction with a 60:40 (v/v %) mixture of ethylene glycol : water, giving the potential to achieve a minimum fluid temperature of  $-50^{\circ}\text{C}$ .<sup>212</sup> Insulated Tygon™ (Saint-Goban®) tubing connected the recirculator to the external coil of the HPR. For the preliminary investigations the recirculator was not connected to the centre of the reactor. Previous experiments within our group involving UV irradiation of an ethylene glycol/water mixture observed significant fouling of the reactor walls. Therefore, water was flowed through the centre to act as the coolant of the Hg lamp.

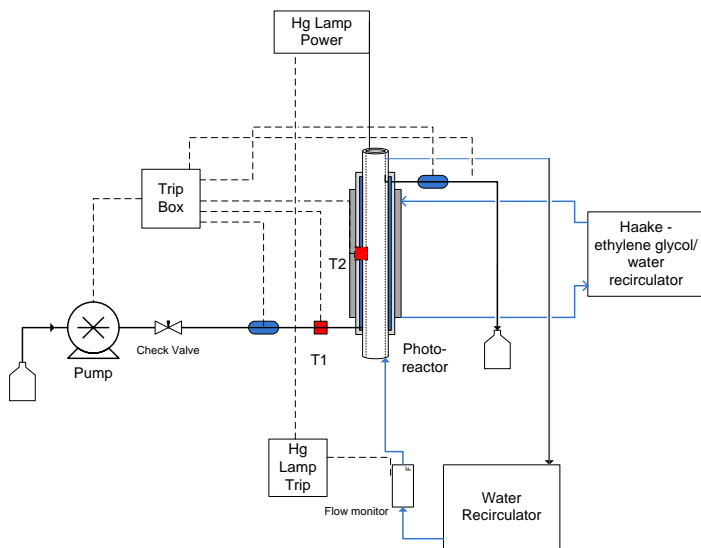


Figure 2.14: Schematic of the HPR set-up for low temperature photochemistry. A Haake ethylene glycol chiller supplies low temperature heat exchange fluid to the exterior coil of the reactor.

With ethanol flowing through the reactor and the recirculating chiller set to  $-50^{\circ}\text{C}$ , the glycol/water reached a low of  $-45^{\circ}\text{C}$ . However, an internal reactor, T<sub>2</sub>, temperature of only  $5^{\circ}\text{C}$  was achieved, this primarily being due to the large amount of heat emitted by the Hg arc lamp and the use of water as the internal cooling fluid.

### 2.7.2. Adaptations to the Reactor

It was clear that to achieve the lower temperatures that were desired, a number of adaptations would have to be implemented:

- Replacement of the Hg arc lamp with a PhotoLED array that can operate at far lower temperature.

- Replace the ethylene glycol/water with another heat exchange fluid that can be used at lower temperatures that also suffers no adverse effects when irradiated with UV light, and as such can be pumped through the centre of the reactor.
- Replacement of the Haake® F-3 recirculating chiller with another that has greater cooling capacity.
- Cooling within the reactor body itself would not be enough to allow for a reaction solution to be chilled appropriately before the desired photochemistry takes place. Therefore a method for achieving the desired reaction temperature before entering the reactor is required.

The first-generation PhotoLED ( $\lambda_{\max}$  424 nm) is wider than the Hg arc lamp, as such, the corresponding borosilicate sheath that protects the light from the reactor's internal cooling fluid does not fit down the centre of the quartz tube. Therefore, the PhotoLED would have to be in place without the sheath, and consequently without internal reactor cooling.

Initial investigations into the pre-cooling of the solution involved placing a stainless steel coil ( 1/16" o.d, length 3 m, volume 0.77 cm<sup>3</sup>) in a Dewar filled with a salt/ice mixture at -20°C prior to the inlet of the HPR. With ethanol flowing through the reactor the inlet, T<sub>1</sub>, and interior , T<sub>2</sub>, registered -10°C and -9°C respectively, a marked improvement on the previous result. These temperatures gradually increased over time, due to the exchange of heat at the pre-cooler. After a number of such tests, it became clear that the use of a salt/ice bath and the planned use of dry ice/acetone would prove to be impractical. This preliminary test showed the importance of cooling the reaction solution prior to its entry of the reactor. As such, the pre-coil was wrapped around the external copper coil of the reactor and heavily insulated. This would effectively reduce the distance between the pre-cooling and the reactor inlet while also giving a secondary use to the outer cooling, nullifying the need to continuously replenish any cooling baths, and allowing for the temperature to remain constant and to be easily controlled. Furthermore, this reduces the physical footprint of the reactor, making it far more compact.

The Haake recirculating chiller was replaced with the Julabo® FP-89 ME, an ultra-low refrigerated circulator, with a working temperature range of -90 to 100°C. Thermal

HY™ also from Julabo, replaced the ethylene glycol mixture. Thermal HY is a silicone based fluid that is rated down to -80°C.

The effect of the new pre-cooling set up and apparatus was first tested without the light source *in situ*, the results of which are shown in

Table 2.6. Despite the capacity to reach temperatures down to -80°C, a minimum temperature of -60°C was selected, due to potential incompatibilities of the plastic fittings and seals in the reactor at lower temperatures.



Figure 2.15. Photo of the HPR during low-temperature testing with the PhotoLED *in situ*. There was a need for a high level of insulation to achieve low internal reactor temperatures.

Table 2.6. Temperature test of the HPR. Ethanol was pumped through the reactor at a flow rate of 5 mL min<sup>-1</sup>.

Circulator Temp /°C	Inlet temp /°C	Interior temp /°C
-20	-7	-13
-50	-24	-36
-60	-30	-43

With the PhotoLED *in-situ*, and purged with nitrogen to avoid ice formation the circulator temperature was gradually lowered to -65 °C. During which the flow rate was alternated between 1 and 5 mL min<sup>-1</sup> to observe the effect on the inlet and interior temperatures. The internal temperature, T<sub>2</sub>, reached a low of -39°C at a flow rate of 5.0 mL min<sup>-1</sup> with a corresponding inlet temperature, T<sub>1</sub>, of -34°C. Increasing the flow at a particular circulator temperature resulted in significant increase in the respective inlet

temperatures, indicating that significant heat is being gained between the outlet of the pre-cooling coil and the inlet of the reactor. Increased insulation was therefore required for this section of the reactor.

Table 2.7. Results for the temperature test with the PhotoLED in situ.

FP-89 ME Temperature / °C	Flow Rate / mL min <sup>-1</sup>	T <sub>1</sub> / °C	T <sub>2</sub> / °C
-	1.0	18	18
-20	1.0	0	-9
-35	1.0	-6	-21
-35	5.0	-18	-21
-50	5.0	-27	-31
-50	1.0	-15	-32
-60	1.0	-15	-36
-60	5.0	-31	-37
-65	5.0	-34	-39

The LED interior cooling was set to 10°C throughout the experiment. The temperature was lowered from ambient to -65°C, the flow rate was altered between 1 and 5 mL min<sup>-1</sup>.

The Julabo® FP-89 ME was originally connected to the reactor with Tygon® tubing, this was rather rudimentarily insulated with cotton wool and foam pipe insulation. The Tygon® tubing was replaced with Julabo® M series triple insulated metal tubing, with a rating down to -100°C. Despite the improvement in the insulation of the transfer tubing, no improvement in the interior temperature was observed when the previous conditions were repeated. The pre-cooling coil flow direction was then set to counter the flow of the copper coil coolant to assess if this had any effect on the inlet or interior temperatures. The interior temperature registered a low of -38°C. A thermocouple was placed at the outlet of the reactor. The temperature test was repeated with a lower recirculator temperature of -70°C, reaching an interior temperature of -42°C. The outlet temperature highlights the extent to which the solution gains heat through the reactor. This phenomenon is exacerbated at the lowest fluid velocities.

Table 2.8. Temperature testing without interior cooling at a flow rate of 1.0 mL min<sup>-1</sup>.

FP-89 ME Temperature / °C	T <sub>1</sub> / °C	T <sub>2</sub> / °C	T <sub>3</sub> / °C
15	20	19	22
0	14	7	19
-20	6	-8	13
-40	-5	-24	3
-60	-14	-37	-4
-70	-18	-42	-9
-70 <sup>a</sup>	-33	-42	-16

With the circulator set to -70°C the lowest interior temperature reached was -42°C. The increase in flow rate only has an effect on the inlet temperature. <sup>a</sup>flow rate set to 5 mL min<sup>-1</sup>.

The second generation PhotoLED was then installed in the reactor. Temperature tests were conducted with the current set to the maximum of 500 mA. Importantly the second-generation PhotoLED has a smaller diameter mounting than the first-generation, to the extent whereby, the light source and its protective borosilicate sheath can both be placed within the reactor. Therefore the heat exchange fluid can be flowed up the centre of the quartz tube. However, as both Thermal HY and the Bola gaskets holding the tubes in place are both silicone based, they are incompatible with this fluid because the gaskets absorb the fluid, causing swelling, deformation and eventual dissolution. Therefore, a 60:40 (v/v %) ethylene glycol/ water mixture was used as the internal cooling fluid, with the Haake recirculating chiller.

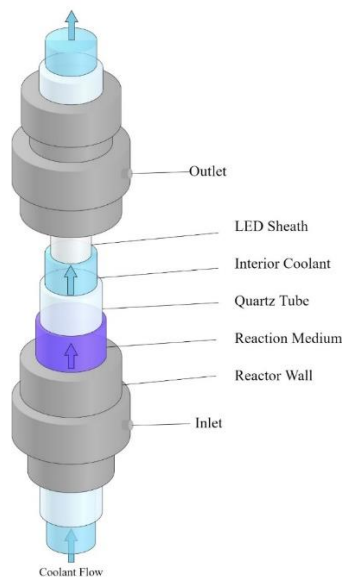


Figure 2.16: 3D CAD model of the HPR with the outer sections cut away to highlight the positions of each of the interior components and to show the path of the interior coolant.

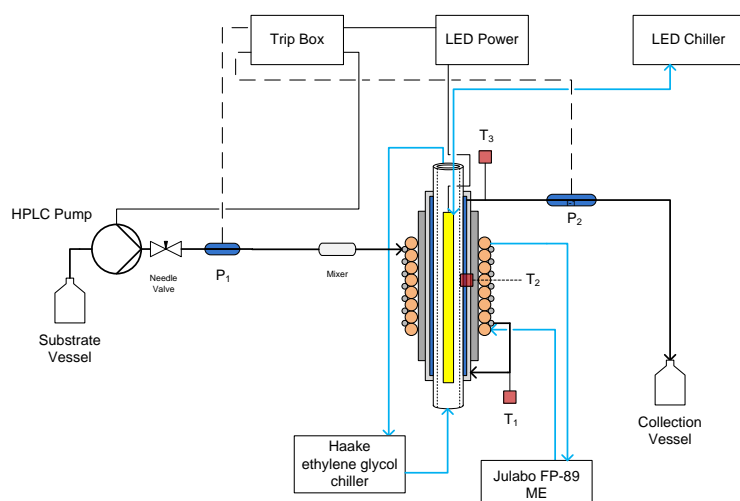


Figure 2.17: Reactor set-up indicating the addition of the recirculating chillers, the pre-cooling coil and the placement of the thermocouples.

Table 2.9. Results from temperature testing the HPR with ethylene glycol / water interior cooling.

FP-89 ME / °C	Haake / °C	T <sub>1</sub> /°C	T <sub>2</sub> /°C	T <sub>3</sub> /°C	LED Temp /°C
-	-10	-	17	-	-
-40	-20	-6	-21	0	9.9
-50	-20	-9	-26	-2	9.8
-50	-30	-10	-27	-4	9.6
-60	-33	-12	-32	-5	9.1

Tests were conducted at a flow rate of 1.0 mL min<sup>-1</sup> with the recirculator connected to the PhotoLED set to 5°C.

The lowest temperature reached by the ethylene glycol chiller was -33°C. With this as the interior cooling and the outer cooling set to -60°C an interior temperature of -32°C was reached, higher than the -37°C reached at the same circulator temperature without interior cooling. A direct comparison test was then made between the two conditions. During another temperature test the exterior cooling was set to -75°C. With an internal cooling of -35°C the reactor interior reached -42°C. This decreased to -45°C upon stopping the flow of the internal cooling and leaving the interior to drain of fluid. The inlet temperature also decreased from -19°C to -22°C. The internal cooling is beneficial in reducing the reactor temperature when the external cooling is greater than -60°C, below this point the glycol/water mixture inhibits the reactor. With air being a good insulator, the empty quartz tube exhibits more desired thermal properties when achieving low reactor temperatures.

To further decrease the interior temperature of the reactor, the silicone gaskets in the end T- and L- joints were replaced with FEP encapsulated silicone o-rings and PEEK back-up o-rings. These o-rings were found to adequately hold the quartz and borosilicate tubes, and therefore allowed for Thermal HY to be used as the interior coolant. Two-way splitters were added to the outlets of the triple insulated stainless steel tubing such that coolant flow could be diverted to the inlet of the external jacket and through the centre of the reactor.

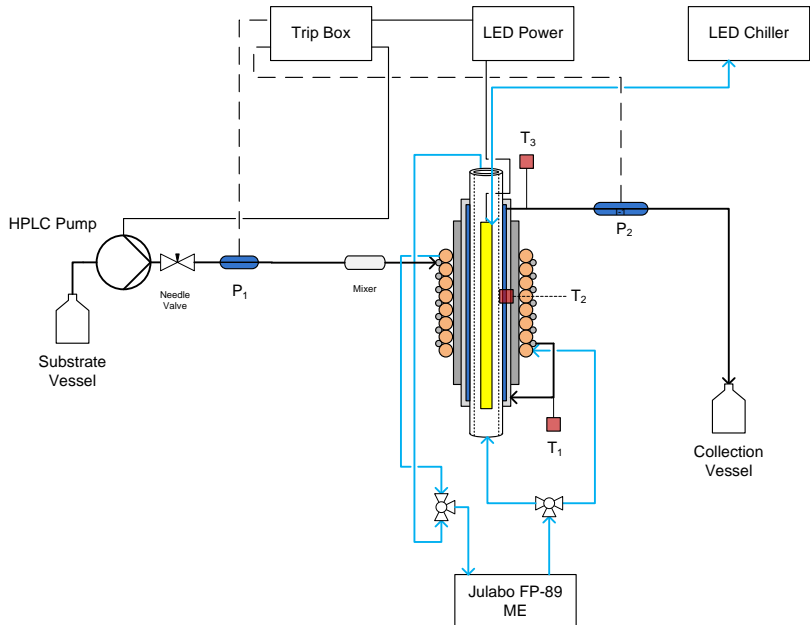


Figure 2.18: Reactor diagram for low temperature testing with internal cooling supplied by the Julabo FP-89 ME ultra-low temperature recirculator with the silicone oil based fluid Thermal HY.

Temperature testing was undertaken with the PhotoLED (500 mA) *in situ*. The recirculating chiller was set to -80°C, however the temperature of the Thermal HY fluid reached a minimum at -73°C. With the coolant now flowing through both the external jacket and the centre of the reactor, a greater thermal mass is being cooled and therefore a greater cooling capacity is required to achieve the set temperature, of which the FP-89 ME does not possess. With the recirculator only reaching -73°C, a minimum internal temperature of -56°C was achieved. This result was a disappointment since there was only a -10°C improvement over the previous set up in spite of the extensive modifications..

The reason for this disappointing result was most likely the fact that the insulation of the Bola® L- and T-joints was insufficient, with considerable initial heat gain as the fluid reached the reactor. An important post-experiment observation was the fact that the Thermal HY heat transfer fluid, had leaked from the Bola® screw joints. On inspection of the interior of the screw fitting, it was found that one piece, in the lower L-joint, had fractured. Clearly, the low temperature had increased the brittleness of the material leading to its malfunction. The majority of the components of the screw fittings are made from PTFE, a material with good resistance to low temperature. However polyphenylene sulfide (PPS) is used to construct two of the inner ferrules. PPS is rated to have a temperature resistance down to -20°C. These fittings are therefore unsuitable

for use at the temperatures being investigated. Furthermore, it was discovered that both the screws fittings had come slightly loose during the experiment, potentially through repeated contraction and expansion during the temperature cycles. It therefore became apparent that with the current set-up, the silicone oil could not be used at such low temperatures to cool the centre of the reactor.

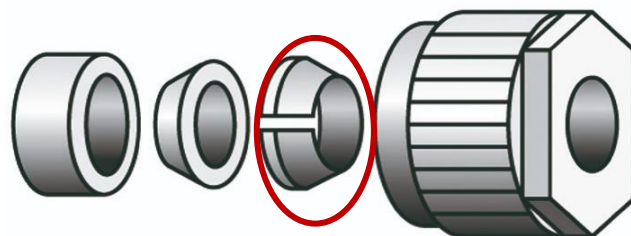


Figure 2.19. The components of the screw fittings, the PPS Ferrule that fractured is circled in red.

The recirculator was set to -80°C and, without interior cooling, was able to reach -77°C, giving a corresponding internal temperature of -46°C. It was therefore decided to proceed without interior cooling until an alternative method for delivering the Thermal HY could be developed.

## 2.8. Low-Temperature Photo-Oxidations in the HPR

Reaching an internal temperature of -46°C with a light source *in situ* established that there was a potential to undertake continuous photochemical reactions at low temperatures. Hence, an investigation into photochemical reaction types that would benefit from these conditions was initiated. The photo-oxidation of citronellol (see Chapter 1) seemed to be a good place to start.<sup>141,142,144,145,189,213,214</sup>

### 2.8.1. Rig Modifications needed to permit Photo-Oxidations

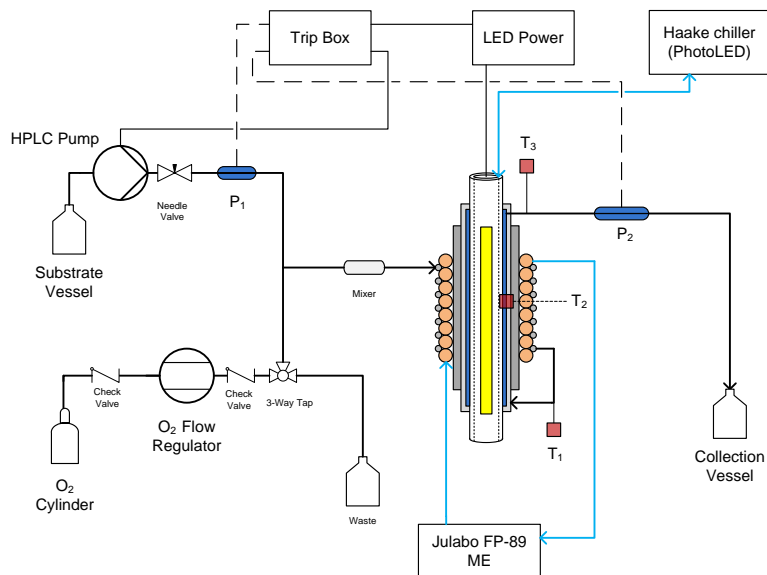


Figure 2.20: Schematic of the reactor set up, highlighting the placement of non-return valves (check valves). The two streams intersect at a T-piece (Swagelok® 1/8" o.d) to form plug flow, then entering a section of PTFE tubing filled with glass beads (212-325  $\mu\text{m}$ ) to induce turbulent mixing. The streams then enter the pre-cooling coil wrapped around the external copper coil of the reactor. Thermocouples are placed at the inlet,  $T_1$ , in the interior,  $T_2$ , and at the outlet,  $T_3$ , of the reactor.

Only minor adjustments had to be made to allow for the delivery of oxygen into the system. An oxygen cylinder (200 bar) was connected through PTFE tubing (1/8" o.d) to a Bronkhorst® gas flow controller. Non-return valves (Swagelok® 1/3 psi) were placed at the outlet of the oxygen regulator and the outlet of the flow controller. The controller was attached to a 3-way valve, with one line directed to the reactor and the other to the back of the fume hood, giving the ability to divert the oxygen flow away from the reactor in case of problems. The oxygen and substrate flows intersect one another at a Tee piece (Swagelok® 316 stainless steel, 1/8" o.d) to initiate Taylor flow. The alternating liquid and oxygen plugs subsequently pass through a short section of tubing (PTFE, 1/8" o.d, 20 cm length) filled with glass beads (425-600  $\mu\text{m}$ ) to act as a static mixer, inducing turbulent mixing. The remainder of the reactor shown in Figure 2.x was unaltered from that previously described.

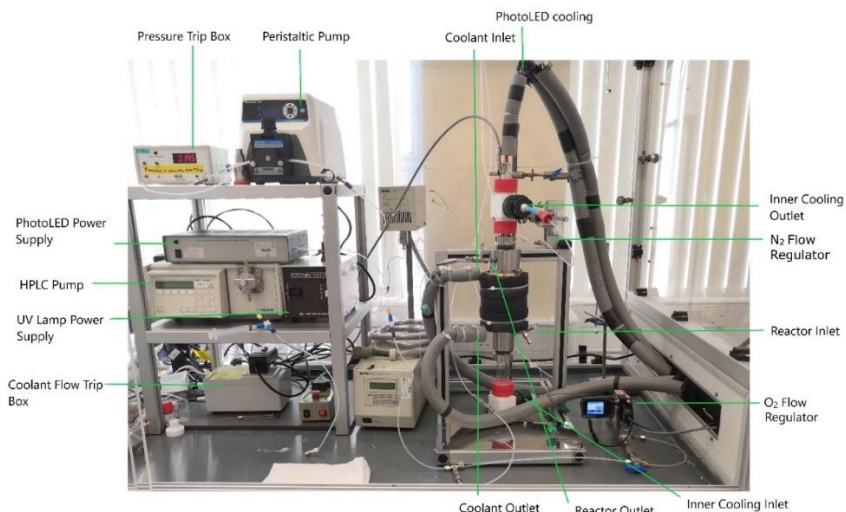


Figure 2.21. Photo of the reactor set-up for the low-temperature photo-oxidation of citronellol. The key components are labelled.

## 2.9. Photo-Oxidation of Citronellol in the HPR

The photo-oxidation of (S)-(-)- $\beta$ -citronellol, **8**, a key step in the synthesis of the commercially valuable fragrance, (-)-rose oxide, was chosen as the test reaction for the low-temperature HPR.<sup>154,157,215</sup> **8** reacts with  ${}^1\text{O}_2$  *via* an ene-reaction to produce two hydroperoxides, **9** and **10**, these are reduced to form the corresponding diols, **11** and **12**, however it is only the terminal diol, **11**, that undergoes an acid catalysed cyclisation to form rose oxide, **13**, as shown in Figure 2.22.<sup>193</sup>

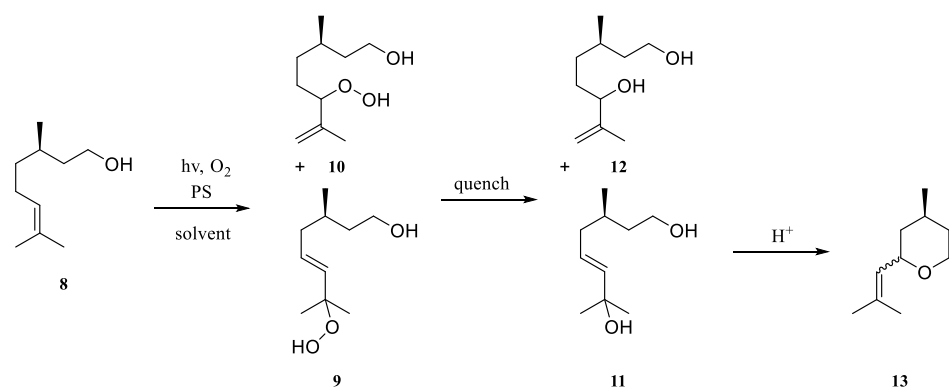


Figure 2.22. Scheme for the photo-oxidation of citronellol to the corresponding hydroperoxides. Followed by subsequent quenching to the relevant diols and acidification to produce the commercially relevant molecule rose oxide.

Initial conditions for the photo-oxidation of citronellol were based on the published Dragoco patent,<sup>156</sup> along with research conducted by Meter *et al.* and Seeberger *et al.*<sup>140,154</sup> The Dragoco patent focusses on the commercial production of rose oxide, here rose bengal is selected as the preferred photosensitiser.<sup>156,157</sup> Rose bengal exhibits a

maximum absorbance at ca. 550 nm in ethanol, this overlaps poorly with the blue PhotoLED ( $\lambda_{\text{max}}$  of 424 nm). Therefore it was decided to use the broad spectral emission of the ‘white light’ PhotoLED with rose bengal.

An alternative photosensitiser, the ruthenium complex, tris(2,2'-bipyridine)ruthenium(II) hexafluorophosphate,  $[\text{Ru}(\text{bpy})_3][\text{PF}_6]_2$ , with a  $\lambda_{\text{max}}$  of 453 nm was also investigated in conjunction with the first-generation blue PhotoLED ( $\lambda_{\text{max}}$  424 nm). As shown in Figure 2.6, both the 1<sup>st</sup> and 2<sup>nd</sup> generation of the blue PhotoLED exhibit far greater emission intensities than the white LED. Furthermore, the use of near monochromatic light, with good overlap with the absorption band of the photosensitiser will minimise the chances of unwanted side reactions. In contrast to rose bengal, the ruthenium complex has greater stability against quenching by  $^1\text{O}_2$  and a higher quantum yield for  $^1\text{O}_2$  generation,  $\text{Ru}(\text{bpy})_3^{2+}$ , has been found to have a  $^1\text{O}_2$  quantum yield of  $\phi_{\Delta}$  0.86 in methanol, while rose bengal has  $\phi_{\Delta}$  0.68.<sup>154,216</sup>

The concentrations of **8** and each photosensitiser were chosen to be 0.1 M and 0.5 mM (0.5 mol %) respectively.  $[\text{Ru}(\text{bpy})_3][\text{PF}_6]_2$  (0.5 mM) precipitated out in ethanol at a temperature of -45°C, but was soluble in methanol at this temperature. Photo-oxidations of **8** were carried out at various temperatures with a 1:10 ratio of flow rates of substrate : gas, corresponding to a molar ratio of 1:4.2.

*Table 2.10. Results from the photo-oxidation of citronellol to the respective hydroperoxides. The ratio of the two isomers increases with respect to peroxide **9** upon reduction in the reaction temperature for both photosensitisers.*

PS	Solvent	LED	Liquid FR / mL min <sup>-1</sup>	$\text{O}_2$ FR / mL min <sup>-1</sup>	Temp. / °C	Conv. / %	<b>9</b> / %	<b>10</b> / %	<b>9:10</b>
$[\text{Ru}(\text{bpy})_3][\text{PF}_6]_2$	MeOH	424 nm	1	10	20	100	48	45	1.1
					-41	100	58	41	1.4
$[\text{Ru}(\text{bpy})_3][\text{PF}_6]_2$	MeOH	424 nm	2	20	19	100	53	41	1.1
					-42	86	49	35	1.5
rose bengal <sup>a</sup>	EtOH	White	1	10	15	100	54.5	44	1.3
					-22	77	45	32	1.4
					-34	64	37	25	1.5
rose bengal <sup>a</sup>	EtOH	White	2	20	17	61	40	32	1.2
					-22	80	52	37	1.4
					-35	58	34	23	1.5

For ruthenium, full conversion is achieved for both conditions at the slower flow rate of 1.0 mL min<sup>-1</sup> while a conversion of 86 % is reached for the low temperature oxidation run at a liquid flow rate of 2.0 mL min<sup>-1</sup>. While full conversion is not achieved when rose Bengal has been used as the photosensitiser. <sup>a</sup>photo-oxidation with ethylene glycol/water internal cooling.

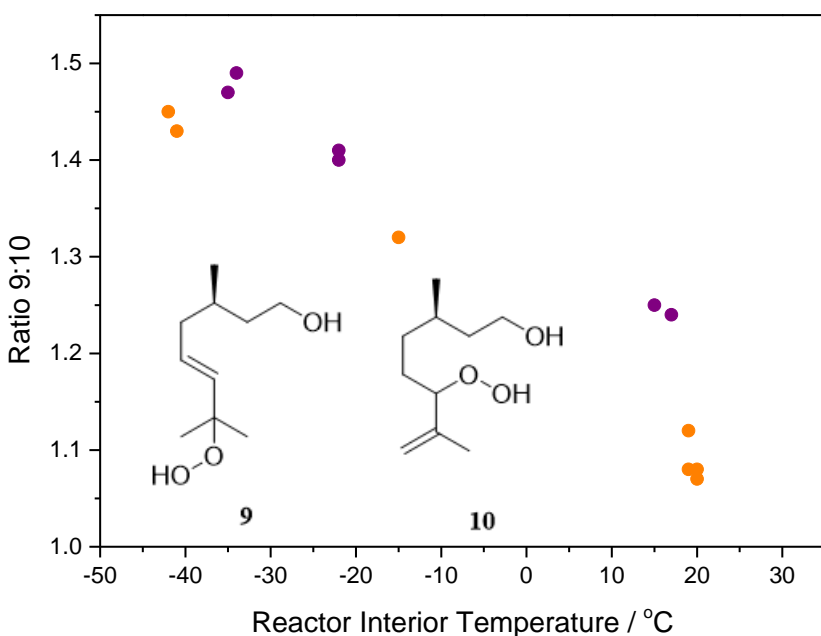


Figure 2.23. Ratios of products 9:10 for all all citronellol oxidations carried out plotted against temperature, indicating a general increase in selectivity for hydroperoxide 9 with decreasing reaction temperature. Experiments using tris(2,2'-bipyridine)ruthenium(II) hexafluorophosphate/MeOH are highlighted in orange while those conducted with rose bengal/EtOH are sown in purple.

Figure 2.23 highlights the effect of reactor temperature on the ratio of the two hydroperoxides, with a general increase in the formation of the desired hydroperoxide (**9**) with decreasing temperature. The increased ratio of the hydroperoxides for the reactions carried out with rose bengal primarily attributed to the lack of quantitative conversion, a result of the inferior  ${}^1\text{O}_2$  quantum yield of rose bengal and the low emission intensity of the white LED. The initial photo-oxidations of **8** have provided evidence of the effect of low temperatures on the selectivity of ene- type oxidations. These investigations have also highlighted the ability of the HPR to undertake photo-oxidations down to  $-45^\circ\text{C}$ .

## 2.10. Photo-Oxidations of DHAA in the HPR

Chapter 1 discussed the photo-oxidation of dihydroartemisinic acid (DHAA, **14**), a key step in the synthesis of the antimalarial drug, artemisinin (**18**), like the oxidation of citronellol, proceeds *via* an ene-mechanism forming three hydroperoxides, **15** – **17**, Figure 2.24. It is generally believed only the tertiary hydroperoxide (**15**) is capable of undergoing the subsequent synthetic steps to afford **18**. Therefore increasing the relative amount of **15** through the use of low temperature photo-oxidation is likely to have a positive effect on the overall yield of **18**.<sup>5</sup>

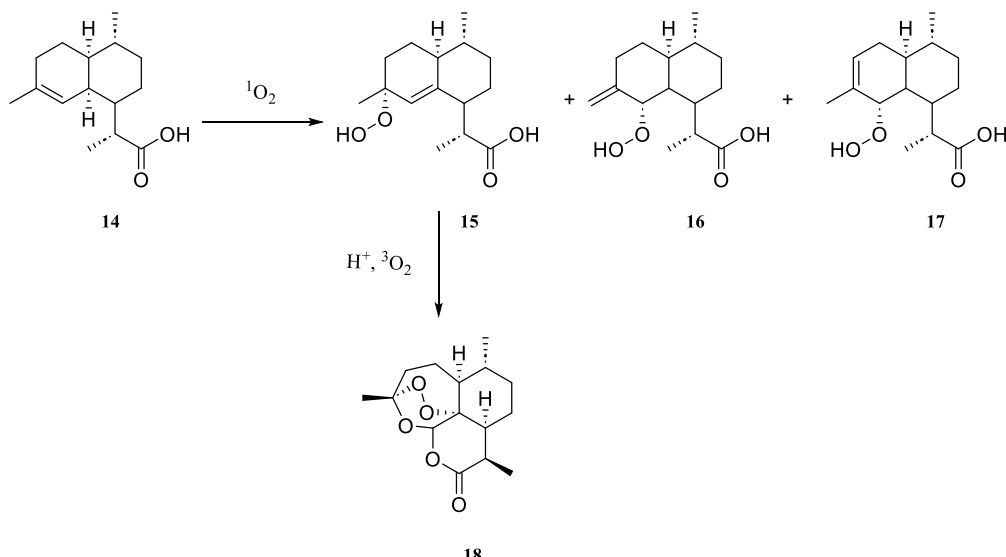


Figure 2.24: Simplified synthesis of artemisinin through the photo-oxidation of DHAA, **14**, to hydroperoxides, **15**, **16** and **17**, with subsequent acid catalysed Hock cleavage and oxidation to artemisinin, **18**. It is commonly accepted that only **15** can proceed to form **18**.

Kopetzki *et al.* in their work of 2013, made considerable advances in this domain.<sup>8</sup> Their work on developing a ‘one-pot’ photochemical continuous-flow approach led to an artemisinin yield of 69 %, this yield being based on the hydroperoxide **15** and not on the initial DHHA concentration. Their synthesis of artemisinin was best performed at a photoreactor temperature of -20°C. Moreover, they demonstrated that the reduced temperature improved the selectivity towards **15** as shown in Table 2.11.

Table 2.11: Temperature effect on the photo-oxidation step as undertaken by Kopetzki *et al.*<sup>8</sup>

Temperature / °C	Conversion / %	15 / %	16 / %
75	86	62	10
60	99	70	11
40	99	73	12
20	99	78	11
0	99	81	11
-20	98	84	10

Kopetzki investigated a number of other factors that will affect the reaction including the solvent. They led efforts to maintain a balance of optimum reaction yield with economic, environmental and health factors, concluding that toluene was the preferred option, over fluorinated hydrocarbons that slightly improved upon the yield.

The low-temperatures used during the following work could lead to a number of issues, not experienced by Kopetzki at the relatively mild temperature of -20°C.<sup>8</sup> The viscosity of a liquid,  $\eta_L$ , increases with decreasing temperature, as described by the Andrade equation (2.1), where A and B are constants and T is the temperature in kelvin.<sup>217</sup>

$$\eta_L = Ae^{B/T} \quad (2.1)$$

As such, the viscosity of the solvent may increase to a point whereby significant pressure is built up within the system. According to Henry's law, an increase in pressure in a fixed volume will lead to an increase in the oxygen concentration within the liquid.<sup>218</sup> If this value exceeds the limiting oxygen concentration (LOC) then the risk of combustion is greatly heightened.<sup>130,219</sup> For the avoidance of this risk, initial reactions would be carried out in the non-flammable, dichloromethane. Furthermore, <sup>1</sup>O<sub>2</sub> exhibits a longer lifetime of 99 μs in DCM compared to 29 μs in toluene.<sup>53</sup>

The solubility of organic compounds is known to decrease with decreasing temperature.<sup>220</sup> There is the potential that the substrate or the photosensitiser may become insoluble at the reaction temperature being investigated. Due to the fact that, within the current set-up, the solution is cooled in the pre-cooling coil constructed from narrow stainless steel (1/16" o.d, 0.0225" i.d), any precipitation might block the current flow system leading to a rapid increase in pressure.

Solubility tests were carried out for multiple photosensitiser/solvent combinations at various temperatures. Ru(bpy)<sub>3</sub>Cl<sub>2</sub> which was previously selected for the photo-oxidations of citronellol has been used in the literature for the photo-oxidation of DHAA to artemisinin.<sup>141,189,221</sup> It was found that at -40°C, TPP at a concentration of 0.25 mM remained in solution in DCM, while Ru(bpy)<sub>3</sub>Cl<sub>2</sub> at the same concentration required a mixture of 98:2 DCM:EtOH to avoid precipitation. DHAA at 0.05 M, the typical concentration used within our group, remained soluble in both solvent systems.<sup>141</sup>

The photo-oxidations of citronellol (above) revealed some limitations of the reactor and for subsequent modifications to be carried out. As expected, the back-pressure in the system increased with decreasing temperature. At a value around 40 psi, this level of back-pressure was sufficient to disrupt the Taylor mixing of the gas and substrate, eventually reaching the point at which the pressure was too high for the oxygen stream to maintain flow, resulting in the substrate flowing towards the outlet tubing of the gas flow controller.

Wide fluctuations were observed in the flow rate of the gas, the regulator struggled to maintain a constant flow of O<sub>2</sub>, were also attributed to the increase in the pressure of the system. These fluctuations resulted in incomplete Taylor flow and variations in the quantified data. To alleviate this, the original stainless steel pre-cooling coil (1/16" o.d, 0.0225" i.d) was replaced with a wider bore stainless steel coil (1/8" o.d, 1/16" i.d) at the cost of less efficient heat transfer.

Initial experiments, however, consistently resulted in pump failures, with the gas in fact flowing towards the HPLC pump head. It was found that for the pump to work efficiently, an appropriate level of back-pressure has to be in the system. Therefore, a short length of stainless steel (1/16" o.d, 0.0225" i.d, length 10 cm) tubing was added directly after the pump, producing a constant level of back-pressure.

With the new set-up, a pressure of 18 psi was produced at a substrate flow of 1.0 mL min<sup>-1</sup>, at an internal reactor temperature of -50°C. Without the short section of narrow tubing, an internal temperature of -15°C was sufficient to reach 38 psi and result in flow issues.

Initial experiments with the new set up occurred with no system failures and with the gas flow controller maintaining constant flow. These experiments allowed the two photosensitisers, Ru(bpy)<sub>3</sub>Cl<sub>2</sub> and meso-tetraphenylporphine (TPP), to be compared. At a photoreactor temperature of -45°C, and flow rates of 1.0 and 5.0 mL min<sup>-1</sup> for the DHAA solution and O<sub>2</sub> gas respectively (corresponding to a DHAA:O<sub>2</sub> molar ratio of 1:4.2), both photosensitisers produced full conversion, however TPP (0.25 mM, 0.5 mol %, 424 nm PhotoLED) was found to outperform Ru(bpy)<sub>3</sub>Cl<sub>2</sub> (0.25 mM, 0.5 mol %, White PhotoLED), giving a superior yield of 77 % for hydroperoxide **15**, compared to 59 % with the ruthenium complex.

Subsequent photo-oxidations of DHAA in the HPR were therefore carried out using TPP (0.5 mol %) as the photosensitiser in conjunction with the first-generation blue PhotoLED ( $\lambda_{\text{max}}$  424 nm). Several photoreactor temperatures were studied with a range of substrate and gas flow rates. Samples were dried over N<sub>2</sub> and prepared for NMR with biphenyl as an external standard in CDCl<sub>3</sub>. The ratios of the main hydroperoxides, **15** and **16** were calculated within the NMR software (Mnova<sup>TM</sup>) by setting the integral value of the main hydroperoxide, **15** ( $\delta$  5.24 ppm), to 1000 and dividing by the subsequent value of the minor hydroperoxide, **16** ( $\delta$  5.06 ppm). The results of the

various photo-oxidations of **14** are expressed in Table 2.12. High levels of conversion are achieved even with residence times in the photoreactor down to 20 seconds. The high conversion achieved at low residence time highlight the potential for the HPR to be used as an efficient high-throughput photoreactor. Furthermore, the effect of the temperature on the selectivity of the reaction can be clearly seen in Figure 2.25, the ratio of **15** to **16** gradually increases as the photoreactor temperature decreases. This is highly encouraging for the potential use of the HPR and low temperature photo-oxidation in improving the synthesis of artemisinin.

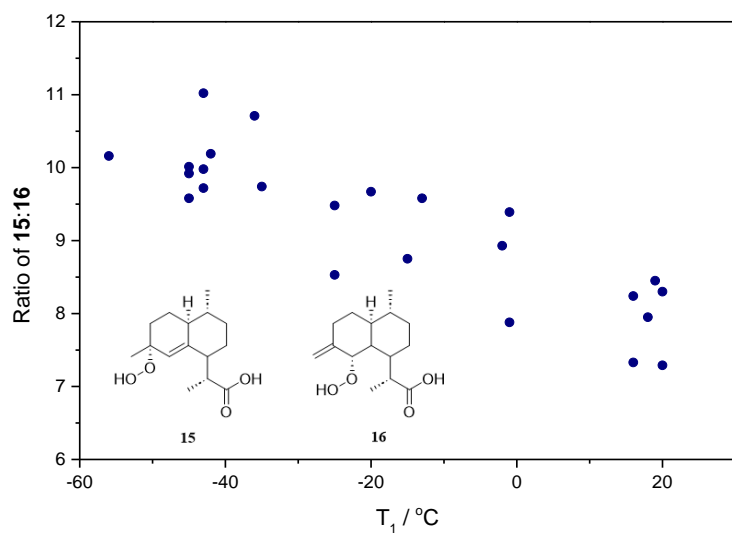


Figure 2.25. Relationship between the temperature of the photo-oxidation of DHAA and the corresponding hydroperoxide ratio, indicating an increase in selectivity towards hydroperoxide **15** with decreasing temperature. All reactions shown were carried out with TPP (0.25 mM, 0.5 mol %) in dichloromethane.

Table 2.12. Result from the photo-oxidation of DHAA in the HPR reactor.

Liquid Flow Rate /mL min <sup>-1</sup>	O <sub>2</sub> Flow Rate /mL min <sup>-1</sup>	Residence Time / min	Temp. /°C	Conv. /%	15 /%	16 /%	15:16
1	5	3:20	20	100	15	9	1.7
			-15	100	76	9	8.8
			-45	100	77	8	10.0
2	10	1:40	20	100	68	9	7.3
			-2	100	77	9	8.9
			-25	100	82	9	9.5
			-36	100	86	8	10.7
			-45	100	77	8	9.6
3	15	1:00	19	100	74	9	8.5
			-1	100	76	8	9.4
			-20	100	70	7	9.7
			-35	100	75	8	9.7
			-45	100	80	8	9.9
5	25	0:40	16	100	88	12	7.3
			-1	100	87	11	7.9
			-43	100	90	9	10.0
	12.5	1:10	-43	98	87	8	11.0
10	50	0:20	16	92	77	9	8.2
			-43	89	81	8	9.7
20	50	0:15	20	74	57	7	8.3
			-13	73	63	7	9.6
			-42	63	58	6	10.2

## 2.11. Summary

In relation to the aims set out at the beginning of this chapter, a reasonable deal was ultimately achieved:

First, the studies of the two [2+2] photocyclisations at close to ambient temperature highlighted issues with the reactor that could be alleviated by improving the mixing and reducing the optical path length. This was initially achieved by the addition of glass beads, however due to their difficulties in handling and potential negative effect on the pressure rating of the reactor they were ultimately replaced by the more robust PTFE spiral.

Second, the modification of the reactor to facilitate low photochemistry, was carried out with a reasonable degree of success. Simple approaches were investigated including the use of a coil submerged in a salt-ice bath, for pre-cooling of the reaction solution, and a Haake® F3 recirculating chiller with ethylene-glycol for the external cooling of the reactor, resulted in only slight reductions in the internal temperature of the reactor, these were subsequently replaced. In addition, replacement of the Hg arc lamp, with a custom built LED assembly allowed lower temperatures to be reached because, the Hg arc operated at undesirable temperatures in excess of 100°C and required external cooling while the LED assembly is internally cooled and operates at far lower temperature, typically controlled to be 10°C.

Third, the cooling capacity of the rig was then greatly improved. The Julabo® FP-89ME ultra-low temperature recirculating chiller, with Thermal HY™ silicone heat transfer fluid, replaced the ethylene-glycol chiller. The extent of heat gain to the Thermal HY fluid was reduced between the chiller and the reactor, by replacing the foam insulated Tygon® transfer tubing with Julabo® M-series triple insulated metal tubing. The pre-cooling coil was then fitted external copper coil of the reactor and insulated, thereby utilising the increased cooling capacity of the system and reducing the need for operator input to maintain a constant pre-cooling temperature.

Fourth, to further attempt to reduce the internal temperature of the reactor the use of Thermal HY as an internal coolant was investigated. The silicone gaskets of the Bola® joints used to hold the quartz and borosilicate tubes were replaced by FEP encapsulated silicone O-rings. The use of the internal cooling gave a slight improvement on the internal temperature, but the interaction of the low temperature fluid with the Bola screw joints led to cracking of the internal ferrule and subsequent leaking of the fluid. Furthermore a negative effect on the temperature achieved by the recirculating chiller was also observed, indicating that the power capacity of the recirculator had been reached. Internal cooling was therefore omitted.

Fifth, adaptation of the rig with the addition of an oxygen cylinder and gas flow controller allowed investigations into the effect of low temperature on the outcome of the photo-oxidations of citronellol and dihydroartemisinic acid. Attention was directed in particular to the latter oxidation, in which significant improvements in the reaction selectivity were observed with decreasing reactor temperature. This observation has the potential to greatly improve the synthesis of the highly important anti-malarial drug,

artemisinin. As such, a great deal of attention was then focussed on improving the selectivity even further through the reduction in reactor temperature. It was however realised that the limitation of the reactor had been reached, and for photochemistry to be performed at lower temperature a different design of reactor should be used.

The above conclusions demonstrate that a robust reactor for low temperature photochemistry has been developed. The adaptations made resulted in an internal reactor temperature of -46°C being achieved. This temperature is low enough for potential photochemical reactions to be performed in solvents such as liquid ammonia and liquid- and supercritical-CO<sub>2</sub>. However, further improvements can be made, including the replacement of the Bola screw joints, manufactured from polyphenylene sulfide, for resistant material, thereby allowing for the use of internal cooling.

## Chapter 3. Development of a Continuous-Flow Reactor for Low Temperature Photo-Oxidations

The aims of this Chapter follow on from Chapter 2 to: i) exploit further the improvements observed in the selectivity of the photo-oxidation of dihydroartemisinic acid, DHAA, obtained through the development of a new photoreactor capable of achieving internal temperatures below those reached with the high-pressure reactor (HPR) in Chapter 2; ii) investigate the effect of the improvements on selectivity into the full synthesis of artemisinin from dihydroartemisinic acid. To address these aims the following strategies were implemented:

- To design a photo-reactor that encompasses the positive features of the HPR while also allowing for efficient photo-oxidations to be performed at temperatures down to -80°C, the limit of the Thermal HY cooling fluid.
- To perform the photo-oxidation of dihydroartemisinic acid, specifically the effect of the lower reactor temperatures on the hydroperoxide selectivity towards the synthesis of artemisinin.
- To investigate the use of the photoreactor in the full synthesis, using so-called ‘one-pot’ and ‘two-pot’ regimes with alterations to the reactor and the reaction parameters in order to optimise the yield of artemisinin.

### 3.1. Reactor Design

A positive feature of the original HPR described in Chapter 2 is its annular design, allowing for the maximum capture of the radial emission from the internal light source. This feature is the first consideration for a second-generation low temperature photoreactor.

The main issue with the HPR was the incompatibility of particular materials with first, the silicone heat transfer fluid and second, the low fluid temperature. Therefore, it was decided to construct a second-generation reactor from temperature resistant materials, while also exhibiting high thermal conductivity.

Furthermore, reducing the size and the number of components of the reactor was important to achieve ultra-low reaction temperatures. It was found that the large thermal mass of the HPR resulted in the Julabo® recirculating chiller achieving a minimum of -73°C. A smaller reactor reduces the power requirement of the chiller, therefore increasing the likelihood that the system might achieve the desired temperature of -80°C.

The first approach employed an FEP coil reactor submerged directly into the fluid reservoir of the Julabo® FP89-ME recirculating chiller. The FEP coil reactor, frequently used for continuous flow photochemistry, was developed by Brooker-Milburn *et al*, and possesses the attributes that adhere to the design stipulations laid out above.<sup>1141</sup> The design maximises photon flux capture, while its construction is simple and cheap. It can therefore be employed and adapted with ease.<sup>24</sup> By submerging the FEP and a ‘pre-cooling’ coil into a reservoir of cold fluid, the photoreactor is in direct contact with the Thermal HY. This eliminates the need to transport the fluid beforehand, avoiding the heat gain that proved to be a limiting factor in the HPR’s capacity to achieve low temperature. Furthermore, there is a significant reduction in both the thermal mass of the material and the number of components compared to the HPR. The use of FEP rather than stainless steel also contributes to an improvement in the safety aspects of the new system. Stainless steel can catalyse the decomposition and isomerisation of organic peroxides and is incompatible with acidic conditions.<sup>222,223</sup> FEP on the other-hand is chemically inert, resisting strong acidic and alkaline media, and is compatible with a wide range of solvents. However, a disadvantage of FEP is its low thermal conductivity,  $0.19\text{--}0.24 \text{ W m}^{-1} \text{ K}^{-1}$ , compared to  $12\text{--}45 \text{ W m}^{-1} \text{ K}^{-1}$  for stainless steel.<sup>104</sup> The use of a ‘pre-cooling’ coil prior to the photoreactor allows for the

reaction solution to reach the fluid reservoir temperature before the photochemical reaction is initiated.

*Table 3.1. Thermal conductivity of some materials commonly employed for the fabrication of reactors.*<sup>104</sup>

Material	Thermal Conductivity (W m <sup>-1</sup> K <sup>-1</sup> )
PFA (perfluoroalkoxy alkane)	0.195
FEP (fluorinated ethylene propylene)	0.19-0.24
Glass	1
Stainless Steel	12-45
Aluminium (pure)	237
Aluminium (alloy)	120-180
Copper	401

The first iteration of the reactor was constructed out of a single layer of thin-walled FEP tubing (1/8" o.d., 0.01" wall thickness, length 5.20 m, volume 40 cm<sup>3</sup>) coiled around a borosilicate closed end tube. Due to the fragility of the thin-walled FEP, it was not possible to confidently secure Swagelok® metal ferrules. Therefore, flangeless ETFE (ethylene tetrafluoroethylene) ferrules were used in conjunction with an ETFE nut.

As with the HPR, the reaction solution was pumped through a Gilson® HPLC pump and combined with the oxygen flow at a Swagelok® T-piece (1/8") to produce Taylor flow. The liquid/gas flow pattern then passes through a short section of PTFE tubing (1/8" o.d., length 15 cm) filled with glass beads (400-625 µm) to induce turbulent mixing. The flow then enters the recirculator fluid reservoir, through an insulated lid constructed of expanded polystyrene and into the copper pre-cooling coil (1/4"o.d., length 3 m, volume 12 cm<sup>3</sup>), before then entering the FEP photoreactor.

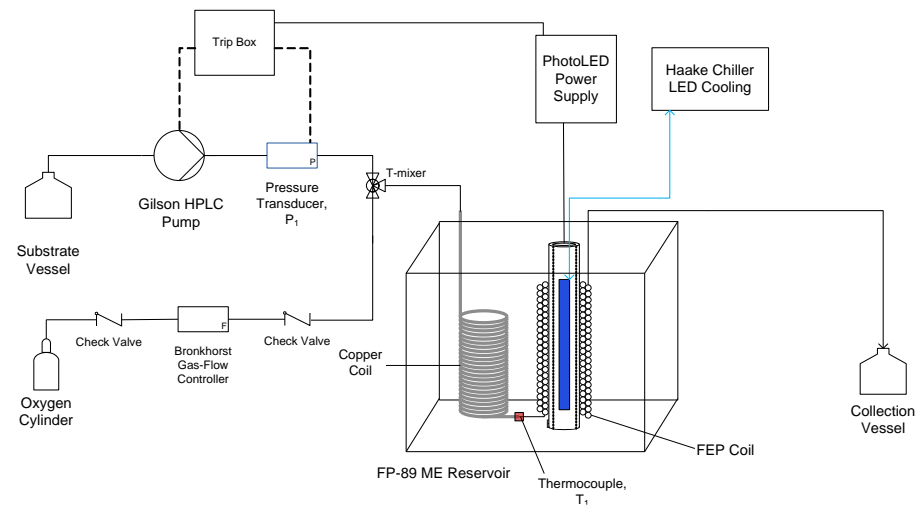


Figure 3.1: Schematic of the FEP photoreactor submerged in the fluid reservoir of the Julabo FP-89 ME recirculating chiller.

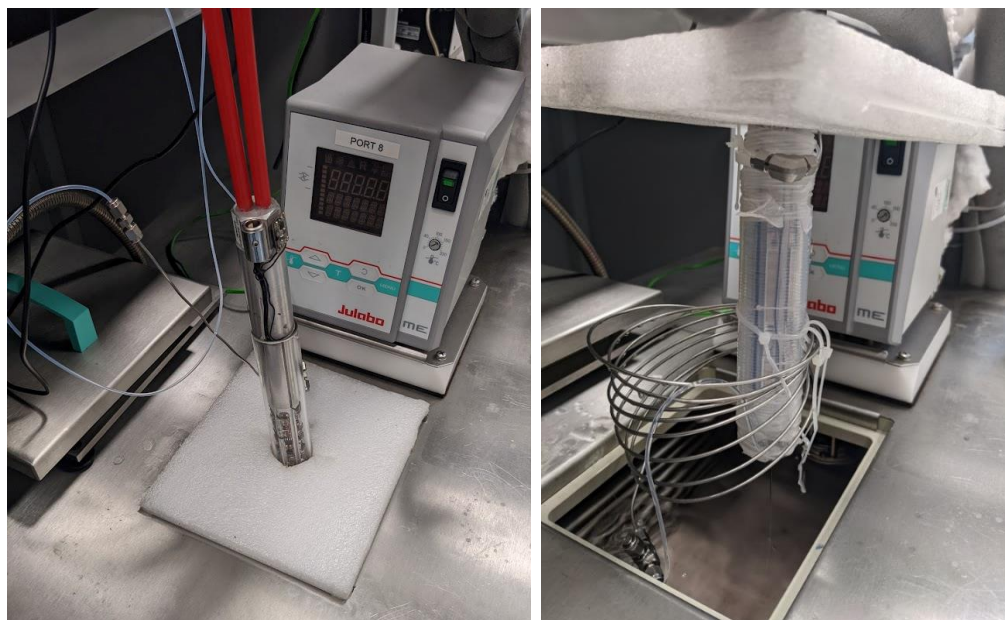


Figure 3.2: (Left) Photo of a later version of the FEP photoreactor in position in the cooling bath. (Right) The thin diameter FEP (1/16" o.d., 1/32" i.d.) wrapped in a double coil around a borosilicate tube that houses a first-generation 424 PhotoLED. The photoreactor is submerged directly into the fluid reservoir of the FP89-ME containing the ultra-low cooling fluid – Thermal HY. Expanded polystyrene that has been cut to the dimensions of the reservoir and the photoreactor acts effectively as an insulating lid. The reaction solution first passes through a cooling coil (Swagelok® 316 stainless steel, 1/16" o.d., 0.0225" i.d., length 3m, volume 0.77 cm<sup>3</sup>), a thermocouple is placed at the outlet of the cooling coil, prior to the solution entering the inlet of the FEP photoreactor.

### 3.2. Temperature Testing

Temperature tests were carried out with the recirculating chiller set to -70 °C using the second-generation blue PhotoLED ( $\lambda_{\text{max}} = 411$  nm). As discussed in Chapter 2, the second-generation PhotoLED allows for the LED current to be controlled and for the temperature to be monitored. The thermocouple reading,  $T_1$ , is taken prior to the solution entering the photoreactor as indicated in Figure 3.1. Qualitatively, the measured temperature showed an inverse dependency on the solution flow rate and the maximum LED current, with a low of -68.6°C measured for a flow rate of 1.0 mL min<sup>-1</sup> at 100 mA. Encouragingly, at the highest flow rate of 10.0 mL min<sup>-1</sup>,  $T_1$  was measured to be -63°C, indicating the effectiveness of the pre-cooling coil and the fact that relatively high flow rates can be operated while still achieving low temperatures. As  $T_1$  is measured prior to the inlet of the FEP coil, the increase in the measured temperature with LED current indicates that heat transfer fluid absorbs the emitted light causing an increase in the temperature. As the solution enters the FEP section of the reactor, it too will increase in temperature due to the absorption of light. It is, therefore, imperative to minimise the solution temperature prior to the photoreactor.

The photochemical reactions discussed in this work operate either the first-generation blue PhotoLED, with no control of the current, or the second-generation blue and white LEDs at the maximum current of 500 mA.

Table 3.2 Results from the initial temperature test of the low-temperature FEP reactor.

Flow Rate / mL min <sup>-1</sup>	I <sub>LED</sub> / mA	P <sub>1</sub> / psi	T <sub>1</sub> / °C
1	100	18.8	-68.6
	200	18.5	-68.5
	300	17.8	-67.3
	400	17.3	-66
	500	16.9	-65
2	500	20.5	-64.8
3	500	24.2	-64.6
4	500	27.5	-64.6
5	500	30.5	-64.3
10	500	42.6	-63

Ethanol was used as the test solution. All tests were carried out with the Julabo FP-89ME at -70°C. There is a clear temperature dependence on the flow rate and on the operating current of the PhotoLED; both can therefore be adjusted to achieve a desired temperature. I<sub>LED</sub> indicates the maximum current delivered to the LED strips.

The observed increase in backpressure, up to 42.6 psi, can be attributed to both the high flow rate and the relatively high viscosity of ethanol.<sup>224</sup> Increased pressure can pose risks to the FEP coil, with rupture a possibility. Pressure tests found an FEP coil (1/8" o.d., 0.01" wall thickness) could withstand pressures up to 220 psi (15 bar), therefore

the pressures experienced in the low temperature reactor do not present a risk of malfunction. However, an increase in the back-pressure was found to disrupt the flow equilibrium between the oxygen and the liquid. This phenomenon has been observed at pressures approaching 40 psi. The oxygen plugs within the Taylor flow gradually decrease in size, depicted in Figure 3.3, until a point where none are present and only liquid flows from the mixing T-piece. Next, the liquid will flow up the oxygen line towards the gas-flow controller. This has the potential to flow through the controller and into the oxygen cylinder. As such, the pressure trip,  $P_1$ , is set to 40 psi and non-return valves (Swagelok, 1/3 psi) are placed before and after the gas-flow controller, as shown in Figure 3.1. Clearly, the gas-flow controller is unable to deliver the oxygen flow at sufficient pressure to overcome the system pressure once the latter has reached a critical value. The substrate solution on the other hand is delivered *via* a HPLC pump, designed specifically to deliver solution at high pressures. Hence, the solution easily overcomes the oxygen flow, causing back flow towards the gas controller. To further alleviate the pressure issues, the primary solvent used for the photo-oxidations of DHAA is DCM. DCM has the advantage of possessing a much lower viscosity than ethanol, 0.41 cP (25°C) and 1.07 cP (25 °C) respectively.<sup>225</sup>

Despite the use of DCM, disruption to the Taylor flow was often observed to occur when the photoreactor had been operating at low temperature and for a significant period of time, typically upwards of two hours. This phenomenon is an indication that despite the flow equilibrium appearing to be in a steady-state, the true equilibrium of the system had not yet been reached. During the course of the reaction, and as the system approaches the steady-state, the viscosity of the solution will gradually increase, resulting in an increase in the force required to flow the solution at the same velocity and, hence, the increase in back-pressure of the system. The effect is most obviously observed upon entry of the solution the submerged photoreactor when at low temperature, due to this increase in viscosity, however, another significant effect occurs within the subsequent portions of the reactor that too will have an effect of the back-pressure. As these subsequent sections reach an equilibrium with the solution they too will result in gradual increases in the back-pressure. The disruption to the flow after a long reaction time is indicative of the subsequent sections reaching the equilibrium with the solution, and the compounding effect of the increased viscosity on the system pressure.

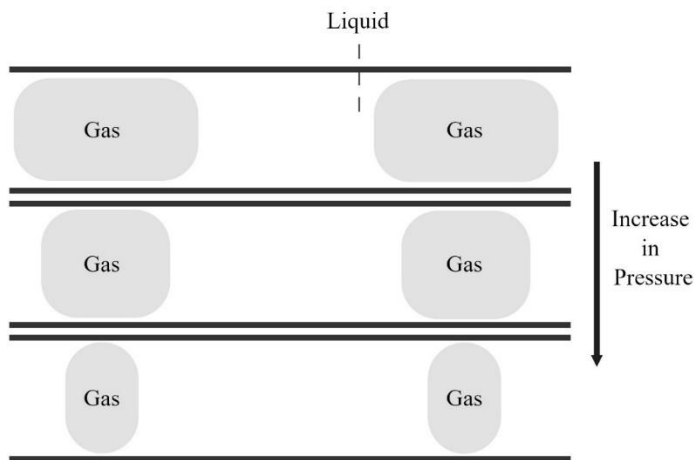


Figure 3.3: Schematic showing the effect on liquid and gas plug size with increased back-pressure of the reactor. As the pressure increases the size of the gas plug decreases, eventually to a point where no gas is present. This eventually leads to the liquid flowing through the mixing T-piece towards the gas-flow controller.

### 3.3. Photo-Oxidations in the Low Temperature FEP Coil Reactor

#### 3.3.1. Photo-Oxidation of DHAA

To first test the ability of the FEP reactor, the photo-oxidation of **14** was performed at low temperature following a standard procedure outlined in Chapter 5. The results were encouraging, with quantitative conversion being achieved at residence times down to 40 seconds, with 96% reached at 20 seconds. The ability of the reactor to fully convert **14** at high substrate and gas flow rates demonstrates the potential of the reactor to operate with high levels of productivity. The hydroperoxide ratios for the higher gas ratios are consistent; this is expected considering the levels of conversion are equally consistent. The reduction in gas molarity appears to have a slight positive effect on the ratio of **15** and **16**, with near quantitative conversions of 99% and 97% resulting in ratios of 10.7 and 10.8 respectively. Less than full conversion results in slight increases in the hydroperoxide ratio, indicating that **15** is preferentially formed in the initial stages of the reaction.

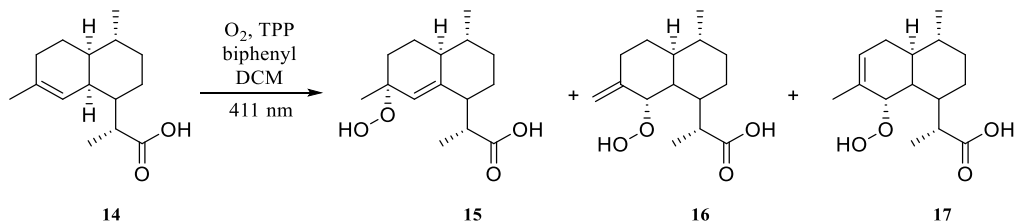


Figure 3.4: Photo-oxidation of DHAA, **14**, to hydroperoxides, **15**, **16** and **17**. It is commonly accepted that only **15** can proceed to form **18**. The reaction was conducted using a standard procedure - Photo-oxidation of DHAA (0.05 M) in DCM with TPP (0.5 mol %) in the FEP photoreactor using the 411 nm PhotoLED at 500 mA at chiller temperatures around -65°C.

Table 3.3. Photo-oxidation of DHAA (0.05 M) in DCM with TPP (0.5 mol %).

Liquid Flow Rate / mL min <sup>-1</sup>	Oxygen Flow Rate / mL min <sup>-1</sup>	Residence Time / min	Temp. / °C	Conv. /%	15 / %	16 / %	15:16
O <sub>2</sub> Ratio 4.16							
2	10	3:20	-64	100	83 ± 7	9 ± 2	9.7 ± 1.3
3	15	2:10	-65	100	87 ± 15	9 ± 1	9.9 ± 0.8
4	20	1:40	-63	100	83 ± 3	8 ± 2	10.1 ± 1.3
5	25	1:20	-65	100	85 ± 9	9 ± 2	9.7 ± 0.2
10	50	0:40	-64	100	83 ± 4	8 ± 2	10.1 ± 0.8
20	100	0:20	-65	96	84 ± 2	8 ± 1	10.2 ± 0.5
O <sub>2</sub> Ratio 2.08							
10	25	1:10	-64	99	83 ± 0	8 ± 1	10.7 ± 0.7
15	37.5	0:50	-63	97	83 ± 3	8 ± 1	10.8 ± 0.2
20	50	0:30	-61	92	78 ± 3	7 ± 1	11.2 ± 1.4
30	75	0:20	-58	80	67 ± 3	6 ± 1	11.4 ± 1.0

Reaction performed in the FEP photoreactor using the 411 nm PhotoLED at 500 mA at chiller temperatures around -65°C. These reactions were carried out with either a molar gas ratio of 4.2 or 2.1.

### 3.4. Investigating the Photo-Oxidative Synthesis of Artemisinin

The ability of the preliminary FEP reactor to perform the photo-oxidation of DHAA at -65°C and achieving quantitative conversion at low residence times with high selectivity towards **15**, led to the progression of the investigation towards the full synthesis of artemisinin, **18**. The synthesis can be divided into two distinct stages. First, the oxidation with  $^1\text{O}_2$  to form the hydroperoxides, **15-17**, performed within the photoreactor and, second, an additional oxidation with  $^3\text{O}_2$  in the dark followed by an acid catalysed Hock Cleavage and cyclisation to afford **18**.

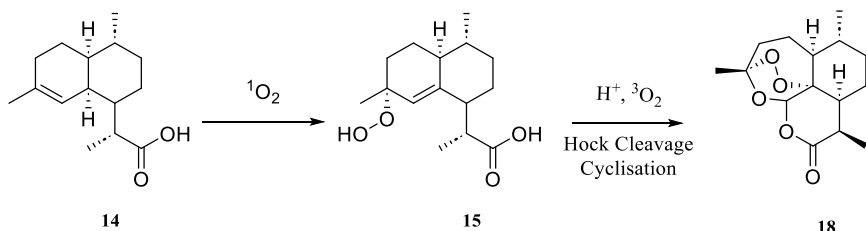


Figure 3.5: Simplified formation of artemisinin through the photo-oxidation of DHAA, **14**, to hydroperoxides, **15**, **16** and **17**, with subsequent acid catalysed Hock cleavage and oxidation to artemisinin, **18**. It is commonly accepted that only **15** can proceed to form **18**. Although research described in the introduction disputes this, with each of the hydroperoxides forming a common oxonium ion that eventually forms artemisinin.<sup>184</sup>

In their work to optimise the synthesis of **18**, Kopetzki *et al.* found that trifluoroacetic acid (TFA) at a molar equivalence of 0.50 best catalysed the Hock Cleavage.<sup>8</sup> TFA will, however, protonate TPP, shifting its absorption maximum ( $\lambda_{\text{max}}$ ) from 419 nm to 436 nm, thus reducing the spectral overlap with the PhotoLED and lowering the singlet oxygen quantum yield,  $\phi_{\Delta}$ , of TPP.<sup>47,194</sup> The presence of the acid during the photo-oxidation would cause an immediate reaction between the newly formed hydroperoxide and the acid. To negate this, and to assess the effect of the peroxide ratio on the final artemisinin yield, the acid was omitted from the photochemical step. Therefore, initial investigations into the full synthesis were carried out in semi-continuous ‘two-pot’ regime, rather than the continuous ‘one-pot’ developed by Kopetzki *et al.*<sup>8</sup>

The photo-oxidation is performed under continuous conditions; the hydroperoxide product was collected in a secondary vessel to which the acid is added and additional oxygen continuously bubbled through to initiate the subsequent synthetic steps in batch.

### 3.4.1. Initial Semi-Continuous Synthesis of Artemisinin

The initial investigations towards the semi-continuous synthesis of artemisinin followed a standard procedure outlined in Chapter 5. The results from the synthesis once again show the increase in selectivity of **15** as the temperature decreases; however, this did not translate into improved yields of **18**. The use of an external NMR standard (biphenyl) results in variability due to solvent loss during the secondary oxidation. In fact, it was found that on collection of the peroxide sample at 22°C, the solution was discoloured and close to boiling. Oxidations are exothermic processes and light absorption is also likely to increase the solution temperature; these factors, in conjunction with the use of a low boiling point solvent (DCM, b.p. = 39.6 °C), all contribute to solvent loss and subsequent inflation of the observed yield.<sup>118,121,123</sup> The negative effect of the increased reaction solution temperature can also be observed in the high level of error for this sample set. It should be noted that it would be hazardous

to use a flammable solvent with at a temperature close to its boiling point, reinforcing the notion that photo-oxidations will be safer at low temperature.

*Table 3.4 Results from the initial full synthesis of artemisinin from DHAA carried out in a two-step process; the photo-oxidation of DHAA, followed by addition of TFA and triplet oxygen in a secondary vessel.*

Temperature / °C	Conversion / %	<b>15</b> / %	<b>16</b> / %	Ratio <b>15:16</b>	<b>18</b> / %
22	98	78 ± 4	10 ± 2	7.6 ± 0.7	52 ± 11
-14	99	76 ± 5	8 ± 1	9.4 ± 1.6	51 ± 2
-40	99	80 ± 3	8 ± 1	10.3 ± 0.1	49 ± 3
-64	99	86 ± 3	8 ± 1	10.9 ± 0.7	54 ± 3

To counter the yield variation due to solvent loss, an internal NMR standard was used. Adding a standard, such as biphenyl, to the starting material solution allows compensation for any changes in concentration unconnected with the reaction, be it an increase *via* solvent evaporation or a decrease due to dilution. The standard and analyte concentrations should be affected to the same extent; therefore, the relative concentration between the two should remain constant irrespective of changes in solvent volume.

### 3.4.2. Continuous ‘One-Pot’ Synthesis of Artemisinin

The synthesis of artemisinin was also investigated following the ‘one-pot’ regime described by Kopetzki and co-workers.<sup>8</sup> In that protocol, toluene replaces DCM, while TPP is replaced by dicyanoanthracene, DCA. The research found that the selectivity of **15** was similar when TPP or DCA were employed, while the yield of **18** (based on **15**) increased from 69 % in DCM to 81 % in toluene at -20°C.

The influence of the polarity of a range of solvents was also investigated, finding that polar aprotic solvents led to a low yield of artemisinin with high levels of side products including the 6-lactone (**19**) and dihydro-*epi*-deoxyartemisinin B (**20**). Conversely, a reduction in polarity reduces the amount of side-products, enhancing the formation of **18**. Toluene possesses a lower relative polarity than dichloromethane, 0.099 versus 0.309, and corresponding improvements in the yield of **18** were observed.<sup>226</sup> This appears to counteract the fact that  $^1\text{O}_2$  exhibits a shorter lifetime of 29  $\mu\text{s}$  in toluene than it does in dichloromethane, 99  $\mu\text{s}$ .<sup>51,53</sup> However, this implies that the lifetime of  $^1\text{O}_2$  is not a limiting factor in the reaction.

Toluene and DCM exhibit similar melting points of -93°C and -96.7°C respectively, and so will remain in the liquid phase within the low temperature photoreactor.<sup>227,228</sup> However, the higher viscosity of toluene, 0.553 cP versus 0.42 cP for DCM, was found on numerous occasions to have a detrimental impact on the back-pressure within the system as the temperature was lowered, leading to disruptions of the Taylor flow equilibrium.

An advantage of DCA over TPP is the former's superior  $^1\text{O}_2$  quantum yield, measured from the quenching of  $^1\text{DCA}$  to be  $\phi_\Delta = 0.86$  in benzene and 0.76 in acetonitrile, while TPP has been measured to have  $\phi_\Delta = 0.63$  in benzene and  $\phi_\Delta = 0.60$  in both DCM and toluene.<sup>47,57,197</sup> Furthermore, DCA does not possess any protonation sites and is therefore insensitive to the pH of the solution; hence it may be used in the presence of TFA at the beginning of the reaction without causing a shift in the  $\lambda_{\text{max}}$  or  $\phi_\Delta$ . The unprotonated form of TPP,  $\text{H}_2\text{TPP}$ , possesses a quantum yield for triplet-state formation ( $\text{S}_1 - \text{T}_1$ ),  $\phi_T = 0.70 - 0.80$ , with an absorption maximum of 419 nm, in toluene.<sup>196</sup> The protonated form  $\text{H}_4\text{TPP}^{2+}$  has a substantially lower value of  $\phi_T = 0.26$ , while the  $\lambda_{\text{max}}$  shifts to a longer wavelength of 440 nm.

Owing to the lower molar extinction coefficient of DCA, a higher concentration is needed compared to TPP.<sup>8,229</sup> Therefore, DCA was used at a concentration of 2.5 mM (5 mol %), following that used by Kopetzki *et al.*<sup>8</sup> DCA exhibits relatively low solubility in toluene and, at 2.5 mM, sonication was required to solubilise the full amount; therefore, higher concentrations were not investigated.

A 'one-pot' synthesis, following a standard procedure outlined in Chapter 5, was performed at -20°C. The photoproduct was analysed directly after the photo-oxidation and after additional stirring with oxygen. There was little difference in the conversion or yield of **18** between the samples. The additional oxygen has a negligible effect, indicating the acid catalysed cleavage and secondary oxidation occurs rapidly after hydroperoxide formation. This also shows that there is sufficient ground-state oxygen,  $^3\text{O}_2$ , in the plug-flow mixture to complete the synthesis and that extra dosing is not required.

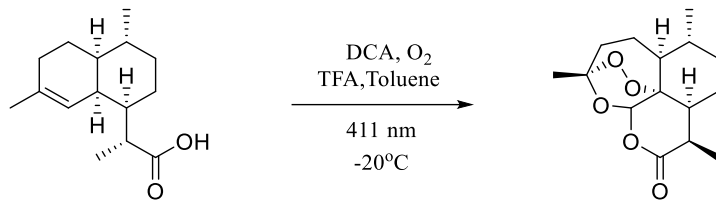


Figure 3.6: ‘One-pot’ synthesis of artemisinin using DCA in toluene at a temperature of -20°C.

Table 3.5: Conversion of DHAA and yield of artemisinin from photo-oxidation carried out in FEP reactor following the conditions set out by Kopetzki *et al.*<sup>8</sup>

	Conversion /%	<b>18</b> /%
Directly after photoreactor	79 ± 3	33 ± 3
After further oxidation	80 ± 3	34 ± 2

TFA was present at the start of the reaction. Photoproduct was collected directly after exiting the photoreactor and immediately prepared for NMR analysis; further 20 mL of solution was collected, placed in a secondary container to which O<sub>2</sub> was bubbled through with stirring at a rate of 2 mL min<sup>-1</sup> for 20 minutes. No significant difference can be observed between the results. Error calculated using RStudio, to 95 % confidence interval, *n* = 3.

The level of conversion and the yields of **18** were not as high as those previously achieved with TPP, despite the latter being at far lower concentrations. To gain a more accurate comparison between the two photosensitisers the reaction was repeated, with a DCA concentration of 0.25 mM (0.5 mol %) to match that of TPP. For these reactions, a stainless steel coil (1/8" o.d., 1/16" i.d., length 3m, volume 4.6 cm<sup>3</sup>) was connected to the outlet of the photoreactor and placed within a water bath held at 30°C, as shown in Figure 3.7. A conversion of 52 ± 6 % was achieved with a corresponding artemisinin yield of 29 ± 1.5 %.

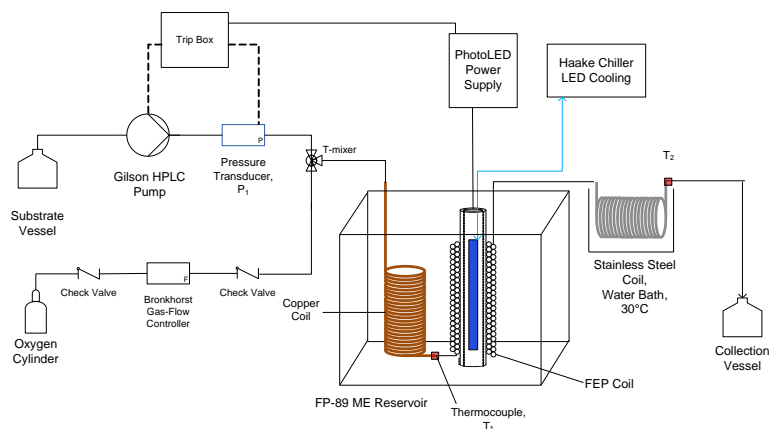


Figure 3.7: Schematic of the reactor set-up for the ‘one-pot’ continuous flow synthesis of artemisinin at low temperature.

An investigation into the performance of the DCA-toluene combination was attempted with the photoreactor at -70°C. However, as the temperature decreased the pressure increased to 50 psi, a level above the threshold for acceptable Taylor flow. The increase

in pressure is a severe safety risk when using a flammable solvent such as toluene. As the pressure increases the amount of oxygen dissolved into the solvent will increase; if the amount of oxygen increases above the limiting oxygen concentration of the solvent there is the potential for combustion to occur.<sup>230</sup> To reduce this risk, the pressure trip was set to a value of 40 psi, stopping the substrate pump before serious disruption to the Taylor flow can occur. To further improve safety, several non-return valves are in place to prevent the solvent reaching the O<sub>2</sub> cylinder as depicted in Figure 3.7, and the pressure and flow pattern of the reaction are constantly monitored. If Taylor flow is disrupted prior to reaching the pressure trip value, the substrate pump is stopped, the reaction terminated, and the system shut down.

The preliminary investigations showed that the higher viscosity of toluene prevents its use at the low temperatures achieved previously with the DCM. The increase in back-pressure to unacceptable levels was a common occurrence despite the reactor temperature being around or above -20°C. On inspection of the reactor after shutdown, multiple kinks were found in the FEP coil. These kinks reduce the effective diameter at which fluid can flow through the reactor, leading to increased pressure and a potential for blockages. The reactor was subsequently adapted, reducing the angles at which the FEP would have to bend to be connected to the metal sections of the reactor. However, despite these adaptations, the flow issues with toluene at -20°C still remained.

### 3.4.3. Semi-Continuous ‘Two-Pot’ Synthesis using DCA in DCM

Due to the inability to pump toluene around the system at temperatures below -20°C, the use of DCA in dichloromethane was investigated. It was first determined that DCA was sufficiently soluble in DCM at -70°C at a concentration of 2.5 mM. The synthesis of artemisinin followed a standard ‘two-pot’ regime, producing a low conversion of 50 % and correspondingly low yield of **18** of 28 %. The reduced effectiveness of DCA led to the selection of TPP as the primary photosensitiser for the majority of the subsequent research.

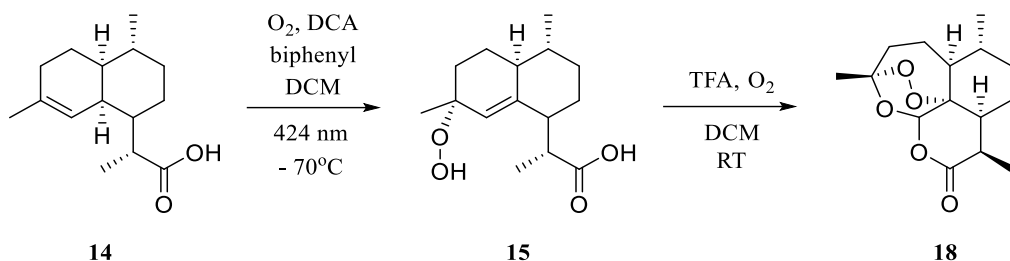


Figure 3.8. 'Two-step' synthesis of artemisinin from DHAA. DCA in toluene is irradiated with 424 nm light in the presence of oxygen to produce several hydroperoxides. On addition of TFA and oxidation in the dark, the subsequent synthetic steps occur to form the final product, artemisinin.

### 3.4.4. Effect of TPP Concentration

The effect of the TPP concentration was then investigated using a semi-continuous 'two-pot' regime. Concentrations ranging from 0.125 mM (0.25 mol %) to 2.5 mM (5 mol %) were used. To improve the spectral overlap between TPP and the light source, the first-generation blue PhotoLED ( $\lambda_{\text{max}}$  424 nm) was employed.

The highest TPP concentration of 2.5 mM resulted in the lowest levels of conversion and yield at 40% and 28% respectively, as shown in Table 3.6. These low levels can be attributed to the phenomenon of auto-quenching of the TPP. Singlet oxygen has the ability to oxidise TPP, cleaving the conjugated ring system, thus disrupting the photophysical properties of the compound.<sup>195</sup> At high photosensitiser concentrations, a sufficient amount of  $^1\text{O}_2$  is generated that can rapidly react with the TPP, reducing the ability of the photosensitiser while, in turn, diminishing the  $^1\text{O}_2$  before it can react with DHAA. Burgard *et al.* found that reducing the concentration of TPP and, thus, reducing the concentration of  $^1\text{O}_2$ , resulted in the vast majority of  $^1\text{O}_2$  molecules reacting with DHAA, leading to less significant photobleaching of TPP.<sup>194</sup>

Table 3.6: Results of the two-step synthesis of artemisinin with varying concentrations of the photosensitiser tetraphenylporphyrin (TPP) in dichloromethane (DCM) at a photo-reaction temperature of approximately -70°C and the secondary oxidation occurring under ambient conditions however, without measurement of the temperature.

PS Conc. (mM/mol %)	Conversion / %	<b>18</b> / %
0.125/0.25	100 ± 0	56 ± 3
0.25/0.5	100 ± 0	54 ± 3
1/2	98 ± 2	54 ± 3
2.5/5	40 ± 5	28 ± 7

The results showed there was very little variation in artemisinin yields for the TPP concentration between 0.125 – 1 mM. The yield of 56% achieved from the lowest concentration of 0.125 mM is very encouraging from an economical and environmental point of view, resulting in significant benefits for the scale-up of this process.

### 3.4.5. ‘One-Pot’ Synthesis of Artemisinin with TPP in DCM

Despite the negative photophysical effects caused by the protonation of TPP to  $\text{H}_4\text{TPP}^{2+}$ , the ‘one-pot’ synthesis of artemisinin was investigated with TPP in DCM. Due to the shift in the absorption maxima of  $\text{H}_2\text{TPP}^{4+}$ , the first-generation blue PhotoLED,  $\lambda_{\text{max}} = 424 \text{ nm}$ , was selected over the second generation with  $\lambda_{\text{max}} = 411 \text{ nm}$ , despite the latter exhibiting greater intensity, as shown previously in Figure 2.6.

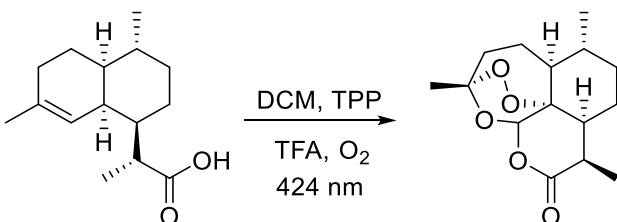


Figure 3.9. ‘One-pot’ synthesis of artemisinin from DHAA. The photosensitiser TPP is used in conjunction with TFA in DCM under 424 nm irradiation and in the presence of oxygen. On addition of TFA, TPP is protonated, causing a change in its photophysical properties. Conducted at photoreactor temperature between 15 and -75°C.

The reaction was performed under the standard conditions at a photoreactor temperature of -74°C with substrate and O<sub>2</sub> flow rates of 5 and 25 mL min<sup>-1</sup>. Samples were collected directly after photo-oxidation and analysed *via* NMR, while remaining photoproduct was collected and stirred with an additional flow of O<sub>2</sub> (2 mL min<sup>-1</sup>) for 20 minutes in the dark. Yields of 47 % and 53 % were achieved, indicating that the effect of the protonation of TPP is not as severe as first thought. There is, however, a large error associated with the results from the samples collected directly after photo-oxidation. The associated error can be assessed through the varying levels of the 6-lactone, **19**, which appears to be interdependent with the yield of **18**. The <sup>1</sup>H NMR spectra shows large variations in the levels of **18** and **19** within each sample set, with the former being observed in high yields with correspondingly low yields of **19**.

The additional oxidation appears to drive the equilibrium between **18** and **19** to favour the formation of **18**, increasing the yield and reducing the associated error. The formation of dihydro-epi-deoxyartemisinin B, **20**, appears consistent between the measurements.

Table 3.7. Calculated  $^1\text{H}$  NMR yields from the 'one-pot' synthesis of artemisinin in the low temperature FEP (1/8" o.d., 0.01" wall thickness) reactor, shown in Figure 3.7, using the first generation 424 nm PhotoLED.

T <sub>1</sub> / °C	Secondary oxidation / °C	Conversion / %	18 / %	19 / %	20 / %
-74	-	89 ± 2	47 ± 16	8 ± 6	9 ± 2
-74	20	89 ± 2	53 ± 5	2 ± 1	9 ± 1

The Product was prepared and analysed in triplicate directly after exiting the reactor, while a further 20 mL of product was further oxidised in a secondary vessel for 20 minutes.

The effect of temperature on the 'one-pot' synthesis was next investigated. The following reactions were completed using standard conditions with liquid and gas flow rates at 5- and 25-mL min<sup>-1</sup> respectively. The placement of T<sub>2</sub>, as shown in Figure 3.7, allowed for the temperature to be measured after the secondary reaction coil, the mild heating having a minor effect on the heat gain of the solution during this stage. There is a clear inverse temperature dependence on the level of conversion achieved; this is translated into a similar dependence on the yield of **18** and other products, with high errors being exhibited for **18** and **19**.

Table 3.8. Results from the temperature dependent 'one-pot' synthesis of artemisinin using protonated TPP.

T <sub>1</sub> / °C	T <sub>2</sub> / °C	Conversion / %	18 / %	19 / %	20 / %
15	20	38 ± 9	15 ± 4	0	2 ± 2
-20	5	57 ± 10	31 ± 9	3 ± 10	5 ± 1
-45	-10	79 ± 2	44 ± 11	5 ± 5	7 ± 1
-74	-20	92 ± 3	49 ± 20	5 ± 8	8 ± 1

DHAA (0.05M) was combined with TPP (0.25 mM, 0.5 mol %) and TFA (0.025 M, 0.5 eq) in DCM. The 'thin-walled' FEP (1/8" o.d., 0.01" wall thickness) was used with the first-generation 424 nm PhotoLED.

### 3.5. Pressure Issues Encountered with the 'Thin-Walled' FEP Reactor

Issues with the backpressure increasing in the system were commonplace during the initial investigations, primarily for reactions conducted in toluene. However, the issue was also experienced with DCM, albeit at a far lower frequency.

The 'thin-walled' FEP Tubing (1/8" o.d., 0.01" wall thickness, volume 40 cm<sup>3</sup>) was found to be prone to kinking once the tubing had been bent past a certain threshold, and is a common occurrence when using this tubing to produce a coiled reactor of a narrow diameter. After a series of adjustments to alleviate the kinking within the tubing failed, it was clear that this problem would repeatedly occur with this type of FEP.

Furthermore, due to the narrowness of the tubing walls, attaching Swagelok® fittings was not an appropriate option. In their place, PTFE fittings and ferrules were used. However, it was found that leakages regularly occurred from these fittings, likely due to a degree of contraction when exposed to low temperatures.

### 3.6. Alternative Photoreactor Materials

Due to the issues experienced with the ‘thin-walled’ FEP, construction of a photoreactor from an alternative material was investigated. Coiled photoreactors were constructed from: i) ‘thick-walled’ FEP (1/8” o.d. 1/16” i.d. volume 5.8 cm<sup>3</sup>), ii) narrow diameter FEP (1/16” o.d. 1/32” i.d. length 25 ft, volume 3.77 cm<sup>3</sup>), and iii) PFA (perfluoroalkoxy) tubing (1/8” o.d. volume 12 cm<sup>3</sup>). It was possible to attach Swagelok® fittings to each of these materials.

#### 3.6.1. PFA Photoreactor

A prototype reactor constructed from a single-layer of PFA tubing (1/8” o.d. 1/16” i.d. volume 12 cm<sup>3</sup>) was made. The first observation is that the PFA appears to be less transparent than the FEP tubing. A ‘two-pot’ photoreaction was completed at T<sub>1</sub> = -81°C, and is described in Chapter 5. Less than ideal levels of conversion and corresponding yields were obtained, most likely explained by the reduced optical properties of the tubing.

Table 3.9. Results from the ‘two-pot’ synthesis of artemisinin using the PFA photoreactor.

	Conversion / %	15 / %	16 / %	18 / %	19 / %	20 / %
Pre-H <sup>+</sup>	74 ± 2	28 ± 10	7 ± 1	-	-	-
Post H <sup>+</sup>	75 ± 2	-	-	40 ± 2	1 ± 1	3 ± 2

The photo-oxidation was performed at -81°C using standard concentrations of DHAA (0.05 M), TPP (0.5 mol %), and TFA (0.5 equivalents).

#### 3.6.2. ‘Thick Wall’ FEP

A reactor was constructed from ‘thick wall’ FEP (1/8” o.d. 1/16” i.d., 5.8 cm<sup>3</sup> volume). The ‘two-pot’ synthesis of **18** was performed with a reduction in the TPP concentration from 0.25 mM to 0.125 mM (0.25 mol %); the other constituent concentrations remained the same. The photo-oxidation was performed at -76°C. The residence times quoted in Table 3.10 apply to the photoreactor section only.

Reactions were initially conducted using the 424 nm PhotoLED, which was then replaced with the second-generation 411 nm PhotoLED to compare the two light sources. The 411 nm LED achieved higher levels of conversion than the 424 nm, most likely due to the increased emission intensity of the second-generation LED. However, the yields of **18** are only slightly improved, if at all. Furthermore, for each light source, there is little variation in either the conversion or the yield of **18** between the differing residence times - an indication that the photo-oxidation occurs rapidly.

Table 3.10: Results for the ‘two-pot’ synthesis of artemisinin using the ‘thick wall’ FEP reactor.

Substrate flow rate / mL min <sup>-1</sup>	O <sub>2</sub> flow rate / mL min <sup>-1</sup>	Residence Time / s	T <sub>1</sub> / °C	Conv. /%	18 / %	19 / %	20 / %
424 nm PhotoLED							
1	5	60	-76	46 ± 2	24 ± 2	0	6 ± 3
2	10	30	-76	49 ± 5	27 ± 4	0	4 ± 1
3	15	20	-76	51 ± 13	27 ± 4	0	5 ± 2
4	20	15	-76	46 ± 5	24 ± 2	0	5 ± 2
411 nm PhotoLED (500 mA)							
1	5	60	-76	65 ± 7	29 ± 2	1 ± 1	7 ± 1
2	10	30	-76	61 ± 5	26 ± 4	1 ± 1	8 ± 1
3	15	20	-76	64 ± 5	28 ± 2	1 ± 1	9 ± 1
4	20	15	-76	65 ± 9	27 ± 2	0	7 ± 2
5	25	12	-76	59 ± 4	23 ± 2	0	8 ± 1

DHAA (0.05M) was photo-oxidised in the presence of O<sub>2</sub> (4.16 eq) using TPP (0.125 mM, 0.25 mol %) before 10 mL was collected and acidified with TFA (0.5 eq) to which O<sub>2</sub> was passed through at a rate of 2.0 mL min<sup>-1</sup> while stirring in the dark for 20 minutes.

A comparison between the two light sources was then made in performing the ‘one-pot’ synthesis of artemisinin. Again, superior conversion was achieved with the 411 nm PhotoLED, despite the absorption maxima of TPP shifting further away from the LED emission when in the presence of the acid. As is expected, the yields of **18**, **19**, and **20** were also higher for the 411 nm LED, due to the increased levels of conversion.

Table 3.11: Results for the ‘one-pot’ synthesis of artemisinin using the thick wall FEP reactor.

Substrate flow rate / mL min <sup>-1</sup>	O <sub>2</sub> flow rate / mL min <sup>-1</sup>	Residence Time / s	T <sub>1</sub> / °C	Conv. /%	18 / %	19 / %	20 / %
424 nm PhotoLED							
1	5	60	-72	47 ± 3	24 ± 3	2 ± 4	4 ± 2
2	10	30	-72	67 ± 2	35 ± 2	1 ± 1	6 ± 6
3	15	20	-72	57 ± 3	22 ± 8	2 ± 6	4 ± 1
4	20	15	-72	48 ± 2	18 ± 4	2 ± 3	3 ± 2
411 nm PhotoLED							
1	5	60	-72	98 ± 2	49 ± 9	6 ± 9	9 ± 2
2	10	30	-72	97 ± 3	47 ± 23	8 ± 18	9 ± 1
3	15	20	-72	90 ± 3	43 ± 19	5 ± 11	8 ± 1
4	20	15	-72	81 ± 3	43 ± 8	2 ± 2	7 ± 2

DHAA (0.05M) was photo-oxidised in the presence of O<sub>2</sub> (4.16 eq) using TPP (0.125 mM, 0.25 mol %) and TFA (0.025 M, 0.5 eq).

To improve the conversion of DHAA, the volume of the photoreactor was increased from  $5.8\text{ cm}^3$  to  $15\text{ cm}^3$ . An additional thermocouple,  $T_3$ , was introduced at the inlet of the secondary coil, Figure 3.10.

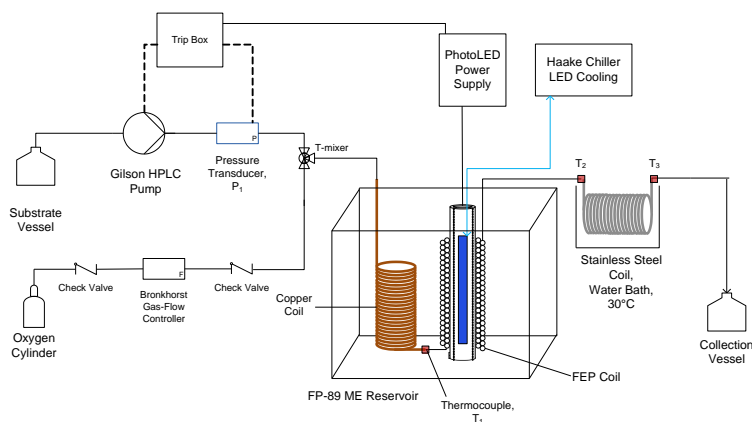


Figure 3.10: Schematic of the reactor set-up. A third thermocouple is added to the inlet of the secondary reactor coil,  $T_2$ .

The concentration of TPP was doubled from  $0.125\text{ mM}$  to  $0.25\text{ mM}$  ( $0.5\text{ mol }\%$ ). One- and two- pot syntheses of artemisinin were performed with the  $411\text{ nm}$  LED. The ‘two-pot’ reactions were carried out at a photoreactor temperature of  $-75^\circ\text{C}$ , while the flow rate was varied. High levels of conversion were achieved for all flow rates, again highlighting the potential for relatively high throughput reactions to be performed. Reasonable yields of **18** were also observed; however, the calculated errors of  $\pm 13\%$  and  $\pm 15\%$  for the residence times of 50 and 30 seconds respectively are unusually high for the ‘two-pot’ regime. The increased error of **18** does not correspond with a similar variation in the yields of **19** as has been previously observed, with the latter being produced in small quantities with low error. The yields of **20**, ranging between  $10 \pm 2\%$  and  $14 \pm 4\%$ , are slightly higher than the previously found highest value of  $9 \pm 2\%$ .

Temperature dependence was investigated during the ‘one-pot’ reaction, down to a minimum temperature of  $-75^\circ\text{C}$ . Once again, the level of conversion and, hence, yield of **18** declined with increasing temperature. Large errors were observed for the yields of **18** and **19**, while **20** remained relatively consistent and values were lower than those measured during the ‘two-pot’ reaction.

Samples were analysed in triplicate; analysing each sample individually gives an insight into why the variation was occurring. A common occurrence in each triplicate sample set was the deviation of one sample from the other two, typically through a large reduction in **18** with a corresponding increase in **19**. As shown in Table 3.13, sample

2A exhibited yields of **18** and **19** of 36% and 16% respectively, while in the subsequent sample the value of **18** increased to 51% and **19** reduced to 4%. Furthermore, there appears to be no pattern as to which sample exhibits the largest variation. These results indicate that the interrelated variation between **18** and **19** occurs most prevalently with the ‘one-pot’ reactions, a phenomenon that is further explored in section 3.8.

*Table 3.12: Results for the two- and one-pot synthesis of artemisinin using the thick walled FEP reactor and the 411 nm PhotoLED.*

Substrate / mL min <sup>-1</sup>	O <sub>2</sub> / mL min <sup>-1</sup>	Residence Time / s	T <sub>1</sub> / °C	T <sub>2</sub> / °C	T <sub>3</sub> / °C	Conv. /%	18 / %	19 / %	20 / %
Two-pot reaction									
1	5	150	-75	-	-	99 ± 1	44 ± 2	1 ± 1	10 ± 2
3	15	50	-75	-	-	100	57 ± 13	2 ± 2	14 ± 4
5	25	30	-75	-	-	99 ± 1	50 ± 15	3 ± 2	12 ± 6
One-pot reaction									
1	5	150	-75	24	26	100	52 ± 5	3 ± 5	9 ± 2
2	10	75	-75	24	26	100	47 ± 23	8 ± 18	9 ± 1
5	25	30	9	24	25	58 ± 6	25 ± 5	1 ± 4	4 ± 4
5	25	30	-15	24	25	74 ± 4	33 ± 4	4 ± 9	6 ± 3
5	25	30	-41	19	26	87 ± 2	36 ± 15	8 ± 10	7 ± 1
5	25	30	-60	17	26	94 ± 3	40 ± 15	8 ± 10	8 ± 1
5	25	30	-75	17	24	98 ± 2	51 ± 9	5 ± 5	9 ± 1

For the two-pot: DHAA (0.05M) was photo-oxidised in the presence of O<sub>2</sub> (4.16 eq) using TPP (0.25 mM, 0.5 mol %) before 10 mL was collected and acidified with TFA (0.5 eq) to which O<sub>2</sub> was passed through at a rate of 2.0 mL min<sup>-1</sup> while stirring in the dark for 20 minutes. For the one-pot, reagents were combined together and pumped through the photoreactor at various flow rates corresponding to a substrate and oxygen molar gas ratio of 4.16.

*Table 3.13: Variation within a <sup>1</sup>H NMR sample set. Sample set 2A-C corresponds to the ‘one-pot’ synthesis highlighted in Table 3.12, carried out at a substrate flow rate of 2 mL min<sup>-1</sup>.*

Sample	Conversion /%	18 / %	19 / %	20 / %
2A	100	36	16	9
2B	100	51	4	9
2C	100	53	3	9

Issues were encountered with the 411 nm PhotoLED, whereby only one of the 6 LED strips remained working. Due to the ability of the second-generation PhotoLEDs to measure the current delivered to each of the strips, this malfunction was easy to spot. It was then considered that similar malfunctions may have occurred for the first-generation 424 nm PhotoLED, resulting in its reduced performance. As such, both LEDs were inspected and repaired by the electronics workshop. It was determined that a number of the strips were indeed damaged, and were subsequently replaced. To test the performance of the repaired first-generation PhotoLED, a standard ‘one-pot’ reaction was carried out. It should be noted that at this point in time NMR facilities at the university were heavily reduced and therefore it was not possible to continue analysing samples in triplicate. Replacing this regime with duplicate analysis renders

the calculation of error statistics somewhat meaningless. The reaction with the repaired LED produced far superior results to those previously found under the same conditions. In that full conversion was achieved for all photoreactor temperatures along with high yields of **18**. The presence of significant levels of **19**, however, suggest that large errors would be associated with these estimates. These reactions do, however, indicate that **19** appears to be more prevalent at lower photoreactor temperatures.

Table 3.14. One-pot photo-oxidation using the repaired 424 nm PhotoLED.

T <sub>1</sub> / °C	T <sub>2</sub> / °C	T <sub>3</sub> / °C	Conversion /%	18 / %	19 / %	20 / %	18 selectivity / %
-77	20	23	100	51	17	7	51
-49	21	23	100	61	17	9	61
-26	21	23	100	54	10	7	54
5	22	23	100	51	5	11	51

A substrate flow rate of 2mL min<sup>-1</sup> and O<sub>2</sub> rate of 10 mL min<sup>-1</sup> were used to allow for conversion over all temperatures so the artemisinin yield could be more accurately assessed.

### 3.6.3. Issues with the ‘Thick-Walled’ FEP Reactor

Construction of a coiled photoreactor out of the ‘thick walled’ FEP proved to be challenging. The thickness results in the tubing being unmalleable and, therefore, to form a coil around the glass tube of the PhotoLED, Parafilm® was taped around the entirety of the coil to prevent it from uncoiling. However, it was commonly found that the FEP had partially uncoiled after the majority of reactions. The lack of flexibility of the material proved to be impractical for the required dimensions of the photoreactor. However, it was noted that this type of tubing could be useful for photoreactors with a larger coil diameter.

### 3.7. ‘Near-micro’ FEP reactor

Due to the regular uncoiling of the ‘thick-walled’ FEP the next tubing that was investigated possessed a narrow outer diameter of 1/16“, and an internal diameter of 1/32”. A photoreactor was initially produced using 7.6m of a single layer of the FEP tubing, giving a total volume of 3.8 cm<sup>3</sup>. A photo of the FEP reactor was shown above in Figure 3.2. Tubing of these dimensions is less prone to kinking than the ‘thin walled’ FEP, possessing a far lower bend radius than any of the tubing so far tested. Moreover, stainless steel Swagelok® fittings and ferrules can be attached. Although far narrower than the other options assessed, the reactor still constitutes a macro-flow reactor and does not fall into the region of microflow (these are accepted to define reactors of internal diameters below 0.5 mm).<sup>22</sup> There are multiple advantages for using tubing of such dimensions, from both photochemical and safety perspectives. The narrow diameter greatly reduces the optical path length, leading to more uniform irradiation of the reaction solution. The interfacial area between the liquid and gas will also be increased compared to the wider diameter reactors. In terms of safety, the power of an explosion is proportional to the mass of the explosive mixture to the power of 1/3.<sup>231</sup> This relation immediately explains why microreactors are safer when employing hazardous reaction conditions.<sup>232</sup>

#### 3.7.1. Initial Reactor Testing

Initial testing of the ‘near-micro’ FEP reactor involved both the ‘two-pot’ and ‘one-pot’ regimes, under standard conditions, utilising the 411 nm PhotoLED at a photoreactor temperature of -71°C. First, the formation of the hydroperoxides was investigated; the photo-oxidation of DHAA was performed with relatively high liquid and oxygen flow rates of 5 and 25 mL min<sup>-1</sup> respectively, producing conversion of 81 ± 4 % with yields of 61 ± 6 % for **15** and 5 ± 0.25 % for **16**. The ‘one-pot’ reaction was then carried out at the same flow rate, in the presence of trichloroacetic acid (TCA, 0.025 M, 0.5 equivalents). A conversion of 75 ± 8 % was obtained, with high variation within the measured yield of **18** of 39 ± 29 %. Correspondingly high variation was also found for **19** with a yield of 4 ± 10 %. While **20** was found to exhibit a low, consistent yield of 4 %.

To improve the level of conversion, the ‘two-pot’ regime was then performed at lower flow rates of 1.0 and 5.0 mL min<sup>-1</sup> for the substrate and O<sub>2</sub> respectively. The hydroperoxides were analysed prior to the addition of acid. An improved conversion of

$95 \pm 4\%$  was measured with higher yields  $72 \pm 4\%$  and  $7 \pm 1\%$  for **15** and **16** respectively. After acidification and secondary oxidation, yields of **18**, **19**, and **20** were measured to be  $45 \pm 1.5\%$ ,  $1 \pm 0.1\%$  and  $5 \pm 1\%$  respectively. The ‘two-pot’ synthesis was then carried out with TFA, at a similar photoreactor temperature of  $-72^\circ\text{C}$ . A comparable conversion of  $92 \pm 4\%$  was obtained along with yields of  $54 \pm 15\%$ ,  $1 \pm 1\%$  and  $11 \pm 4\%$  for **18**, **19** and **20** respectively.

The initial investigations into the reactor revealed that despite the significant reduction in reactor volume, a high level of conversion and reasonable artemisinin yields could be achieved at reduced flow rates. The result of the ‘one-pot’ synthesis corroborates previous results that indicate the variation in **18** and **19** yields is an inherent aspect of the reaction regime. The variation of the yields of these two products is greatly reduced when the ‘two-pot’ synthesis is performed.

### 3.7.2. Adaptations and Pressure Testing

During the initial reactor investigations, the back-pressure of the system occasionally reached the trip limit of 40 psi. To alleviate this, the short section of tubing containing the glass beads, following the liquid/oxygen mixing T-piece, was removed. Furthermore, to reduce the total volume of the reactor, the original copper cooling coil (1/4” o.d., volume  $12 \text{ cm}^3$ ) was replaced with a narrow diameter stainless steel coil (1/16” o.d., length 3 m, volume  $0.77 \text{ cm}^3$ ). The reduction in bore size of the cooling coil had a positive impact on the Taylor flow dynamics within the photoreactor. Upon entering the 1/4” o.d. copper coil from the 1/8” o.d. PTFE tubing, the flow pattern was found to be disrupted, exhibited by an irregular plug flow pattern. Upon reducing to the 1/16” o.d. coil the resulting flow pattern was observed to possess a more uniform flow pattern. However, the reduction in bore size of the cooling coil can potentially cause back-pressure issues. Therefore, the pressure ( $P_1$ ) was measured with varying flow rates of the reaction solvent, DCM, with an oxygen flow ratio of 1:5. At the highest flow rates of  $5.0$  and  $25.0 \text{ mL min}^{-1}$  for the liquid and oxygen respectively, a pressure of 31 psi was measured, a value sufficiently below the set trip level.

Lower flow rates were attempted: however, these resulted in the gas flow being disrupted. The Bronkhorst ® gas flow controller with a capacity of  $150 \text{ mL min}^{-1}$  was replaced with a lower capacity  $30 \text{ mL min}^{-1}$  (30 sccm Ar) controller to improve the level of control within the gas flow. However issues with the liquid-gas flow equilibrium remained at substrate flow rates below  $0.5 \text{ mL min}^{-1}$ , an indication that disruption to the

Taylor flow equilibrium is not solely due to the increase in back-pressure, but may also occur due to a lack of control at low gas flow rates due to the flow-controller itself.

After pressure testing, a ‘one-pot’ synthesis was performed with the FP-89ME chiller set to -80°C, the advised working temperature limit of the Thermal HY heat transfer fluid. At each of the flow rates tested, the thermocouple, T<sub>1</sub>, read -80°C, while no pressure or flow issues were encountered. The results in Table 3.15 show that high conversion is achieved at low fluid flow rates while a good conversion of 98 % is achieved at a fluid flow rate of 2.0 mL min<sup>-1</sup>. Furthermore, these results highlight the improvement in the reaction when performed at -80°C compared to ambient conditions. For reactions with the longest residence times, comparable conversions are found for the ambient and the low temperature reaction; however, this does not translate to the corresponding yields of artemisinin, with the ambient photoreaction yielding 38 % and the low temperature 44 %. This situation is exacerbated once the flow rate is increased; the levels of conversion of the ambient photoreactions diminish greatly and hence reduce the yield of artemisinin, indicating that the use of low temperature will not only improve the selectivity of the reaction, but also improve conversion, allowing for higher flow rates and, therefore, higher throughput reactions to be performed.

Table 3.15. ‘One-pot’ synthesis of artemisinin in the 1/32” ID FEP reactor.

Substrate /mL min <sup>-1</sup>	O <sub>2</sub> /mL min <sup>-1</sup>	T <sub>1</sub> /°C	T <sub>2</sub> /°C	Residence Time / sec	Conv. /%	<b>18</b> / %	<b>19</b> / %	<b>20</b> / %
0.25	1.25	-80	20	150	100	44 ± 8	1 ± 1	7 ± 2
0.25	1.25	18	21	150	98 ± 2	38 ± 3	1 ± 1	7 ± 1
0.5	2.5	-78	20	75	99 ± 1	59 ± 14	1 ± 1	8 ± 3
0.5	2.5	17	21	75	85 ± 5	35 ± 1.5	1 ± 1	7 ± 1
1.0	5.0	-80	21	38	98 ± 6	55 ± 15	3 ± 3	9 ± 3
2.0	10.0	-80	19	19	97 ± 5	45 ± 23	10 ± 24	9 ± 2
3.0	15.0	-80	19	13	87 ± 4	39 ± 18	5 ± 8	7 ± 2
5.0	25.0	-80	19	7.5	76 ± 5	38 ± 5	2 ± 3	6 ± 2

TPP was used at 0.25 mM (0.5 mol %) and TFA (0.5 eq). 424 nm PhotoLED.

### 3.7.3. Double-Layer FEP

To enhance the photo-oxidative step and to ensure that full conversion of **14** was routinely achieved, the FEP reactor was remade with a double layer of FEP tubing (1/16 “ o.d., 1/32” i.d., volume 7.54 cm<sup>3</sup>). The extra layer of FEP enhances the productivity through the increase in residence time and in the capture of photons that are previously lost through the gaps in the channels, as shown in Figure 3.11, which highlights the advantage of multi-layered reactors.

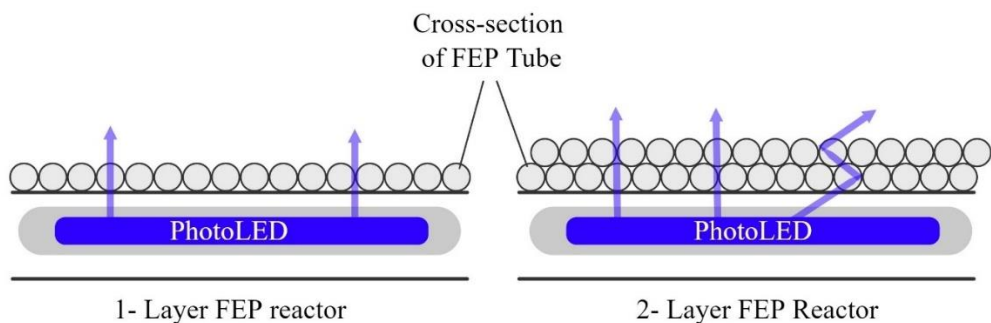


Figure 3.11: light- transmission scenarios through one-layer and two-layer FEP reactors. A one-layer FEP reactor is subjected to relatively short path lengths with absorption of the light by the FEP itself (scenario A) and gaps between the channels (scenario B). Increasing the number of layers of the FEP enhances productivity via the increase in residence time and in the capture of photons previously lost through gaps in the channels, increasing the effective path length.

The low temperature synthesis of **18** under ‘one-pot’ conditions using the double-layer FEP produced conversion around 90%, measured both with  $^1\text{H}$  NMR and HPLC. This is a significant improvement on the similar reaction conducted in the single-layer reactor which resulted in conversion levels between 60% and 75%. Subsequent analysis of the product at various time points indicated a variation in the HPLC conversion. However, due to the lack of an internal standard calibration, this result cannot be confirmed. HPLC analysis also revealed negligible yields **18**, with peak areas below the intercept value of the calibration equation. These values, as previously seen, are not translated into the NMR yield.

After the reaction was complete, a sample was collected into a sealed glass vial and left overnight before being analysed by NMR and HPLC. According to the NMR, full conversion occurred with a 58% yield of **18**. There is, however, a clear discrepancy between the NMR and the HPLC data, with the HPLC returning values of 96 % and 43 % for the conversion and artemisinin yield respectively. The large increase in yield of **18** for the sample left overnight adds to evidence that, at the time of sampling immediately after collection from the reactor outlet, the reaction is at an intermediate stage where **14** has been largely converted, but negligible amounts of **18** are detected.

Table 3.16 ‘One-pot’ synthesis of artemisinin, in the double layer FEP (1/32” i.d 7.54 cm<sup>3</sup>) reactor.

Sample Time	DHAA				Artemisinin			
	Peak Area	Concentration / mM	HPLC Conversion / %	NMR Conversion / %	Peak Area	Concentration / mM	HPLC Yield / %	NMR Yield / %
25	3573	4.25	91	92	37	-0.32	0	43
45	7375	10.57	78	94	36	-0.34	0	47
75	4220	5.32	89	93	21	-0.70	0	44
12 hours <sup>a</sup>	2224	2.00	96	100	911	20.88	43	58

Photo-oxidation carried out at a temperature of -80°C, with the 424 nm PhotoLED, with liquid and O<sub>2</sub> flow rates of 1.0 and 10.0 mL min<sup>-1</sup> respectively. <sup>a</sup> The 12 hour sample is a solution of the 25 minute sample that was left in a sealed glass vial overnight and the NMR prepared the following morning.

### 3.7.4. Comparison of TFA and TCA

A comparison between the two acids, TCA and TFA, was then made to determine the optimum acid for undertaking the ‘two-pot’ synthesis of **18**. A standard photo-oxidation of DHAA was performed at low fluid and oxygen flow rates to ensure full conversion of the starting material. Two separate aliquots of the photo-product were then acidified with 0.5 equivalents of acid and stirred with a flow of oxygen in the dark. NMR analysis was carried out in triplicate, the results of which are shown in Table 3.17. The data reveals the superiority of TCA in forming **18**.

Table 3.17. Results for the comparison of acids used in the two-pot synthesis of artemisinin.

Acid	Conversion / %	18 / %	19 / %	20 / %
TFA	100 ± 0	44 ± 3	4 ± 2	12 ± 3
TCA	100 ± 0	57 ± 3	2 ± 1	6 ± 1

Reactions were carried out at a photoreactor temperature of -80°C with substrate and oxygen flow rates of 0.5 and 2.5 mL min<sup>-1</sup> respectively. TPP (0.25 mM, 0.5 mol %) was used as the photosensitiser. Each acid was used at the typical concentration of 0.025 M (0.5 equivalents). The 424 nm PhotoLED was used for these reactions. 10 mL of each photoproduct was acidified and O<sub>2</sub> bubbled through the stirred solution at a rate of 2 mL min<sup>-1</sup> for 20 minutes.

The formation of **20** appears more prevalent when TFA is used to initiate the Hock Cleavage. This is also exhibited in the results of the initial testing of the near micro FEP reactor. The yields of **20** obtained from each of the ‘two-pot’ reactions were found to be 11 ± 4 % and 5 ± 1 % for TFA and TCA respectively. While the ‘one-pot’ synthesis with TCA gave a yield of 4 ± 0 %, the reaction with TFA at the same flow rates, albeit at a slightly lower photoreactor temperature (-80°C versus -71°C), produced **20** in a yield of 9 ± 3%. In fact, all of the reactions with TFA that produced comparable levels of conversion gave similar yields of **20** between 7 – 9%. The formation of **20** follows an acid-initiated intramolecular S<sub>N</sub>2' displacement of hydrogen peroxide by the

carboxylic acid moiety in DHAA hydroperoxide **15**, shown previously in Figure 1.31.<sup>178</sup> The greater propensity of TFA to initiate this reaction can, in part, be explained by comparing the pKa values of the two acids: TFA is a slightly stronger acid than TCA, having a pKa of 0.23 *versus* 0.66 for TCA; as such, TFA is better able to initiate the displacement reaction.

### 3.7.5. Reactions with TCA

The effect of varying TCA concentration in the ‘two-pot’ synthesis was initially investigated. The data outlined in Figure 3.12 indicates that 0.5 equivalents of TCA is the optimum concentration, confirming the early work conducted by Kopetzki et al.<sup>8</sup> Further deductions can be made from this data; the formation of **19** decreases as the acid concentration increases, indicating the higher level of acid helps drive the reaction towards the formation of **18** and away from **19**. Furthermore, the increase in acid concentration generally leads to an increase in **20**, this is expected for the reasons explained in 3.7.4. The reduction in the yield of **18** as the acid concentration increases past 1 equivalent (0.05 M) is potentially due to acid hydrolysis of the lactone ring of **18**.<sup>143</sup>

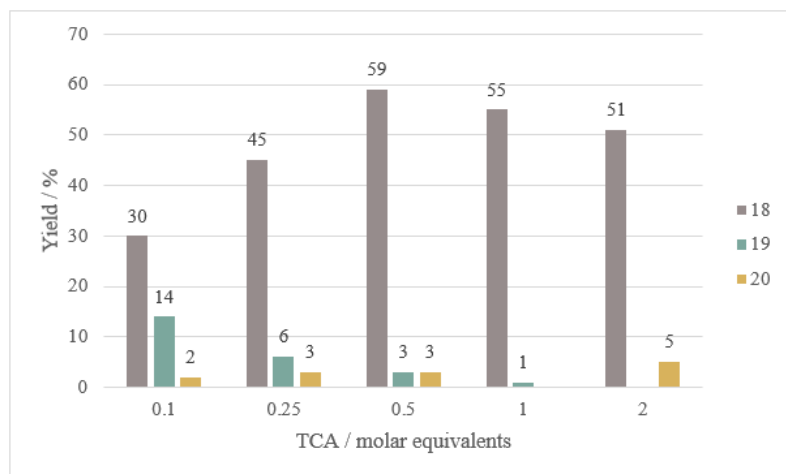


Figure 3.12: ‘Two-pot’ synthesis with varying concentrations of TCA. Photo-oxidation was undertaken at -80°C and at substrate and oxygen flow rates of 1.0 and 5.0 mL min<sup>-1</sup> respectively. The 424 nm PhotoLED was used for this investigation in conjunction with TPP (0.5 mol %). 10 mL of photoproduct was collected after the appropriate equilibrium time, to which the acid was added and oxygen pumped through the stirred solution for 20 minutes. 100 % conversion was achieved for all reactions.

A common interference is the observation of a broad NMR signal due to the acid. This peak has been found to drift and overlap randomly with analyte signals, preventing reliable quantification. Not only does the broad acid peak mask certain signals but it

also causes a slight shift of the other compounds. Removal of the acid is possible through neutralisation and phase separation and has been tested. However, this process has itself a substantial impact on the analysis of all analytes of interest. This finding was later corroborated using HPLC and  $^1\text{H}$  NMR analysis, discussed in Chapter 4. HPLC revealed a yield of **18** of 49%, this value increased to 58% for a sample of neutralised product produced under identical conditions. Therefore, neutralisation prior to NMR analysis was not routinely performed, and as a consequence, some spectra are impacted by analyte-acid signal overlap.

*Table 3.18: Comparison of  $^1\text{H}$  NMR analyte signal before and after neutralisation of the photo-product solution.*

	Reaction	<b>14</b> / %	<b>18</b> / %	<b>19</b> / %	<b>20</b> / %
Un-neutralised	1	10	51	4	3
	2	2	60	0	5
Neutralised	1	0	33	0	2
	2	0	48	0	5

*Un-neutralised sample was prepared by drying 0.5 mL of photoproduct after the ‘two-pot’ synthesis of artemisinin, and re-dissolving in 0.7 mL  $\text{CDCl}_3$ . Neutralisation was performed by combining ca. 10 mL of product with an aqueous solution of sodium carbonate in a separation funnel, mixing until a colour change from green to purple occurred and separating the layers. 0.5 mL of the organic layer was then dried over  $\text{N}_2$  and re-dissolved in 0.7 mL of  $\text{CDCl}_3$ .*

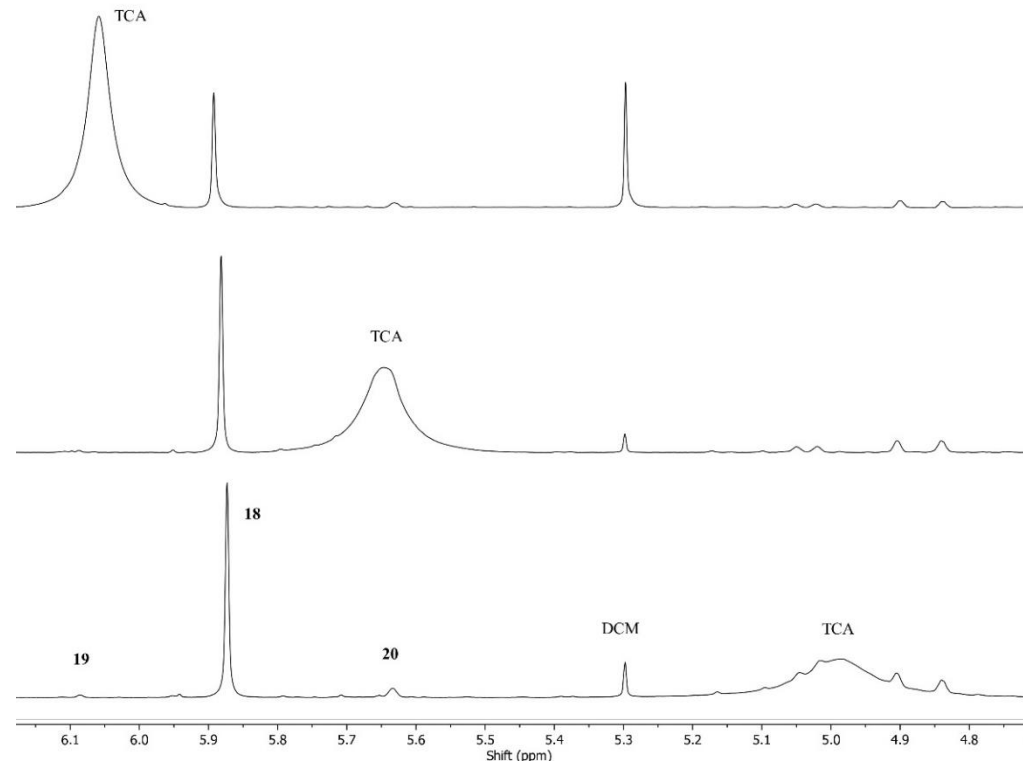


*Figure 3.13: Stacked  $^1\text{H}$  NMR spectra of product from varying TCA concentration, 0.5 (Bottom), 1 (Middle) and 2 (Top) equivalents, the TCA peak increasing in shift with increasing concentration.*

The effect of the photoreactor temperature was then assessed using both synthetic regimes. An inverse relationship between the reactor temperature,  $T_1$ , and the yield of

**18** is observed. Relatively consistent levels of conversion and yields of the main side-products, **19** and **20**, occur for all temperatures within the ‘two-pot’ reactions. This suggests that the temperature has no effect on the overall consumption of DHAA when the photo-oxidation is in isolation from the subsequent acid catalysed steps. However, as the selectivity of the photo-oxidation towards hydroperoxide **15** has been regularly shown to increase inversely with temperature, the corresponding increased selectivity of **18** at lower temperature can be indicative of the direct transformation of **15** to **18**.

The ‘one-pot’ syntheses exhibit lower conversions at all temperatures compared to the ‘two-pot’. This can be attributed to the dual effect of the protonation of TPP: first, the shift in absorption maxima, lowering the spectral overlap with the 424 nm LED and second, the reduction in the quantum yield of triplet state generation. These phenomena contribute to a reduction in the proportion of  $^1\text{O}_2$  generated within the ‘one-pot’ system relative to the ‘two-pot’. The first observable temperature effect on the ‘one-pot’ reactions is the increase in conversion at lower temperature, likely due to the higher solubility of oxygen at lower temperature. However, unlike the ‘two-pot’ synthesis, the temperature appears to have no significant effect on the yield of **18**. This could be an indication that during the photo-oxidation, the selectivity towards **15** remains constant, hence no improvement in selectivity towards **18** occurs.

There is an explicit difference in the levels of **19** between the two regimes. This has been previously noted but through this mirrored experiment it is clear that a far greater amount of **19** is formed during the ‘one-pot’ reactions. The increased formation of **19** has an effect on the associated error for both **19** and **18**, with an interdependency being continually observed. Furthermore, as can be seen in Figure 3.14, there appears to be a temperature effect on the yield of **19**. This is only observed in the ‘one-pot’ reactions as these variations in photoreactor temperature directly impact the acid catalysed Hock Cleavage and secondary oxidation, whereas the Hock Cleavage of the ‘two-pot’ reactions are all initiated at ambient temperature.

A significant result from this experiment is that of the ‘two-pot’ reaction performed at a  $T_1$  of  $-80^\circ\text{C}$ . Six samples of the product were analysed by  $^1\text{H}$  NMR to reduce the potential variation in the analyte yields. The results exhibited the highest yield of **18** so far of 68 % with a suitably low associated error of 2%. The yields of **19** and **20** were encouragingly low and precise, with values of  $2 \pm 1\%$  and  $6 \pm 1$  respectively.

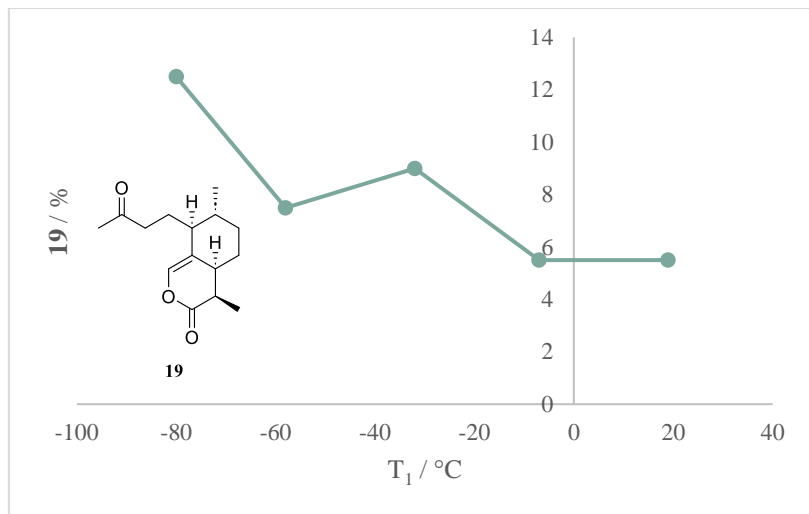


Figure 3.14: Graph highlighting the temperature dependence on the formation of **19** during the 'one-pot' synthesis of **18**.

Table 3.19: Comparison between the 'One-pot' and 'Two-pot' synthesis of **18**. Sample sets are shown individually as the duplicate analysis leads to exceptionally large errors.

Sample	T <sub>1</sub> /°C	Conversion / %		18 / %		19 / %		20 / %	
		Two-pot	One-pot	Two-pot	One-pot	Two-pot	One-pot	Two-pot	One-pot
1	-81	97	87	60	30	1	14	6	4
2		96	87	62	34	1	11	7	4
3	-58	99	85	59	31	1	6	6	5
4		99	85	60	32	1	9	6	4
5	-32	93	-	54	32	2	7	6	4
6		94	76	55	26	1	11	6	3
7	-7	94	67	55	23	2	8	5	3
8		94	70	63	31	1	3	6	3
9	19	98	-	54	31	1	5	6	3
10		98	-	54	25	1	6	6	3

Two-pot reactions: Substrate and oxygen flow rates of 1 and 5 mL min<sup>-1</sup>. TCA (0.5 eq), TPP (0.5 mol %), 424 nm PhotoLED. The second oxidation was carried out under ambient conditions, TCA (0.5 eq) was added to 10 mL of collected photoproduct and the solution stirred with a flow of oxygen at 2.0 mL min<sup>-1</sup> for 20 minutes. One-pot reactions: Substrate and oxygen flow rates of 1- and 5-mL min<sup>-1</sup>. TCA (0.5 eq), TPP (0.5 mol%) and TCA (0.5 eq), 424 nm PhotoLED.

### 3.8. Investigation into the formation of 6-lactone, **19**.

Following on from the observation of the interdependency of the formation of **18** and **19** along with the prevalence of the 'one-pot' reactions to afford **19** in relatively high yields, a brief investigation into the formation of **19** was conducted. By understanding the formation of **19** the reaction conditions can be adjusted to ensure that formation is minimised and hence increase the selectivity of the reaction towards **18**.

As explained in Chapter 1, during the investigations carried out by G. Brown and L. Sy in 2002, into the mechanism of the auto-oxidation of DHAA, a pathway was discovered from the tertiary hydroperoxide, **15** to **19**.<sup>178</sup> Upon addition of TFA to a  $\text{CDCl}_3$  solution containing **15** under an atmosphere of  $\text{N}_2$ , immediate conversion into **19** was observed. The Hock Cleavage of **15** produces an enol intermediate, from which artemisinin, **18**, is synthesised *via* the addition of  $^3\text{O}_2$ . The enol can tautomerise to the corresponding aldehyde. The aldehyde tautomer has been found to be far less reactive to  $^3\text{O}_2$  than the enol, and does not convert to a 1,2,4-trioxane ring system. It is through the intramolecular cyclisation of this aldehyde tautomer that **19** is formed.

The researchers at Sanofi made a similar discovery during their work to develop the industrial photochemical synthesis of **18**.<sup>194</sup> Noting that insufficient oxygen during the second stage of the synthesis leads to the increased formation of **19**.

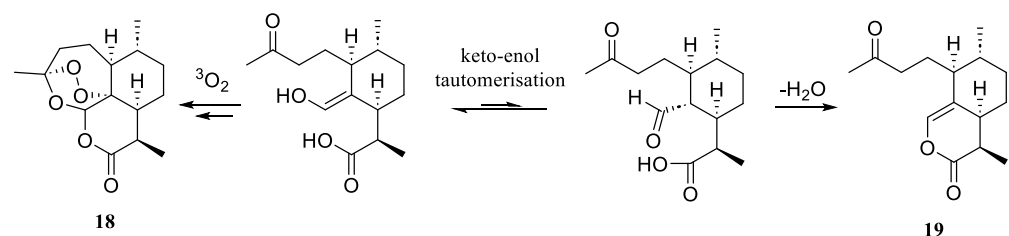


Figure 3.15: Simplified mechanism for the formation of the 6-lactone, **19**, and artemisinin, **18**, from the tertiary hydroperoxide, **15**. After Hock cleavage, an enol is formed which can tautomerise to the corresponding ketone. From this aldehyde the cyclisation occurs to form **19**.

In a study conducted by our group, to determine whether **18** could be synthesised from **19**, it was found that under an atmosphere of  $\text{N}_2$ , **19** initially formed the enol intermediate ( $\delta$  6.24 ppm) before both signals fully decayed.<sup>143</sup> Signals for **18** and **20** were measured, albeit in very low yields, along with other unidentified side products. The experiment was repeated in the presence of  $\text{O}_2$ . Full consumption of **19** led to an appreciable amount of **18** and deoxyartemisinin. This study concluded that **19** can be converted into **18** but due to the susceptibility of **18** to acid hydrolysis, the amount produced is not sufficient to serve as an alternative route.

Throughout the investigations performed as part of this Thesis, it has often been found that **19** appears to be produced far more abundantly during the ‘one-pot’ synthesis, than the ‘two-pot’. It is almost certain that the increase in **19** during these reactions is due to an oxygen deficiency, causing a shift in the equilibrium for the formation of the aldehyde and hence towards **19**. The ‘two-pot’ reactions on the other-hand have an abundance of oxygen with a continual flow passing through the solution.

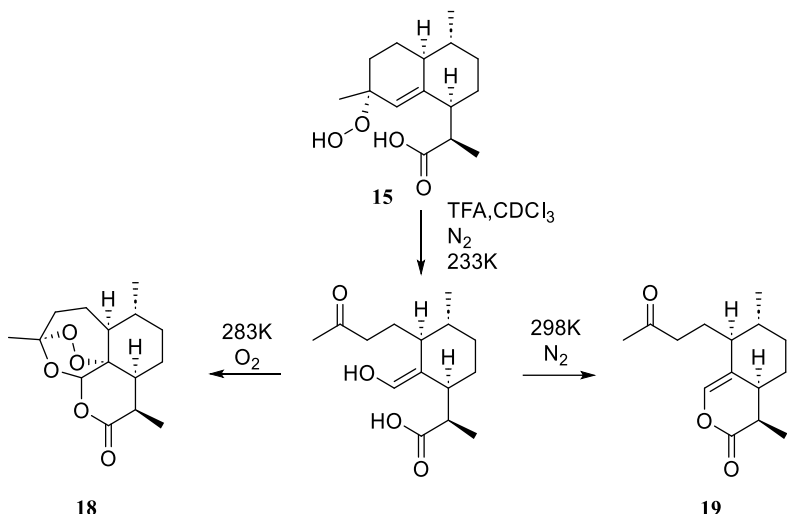


Figure 3.16: The investigation into the auto-oxidation of DHAA by Brown and Sy led the researchers to the discovery of the immediate formation of the 6-lactone, **19**, from the tertiary hydroperoxide, **15**, upon addition of TFA under an atmosphere of nitrogen. Hock cleavage occurs to afford the enol intermediate, with the absence of oxygen and an increase in temperature the enol tautomerises to form the corresponding aldehyde. Intramolecular cyclisation of this aldehyde produces **19**.

To concur with the outcomes of the investigations of Brown and Sy, a ‘two-pot’ synthesis was carried out using  $N_2$  in the second stage of the reaction. Two lots of 10 mL of solution were collected after photo-oxidation. To one of these,  $N_2$  was bubbled through for 5 minutes to remove excess  $O_2$  after which TCA (0.5 eq) was added and the reaction stirred for 10 minutes before sampling. The remaining 10 mL of photo-product followed the typical procedure with  $O_2$  flowing through. The results shown in Table 3.20 somewhat confirm the findings of Brown and Sy, and give an indication that the increase production of **19** within the ‘one-pot’ reactions is due to a lack of oxygen.

Table 3.20 'Two-pot' photo-oxidation of DHAA carried out under typical conditions at a photo-reactor temperature of -30°C, with the 424 nm PhotoLED, and liquid and oxygen flow rates of 1.0- and 5.0-mL min<sup>-1</sup> respectively. Reaction carried out in 1/32" FEP reactor.

Gas	Conversion /%	18 / %	19 / %	20 / %
N <sub>2</sub>	80	26	16	5
O <sub>2</sub>	91	50	2	5

To improve the outcome of the ‘one-pot’ synthesis, an investigation into the equilibration time and, therefore, the time of sampling, was undertaken. The reactor during this time had a total volume of 18 cm<sup>3</sup> and thus had an equilibrium volume of 36 cm<sup>3</sup>. The effect of the time of sampling was examined; photoproduct was analysed at various times during the reaction. Table 3.15 reveals that an increase in the equilibrium volume and hence, time, may be required to improve the results of the synthesis. At the

longest sampling time of 75 minutes a volume of 150 cm<sup>3</sup> will have passed through the reactor, the samples from which indicated the highest levels of conversion, yield of **18** and lowest yield of **19**.

*Table 3.21. ‘One-pot’ synthesis of artemisinin carried out at -76°C with substrate and oxygen flow rates of 2 and 10 mL min<sup>-1</sup> respectively.*

Sampling Time / min	Conversion / %	<b>18</b> / %	<b>19</b> / %	<b>20</b> / %
30	95	40	9	5
45	94	43	12	4
60	95	46	12	7
75	98	46	7	9

*Sampling occurred at different time interval to ascertain information regarding the formation of the 6-lactone. Large variation was observed within each data set with the yield of artemisinin varying significantly.*

The effect of the oxygen molar ratio was then assessed in the ‘one-pot’ synthesis. The molar ratio of oxygen to the substrate was increased from the typical ratio of 1:4.2, corresponding to a flow rate ratio of 1:5 mL min<sup>-1</sup>. However, changing conditions had no effect on yields of **18** or **19** nor the variability typically observed in the ‘one-pot’ reactions. This shows that despite the increase in oxygen present, it does not necessarily translate into a higher concentration of oxygen dissolved into the substrate solution. To reduce the oxygen deficiency of the ‘one-pot’ reactions it is necessary to increase the system back-pressure, thereby forcing a higher proportion of oxygen into the liquid phase.

*Table 3.22. ‘One-pot’ reaction in 1/32” FEP with varying oxygen ratios/flow rates, this also affects the residence time. TFA (0.5 eq) with 424 nm PhotoLED. TPP (0.5 mol %).*

Substrate flow rate /mL min <sup>-1</sup>	O <sub>2</sub> flow rate /mL min <sup>-1</sup>	T <sub>1</sub> / °C	T <sub>2</sub> / °C	Conversion / %	<b>18</b> / %	<b>19</b> / %	<b>20</b> / %
1.0	5.0	-80	23	97 ± 2	52 ± 28	12 ± 16	6 ± 2
1.0	7.5	-80	23	97 ± 3	59 ± 32	9 ± 24	9 ± 4
1.0	10.0	-80	23	97 ± 3	51 ± 31	14 ± 32	9 ± 2
1.0	15.0	-80	23	94 ± 1.5	54 ± 12	7 ± 8	10 ± 1

‘One-pot’ photo-oxidations were completed with sampling occurring straight after the equilibration time had completed, while some samples were stored at -20°C for 48 hours. There is a slight increase in the yield of **18** in the samples that have been stored at -20°C over 48 hours, with a slight drop in the yield of **19**. These results indicate that **19** can potentially form **18**. However, further experiments would have to be conducted to draw a more confident conclusion.

Table 3.23. ‘One-pot’ synthesis of artemisinin carried out at -50°C and -76°C with substrate and oxygen flow rates of 2 and 10 mL min<sup>-1</sup> respectively.

Sampling	T <sub>1</sub> / °C	Conversion /%	<b>18</b> / %	<b>19</b> / %	<b>20</b> / %
Immediate	-50	83 ± 4	39 ± 12	4 ± 4	6 ± 3
48 hours	-50	83 ± 5	44 ± 12	3 ± 2	7 ± 3
Immediate	-76	97 ± 2	45 ± 7	5 ± 7	8 ± 1
48 hours	-76	99 ± 1	50 ± 4	1 ± 1	8 ± 2

Samples were collected after 3 reactor volumes of reactant had passed through, were dried down and a sample set was analysed straight away while a second set was stored at -20°C over 48 hours.

The effect of the acid concentration was then briefly assessed, with findings that the higher acid concentration reduced the level of **19** formed and increased the yields of **18** and **20**. The higher proportion of acid drives the reaction through the enol tautomer and towards the formation of **18**. Furthermore, these results concur with previous ‘one-pot’ reaction observations in that the formation of **19** is more prevalent at lower temperature. This poses the question – does the lower temperature help stabilise the tautomerisation of the intermediate enol to the aldehyde, resulting in more favourable cyclisation to **19**?

Table 3.24. One-pot synthesis of artemisinin. 0.05 M DHAA, 0.5 mol % TPP, 424 nm PhotoLED. Flow rates of 2 (substrate) and 10 (oxygen).

TFA / eq	T <sub>1</sub> / °C	T <sub>2</sub> / °C	T <sub>3</sub> / °C	Conversion /%	<b>18</b> / %	<b>19</b> / %	<b>20</b> / %
0.25	-78	21	22	97	38	14	4
	20	22	22	53	16	2	3
1.0	-78	19	21	95	49	4	8
	20	21	21	74	28	0	9

Photo-oxidation carried out at -78°C and 20°C. Conversion and subsequently yield greatly reduced with the photoreaction at 20°C. Yields lower than when using 0.5eq TFA, while discrepancies with 6-lactone continued. Samples were run in duplicate.

HPLC analysis of photochemically produced **18**, discussed in Chapter 4, showed that at the point of sampling, typical for reactions conducted in this Chapter, the reaction solution is in an intermediate stage; quantitative conversion of **14** is achieved, however, **18** is found in negligible, while large intermediate signals are observed. Therefore, at the point at which samples are prepared for NMR, they are in an intermediate stage. The NMR samples are first prepared by drying the solution under nitrogen; this will increase the concentration of the intermediates and hence the rate of reaction, this has the potential to alter the outcome of the reaction. Samples that are prepared under different time frames are likely to exhibit differing yields of, in particular, **18** and **19**. Furthermore, the use of nitrogen to dry the sample could be driving the reaction towards the formation of **19**. This phenomenon will be exacerbated for the first sample prepared in this way, while the reaction profiles of the subsequent samples, which are open to the air for longer time periods, may progress favouring the formation of **18**. This finding goes some way as to explain the large variations between **18** and **19** within the same sample set.

### 3.8.1. Synthesis of Artemisinin using DHA Ethylcarbonate

Lactonisation of carboxylic acids can be prevented through derivatisation to the corresponding ester and carbonates, this method has been employed by Sanofi for their industrial scale synthesis of **18**.<sup>5,178,194</sup>

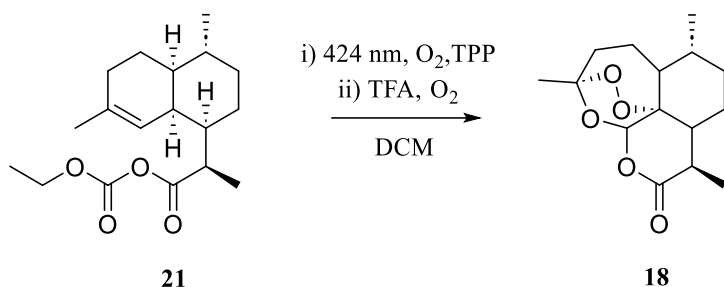


Figure 3.17: Schematic for the 'two-pot' synthesis of **18** from DHAA ethylcarbonate, **21**.

The continuous 'one-pot' synthesis of **18** was undertaken under standard conditions using dihydroartemisinic ethylcarbonate, **21**. The reaction was carried out in the 'thick walled' FEP (1/8" o.d., 1/16" i.d.) reactor under standard conditions. High levels of conversion were achieved at all reactor temperatures, with the highest conversion and yields of **18** being achieved at the lowest temperature. However, despite the hopes to reduce the formation of **19** due to the derivatisation of DHAA, the lactone has been formed in the highest proportion so far measured. The formation is not consistent, as has been previously observed there is a large variation within each sample set, indicating an interdependence between **18** and **19**.

Table 3.25:  $^1H$  NMR yields from the 'one-pot' synthesis of **18** from **21**.

Sample	T <sub>1</sub> / °C	T <sub>2</sub> / °C	T <sub>3</sub> / °C	Conv. /%	<b>18</b> / %	<b>19</b> / %	<b>20</b> / %
1	-76	17	20	100	45	26	2
2				100	65	10	2
3	-60	18	20	100	34	27	2
4				100	56	7	2
5	-18	20	21	94	30	13	2
6				94	39	4	2
7	13	21	23	95	31	12	2
8				94	37	4	3

The substrate and  $O_2$  stream were flowed at 2 and 10  $mL\ min^{-1}$  respectively into the 'thick-wall' FEP (1/8" o.d., 1/16" i.d.) low temperature reactor and irradiated with 424 nm light.

The semi-continuous 'two-pot' synthesis of **18**, conducted in the 'near-micro' FEP reactor, exhibited full conversion for both reactor temperatures. Along with higher selectivity towards hydroperoxide **15**, as has been observed during the oxidation of **14**. The increased selectivity of the photo-oxidation subsequently led to a slight increase in

the yield of **18**. The yields of **19** and **20** remain low and consistent over both temperatures, indicating two points. First, the use of TCA subdues the formation of **20**. Second, the ‘two-pot’ synthesis with the secondary reaction conducted at ambient temperature is sufficient in oxygen to prevent significant formation of **19**.

Table 3.26: ‘Two-pot’ synthesis of **18** from **21** in the ‘near-micro’ FEP 424nm reactor.

Sample	T <sub>1</sub> / °C	Conv. /%	<b>15</b> / %	<b>16</b> / %	<b>18</b> / %	<b>19</b> / %	<b>20</b> / %
1	18	100	70	9	-	-	-
2		100	67	9	-	-	-
3	18	100	-	-	47	1	0
4		100	-	-	48	1	0
5	-80	100	73	7	-	-	-
6		100	73	7	-	-	-
7	-80	100	-	-	51	1	0
8		100	-	-	56	1	0

Reactions were conducted at photo-reactor temperatures of 18°C and -80°C; at substrate and oxygen flow rates of 0.5 and 2.5 mL min<sup>-1</sup> respectively. Hock Cleavage initiated by the addition of TCA.

### 3.9. Summary

The aims set out at the start of this chapter were to: i) exploit further the improvements observed in the selectivity of the photo-oxidation of dihydroartemisinic acid, DHAA, obtained through the development of a new photoreactor capable of achieving internal temperatures below those reached with the high-pressure reactor (HPR) in Chapter 1; ii) investigate the effect of the improvements on selectivity into the full synthesis of artemisinin from dihydroartemisinic acid.

Progress described during this chapter achieved the first of these aims. First, a new photoreactor, the submerged ‘near-micro’ FEP reactor was developed. This design exhibited superior physical properties and reaction dynamics compared to other materials tested. The reactor was shown to regularly facilitate continuous-flow photo-oxidations down to -80°C and, in the process, highlighted the effect of reduced temperatures on the selectivity of the ene-oxidation of DHAA.

The reaction was then progressed to the full synthesis of artemisinin using two regimes: the continuous ‘one-pot’ and semi-continuous ‘two-pot’. A comparison of these regimes found the oxygen deficiency of the ‘one-pot’ reactions resulted in increased formation of the 6-lactone. Moreover, the reduced photophysical properties of the

photosensitiser, TPP, due to protonation, led to reduced conversion and artemisinin yield. The 6-lactone was found to form preferentially at lower temperatures, indicating the requirement for the secondary reactions to be conducted at ambient temperature.

The investigation into the effect of the acid found that TCA restricted the formation of dihydro-*epi*-deoxyartemisinin, the formation of which appears to be relatively independent of the other reactor factors. The optimum concentration of acid was determined to be 0.5 equivalents; lower levels resulted in higher yields of the 6-lactone whereas higher levels diminished the yield of artemisinin.

The reduced photoreactor temperature had a large effect during the ‘one-pot’ syntheses, providing increased conversion and, thus, yields of artemisinin due to the increased oxygen concentrations. The improved selectivity towards the desired tertiary hydroperoxide was found to translate marginally into increased yields of artemisinin: the highest yield of artemisinin of  $68 \pm 2\%$  being achieved using the ‘two-pot’ regime at a photoreactor temperature of -80°C.

The development of the photoreactor in tandem with the reaction development has provided a good level of insight into the synthesis of artemisinin at low temperature. Moreover, this has provided a foundation for the development of a self-optimising reaction for low temperature photo-oxidative reactions.

## Chapter 4. Development Towards a Self-Optimising Reactor for Photo-Oxidative Reactions

The focus of this Chapter is the development of a self-optimised system for low temperature photo-oxidative synthesis. This Chapter will present the evolution of the low temperature continuous flow photoreactor towards a self-optimised system using On-line HPLC analysis. The following strategies were implemented to address these aims:

- To develop robust HPLC methods for the quantification of i) artemisinin and dihydroartemisinic acid, ii) rose oxide and citronellol
- To implement the HPLC methods into the self-optimisation framework built within MatLab and Labview softwares and to test this framework using the continuous flow syntheses of artemisinin and rose oxide.
- To further develop the reactor such that ‘two-pot’ syntheses can take place in flow, and to implement the additional factors into the self-optimisation framework in order that continuous ‘two-pot’ reactions may be automated.
- Utilise design of experiment techniques to reduce the number of variable parameters to those with the greatest impact to reduce computational cost.
- Run fully automated experiments using the SNOBFIT algorithm for the optimisation of the reaction yield.

## 4.1. Background

### 4.1.1. Self-Optimisation

Manual optimisation procedures that endeavour to find the optimal reaction temperature, retention time and reagent concentrations to maximise yield, productivity and other metrics, are often complicated by poorly understood side reactions and potential interdependencies among the reaction parameters.<sup>233</sup>

Traditional reaction development is labour, material and consequently cost inefficient. Precursors in the syntheses of complicated drug molecules are typically expensive. Reduction in the number of reactions required to reach optimal conditions not only reduces the use of expensive precursors, but also limits the use and disposal of hazardous waste, thereby ensuring minimal labour costs.

Self-optimisation describes the combination of *in situ* analysis with adaptive feedback algorithms to produce an autonomous computer-controlled reactor. The combination of an integrated analytical technique with an evolutionary algorithm, produces a feedback loop whereby the reaction parameters are altered within predefined limits based on the results of the preceding experiments. Conditions are iteratively adapted until convergence to the optimum is achieved without any user intervention.<sup>234–236</sup>

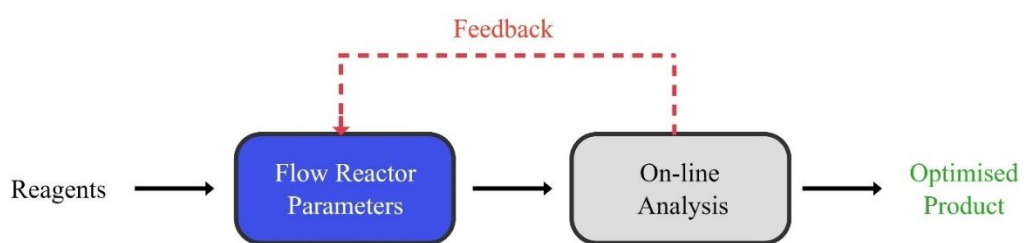


Figure 1.1: Schematic of a self-optimising reactor. On-line analysis provides a feedback loop to the flow reactor parameters such as the pump flow rate, oxygen flow rate, and reactor temperature etc. These are iteratively adjusted until the optimised conditions have been achieved.

Flow reactors are ideal for the integration of online analytics and equipment automation; offering a greater degree of control and reliability compared to batch systems.<sup>234,237,238</sup> This technology also offers improved safety, closer reaction control, enhanced reaction kinetics and the potential to access previously forbidden reaction space.

22,126,128,130,234,236,237,239–243

Self-optimisation has grown into a prominent field of research, so much so, that the term ‘Chemistry 4.0’ has been coined to define the chemistry of the fourth industrial

revolution, wherein chemical synthesis will be revolutionised by the integration of information technology systems, algorithms and automated machines.<sup>239,244–248</sup> The combination of a continuous reactor with an optimised feedback loop was first introduced in 2007 by Krishnadasan *et al.* in the synthesis of CdSe nanoparticles.<sup>249</sup> Further development in the field of organic synthesis was led by the groups of Jensen<sup>233,250–252</sup> and Poliakoff.<sup>253–255</sup>

#### 4.1.1. Design of Experiment

Statistical Design of Experiments (DoE) is a powerful approach to screen and optimise chemical processes, in which a series of experiments with predefined parameters (factors) are performed, with the aim of identifying the effect of each factor and of synergistic and antagonistic interactions between the factors.

The traditional approach to reaction optimisation in which one variable is changed at a time (OVAT) is inefficient and suffers from several drawbacks.<sup>256,257</sup> First, the optimal conditions are rarely discovered, in a large part due to the fact that the outcomes are highly dependent on the starting position.<sup>258</sup> Secondly, the OVAT approach is unable to distinguish between the inherent run to run variations of a system from actual improvement in the reaction, unless a large number of reactions are performed using the same conditions. The systematic approach of DoE on the other hand eliminates research bias, while the ability to simultaneously vary parameters greatly improves efficiency. The most significant advantage of DoE and why it is being used in this instance is the ability of the technique to detect which factors influence the result of the reaction in a statistically relevant manner and which of those are interdependent. The aim of the following DoE experiments is to eliminate redundant factors and hence reduce the computational complexity of self-optimised experiments.

A DoE is commonly constructed using a full factorial design (FFD). Each factor is assigned a discrete level, corresponding to the maximum, minimum and middle value range (+1, 0, -1), and experiments are conducted at all possible combinations of these levels across all factors. Experiments are also conducted in replicate at the centre-point conditions to give a measure of repeatability. The number of experiments required,  $N$ , is given by equation 4.1, where  $n$  is the number of levels,  $k$  is the number of factors and  $m$  is the number of centre-point replicates.

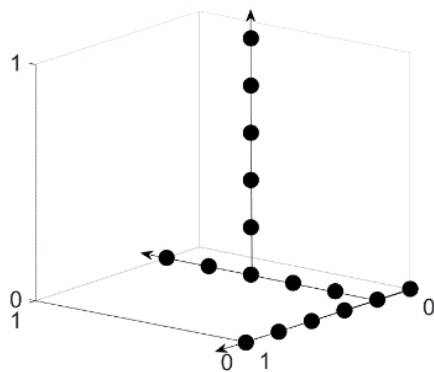


Figure 4.1: An example of a three-variable OVAT optimisation. Each factor is optimised independently, this leads to an inefficient process, requiring a large number of experiments and a low chance of reaching the true optimum.

$$N = n^k + m \quad 4.1$$

The use of fractional factorial design can be employed when the number of factors is high. The face centred composite, CCF, design is best suited for the optimisation of chemical reactions.<sup>259</sup> The number of experiments required for a CCF design is given by equation 4.2.<sup>260</sup>

$$N = 2^k + 2k + m \quad 4.2$$

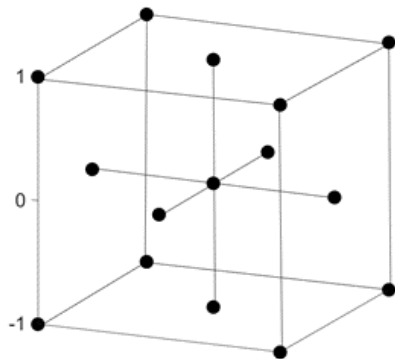


Figure 4.2: A 3-factor CCF design with 1 centre-point. The design requires 15 experiments.  $2^3 + (2 \times 3) + 1 = 15$ .

#### 4.1.2. Process Analytical Technology

Online analysis describes the *in-situ* analysis of the reaction. This allows for rapid determination of reaction metrics such as yield, conversion and productivity, and can be used to determine reaction kinetics. A number of analytical techniques have been

utilised for online analysis in flow reactors, these include: HPLC,<sup>261–263</sup> GC,<sup>264–267</sup> IR spectroscopy,<sup>252,264,268–270</sup> Raman spectroscopy,<sup>271</sup> UV-Vis spectroscopy,<sup>270,272</sup> NMR,<sup>273–275</sup> and mass spectrometry.<sup>276,277</sup>

The key to the success of any self-optimised system is the reliability and robustness of the monitoring of process parameters and product quality by process analytical technology (PAT).<sup>278,279</sup> The integration of PAT within the reactor is relatively facile, while the reaction parameters, typically flow rate and temperature, can be easily and closely controlled. PAT tools can be categorised into four main classes: in-line, on-line, at-line and off-line.<sup>279</sup>

In-line analysis refers to the use of an analytical detector placed directly in the reaction stream. These detectors are capable of making rapid measurements, such as IR or Raman probes. Similarly, on-line enables the analysis of the product stream at all times; however, a section of the main stream is diverted to a bypass line where the analysis takes place. The use of non-destructive analytical methods allows the secondary stream to return to the mainstream unchanged.<sup>279</sup>

Off-line PAT involves the analysis at an offline facility; no automated sample delivery technology is incorporated. A sample is manually extracted from the system, prepared and delivered to the analytical instrument. Off-line analysis is useful when further sample preparation is necessary, or when analytical devices cannot be easily automated or connected to the reactor.<sup>279</sup>

At-line sampling (often misattributed to on-line) requires automated extraction of the sample from the reaction stream to the analyser, with or without a sample preparation step between the process and the analysis. Chromatographic techniques (GC, LC, IC) that use one or more detectors, and techniques that are destructive, fall into the ‘at-line’ category. Chromatography generates data that is easy to interpret, an important consideration when establishing the foundation of an automated process. However, the relatively long analysis time, when compared to in-line and on-line techniques, is detrimental to throughput.<sup>280</sup>

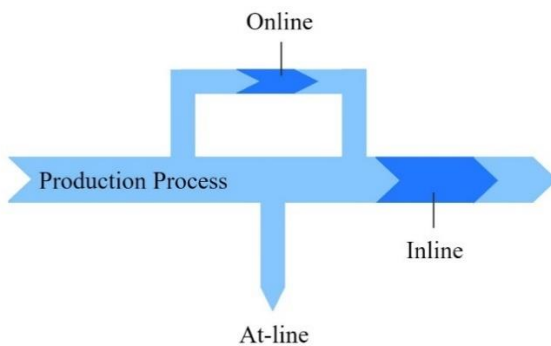


Figure 4.3: Diagram depicting the four categories of PAT tools in a continuous flow reactor.

Automatic sample removal and transfer to the analyser often requires sophisticated hardware. Rotary valves, shown in Figure 4.4, are commonly used in continuous manufacturing for sample delivery to a chromatographic system, as they can be placed in the main flow of the reaction stream.<sup>281</sup>

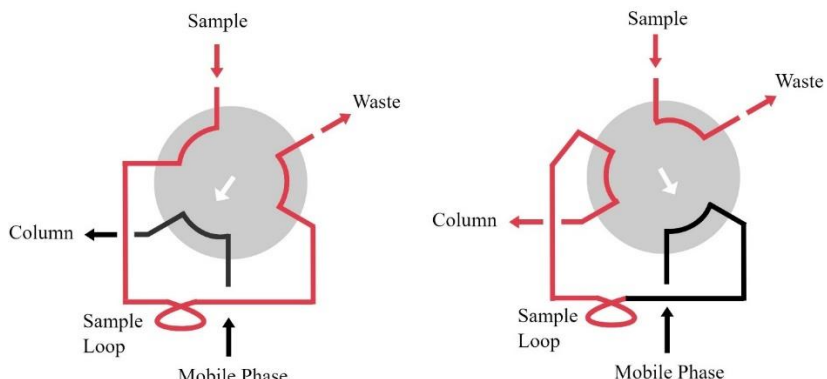


Figure 4.4: Six-port rotary valve with a single sample loop. Left: Load configuration, reaction mixture is pumped from the reactor and through the sample loop towards the waste. Right: Inject configuration – the injector is rotated and connects the sample loop to the HPLC mobile phase. Schematic adapted from manufacturer's website(Vici).

On-line and In-line PAT, using techniques such as IR, Raman and NMR spectroscopy, provide the most rapid, high-throughput analysis.<sup>279,281</sup> There are, however, significant caveats associated with these techniques; vibrational spectroscopy generates convoluted spectra, the analysis of which is complex and results in significant computational cost. The use of NMR as a tool for In/On-line analysis was first presented by V. Sans *et al.* in which benchtop NMRs were implemented into a flow reactor to achieve real time reaction analysis and self-optimisation.<sup>282</sup> In/On-line NMR presents an exciting tool for kinetic and mechanistic studies in real-time and the ability for self-optimisation based on NMR signatures. However, the resolution and sensitivity

of low-field benchtop NMR spectrometers hampers their ability to provide accurate quantification especially at low analyte concentrations.<sup>280,282</sup>

#### 4.1.3. Online-Process Analytical Technology for the Detection of Artemisinin

Artemisinin has been previously quantified using various On-line analytical methods. Gas chromatography has been used to indirectly measure artemisinin extracted from *Artemisia Annua*, through the detection of two thermal degradation products.<sup>283–285</sup> Reversed-phase HPLC with UV detection (HPLC-UV),<sup>286,287</sup> electrochemical detection (HPLC-ECD),<sup>285,288,289</sup> evaporative light scattering detection (HPLC-ELSD)<sup>290–294</sup> and refractive index detection (HPLC-RI)<sup>295</sup> have all been used to quantify extracted artemisinin.

The most accessible and affordable method for the analysis of artemisinin is HPLC-UV. The first instance of artemisinin detection via HPLC-UV was reported in 1985 by Zhao *et al.*<sup>286</sup> The extinction coefficient of artemisinin and its derivatives are low; therefore, the researchers felt it favourable to transform artemisinin into the more UV active compound, Q-260.<sup>286,296</sup> However, derivatisation, either pre- or post-HPLC column adds a layer of complexity that prevents its implementation into a self-optimised system.

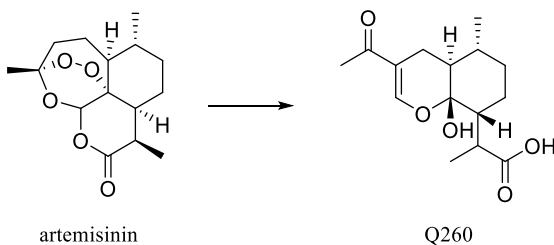


Figure 4.5: Derivatisation of artemisinin to Q260. The derivatisation first proceeds with the base induced endoperoxide ring opening followed by subsequent acidification and cyclisation to afford Q260.

In 2008 Ferrira *et al.* reported the analysis of underivatised artemisinin using 192 nm UV detection.<sup>287</sup> Ferrira showed that HPLC-UV provided accurate, precise and reproducible quantification of artemisinin and its co-extracted compounds. Low thresholds of quantification, high levels of recovery and good intra- and inter-day repeatability were exhibited. Over the 23 year period between the work of Zhao and Ferrira, UV detection was increasingly considered time consuming, with the derivatisation having a negative effect on other extracted compounds; therefore HPLC-ELSD (evaporative light scattering detection) became the preferred technique.<sup>293</sup>

#### 4.1.4. HPLC

High pressure/performance liquid chromatography (HPLC) is a technique used to separate analytes depending on their affinity between a pressurised liquid ‘mobile’ phase and a ‘solid’ stationary phase. To achieve adequate efficiency, columns are packed with the stationary phase particles of sizes typically between 2-10  $\mu\text{m}$ . This also requires high pressures, 70 – 400 bar, to be applied to force the mobile phase through the column.<sup>297,298</sup> The characteristics of both the mobile and stationary phases determine the elution of each of the analytes. The ability of a solvent to displace the adsorbed analyte from the stationary phase is defined as the solvent’s ‘eluent strength’; higher eluent strength indicates a mobile phase that competes strongly with the analyte for active adsorption sites and so the analytes are rapidly eluted.

‘Normal phase’ HPLC typically uses silica as the polar stationary phase in conjunction with either a non-polar or moderately polar mobile phase. Within normal phase HPLC, less polar solutes are eluted most rapidly while more polar compounds have higher affinity to the silica and, hence, higher retention times.<sup>299</sup> In ‘reverse phase’ HPLC, the surface silanol (Si-OH) groups of the silica are modified, most commonly in the form of octadecylsilane, known as C18. Reverse phase HPLC uses these derivatised silanol groups to produce a non-polar stationary phase through which a polar mobile phase, comprised mostly of water, is used to elute polar compounds most rapidly, while retaining non-polar constituents longer.

#### 4.1.5. Evaporative Light Scattering Detection (ELSD)

ELSD is an aerosol-based, mass dependent detector suitable for the detection of non-volatile components in a volatile eluent. The response is not dependent on the spectral or physicochemical properties of the analyte as it is in UV detection.<sup>300</sup>

In this approach, the HPLC eluent is first nebulised into an aerosol followed by evaporation of the solvent using a stream of nitrogen in a heated drift tube. Subsequent detection of the remaining particles with low-volatility then occurs in a light scattering cell.<sup>301</sup> The amount of light scattered is measured by a photomultiplier tube and is directly proportional to the amount of analyte present.<sup>292</sup> All compounds that have a

sufficiently low volatility compared to the mobile phase can be analysed. The ELSD is, therefore, regarded as a universal detector.

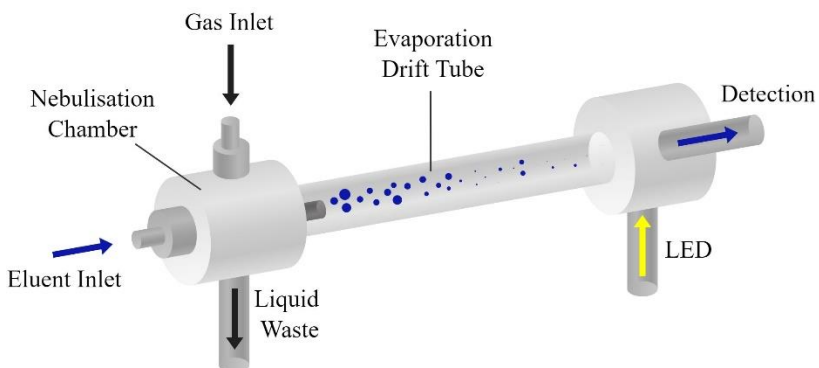


Figure 4.6: Schematic of the operational ELSD properties. The eluent is first nebulised into an aerosol, and transported by a carrier gas ( $N_2$ ) through the evaporation chamber, in which the solvent is volatilised leaving a fine mist of solute particles that scatter the incident light from an LED to a photomultiplier. The signal is amplified and the voltage output relates directly to the concentration of analyte passing through the optical chamber. Schematic taken from an Agilent technical report on the performance of the ELSD.<sup>302</sup>

The sensitivity of the ELSD varies with the composition of the mobile phase, sensitivity increasing with increasing volatility due to the ease with which the solvent is removed in the drift tube.<sup>303</sup> The baseline response is, however, insensitive to the composition of the mobile phase; thus, gradient mobile phase methodologies may be implemented, allowing greater flexibility and enhanced analyte detection.<sup>304</sup> This provides a significant advantage over another regularly used universal form of detection, refractive index (RI), which is highly sensitive both to changes in mobile phase composition and the column temperature; therefore, only isocratic methods can be used.<sup>305</sup>

The relationship between ELSD signal response and the amount of analyte is non-linear. The relationship between response and analyte mass can be expressed by equation 4.3.  $M$  is the mass of the analyte, and  $A$  is the signal response, while  $a$  and  $b$  are coefficients dependent on the analyte and chromatographic conditions. To generate a linear response for the purpose of calibration, equation 4.3 can be transformed into equation 4.4.

$$A = aM^b \quad 4.3$$

$$\log(A) = b \cdot \log(M) + \log(a) \quad 4.4$$

Work carried out by A.A. Lapkin *et al.* compared the use of HPLC-ELSD with the World Health Organisation (WHO) monograph of HPLC-UV analysis.<sup>295</sup> UV detection

exhibited greater accuracy and a lower limit of quantification (LOQ) than HPLC-ELSD. However, the researchers indicated that the HPLC-ELSD method appeared to be the most robust for routine quantification of artemisinin in plant extracts. Due to the low UV absorbance of artemisinin, the corresponding signal can be easily lost in the background noise, therefore HPLC-UV was not recommended for analysis of extracts unless paired with another technique, but may be used for the analysis of the purity of bulk artemisinin.<sup>295</sup> Furthermore, a number of the co-extracted analytes are not detected with ELS therefore this technique provides more facile identification of artemisinin, an important factor when considering automated detection.

## 4.2. HPLC Method Development for the Quantification of Artemisinin

The methodologies for the quantification of plant extract **18**, outlined in detail in **Chapter 5**, formed the foundation for the method development of this investigation.<sup>292–295,306,307</sup>

The first consideration was the choice of technique for the analyte detection. Lapkin *et al.* recommended that UV detection should not be used, instead opting for the more selective ELS detection.<sup>295</sup> The quantification of extract material is complicated by the number of co-extracted compounds with close structural relationships, these overlapping with the weak UV signal of **18**. However, the number of side-products from the photochemical synthesis of **18** is fewer than the co-extraction products, making separation and quantification a simpler task. Furthermore, the concentration of extracted artemisinin is approximately an order of magnitude lower than the concentrations produced in the photochemical syntheses of this investigation, thus making UV detection a viable option for this application.

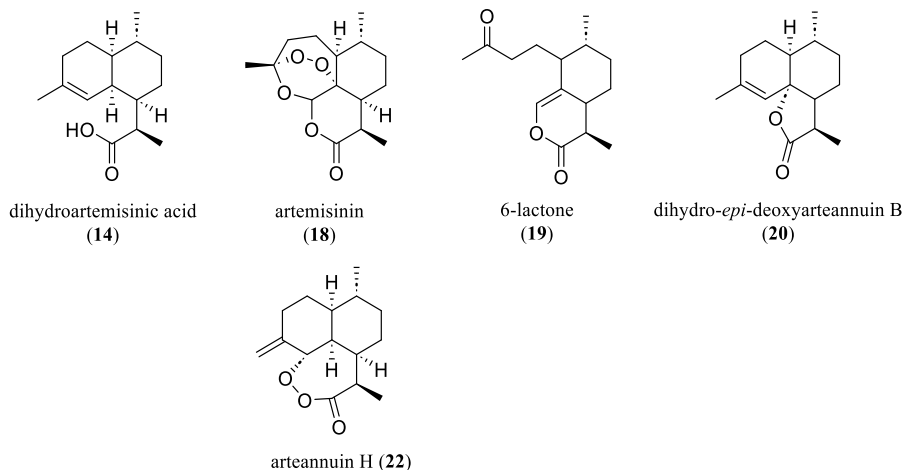


Figure 4.7. Common compounds found after the photochemical synthesis of artemisinin.

The use of multiple detectors is possible with the HPLC (Agilent 1260 Infinity) used in this research. Therefore, with UV being a non-destructive technique, a UV detector was used in series prior to the ELSD (Agilent 1260 Infinity II). The use of dual detection was highly beneficial for determining the identity of analyte compounds from often complex spectra, as well as providing high tunability to the analytes of interest. Furthermore, dual detection provided a reasonable degree of data verification; comparison of data between the detectors enabled the identification and, consequently, the removal of anomalous peak data.

Due to the weak UV absorption of **18**, as discussed earlier, ELSD was used as the primary detector in preliminary investigations. The UV was used to verify the results of the ELSD and to provide further information about the reaction profile; most importantly of compounds that elicited no response in the ELSD.

The implementation of dual detection into the automated synthesis of **18** first required the development of a robust HPLC method for the quantification of **18** and **14**. This included; (i) the creation of a mobile phase and stationary phase combination that sufficiently separates all analytes within an appropriate method time; (ii) optimisation of the ELSD parameters to maximise the sensitivity towards **18** and **14**.

The optimisation of the ELSD parameters while achieving high reproducibility, proved to be challenging. High variability of the ELSD, as detailed in **Chapter 5**, combined with the complexity of the synthesis of **18**, required numerous iterations in the development of both the HPLC method and the reactor set-up. It was found that 210 nm UV was sufficient to detect photochemically produced- and calibration standards of **18** down to low concentrations, exhibiting lower limits of detection and quantification than

the ELSD, in agreement with the finding of Lapkin *et al.*<sup>295</sup> Furthermore, UV detection commonly exhibited far lower levels of variation, in both inter- and intra-day precision. During the HPLC and simultaneous reactor/reaction development the use of 210 nm UV became the preferred detection technique. The ELSD was then used to provide valuable data verification and showed responses related to reaction intermediates and potential terminal side-products, whose corresponding signals in the UV were often masked. Furthermore, during the investigations of the synthesis in toluene it was found that **18** and toluene co-eluted. The strong UV absorption of the latter resulted in the comparably weak signal of **18** being lost. ELSD was therefore used as the primary detector in this instance.

Late on in the research, the presence of a plasticiser that had leached from the photoreactor was detected in the 210 nm UV. The peak possessed a retention time similar to that of **18** and was also found to drift. This discovery and the subsequent failures in attempts to sufficiently and consistently separate the two peaks led to attention being turned to the use of ELSD as the primary detector for the synthesis of **18** in both DCM and toluene.

The development of the fully continuous ‘two-pot’ synthesis of **18** greatly highlighted the inadequacy of external standard calibration, which had been eluded to earlier, primarily due to the effect of solvent loss and, hence, resulted in inflated analyte concentrations. The additional reagent streams required for the fully continuous synthesis and, consequently, the high degree of product dilution, resulted in internal standard calibrations being developed. As was the case with internal NMR standards, discussed in **Chapter 2**, the use of an appropriate HPLC standard will negate the effects of concentration change; either *via* solvent evaporation or through dilution.

The internal standard calibration in DCM was conducted using Lauric acid as the standard for detection of **18** in the ELSD. Trimethoxybenzene (TMB) was used as the standard for detection of **14** at 210 nm UV. Calibrations in toluene were complicated by the co-elution of **18** with the solvent, leading to high variability with the ELS detection of **18**. Efforts to separate the two analytes led to a change of the stationary phase from C18 to C8, resulting in slightly earlier elution of **18** and, thus, its separation from toluene. The calibration of **18** and **14** was then conducted using TMB as a UV standard. Despite, the previously mentioned potential interference of the plasticiser

peak, the use of UV for the detection of **18** in toluene is likely to be more reliable than using the ELSD, as is detailed in Chapter 5.

The development of the HPLC methods not only required confirmation of the reliability when analysing standards of **18** and **19**, but also the reliability when analysing photochemically produced **18**. Therefore, throughout the investigation the developed methods were used to analyse reaction product. First, product from the continuous ‘one-pot’ and semi-continuous ‘two-pot’ regimes, which have been discussed in Chapter 3, were analysed *via* HPLC. These analyses provided some insight into the reaction profile at the time of sampling and influenced further modifications to the reactor hardware to improve the formation of **18**, ultimately leading to adaptations to the reactor to perform the fully continuous ‘two-pot’ synthesis of **18**. With appropriate HPLC methods, Online monitoring could then be implemented into the continuous ‘one-’ and ‘two-pot’ regimes. These investigations allowed for modifications to be made to both the reactor hardware and the automated software. A detailed description of the automated reactor is given in Chapter 5.

### 4.3. Synthesis of **18** to Test the HPLC Methods

To assess the preliminary external calibrations, and, to compare to the yield determined *via* <sup>1</sup>H NMR analysis, the synthesis of artemisinin, **18**, was performed using both the continuous ‘one-pot’ and the semi-continuous ‘two-pot’ regimes.

The products of such reactions were taken directly from the secondary reaction vessel and analysed using HPLC, without any subsequent preparative steps, and <sup>1</sup>H NMR, using the standard preparation outlined in Chapter 5. Typically, injections of the product solution into the HPLC sample loop were made immediately after extraction from the reaction vessel. Subsequent injections from the sample syringe were then made to assess the reproducibility of the method.

The first such analysis produced unexpected results. First, the yields of **18**, as calculated by each of the detectors, were significantly below the NMR yield of 68 % for **18**. Second, the yield of **18**, measured with both detectors increased significantly between subsequent injections, as shown in Figure 4.8. The sample remained closed within the syringe between the four injections and, therefore, evaporation of the solvent was negligible and unlikely to be the cause for this increase. One possibility is that the

increase in **18** could be due to carry over from the previous analysis.<sup>308</sup> To investigate this, a number of blank injections of DCM were made after a sample run; however, these indicated no presence of **18**.

A similar phenomenon was observed when the temperature of the reactor was varied,

Table 4.1. Subsequent injections led to significant increases in **18** for the reactions conducted at -80°C and -40°C, while the yield produced at 5°C remained relatively stable at around 50% for the ELSD and 45% for the 210 nm. These results also give an indication of the effect of temperature on the formation of **18**. At -80°C, the initial HPLC injection exhibits the lowest yield, as measured by both detectors. The yields then increase with the time of injection, appearing to plateau after ca. 60 minutes around 50%. The reactions at -40°C and 5°C also follow a similar pattern when monitored by the 210 nm detector - an increase in yield with a plateau around 45 %, indicating that although these reactions give a higher initial yield, the final yield is 5 % lower than the reaction conducted at -80°C. The detectors do not correspond with one another with the 5°C data: the ELSD shows a slight decrease in **18**, while the 210 nm shows a gradual increase in **18**.

There was no evidence of external factors leading to the observed increase in **18**. This suggests, therefore, that the formation of **18** was incomplete at the point of sampling and the reaction was able to proceed within the syringe, resulting in the later injections exhibiting higher concentrations of **18**.

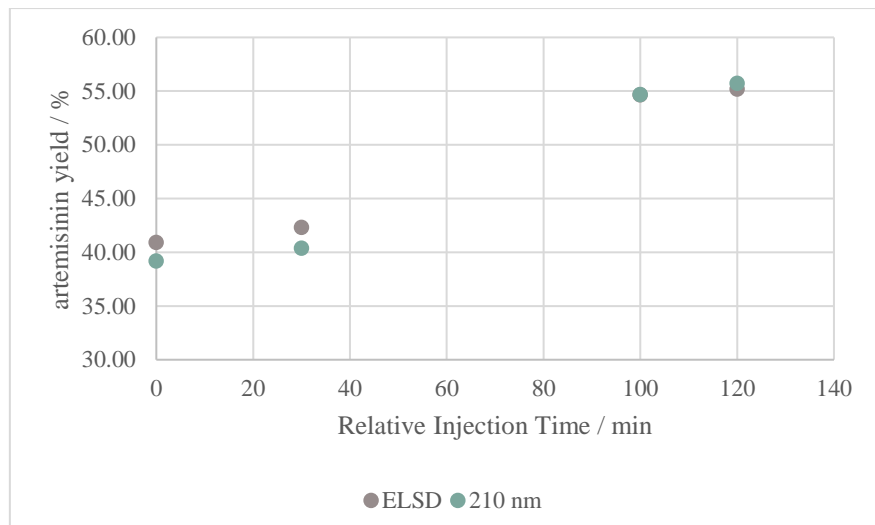


*Figure 4.8: Comparison of the individual injection yields of artemisinin between the ELSD and the 210 nm. The yields are relatively consistent between the two detectors; deviation begins to occur with the later injections. Yields. The yields are plotted for each injection against the relative injection time, highlighting in the increase in artemisinin yield as determined by both detectors. ‘Two-pot’ reaction conducted in the ‘near-micro’ FEP reactor (424 nm, 1/16” o.d., 1/32” i.d., 3.77 cm<sup>3</sup>) at a chiller temperature of -80°C. Hock Cleavage initiated via the addition of TCA (0.5 equivalents). <sup>1</sup>H NMR (CDCl<sub>3</sub>) analysis determined yields of 68 ± 2%, 2 ± 1% and 6 ± 1% for **18**, **19** and **20** respectively.*

*Table 4.1: Calculated yields for the ‘two-pot’ synthesis of artemisinin performed in the ‘near-micro’ reactor (424nm, 1/32” i.d., volume 3.77 cm<sup>3</sup>) photoreactor temperatures of -80°C, -40°C and 5°C.*

Relative time of analysis / min	-80°C		- 40°C		5°C	
	ELSD / %	210 nm / %	ELSD / %	210 nm / %	ELSD / %	210 nm / %
0	34.4	27.9	41.4	37.5	52.0	43.1
19	45.1	41.2	46.8	44.0	50.7	45.5
43	50.6	46.4	49.7	45.5	50.2	46.3
64	53.1	49.4			48.3	43.8
84	54.5	50.5			49.0	44.8
102	50.7	46.1			48.9	45.9
120	53.8	50.0				

*The yields determined by both detectors tend to gradually increase with time, appearing to level around 50 %. Unlike the other two temperatures, the formation of artemisinin at 5°C appears to slightly decrease with the ELSD while the yield increases in the UV.*

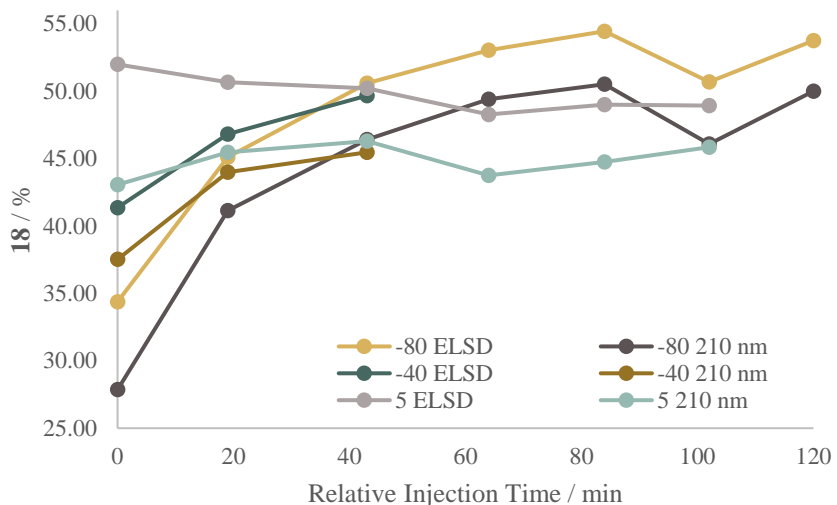


Figure 4.9: Graph highlighting the increase in artemisinin yield with relative injection time. Overall the ELSD exhibits higher yield values than the 210 nm UV. The trends between the two detectors are relatively consistent.

The initial investigations to test the HPLC methods were conducted using the standard conditions used for the majority of experiments described in Chapter 3. The finding that the formation of **18** was incomplete at the time of sampling, in particular for the reactions performed at low photoreactor temperatures, presented a severe issue that halted the implementation of the initial HPLC method into the automated reactor.

Incomplete formation of **18** at the time of sampling would lead to incorrect data being interpreted by the control computer and as such the self-optimisation results will be invalid. To gain an insight into the formation of **18** during the second stage of the synthesis and, consequently, to use the findings to influence the design of the continuous-flow automated reactor, the secondary reaction stage was completed at various intervals.

The ELSD and 210 nm data for each of the three sample sets is shown in Figure 4.10. The shortest reaction time of 30 minutes produces the lowest initial yield of **18** of 27.9 % and 41.3 % as measured by ELS and UV respectively. The two detectors then diverge, with the ELSD exhibiting gradually lower values of **18** until the final sample, in which the level increased to 28.5 %. The peak of **18** steadily increased in area between UV measurements, giving a final yield of 47.2 %. A similar trend occurs for the sample taken after 60 minutes: first the UV exhibits greater yields of **18** than the ELSD with initial values of 52.2% and 35.1% respectively. The UV then gradually increases to 54%, while the ELSD decreases by 6% between the first and second injections, increasing then on to a final yield of 36.7%. The longest secondary reaction

time of 90 minutes produces the highest initial yields, in part due to the effect of solvent loss, of 36.8% and 57.3% in the ELSD and UV respectively. These values remain the most stable, with the ELSD showing a slight increase of 1.5% over the injection period and the UV decreasing by 1.3%. These minimal, but opposing trends could be an indication that the formation of **18** is complete after a secondary oxidation time of 90 minutes. Mass measurements were taken during the secondary oxidation of a fourth sample of hydroperoxide solution, a reduction of 2.8 % was observed over the full 60 minutes. When assessing the 210 nm data, it is clear that the increase in **18** between the initial and subsequent injections is greater than could be attributed solely to evaporation of the solvent.

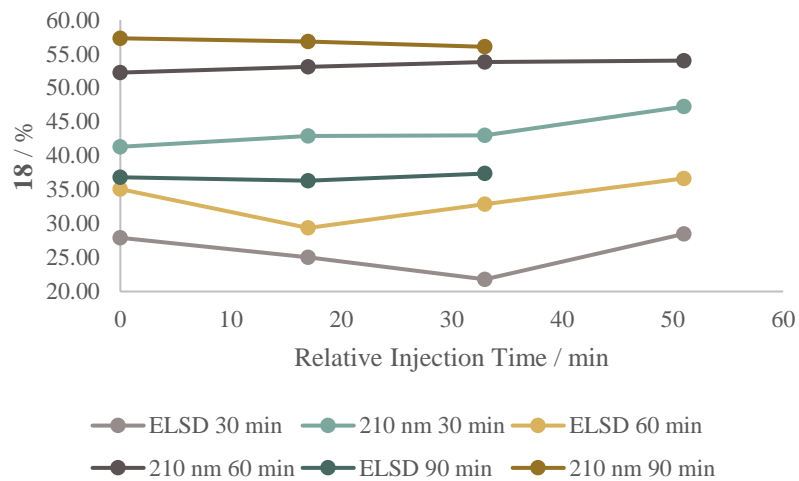


Figure 4.10: 210 nm UV data. 1 mL samples of product solution removed and diluted to 5 mL with DCM before injecting onto the HPLC. Samples were removed from the secondary reaction vessel at time periods of 30, 60 and 90 minutes. Subsequent injections were made from the same syringe after the preceding run had finished.

Comparison between the formation of **18** within an un-neutralised and a neutralised solution provided more information into processes leading to the gradual increase in yield previously observed. The un-neutralised sample, as with all previous samples showed a low yield around 25 % for the initial injection; increasing to 49% over 1 hour. However, the level of conversion only slightly increases from 86% to 90% in the 210 nm UV and from 90 to 100% in the ELSD over this time, indicating that the additional formation of **18** is originating primarily from intermediate products of the photo-oxidation of **14** and not from significant further consumption of **14**.

The neutralisation of the reaction product, also discussed in Chapter 3, appears to have a negative effect on the yield of **18** when analysed *via* NMR. The removal of the acid prevents subsequent reactions from occurring; this is reflected in the relatively constant

yields of **18** as measured by both detectors, which exhibit RSD values of 1.55 % and 4.32 % for the 210 nm UV and ELSD respectively. This indicates that the presence of the acid is essential for the continuation of the reaction after sampling. Once the acid was removed, the formation of **18** halted.

The neutralised samples show a greater yield of **18** along with no detectable **14**, as shown in Table 4.2. The absence of **14** for the initial injection indicates the loss of a proportion of **14** into the polar phase during the neutralisation. This is corroborated in the NMR data of previous neutralisations, discussed in Chapter 3, which also show a reduction in **14**. Furthermore, the partition of **18** is also likely to occur, and is observed in the NMR data. The increase in the biphenyl UV peak area suggests that during the neutralisation and separation of the organic and aqueous layers, solvent loss has occurred resulting in higher concentrations of **18**. This is indeed observed in the HPLC data but the opposite occurs for the NMR.

*Table 4.2:  $^1\text{H}$  NMR data for the product pre- and post-neutralisation: a reduction in DHAA and artemisinin is observed after neutralisation with  $\text{Na}_2\text{CO}_3$  (aq) to remove TCA and separation of the organic and aqueous layers.*

Sample Set	Conversion /%	<b>18</b> / %	<b>19</b> / %	<b>20</b> / %
Un-neutralised	$98 \pm 1$	$60 \pm 1$	0	$5 \pm 5$
Neutralised	100	$48 \pm 1$	0	$5 \pm 5$

These results highlight a clear discrepancy between the NMR and HPLC analyses. The diminished HPLC yields can be attributed to incomplete reactions and, thus, incomplete formation of **18**. HPLC analysis provides a more precise view of the reaction progress and constituents at the time of sampling, due to the short timespan between sampling, introduction to and subsequent separation on the HPLC column. The separation of the reaction constituents on the column prevents further reaction progression. Analysis *via* NMR, however, consists of preparative steps and delays, often in the region of hours, between sample preparation and analysis. This length of delay is likely to be sufficient for the formation of **18** to proceed to completion; occurring either during the preparation or afterwards with the product in the NMR solvent; typically deuterated chloroform ( $\text{CDCl}_3$ ). The drying of the reaction intermediates and subsequent dissolution in  $\text{CDCl}_3$  could also affect the reaction progression and enhance the formation of **18**. Sy and Brown found that **18** was formed from **14** and **15**, when each was stored in  $\text{CDCl}_3$ ; the formation was slow but provides an indication that  $\text{CDCl}_3$  may have an effect on the reaction intermediates.<sup>178</sup>

Table 4.3: HPLC data for the synthesis of artemisinin from DHAA.

Injection time / min	UV		ELSD		Biphenyl UV Peak Area
	Conversion / %	<b>18</b> / %	Conversion / %	<b>18</b> / %	
Pre-neutralisation					
0	85.8	25.7	90.4	25.0	86900
25	89.4	43.5	100	42.1	85900
58	90.1	48.9	100	43.9	79100
Post-neutralisation					
0	100	58.4	100	55.9	93600
24	100	56.9	100	54.6	92100
51	100	56.2	100	53.4	90600
80	100	56.9	100	52.4	88300

Pre-neutralisation samples were collected after 20 minutes of the initiation of the second stage of the synthesis and injected onto the HPLC immediately. Post-neutralisation samples were also collected after 20 minutes of reaction. However, they were subsequently treated with  $\text{Na}_2\text{CO}_3\text{(aq)}$  to remove the TCA before injecting onto the HPLC.

#### 4.4. Assessing the Product Composition at the Time of Sampling

The findings that the formation of **18** appears to be incomplete under typical sampling times in the ‘two-pot’ regime; and that the reaction of the photo-product is halted upon removal of the acid, led to investigations to better understand the composition of the intermediate photoproduct. Due to the early elution of the intermediate peaks, and the complexity of the resulting 210 nm UV spectra, the ELSD was primarily used for detection.

HPLC analysis of the photo-oxidation product, composed mostly of the tertiary hydroperoxide, **15**, exhibited a large peak in the ELSD with an elution time of 4.28 minutes (area 5704), as shown in Figure 4.12. This signal may also be composed of overlapping signals from each of the hydroperoxide intermediates that are also formed. Due to the overlap of the DCM peak and hydroperoxide peaks in the 210 nm UV it was not possible to detect the latter with this detector.

The sample analysed 23 minutes after acidification and additional stirring with oxygen, indicates that the majority of the hydroperoxides have been consumed; the corresponding ELSD peak at 4.18 minutes was down to an area of 100. In the process, a small amount of artemisinin had been formed with peak areas of 520 and 771 in the ELSD and 210 nm respectively. When comparing to the hydroperoxide sample, new peaks of significant areas can be observed with the 210 nm UV, Figure 4.13. The most

prevalent are early eluting peaks with retention times of 2.66 minutes and 3.51 minutes, the latter also giving rise to a signal in the ELSD at 3.62 minutes. This signal was found to grow over time and is, therefore, likely to belong to a terminal side product rather than an intermediate.

As the reaction progresses, the formation of artemisinin increases and in the later samples the early eluting peaks are no longer observed. Clearly these belong to intermediate compounds that form after the Hock Cleavage of **15**. The elution time of these compounds alludes to the fact that they are not well retained on the reverse-phase column and, therefore, possess a high degree of polarity. A potential intermediate that could give rise to an early eluting peak in the UV is the oxonium ion, discussed in Chapter 1, Figure 4.11.

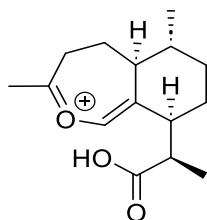


Figure 4.11: The oxonium ion, a potential intermediate in the formation of artemisinin.

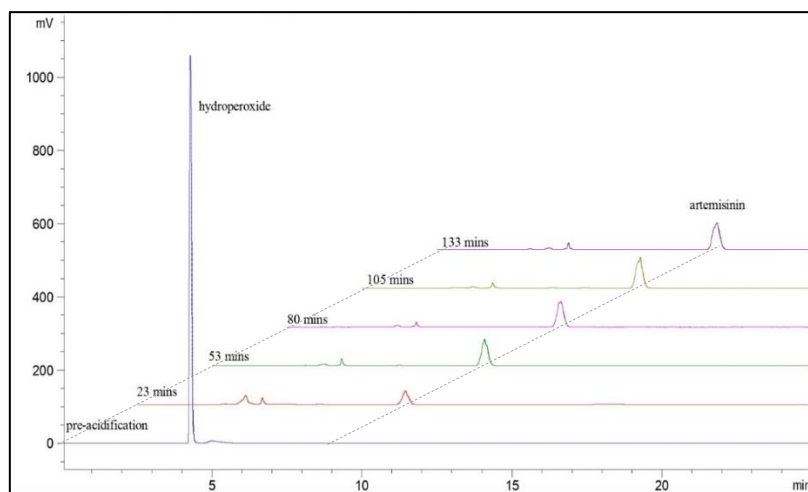


Figure 4.12: HPLC-ELSD stacked chromatoatograms. The bottom signal in blue corresponds to the product of the photo-oxidation pre-acidification. A strong signal for the tertiary, and potentially the secondary hydroperoxides. After acidification and additional stirring with oxygen samples were taken at the time points denoted, these show complete consumption of the hydroperoxide peak along with growth of the artemisinin peak around 9 minutes, and a side product peak at 3.60 minutes.

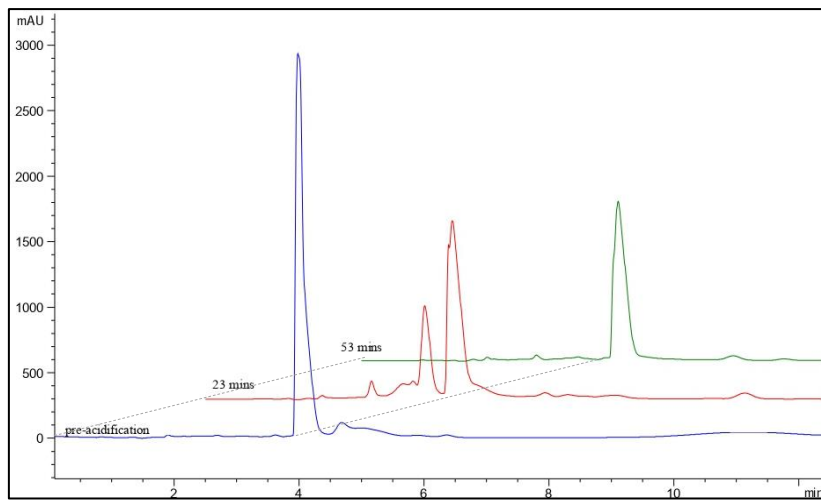


Figure 4.13: HPLC-210 nm stacked Chromatograms. . The bottom signal in blue corresponds to the product of the photo-oxidation pre-acidification. A strong overlapped signal is found for DCM and the hydroperoxides. After acidification and additional stirring with oxygen samples were taken at the time points denoted, these show a reduction in the DCM/hydroperoxide peak indicating consumption of the latter. The initial sample at 23 minutes shows a number of peaks eluting prior to the DCM/hydroperoxide peak, these are consumed between the next sample time of 53 minutes.

The peak area of **18**, as measured by both detectors, was found to gradually grow between subsequent samples. As shown in Figure 4.14, the peak areas follow a similar trend until the final injection of the sample, collected at the 133 minute mark, where the detectors deviated from one another with the 210 nm UV continuing to increase, while the ELSD decreases. **18** should continue to increase with time, either due to additional formation, or via solvent evaporation; hence, the final result of the ELSD is indicative of the higher level of variation of the detector that is discussed in **Chapter 5**.

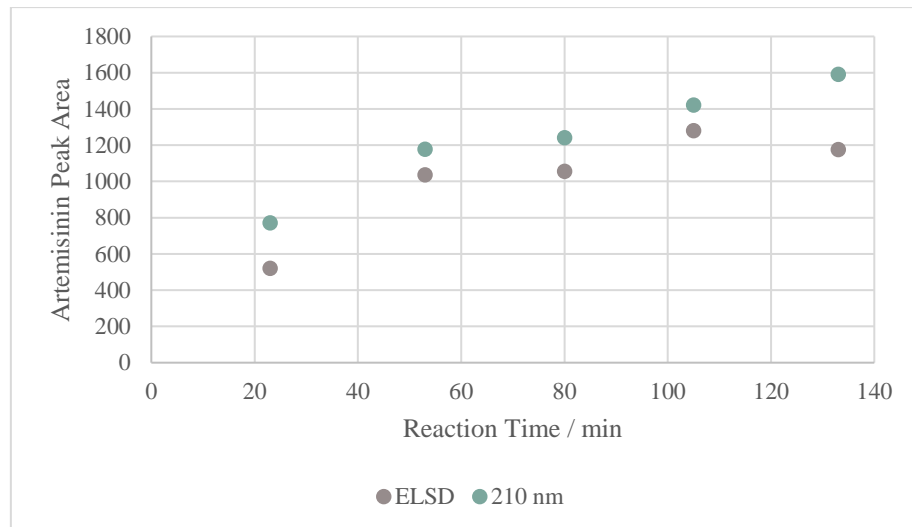


Figure 4.14: Artemisinin peak area as measured by the two detectors over the sampling time of 133 minutes. Both detectors show a gradual increase in peak area over time, both following a similar trend until the final injection whereby the detectors deviate from one another.

## 4.5. Modifications to Increase the Formation of Artemisinin

As stated previously, incomplete formation of **18** at the time of sampling would lead to incorrect data being interpreted by the control computer and, hence, the self-optimisation results would be invalid. It was therefore crucial for the success of the self-optimised reactions to achieve full artemisinin formation prior to analysis. There was, however, a requirement for any adaptations to the reactor to be conducted in a pragmatic way. In the case of reaching reaction completion, the secondary reactor length could, in principle, be increased indefinitely until completion is achieved; however, this would result in an impractical set-up.

### 4.5.1. Heated Secondary Coils

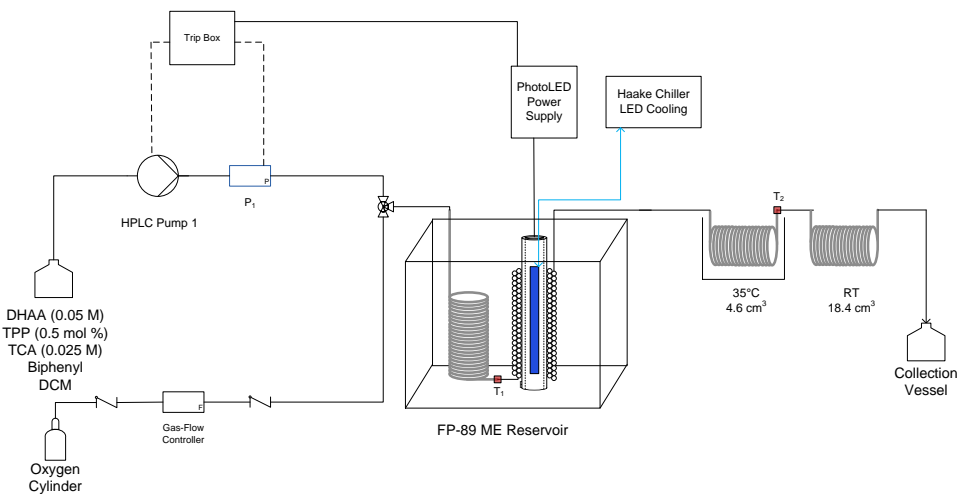


Figure 4.15: Schematic of the reactor set up for the continuous ‘one-pot’ synthesis of **18** using the double-layer ‘near-micro’ FEP reactor. The first secondary reaction coil is placed in a water bath and heated to 35°C.

To further push the thermal reaction to completion, the first of the secondary reaction coils was heated to 35°C. This improved the formation of **18**, albeit slightly, producing an initial yield of 11 %. This highlighted the effect of even a small increase in the coil temperature on the reaction. However, due to the volatility of DCM, temperatures exceeding 35°C cannot be used.

### 4.5.2. Adaptation of the Reactor to Facilitate Continuous ‘Two-Pot’ Synthesis of Artemisinin.

As discussed in Chapter 3, the semi-continuous ‘two-pot’ regime proved to be superior to the continuous ‘one-pot’ synthesis in terms of increased conversion, yield of **18** and

reductions in the yields of the main side-product, **19**. The semi-continuous regime is, however, laborious and impractical when considering implementation into a self-optimising system. Therefore, the set-up of a fully continuous ‘two-pot’ method was investigated.

A third Jasco® HPLC pump was placed after the photo-reactor in order that acid could be delivered and mixed with the stream after the photo-oxidation had taken place. Mixing occurred at a T-piece (Swagelok®, 1/8”), as shown in Figure 4.16. Additionally, the secondary heat exchange coil was quadrupled in volume from 4.6 cm<sup>3</sup> to 18.4 cm<sup>3</sup>. The set-up allows for the control of photo-oxidation in isolation from the conditions of the acidification, thereby allowing enhanced control of the reaction parameters compared to the more limited continuous ‘one-pot’ regime.

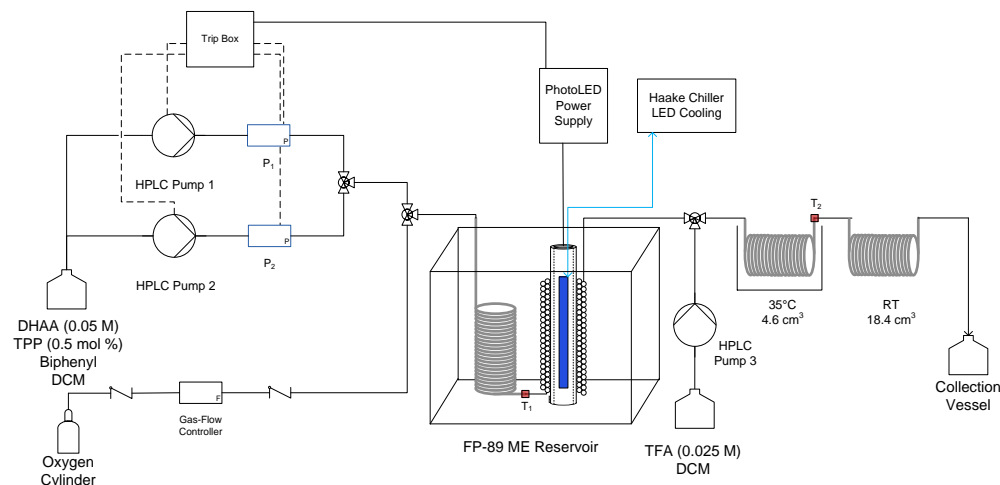


Figure 4.16: Schematic of the reactor set-up for the fully continuous ‘two-pot’ synthesis of artemisinin. A third HPLC pump has been added after the photoreactor to deliver the acid after the photo-oxidation has taken place.

The initial observation made from the preliminary continuous reaction was the colour change of the photoproduct from purple to green upon interaction with the acid flow; indicating the protonation of TPP. The resulting protonated plugs possessed no colour gradient, showing efficient mixing of the two streams.

The first sample analysed *via* HPLC was collected after 70 minutes of reaction time. No signal relating to **18** in either the UV or the ELS was observed. Small peaks were found in the ELS eluting between 2.99 and 4.23 minutes that have been previously observed and reported. The peak at 2.99 minutes in the ELS was also found in the 210 nm, resulting in a strong signal at 2.69 minutes. The sample was left within the injection syringe for 30 minutes before sampling again. The second injection showed the same

peaks as the first as well as a new peak arising at 7.43 minutes in the 210 nm, similar to the unknown peak previously reported, although this peak did not exhibit an ELS response. **18** was detected at 9.05 minutes in the 210 nm, albeit at a concentration too low to elicit a response in the ELS.

The remaining solution was placed in a stoppered vial and stored at -20°C for 16 hours. The resulting spectrum showed significant decreases in the early eluting compounds with only one signal at 3.83 minutes in the ELS, while the large peak previously eluting at 2.69 minutes in the 210 nm was not found. There was also a total decrease in the unknown peak at 7.43 minutes in the 210 nm, while **18** increased in the UV from an area of 161 to 483, and formed an amount sufficient to produce an ELS response with an area of 234.

<sup>1</sup>H NMR analysis was conducted on samples collected after 45 and 75 minutes. These showed high variation in the yield of **18** with values of 25% and 39% for the 45 and 75 minute samples respectively. Typically the variation in **18** coincides with a similar variation in the yield of **19**; however this value remains constant at 7% between the samples. A previously unobserved downfield signal at 6.29 ppm was found in both samples. This peak decreased from a relative yield (measured as 1-H) of 12 % in the earlier sample to 2 % in the latter, coinciding with an increase in **18**. This suggests that this peak could belong to an intermediate in the formation of **18**. NMR studies carried out in our group, and discussed in Chapter 3, have indicated that **19** ( $\delta$  = 6.08 ppm) converts to an enol ( $\delta$  = 6.24 ppm in THFd<sub>8</sub>-D<sub>2</sub>O); this enol intermediate could give rise to the signal at 6.29 ppm (CDCl<sub>3</sub>). The level of **19** indicates that the second stage of the reaction is slightly oxygen deficient, while the formation of **20** is enhanced due to the use of TFA *versus* TCA.

Table 4.4: <sup>1</sup>H NMR yields from the duplicate analysis of product after the continuous 'two-pot' synthesis of artemisinin. The common issue of signal overlap from the acid prevented the DHAA signal from being accurately quantified in Sample 1.

Sample Time / min	Conversion / %	<b>18</b> / %	<b>19</b> / %	<b>20</b> / %	6.29 ppm / % (as 1-H)
45	-	25	7	7	12
75	93	39	7	8	2

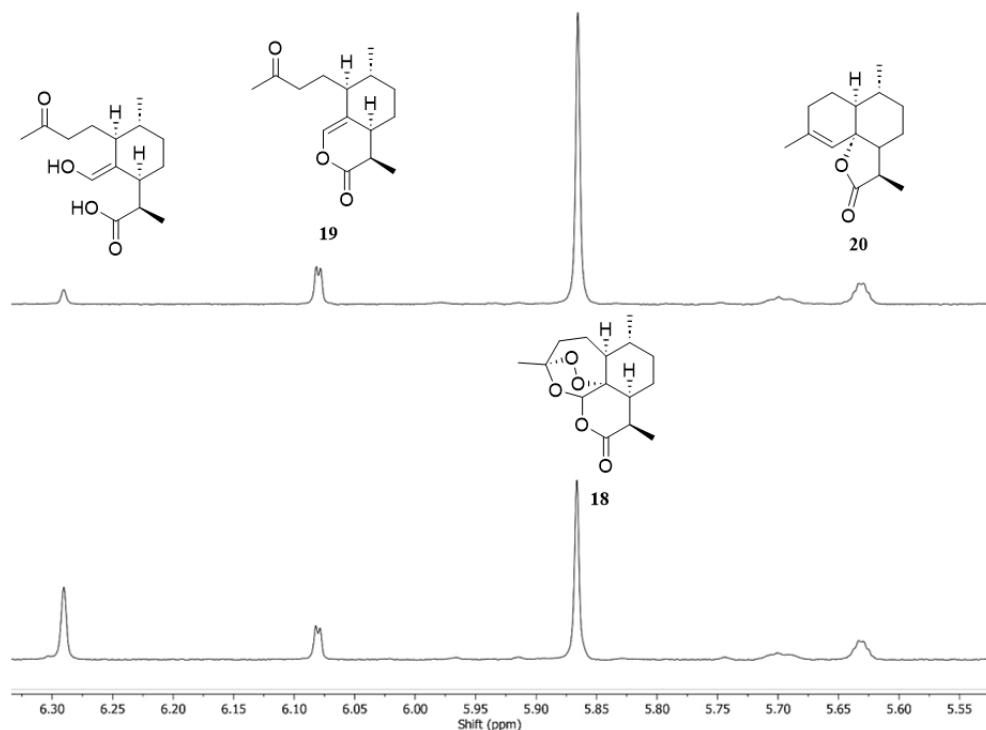


Figure 4.17: Stacked <sup>1</sup>H NMR spectra. Bottom: Sample analysed after 45 minutes reaction time. Top: Sample analysed after 70 minute reaction time, showed an increased signal of **18**. **19** and **20** remained consistent while the unknown peak at 6.29 ppm that may potentially belong to the enol intermediate shown decreased in signal.

The reaction was then repeated at a photoreactor temperature of -80°C. The initial injection showed an improvement in the formation of **18**, albeit very slight, with an area of 34 in the UV but response in the ELSD. The same early eluting peaks were found, with the peak around 2.70 minutes in the UV possessing a large area of 6058. An injection made 40 minutes after the initial from the same syringe showed a reduction in this peak to an area of 436, while the artemisinin peak increased to 506 in the UV and produced a signal of an area of 245 in the ELSD. Comparing the continuous reactions performed at 20°C and at -80°C, it can be seen that the low temperature synthesis is superior in forming **18**. At low temperature a greater concentration of **18** is formed after 40 minutes of sampling than is formed overnight for the room temperature synthesis.

The continuous ‘two-pot’ synthesis is clearly subjected to the same pitfalls found with the continuous ‘one-pot’ and semi-continuous ‘two-pot’ regimes. The formation of **18** after the acidification is slow, with full formation not being achieved within the reactor itself.

Table 4.5: Peak areas of the unknown intermediate and artemisinin with subsequent injections from the fully continuous synthesis of artemisinin at 20°C and -80°C.

Relative injection time / min	20°C			-80°C		
	Intermediate		Artemisinin	Intermediate		Artemisinin
	2.70 min (210 nm)	210 nm	ELSD	2.70 min (210 nm)	210 nm	ELSD
0	5129	-	-	6058	34	-
15	-	43	-	-	-	-
40	2967	161	-	436	506	245
16 hr	53	483	234	-	-	-

The unknown peak at 2.70 minutes in the UV gradually decays as the time of injection increases, eventually to a negligible value of 53 for the sample left in solution over 16 hours at -20°C. The artemisinin peak area correspondingly gradually grows with injection time. The results from the low temperature synthesis highlight the improvement in artemisinin formation under these conditions.

#### 4.5.3. Varying Acid Concentration

To further increase the formation of **18** in the continuous ‘two-pot’ reactor, the concentration of the acid delivered was increased. The corresponding peak areas of **18** and **14** in the UV were compared, and are shown in Table 4.6, highlighting the increase in the initial yield with the concentration of acid.

Table 4.6: Artemisinin and DHAA peak areas in the 210 nm detector with varying concentrations of TFA and TCA. As expected an increase in the acid concentration leads to an increase in the initial artemisinin yield.

Molar Equivalents of Acid	Artemisinin Peak Area (210 nm)		DHAA Peak Area (210 nm)	
	TFA	TCA	TFA	TCA
			31724 (S.M)	30214 (S.M)
0.5	34	95	700	1672
1	158	233	0	428
2	485	301	0	0

The peak areas of **14** show the level of conversion increases with the acid concentration. This infers that the acid is having an effect on the unconverted **14** after the photoreactor. The acid is delivered in equal volume in all experiments. Therefore, the decrease in peak size is not due to a dilution effect. The photo-oxidation step should be relatively consistent in all three reactions. Therefore the amount of **14** should also be identical. If the acid is only taking part in the Hock Cleavage of the hydroperoxides, then it would be expected that the peak of **14** would remain unchanged. This is not the case, and either the acid is aiding in the conversion of **14** to **18** after the photoreactor, or is reacting with **14** to form side products.

The results from the two investigations, exhibited in Figure 4.18, show that over the range of 0.5 – 1 equivalents of acid, TCA produces a greater initial yield of **18** than TFA. However when the concentration is increased to 2 equivalents, TFA outperforms the TCA. However, as has already been shown, TFA produces a higher amount of dihydro-*epi*-deoxyarteannuin B, **20**, than when TCA is used. Therefore, despite seemingly improved initial yields of **18**, the final concentrations are likely to be inferior when using TFA at a high concentration.

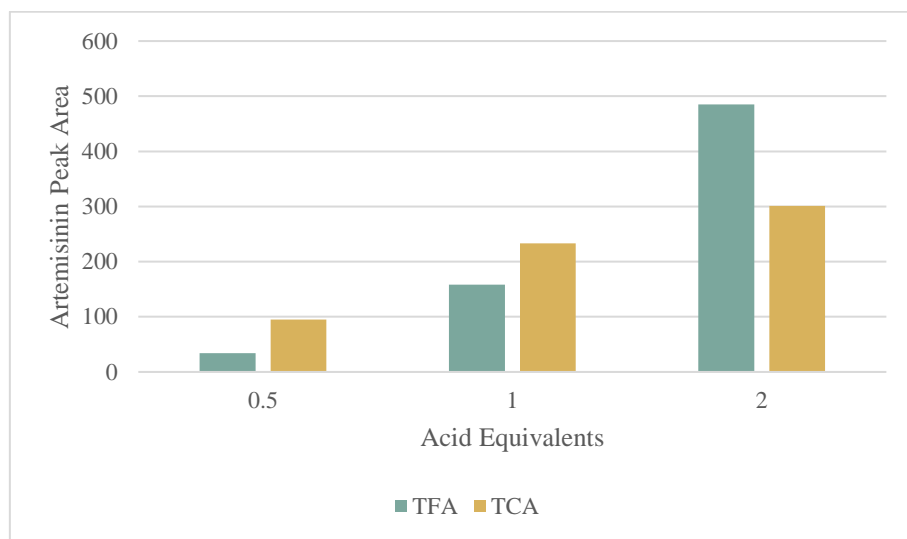


Figure 4.18: Comparison of the effect of the concentration of TFA and TCA on the formation of artemisinin injected immediately after sampling. Note how at the lower acid concentrations TCA performs better than TFA, this is then reversed at the higher acid concentration of  $0.1 \text{ mol dm}^{-3}$  (2 equivalents). Photo-oxidations were performed with the double layer FEP (1/32" i.d. volume  $7.54 \text{ cm}^3$ ) photoreactor at  $-80^\circ\text{C}$ , with the 424 nm PhotoLED. Acid was delivered via a HPLC pump placed after the photoreactor and prior to a heated coil ( $4.6 \text{ cm}^3$ ) at  $35^\circ\text{C}$  and subsequent coils ( $18.4 \text{ cm}^3$ ) without heat control.

#### 4.5.4. Reactions in Toluene

In further efforts to drive the reaction to completion, dichloromethane was replaced with toluene. Toluene, with a high boiling point of  $110.6^\circ\text{C}$ , allows for the secondary thermal stage of the synthesis to be carried out at elevated temperature. By placing the secondary reaction coil, after addition of the acid, in a heated oil bath, the Hock Cleavage and oxidation steps can be accelerated. This would not be possible in DCM due to its low boiling point of  $39.6^\circ\text{C}$ . Furthermore, as discussed in Chapter 3, toluene was found by Kopetzki *et al.* to be superior to DCM in their ‘one-pot’ synthesis of artemisinin, primarily due to the reduction in polarity of toluene compared to DCM and, hence, the reduction in reaction side-products.<sup>8</sup> However, when tested at a photoreactor temperature of  $-70^\circ\text{C}$ , the back-pressure increased eventually tripping the system and

therefore, it was determined that toluene could not be used at very low temperatures in the current set up.

#### 4.5.4.1. Semi-Continuous ‘Two-Pot’ Synthesis in Toluene

A semi-continuous ‘two-pot’ reaction was conducted under standard conditions, with the secondary reaction undertaken at 50°C. This exhibited a high degree of growth of the **18** peak as observed in the ELSD. Figure 4.20 reveals that an amount of artemisinin below the limit of detection had been produced. As with previous observations of the spectra of injections made early on in the second stage of the synthesis of artemisinin, large early eluting peaks are again found in both the UV and ELSD. The most prominent of which gave strong signals at 4.67 and 4.97 minutes in the UV and ELSD respectively, eluting around the retention time of DCM, indicating that this peak is typically masked in the UV in previous experiments.

The injection of the product sampled 1 minute after acidification revealed a severe issue of the detection of **18** in the presence of toluene; not only do toluene and **18** co-elute, but toluene also presents a far larger peak with significant tailing, clearly masking the region of **18** elution, and potentially interfering with other analyte peaks.

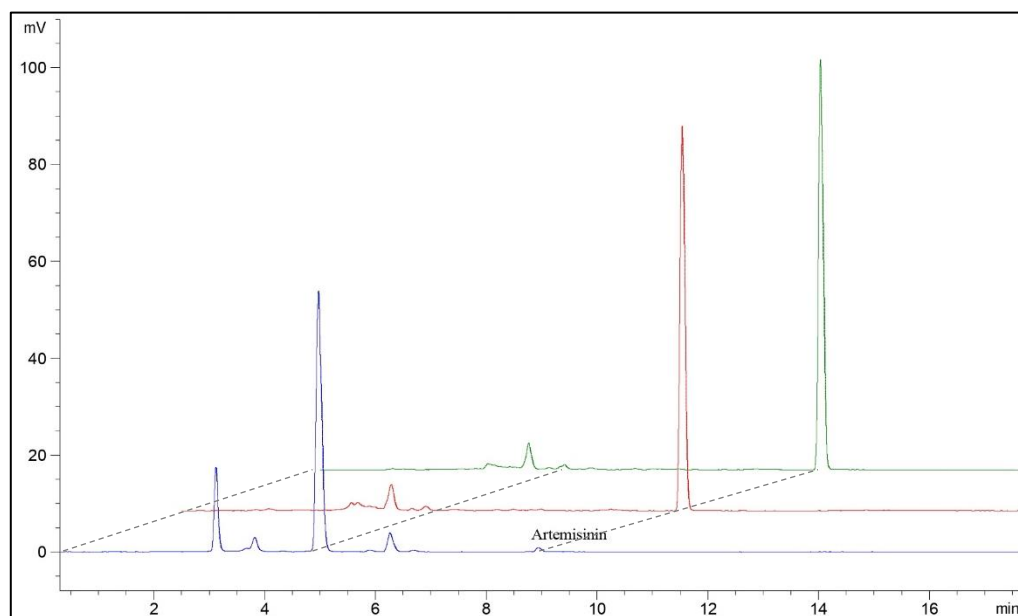


Figure 4.19: HPLC-ELSD chromatograms of the initial product injection after 1 minute. Here a small peak below the limit of detection with an elution time around 9 minutes has been assigned to artemisinin. The ELSD spectra of the solution samples after 40 and 60 minutes after the addition of TCA. The early eluting peaks are no longer present and the artemisinin peak has increased significantly.

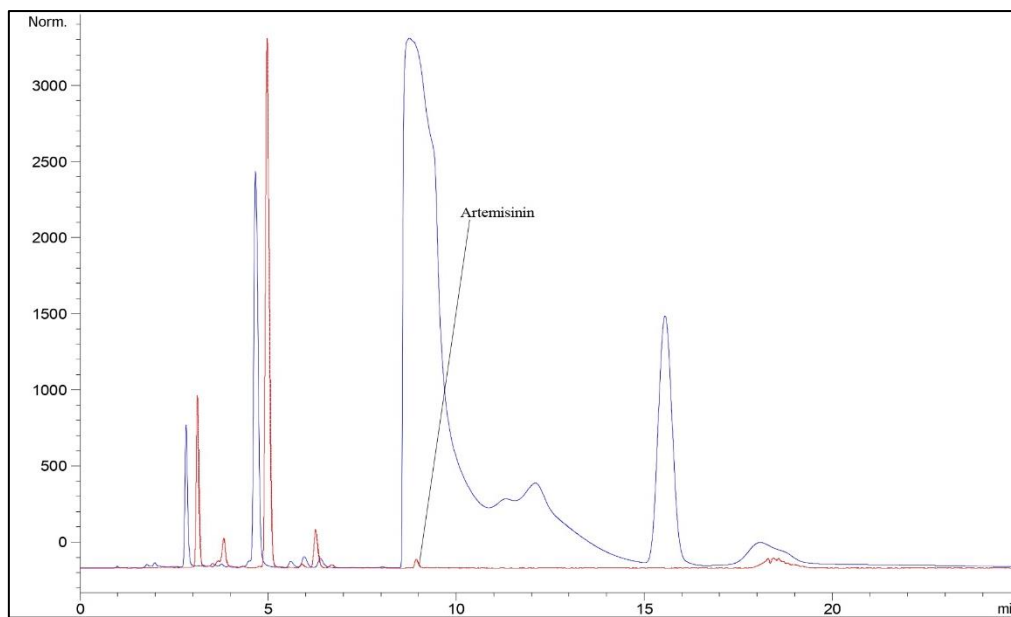


Figure 4.20: HPLC-210 nm chromatograms of the solution sampled immediately after the addition of TCA to the photoproduct. Toluene elutes slightly earlier than previously and overlaps the region of artemisinin elution with a strong tailing peak. A number of early eluting peaks can also be observed. The corresponding ELSD signal also shows these early eluting peaks along with a small peak attributed to artemisinin, clearly showed co-eluting with toluene.

Large, sharp artemisinin signals are present in both of the later samples, while the early eluting compounds have been mostly consumed. The only remaining peak in the ELSD around 3.80 minutes initially increase from an area of 21 in the first sample to 38 for both of the later injections. The artemisinin peak elution times are 9.04 and 9.03 minutes for the 40 and 60 minute injections respectively with peak areas of 509 and 518 corresponding to yields of 19.8 and 20.1 %. The closeness of these areas indicates that the reaction had reached completion prior to sampling at 40 minutes.

#### 4.5.4.2. Continuous ‘Two-Pot’ Reaction

The synthesis of **18** in toluene was then performed using the fully continuous reactor with the first secondary reaction coil heated to 50 °C. During the reaction, thermocouples T<sub>1</sub> and T<sub>2</sub> registered -47°C and 25°C respectively, the heated coil having only a small effect on the temperature of the solution.

<sup>1</sup>H NMR analysis revealed a conversion of 90 % and yields for **18** of 51 %, **19** of 4 %, and **20** of 3 %. The lower yield of **19** when compared to the earlier continuous reaction in DCM indicates that the reaction in toluene is less oxygen limited. This is consistent with the higher solubility of oxygen in toluene *versus* DCM.<sup>125</sup> The initial HPLC injection showed a promising, albeit small, amount of **18**, above the limit of detection. As with previous experiments, **18** formation continues in the solution left in the

injection syringe; this fact along with the detection of the intermediate peaks within the initial ELSD spectra which reduce with subsequent injections, is explicit evidence that the reaction has not reached completion at the time of sampling.

*Table 4.7: ELSD peak areas for the intermediate compounds and artemisinin (RT = 9.30 minutes) for the subsequent injections of the product sample into the HPLC.*

Relative injection time / min	Peak Retention Time / min				
	3.1	3.9	5.1	6.5	9.3 (artemisinin)
0	127	88	129	17	51
30	94	41	0	15	863
55	47	45	0	0	997

*The peak areas of the intermediates decrease as the area for artemisinin increases significantly. The retention times listed refer to the peaks detected in the initial t=0 HPLC spectra that is also shown in Figure 4.21: HPLC-ELSD spectra of the Initial injection of the product from the continuous synthesis of artemisinin in toluene at -50°C. A sharp peak for artemisinin is found with a retention time of 9.29 minutes. The commonly observed intermediate peaks are also present. The spectra of the solution after being left in the injection syringe for 30 and 55 minutes after the first injection. The artemisinin peak eluting 8.939 minutes has increased significantly, while the early eluting peaks have decayed.*

Doubling the volume of the heated coil to 9.2 cm<sup>3</sup> further aided formation, producing an initial artemisinin peak with an area of 93. This is still far from a completed reaction. The peak of **14** in the ELSD was of such a width that it was not quantified by the detector. Adjustments were subsequently made to the mobile phase composition to allow for earlier elution of **14** and hence to produce a more resolved, symmetrical peak shape, thus aiding detection. Earlier elution also reduces the method length, a significant benefit when implementing into a self-optimised system that requires many experimental iterations. A gradient mobile phase was then developed to enhance the elution of **14**.

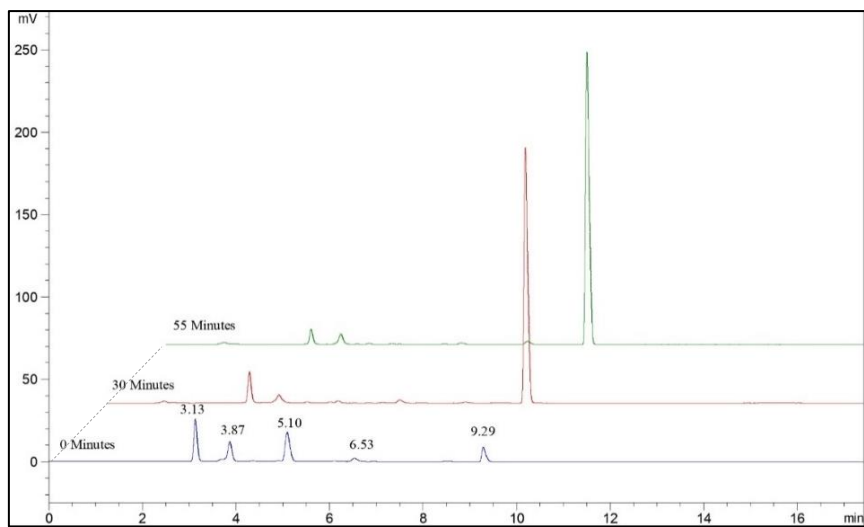


Figure 4.21: HPLC-ELSD spectra of the *Initial injection* of the product from the continuous synthesis of artemisinin in toluene at  $-50^{\circ}\text{C}$ . A sharp peak for artemisinin is found with a retention time of 9.29 minutes. The commonly observed intermediate peaks are also present. The spectra of the solution after being left in the injection syringe for 30 and 55 minutes after the first injection. The artemisinin peak eluting 8.939 minutes has increased significantly, while the early eluting peaks have decayed.

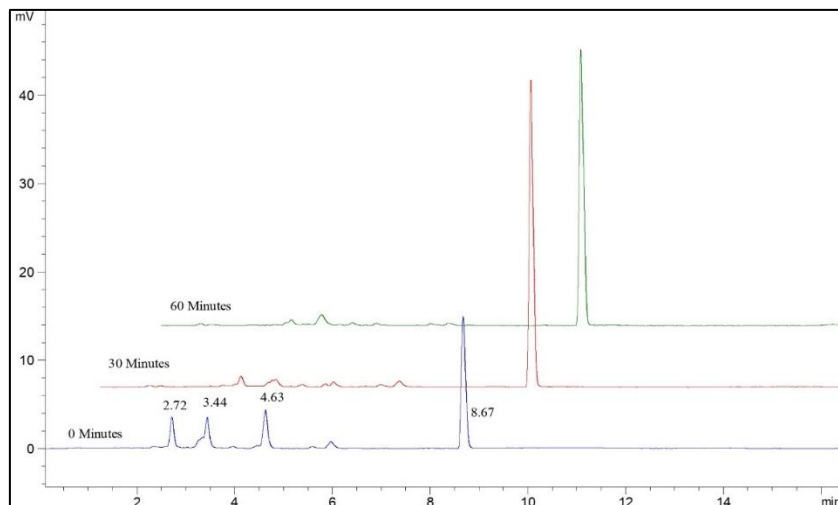


Figure 4.22: HPLC-ELSD spectra of solution analysed *immediately* after collection. The area of the artemisinin peak is greater than previous experiments but still small with a value of 93. Samples left in the closed injection syringe were analysed after 30 and 60 minutes after the initial injection. Isocratic mobile phase of acetonitrile : 0.1% acetic acid 60:40 (v/v %),  $1.0 \text{ mL min}^{-1}$  with a column temperature of  $40^{\circ}\text{C}$ .

The reaction was then repeated reducing the flow rates by half. The initial sample peak area for artemisinin (8.98 minutes, Figure 4.23) was measured to be 241, a large improvement on the area of 93 for the previous experiment. These areas can be compared; despite the change in flow rates, they have been scaled such that the dilution effect of the acid stream is equal in both cases.

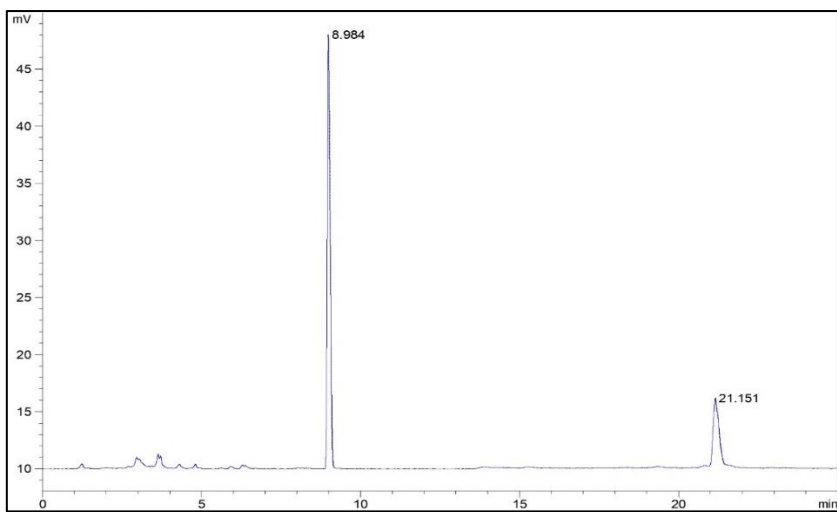


Figure 4.23: HPLC-ELSD spectra of the photoproduct of the continuous synthesis of artemisinin carried out at the lower substrate and oxygen flow rates of 0.5 and 5  $\text{m L min}^{-1}$ . TCA was delivered at 0.25  $\text{m L min}^{-1}$  giving 0.5 equivalents. Artemisinin produced a peak eluting at 8.984 minutes with an area of 241. The gradient mobile phase allowed for the good resolution and shape of the DHAA peak eluting after 21.151 minutes, this was measured to have an area of 78. Gradient mobile phase as stated in Table 5.28.

The reactions carried out in toluene were then repeated in dichloromethane at a photoreactor temperature of -50 °C. Due to the low boiling point of DCM, the oil bath housing the heated coils was reduced from 50°C to 35°C. The ELSD peaks of artemisinin from the sample run immediately after collection revealed peak areas of 18 and 313 for the substrate flow rates of 1.0 and 5.0  $\text{m L min}^{-1}$  respectively. These results highlight an improvement in the formation of **18** at the lowest flow rate when in DCM; for comparison, the area in toluene under these conditions was 241. Furthermore, NMR analysis of the products revealed 99 % conversion for both the DCM runs, while only 90 % was achieved previously in toluene.

Table 4.8: NMR analysis of the photoproduct from the continuous synthesis of artemisinin in dichloromethane.

Substrate / $\text{m L min}^{-1}$	Conv. / %	18 / %	19 / %	20 / %
1	$99 \pm 1$	$55 \pm 1$	$1 \pm 1$	$7 \pm 1$
0.5	$99 \pm 1$	$51 \pm 1$	0	$8 \pm 1$

Biphenyl was used as an internal NMR standard. Samples were submitted in  $\text{CDCl}_3$ , in triplicate and the error calculated to a 95% confidence interval.

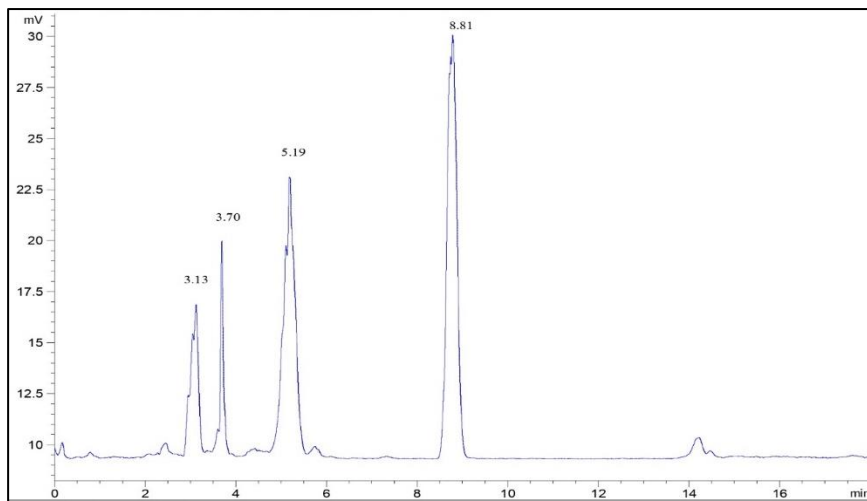


Figure 4.24: ELSD spectra of the photoproduct of the fully continuous synthesis of artemisinin in DCM carried out at the lower substrate and oxygen flow rates of 0.5 and 5  $\text{m min}^{-1}$ . TCA was delivered at 0.25  $\text{mL min}^{-1}$  giving 0.5 equivalents.

#### 4.5.5. Addition of the Vortex Reactor

The heated coils have been replaced by a small vortex reactor to aid in the Hock cleavage and oxidation of the tertiary hydroperoxide. The Vortex reactor, developed in our group, and discussed in Section 1.6.2, uses a rapidly rotating stainless steel cylinder (50 - 4000 rpm) to generate Taylor vortices for continuous flow thermal and photochemical reactions, primarily photo-oxidations.<sup>79</sup> The generation of vortices enhances mixing and thus enables rapid mass transfer between the gas and liquid phase.

The electrochemical used for this research Vortex is constructed using steel and graphite electrodes, the steel rod is the rotating cathode (length 201 mm, diameter 19 mm) and the graphite anode is the outer tube (length 175 mm, 31.7 mm o.d). A PEEK base and cap are used to ensure the electrodes are electrically isolated from one another. The graphite tube is sealed into these PEEK fittings with O-rings. Inlet and outlet tubes fixed into the PEEK base and cap allow the solution to be pumped through the reactor. The steel rod is rotated *via* a belt drive. The use of this type of Vortex was due to lack of availability of the other Vortex reactors, while there is no need for light in the reaction being accelerated in the reactor. The Vortex reactor was connected to the low temperature photoreactor, initially replacing the heated coils. The outlet of the vortex is connected to a peristaltic pump, as shown in Figure 4.25. The pump is required to be set to a flow rate greater than the overall reaction flow rate to draw the solution through the outlet. If the pump is not set to an appropriately high value, the solution can leak through the top of the reactor.

#### 4.5.5.1. Continuous ‘One-Pot’ Synthesis of 18 with the Vortex

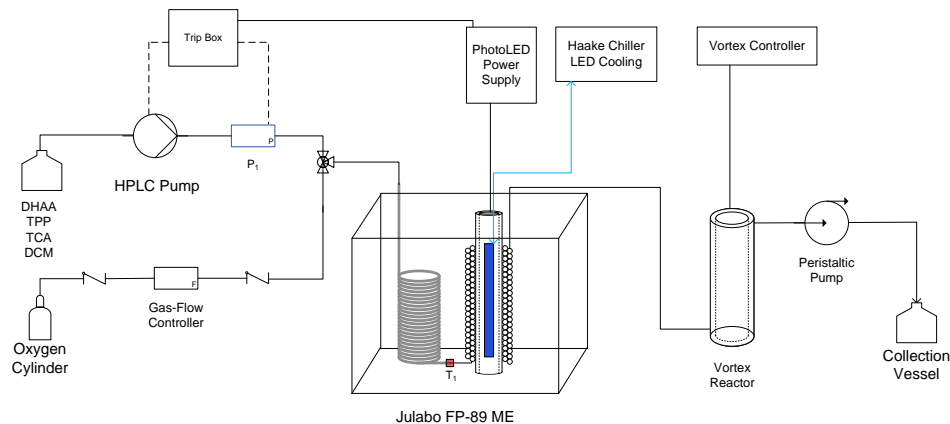


Figure 4.25: Schematic of the reactor set-up for the continuous synthesis of artemisinin. Upon exiting the photoreactor the photoproduct stream enters the bottom of the vortex reactor through a 1/8" o.d screw fitting. To prevent the solution from leaking out of the top seal of the reactor, a peristaltic pump is attached to the outlet to effectively pull the solution out.

To test and assess the impact of the Vortex, a ‘one-pot’ synthesis was performed under the typical conditions at a photoreactor temperature of -80°C. The Vortex was set to the maximum rotation speed of 4000 rpm. HPLC analysis revealed highly promising results. The initial injection exhibited a relatively large peak of **18**, with areas of 730 and 1093 for the ELSD and 210 nm respectively. Small peaks were detected for the intermediates, showing the positive effect of the vortex in driving the reaction through the transition stage and mostly forming artemisinin. NMR analysis of the  $t_0$  sample showed a conversion level of 91 %, and yields of 52 % and 6 % for **18** and **20** respectively. No signal was present for **19**, indicating that the system is not oxygen deficient, this is expected due to the high mixing capabilities of the Vortex.

The HPLC results from this investigation are particularly significant due to the fact the injections into the HPLC were made using the 1  $\mu$ L sample loop as opposed to the 5  $\mu$ L that was used for the previous investigations in Section 4.5.4. The switch from the 5  $\mu$ L to the 1  $\mu$ L is detailed in Chapter 5. Furthermore the nitrogen flow rate of the ELSD was set to 2.25 SLM (standard litres per minute), rather than 2.0 used for the earlier reactions, an increased flow of N<sub>2</sub> will diminish the peak size.

Table 4.9: Artemisinin ELSD peak areas after the 'one-pot' synthesis using the Vortex reactor to aid the formation of artemisinin.

Relative injection time / min	Artemisinin Area		DHAA	
	ELSD	210 nm	ELSD	210 nm
0	730	1093	128	3654
23	1030	990	200	-
62	2733	902	170	3192

The 'one-pot' synthesis was carried out under standard conditions in DCM in the double layer FEP (1/32 ", volume 7.54 cm<sup>3</sup>) photoreactor with the 424 nm PhotoLED at a temperature of -80°C. Substrate and oxygen were flowed at rates of 1.0 and 10.0 mL min<sup>-1</sup> respectively. The ELSD was operated under the following parameters; Nebuliser and evaporator at 40°C, N<sub>2</sub> at 2.25 SLM and the LED at 100%. HPLC injections were made using the 1 μL sample loop.

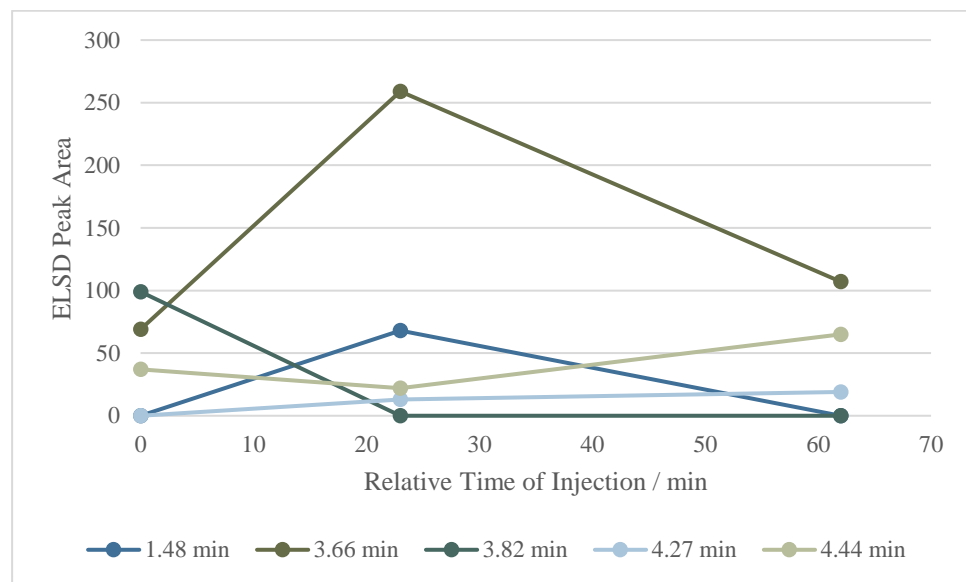


Figure 4.26: ELSD peak areas of the early eluting compounds, some decay as the injection time increases indicating their identity as reaction intermediates while others appear to grow, these may therefore belong to terminal reaction products such as the 6-lactone and dihydro-epi-artemisinin B.

Again, significant discrepancy between the two detectors is observed. With subsequent injections the ELSD exhibits increasingly large **18** peak areas while conversely, the 210 nm decreases. It is most likely that the deviation is due to issues of variation with the ELS detection rather than the UV which typically appears to be more precise. The reduction of the **18** with the UV rather than growth is unexpected, and could indicate that at the reaction profile has reached full artemisinin formation at the time of sampling.

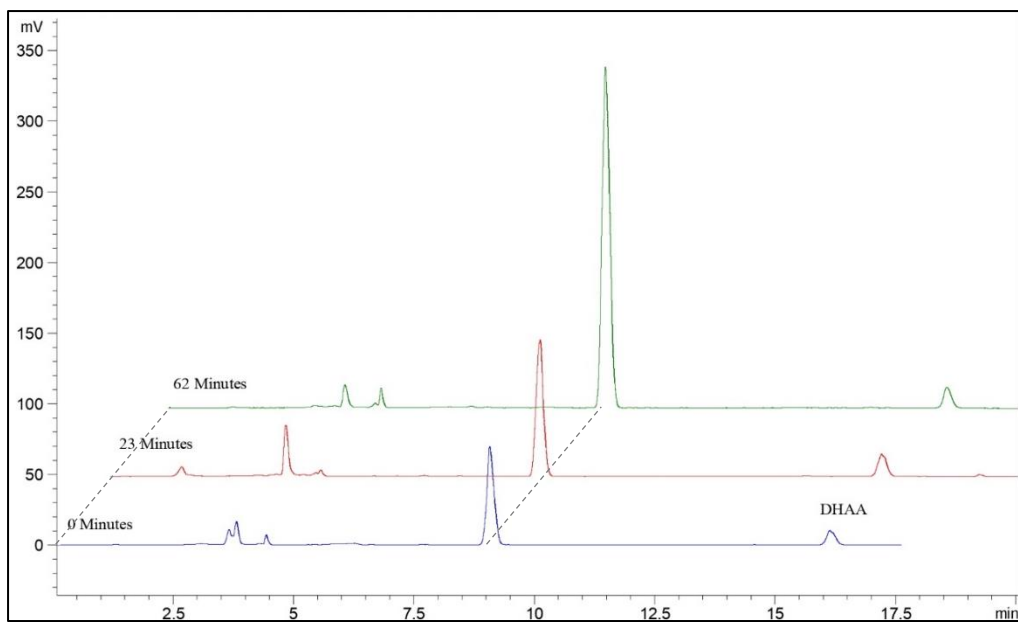


Figure 4.27: ELSD chromatograms of the initial photoproduct sample after the 'one-pot' synthesis of artemisinin using the Vortex reactor (4000 rpm). A significant artemisinin peak is detected at a retention time of 9.073 minutes with a peak area of 730. The 1  $\mu$ L sample loop was used for injections into the HPLC, while the ELSD parameters were set to 40/40°C for the nebuliser and evaporator,  $N_2$  at 2 SLM and the LED at 100 % intensity.

#### 4.5.5.2. Continuous 'Two-Pot' Synthesis of **18** with the Vortex

The reactor was then set up for the continuous 'two-pot' synthesis of **18** with the vortex reactor as shown in Figure 4.28. The standard regime was followed with a photoreactor temperature of -80°C; TCA was delivered to the photoproduct stream to deliver 0.5 equivalents before the protonated plug flow entered the Vortex reactor set to 4000 rpm. After the first analysis, the Vortex rotation was reduced to 3000 rpm and the reaction repeated. NMR analysis of the 4000 rpm product revealed almost quantitative conversion of 98 %, with an **18** yield of 52 % and **20** yield of 8 %. As with the 'one-pot' synthesis with the vortex, no signal for the **20** was detected.

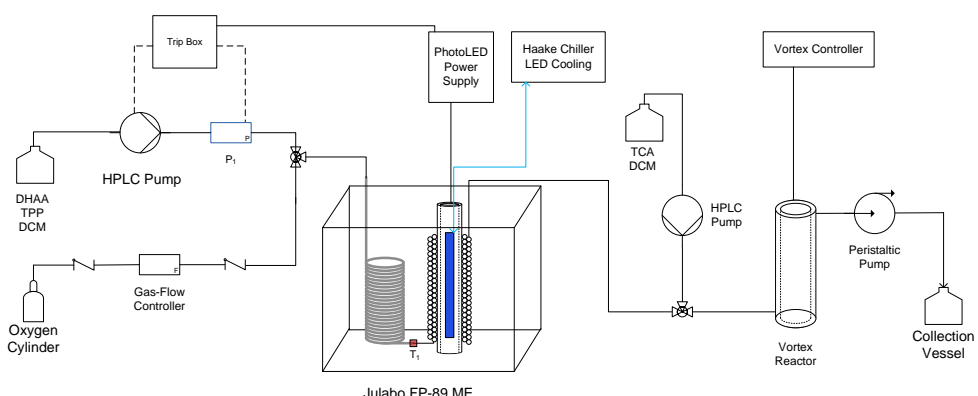


Figure 4.28: Schematic of the reactor set-up for the continuous 'two-pot' synthesis of artemisinin. The addition of the second HPLC delivers TCA in DCM before the vortex reactor.

Table 4.10: Artemisinin ELSD peak areas after the ‘two-pot’ continuous synthesis using the Vortex reactor.

Vortex / rpm	Relative injection time / min	Artemisinin		ELSD		
		ELSD	210 nm	3.60 min	3.80 min	4.40 min
4000	0	601	462	148	294	73
	0	975	447	141	163	90
	25	967	431	305	-	24
	60	1455	496	60		71

The synthesis was carried out under standard conditions in DCM in the double layer FEP (1/32 “, volume 7.54 cm<sup>3</sup>) photoreactor with the 424 nm PhotoLED at a temperature of -80°C. Substrate and oxygen were flowed at rates of 1.0 and 10.0 mL min<sup>-1</sup> respectively. TCA (0.41 g in 50 mL DCM) was delivered at 0.5 mL min<sup>-1</sup> to provide an acid equivalence of 0.50. The ELSD was operated under the following parameters; Nebuliser and evaporator at 40°C, N<sub>2</sub> at 2.25 SLM and the LED at 100%. HPLC injections were made using the 1 μL sample loop.

Relatively large peak areas were once again observed for **18**, albeit lower than the ‘one-pot’ due to the dilution effect of the additional acid stream. The ELS data revealed a that a slightly higher yield of **18** is obtained at a Vortex rotation of 3000 rpm, in opposition to the 210 nm which indicated a very slight decrease in yield at 3000 rpm. Due to the almost inappreciable difference between the UV response between the two rotation speeds, and the increase observed in the ELS for the lower speed, it was decided to select this for future experiments. This decision was also made in the consideration of longevity of the reactor itself: at 4000 rpm significant noise and heat is generated, while both of these factors are greatly reduced at 3000 rpm.

With the Vortex set to 3000 rpm, an experiment was initiated to assess the effect of increasing the acid concentration on the reaction outcomes. Unfortunately, as can be seen in Table 4.11, large discrepancies were once again found between the UV and ELSD measurements. The analysis of the 1 molar acid equivalent sample experienced a highly unusual issue with the UV detection, producing a far greater peak area than is possible. The extent of this phenomenon is reduced with subsequent injections. However, the UV peak areas, in particular, were higher than expected. The anomalous variation is clear when assessing the sample from a subsequent run of 2 acid equivalents on another occasion. The initial sample produced far smaller peaks for **18** in both the ELS and the UV, with a more realistic 210 nm peak of 1434. These results have once again highlighted the challenges that can arise with the detectors in use; of most concern, however, are the anomalies observed with the UV, which has normally been assigned as the most reliable of the detectors.

Despite the variation in the peak areas, a detail that can be assessed is the increase in intermediate and side-product formation when using the higher acid concentration. Two

new peaks eluting at 1.40 and 6.10 minutes have formed, indicating that the use of a high concentration of acid can lead to the prevalence of unwanted side reactions.

*Table 4.11: Results from the ‘two-pot’ continuous flow synthesis of artemisinin in DCM in the low temperature double-layer FEP (1/16” o.d, 1/32” i.d, volume 7.54 cm<sup>3</sup>) at -70°C with the Vortex reactor at 3000 rpm.*

H <sup>+</sup> / equiv	Relative injection time / min	Artemisinin		ELSD					
		ELSD	210 nm	1.40 min	3.10 min	3.60 min	3.80 min	4.40 min	6.10 min
1	0	1225	24521	-	40	579	8	91	-
	25	1410	10983	-	29	397	0	91	-
2	0	1202	8609	-	61	507	711	409	-
	25	2144	7797	19	37	492	222	188	39
2a	0	139	1434	-	91	144	454	149	-

*Substrate and oxygen were flowed at rates of 1.0 and 10.0 mL min<sup>-1</sup> respectively. TCA, 0.82 g in 50 mL DCM, and 1.64 g in 50 mL DCM, was delivered at 0.5 mL min<sup>-1</sup> to provide an acid equivalence of 1 and 2 respectively. The ELSD was operated under the following parameters; Nebuliser and evaporator at 40°C, N<sub>2</sub> at 2.25 SLM and the LED at 100%. HPLC injections were made using the 1 μL sample loop.*

During this investigation, severe flow issues were experienced with a photoreactor temperature of -80°C. These were alleviated at the higher temperature of -70°C, and the reactions repeated.

Despite the lack of absolute data in the form of product yields, these investigations have allowed for important conclusions to be drawn from the addition of the Vortex reactor: First, the Vortex has greatly improved the formation of **18** for both the continuous ‘one-pot’ and ‘two-pot’ methodologies. Moreover, NMR analysis showed no signals of **19**, a good indicator that the Hock Cleavage and secondary oxidation has sufficient oxygen to drive the enol-aldehyde equilibrium towards the enol and, hence, the formation of **18**.

## 4.6. Implementation of On-line Detection into the Automated Synthesis of **18**

The development of the calibrations of **18** and **14**, as discussed in Chapter 5, along with the reactor improvements discussed in Section 4.5, allowed for the continuous synthesis of **18** to be implemented into the automated system. To first test the automation, the more rudimentary approach of the ‘one-pot’ synthesis was conducted.

#### 4.6.1. Automated ‘One-Pot’ Reactions

The ‘one-pot’ synthesis of **18** requires the most basic set-up of the low temperature continuous flow reactor, thus providing the ideal basis for conducting the preliminary investigations into the reactor automation. The rig consisted of the typical low temperature photo-reactor of the double-layer ‘near-micro’ FEP housed within the fluid reservoir of the Julabo FP89-ME recirculating chiller, as shown in Figure 4.22. Secondary reactor coils were in place to provide additional residence time for the thermal reaction to take place. The vortex reactor was omitted to reduce the complexity of the system. Upon exiting the secondary reaction coils the product-gas plug flow enters the top of the gas-liquid separator (GLS, described in Chapter 5). The GLS allows for the separation of the collection of the product which is then transferred through the sample loop of the HPLC *via* a Gilson HPLC pump. The product is continuously pumped through the sample loop, which is then automatically triggered to inject the solution into the HPLC once the reaction is complete. The automated triggering of HPLC analysis provides a more accurate analysis of the product composition at the time of sampling. During manual injections there is a delay between sampling and injection of the product onto the HPLC, thereby allowing for the reaction composition to change in the meantime. Furthermore, the lack of delay between filling of the sample loop and initiation of the method greatly reduces variation in the analyte retention times.

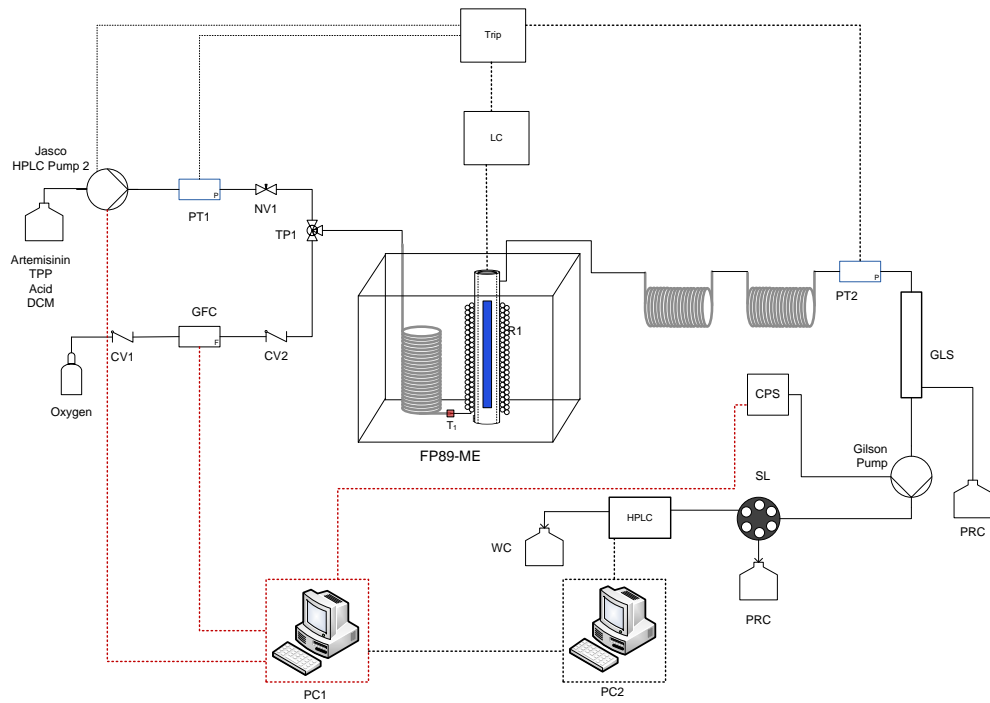


Figure 4.29: Schematic of the reactor set-up for the automated ‘one-pot’ continuous flow synthesis of artemisinin. Trip cables are indicated by black dashed lines. Computer connections are indicated as red dashed lines. Key: CPS – computer controlled power supply, CV – check valve, CY – gas cylinder ( $O_2$ ), HE – heat exchanger, HPLC – Agilent 1260 Infinity HPLC, GLS – gas-liquid separator, LC –LED controller, GFC – Gas flow controller, PT – pressure transducer, PC –personal computer, PRC – product collector, PU – HPLC pump, R – photo-reactor, S – sample reservoir, SL – HPLC sample loop, T – thermocouple, TI – temperature indicator, TP – T-piece, WC – waste collector.

To test the system, the most simple automation sequence was used. The ‘List’ method refers to a sequence of experiments in which each independent variable is pre-defined. The computer initiates the first experiment and upon successful completion, once all defined analytes have been detected and the yields calculated, the next experiment is automatically triggered. For the ‘one-pot’ synthesis of **18** the independent variables are defined as:

- Indepvar(1) = Reactor temperature in  $^{\circ}\text{C}$
- Indepvar(2) = Total substrate flow rate in  $\text{mL min}^{-1}$
- Indepvar(3) = Concentration of the substrate in  $\text{mol dm}^{-3}$
- Indepvar(4) = Molar ratio of oxygen to the substrate

Table 4.12: List run parameters. Parameters were chosen to adjust one at a time to test; (i) the detection of **18** and **14**, (ii) the coding of the calibration equations, and (iii) the ability of the reactor-computer combination to successfully trigger each run.

Run	Independent Variable			
	1 (reactor temperature) /°C	2 (total flow rate) / mL min <sup>-1</sup>	3 (substrate concentration) / mol dm <sup>-3</sup>	4 (molar gas ratio)
1	20	1	0.05	1
2	20	2	0.05	1
3	20	1	0.05	2

The three runs were successfully completed in sequence. In all three experiments **18** was successfully detected and quantified; this is key for triggering the next run. The results are shown below in Table 4.13. The difference and reduction in yield from Run 1 to 2 and 3 can be explained by the decrease in residence time of the runs along with incomplete formation of **18**; the latter being exacerbated due to the relatively short time between the photoreaction taking place and analysis.

The increase in conversion of the subsequent runs is unexpected. From Run 1 to 2, the only parameter changed is the liquid flow rate increasing from 1 to 2 mL min<sup>-1</sup>, it would, therefore, be anticipated that the level of conversion would be lower for Run 2. For Run 3, the molar gas ratio is increased. This is likely to increase the level of conversion, which was observed. The increase in gas ratio has the added effect of increasing the combined liquid-gas flow rate and, hence, reducing the residence time. Thus, the low yield of **18** may be explained through the reaction at the point of sampling being in an intermediate state, where full conversion to artemisinin has not been achieved.

Table 4.13. HPLC results from the computer-controlled list run synthesis of artemisinin.

Run	DHAA				Artemisinin			
	RT /min	Area (210 nm)	Calculated Concentration /M	Conversion /%	RT /min	Area (210 nm)	Calculated Concentration /mM	Yield /%
1	19.128	22980	0.0365	26.9	9.238	757	17.2	34
2	18.591	19135	0.0301	39.7	9.019	89	0.949	2.0
3	19.024	15352	0.0238	52.3	9.12	99	1.18	2.4

In all three experiments artemisinin was successfully detected and quantified, albeit with low yields in the final two reactions. The retention time of DHAA in run 2 was outside of the range defined within the MatLab script.

Table 4.14 shows a similar outcome to Table 4.13 with very low amounts of **18** being detected; in particular, the negative concentration calculated during Run 1. This value highlights an issue with detection of **18** at low concentrations. The 210 nm UV calibration equation at this point had an intercept value of 50; thus, any peak with an area below this value will result in an anomalous negative concentration.

Table 4.14: List experimental parameters and HPLC results.

Run	Independent Variable				DHAA			Artemisinin		
	1	2	3	4	Peak Area	Calculated Concentration /M	Conversion /%	Peak Area	Calculated Concentration /mM	Yield /%
1	20	1	0.045	1	7425	0.011	87.4	43	-0.168	0
2	20	0.5	0.045	1	17454	0.027	50.4	132	1.987	4.4
3	20	1	0.045	2	13673	0.021	64.3	95	1.096	2.4
4	- 20	1	0.052	2	17262	0.027	44.2	21.56	-	-
5	10	1	0.052	2	14144	0.022	54.2	50.118	0.0024	0.005

HPLC of the starting material was carried out to gain a more accurate value for the DHAA concentration. The DHAA peak returned a value of 28211 in the 210 nm, corresponding to a concentration of 0.045 mol dm<sup>-3</sup>. This value is then implemented into the “SubstrateConc\_high” line of code within the *indep2ctrl.m* script file.

As the reaction is reaching a steady state, the product solution is continuously being pumped through the HPLC sample towards a waste container, thereby allowing collection of samples from this stream. Sample from Runs 4 and 5 were collected prior to the automated HPLC analysis. These samples were run after the automated sequence had finished. The additional sample collected from Run 4 was injected onto the HPLC approximately 90 minutes after collection, exhibiting a 33% yield of **18**. The sample of Run 5 was injected 60 minutes after collection and yielded 31 %. These sample were also analysed *via* NMR with Run 4 yielding 34 % of **18** with a 49 % conversion and Run 5 giving a 27 % yield with 53 % conversion. These values correspond reasonably well with the conversion values in Table 4.13, and the yields from the delayed sample injections.

#### 4.6.1.1. Automated ‘One-Pot’ Synthesis using the Vortex

The addition of the Vortex reactor was made to improve the dynamics of the secondary thermal reaction, by providing enhanced mixing capabilities thereby improving the formation of **18**. At this point in the research internal standard calibrations in DCM for the quantification of **18** and **14** had been developed and, therefore, required implementing into the control scripts. A List sequence with manual operation of the Vortex rotation speed was completed successfully.

During Run 1, with the lowest Vortex rotation speed of 2000 rpm, a high level of conversion, 92.7%, was determined; however, no **18** was detected. The intermediate peaks were present while a small peak corresponding to artemisinin appears in the 210 nm spectra. Increasing the rotation speed results led to an expected increase in the yield of **18**. The increase in **18** peak area of approximately 1500 only translates to a yield increase of 4%; this shows the effect of solvent loss which is exacerbated due to the heat formed through the rotation of the Vortex reactor.

*Table 4.15: List run parameters. The independent variables are as follows; 1 – photoreactor temperature; 2 – substrate flow rate; 3 – starting material concentration; 4 – molar ratio of oxygen.*

Run	Independent Variable				Vortex /rpm	Peak Area				Calculated Conversion /%	Calculated Yield /%
	1 /°C	2 / mL	3 / mol min <sup>-1</sup>	4 dm <sup>-3</sup>		18	LA	14	TMB		
1	10	1.0	0.047	2	2000	-	835	2008	14658	92.7	-
2	10	1.0	0.047	2	3000	275	312	2154	16500	93.2	22.9
3	10	1.0	0.047	2	4000	1737	1541	2459	18631	93.1	26.7

The ELSD calibration of **18** used Lauric acid (LA) as the standard. The 210nm UV calibration of **14** used Trimethoxybenzene (TMB) as the standard. HPLC analysis of the starting material showed a concentration of **14** of 0.047 M.

The previous experiment's results once again highlighted the limitations of DCM with regards to driving the second stage of the reaction to completion. The reactor requires far greater volume and, therefore, residence time for the second stage to go to completion before entering the reactor sample loop. Replacing the Vortex with a larger version was not possible at the time. Therefore, in the interest of developing the reactor and reaction constituents that would allow for preliminary investigations of the automated process, the reaction solvent was swapped to toluene. As such, the second stage of the reaction can be heated to a reasonable degree to aid in driving the thermal reaction to completion.

Therefore, as with the investigations in DCM, an internal standard calibration in toluene was required. Due to the co-elution of **18** and toluene and the effect of the latter on the increased ELS selectivity of **18**, the previous calibration in DCM could not be used. The development an internal standard calibration for **18** and lauric acid in toluene proved to be difficult. The crux of the issue is finding the optimum mobile phase conditions and ELSD parameters that exhibit good sensitivity of the detector for each analyte without leading to saturation of the ELSD. Nevertheless, an internal standard calibration was completed in toluene.

An automated List run was initiated to test the set-up. However, severe disruption to the liquid – oxygen flow equilibrium occurred during the Run 1, performed at a photoreactor temperature of -40°C. Subsequent runs were initiated at temperatures up to ambient; however, these too led to the same flow issues. The higher viscosity of toluene in combination with the increased length of tubing and requirement to flow the solution through the Vortex reactor likely led to the need for elevated pressures from the gas-flow controller to maintain equilibrium; however, the gas-flow controller did not have the capacity to maintain the appropriate flow pressure.

#### **4.7. Issues with the Automated Synthesis of 18**

The preliminary investigations showed the successful implementation of On-line HPLC monitoring into the automated synthesis of **18**. The reaction was initiated at the desired photoreactor temperature and with the correct flow rates for the substrate and oxygen. All stages of the automated reaction were performed without error; the HPLC analysis was successfully initiated and the resulting spectra downloaded and interpreted by the computer. After determination of the yields of **18** and the conversion of **14** the subsequent runs were also successfully triggered with the updated reaction parameters. However, the automated analysis identified similar issues to those discussed in earlier sections - the negligible formation of **18** despite reasonable levels of conversion.

The addition of the Vortex reactor led to a marked improvement on the yield of **18**; however the values were still far lower than those produced using the semi-continuous methodology. The limitations of DCM in driving the secondary thermal reaction to completion were also found, this could be alleviated with the use of a larger Vortex reactor and increased residence time. The flow issues experienced when switching to toluene prevented the investigation into the combined use of the Vortex with elevated secondary reaction temperatures.

The limitations of the ‘one-pot’ synthesis have been regularly outlined in this Chapter and in Chapter 3. The use of this protocol provided a preliminary understanding into the abilities of the automated reactor. The continuous ‘two-pot’ set-up provides the level of reaction control that is required for the successful development of a self-optimising reactor for the synthesis of **18**. This reactor has been developed and discussed in this Chapter for manual control; however, due to the complexities found during the continuous synthesis of **18**, the development of the automated ‘two-pot’ reactor for **18** was halted. This work has provided some further understanding of the formation of **18**.

in flow, which has indicated that at present the reaction is still too complicated for self-optimisation.

To develop the reactor and to achieve the ultimate aim of conducting automated photo-oxidations, attention was turned to automating the continuous synthesis of rose oxide, **13**, from citronellol, **8**.

#### 4.8. Continuous Synthesis of Rose Oxide

The following work was completed with the aid of Mr. Jack Webb, and formed the basis of his Masters Research Project.

The issues encountered with the full formation of **18** in the continuous reactor, and the flow issues experienced when using toluene, resulted in attention being given to implementing the synthesis of rose oxide, **13**, into the automated continuous flow reactor. The photo-oxidation of **8** has been discussed in Chapter 2. During the early development of the low-temperature photoreactor, the Schenck-ene oxidation of **8** was found to have a selectivity dependence on the reactor temperature, albeit minor in comparison to the oxidation **14**. This reaction is fundamentally simpler than the synthesis of **18**, with the photo-oxidation providing two hydroperoxides, **9** and **10**, which upon quenching reduce to the corresponding diols, **11** and **12**. Addition of an acid results in only **11** cyclising to afford both the *cis*- and *trans*- isomers of rose oxide, **13**.<sup>156,157</sup>

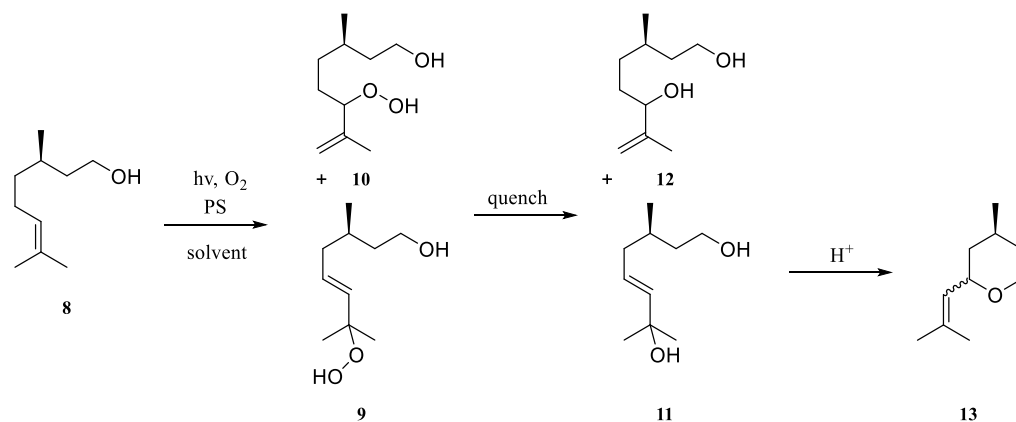


Figure 4.30. Scheme for the photo-oxidation of citronellol to the corresponding hydroperoxides. Followed by subsequent quenching to the relevant diols and acidification to produce the commercially relevant molecule rose oxide.

To first test the reactor the photo-oxidation of citronellol, **8**, was performed under standard conditions with varying temperature. The photo-oxidation resulted in near quantitative conversion, with ratios between 1.05 and 0.97 at -48°C and 10°C.

Table 4.16:  $^1\text{H}$  NMR yields from the photo-oxidation of citronellol at varying reactor temperatures using the low temperature narrow diameter FEP (1/16" o.d, 1/32" i.d, volume 7.54 cm $^3$ ) photoreactor.

Temperature	Conversion / %	9 / %	10 / %	Ratio 9:10
-48	99 $\pm$ 1	57 $\pm$ 3	55 $\pm$ 3	1.05
-20	99 $\pm$ 2	55 $\pm$ 3	55 $\pm$ 3	1.00
10	100 $\pm$ 0	55 $\pm$ 5	57 $\pm$ 4	0.97

#### 4.8.1. Semi-Continuous Synthesis of **13**

The semi-continuous synthesis of rose oxide was conducted to test the HPLC method detailed in Chapter 5. The reaction was performed with sodium sulphite to quench the hydroperoxides. The photo-oxidation was carried out at ambient temperature. HPLC analysis showed peaks eluting with retention times of 11.93 and 12.73 minutes, corresponding to *cis*- and *trans*-rose oxide, while only a small peak appears for citronellol with a retention time of 8.53 minutes. The reaction profile was also monitored by NMR. The ratio of hydroperoxides **9:10** was measured to be 0.95:1.00, while NMR of the reduced diols gave a ratio of 0.96:1.00, the spectra of which are shown in Figure 4.32. The photo-oxidation at ambient temperature showed a preference for the formation of the undesired hydroperoxide, **10**.

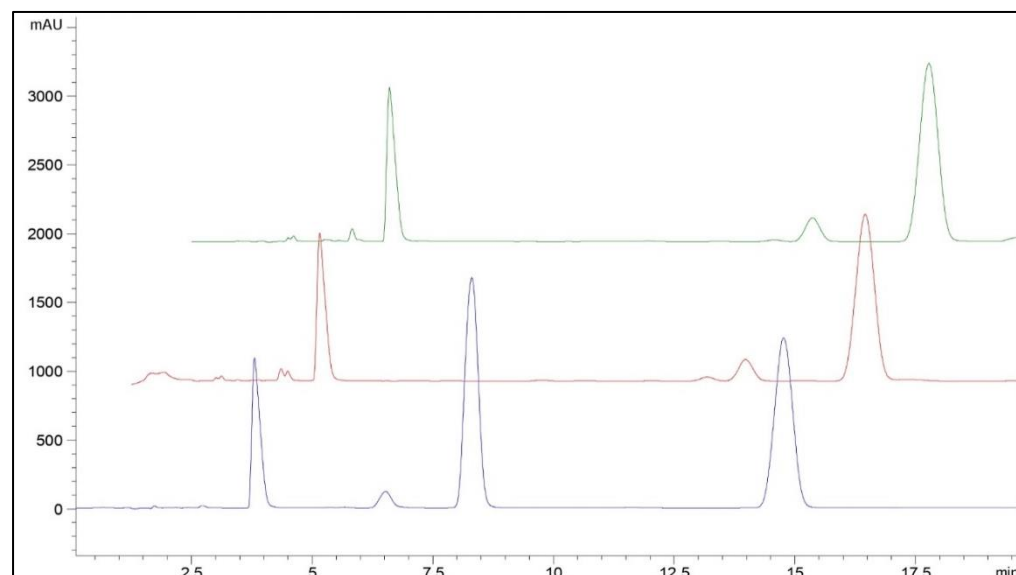


Figure 4.31: HPLC-210 nm chromatograms. *Starting material*, the strong peak eluting at 8.312 minutes is that of citronellol, while the peaks at 3.812 and 14.773 belong to the reaction solvent, DCM, and the

photosensitiser, TPP, respectively. *Post-quench and acidification* the peaks eluting at 11.931 and 12.727 minutes correspond to *cis*- and *trans*-rose oxide. The large peak with a retention time of 15.208 minutes is that of the photosensitiser, TPP, while the early peak at 3.905 minutes belongs to the reaction solvent, DCM. Only a small peak eluting at 8.526 minutes may be attributed to the starting material, citronellol. The product was allowed to stir for an additional 30 minutes with oxygen, the chromatogram is shown in green. The additional large peak found with an elution around 15 minutes belongs to biphenyl, used as an internal NMR standard.

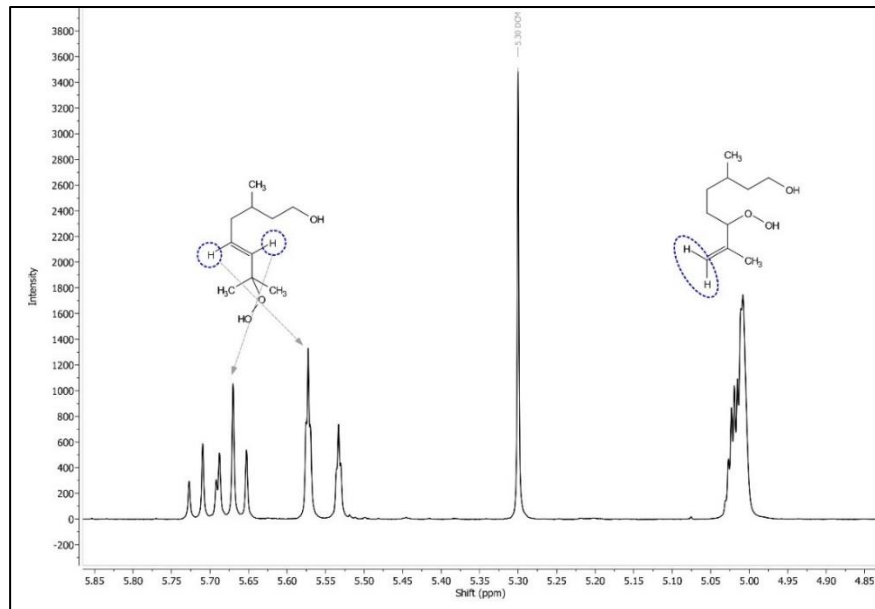


Figure 4.32:  $^1\text{H}$  NMR spectrum of the unquenched photo-oxidative product in  $\text{CDCl}_3$ .

#### 4.8.2. Continuous Synthesis of 13

To achieve the continuous synthesis of **13**, a fourth pump was added to the photoreactor previously developed for the synthesis of **18**. The fourth pump allows for the delivery of the quench solution after hydroperoxides have been produced in the photoreactor. The third Jasco® HPLC pump provided an acid stream to cyclise diols **11** to **13**. Due to limitations on the number of HPLC pumps available and to reduce the complexity of the system, it was decided that for the preliminary flow syntheses of **13**, the quenching solution should be delivered by peristaltic pump (Cole-Parmer Masterflex™) rather than a computer controlled HPLC pump. In this instance the, peristaltic would be manually set to an appropriate RPM to deliver a desired quantity of quenching solution.

To test the set-up and, specifically, the ability to quench the hydroperoxides in flow, photo-oxidation was carried out under standard ambient conditions. First, the product of the photo-oxidation was collected and analysed by  $^1\text{H}$  NMR. The quench stream was then delivered *via* the peristaltic pump. Figure 4.33 directly compares the spectra of the quenched and unquenched solution, showing a clear change in appearance and, in

particular, a shift in the signals. The broad multiplet of **10** ( $\delta$  4.98 – 5.03 ppm) splits into two signals ( $\delta$  4.81 – 4.85 ppm and  $\delta$  4.92 – 4.95 ppm), while the two olefinic signals of **9** merge into one signal ( $\delta$  = 5.55 – 5.65 ppm). The ratio of the two diols was measured to be 0.88:1.00. These shifts and the absence of signals belonging to the hydroperoxides, most easily seen through the full reduction in the signal for **10**, indicate that the quench in flow was successful.

A signal for **8** is observed in the NMR of the quenched product, while this is not found in the unquenched solution. As both photo-oxidations were performed under identical conditions with the same starting material it would be expected that the conversion would be identical. The observation of **8** could be an indication that upon exiting the photoreactor, full conversion is indeed not achieved in both reactions; however, as the quench immediately follows the photo-oxidation, any residual  $^1\text{O}_2$  or excited TPP are deactivated, while the diols and **8** are essentially locked. Whereas, for the unquenched product, residual  $^1\text{O}_2$  and TPP\* may continue the reaction with **8** to reach an apparent full conversion. Additionally, a small peak of *cis*-rose oxide is observed; this is likely due to residual acid present in the NMR solvent,  $\text{CDCl}_3$ , initiating the cyclisation of **9** to rose oxide. The cyclisation of **9** also somewhat explains the reduction in ratio between the two diols with respect to **9**.

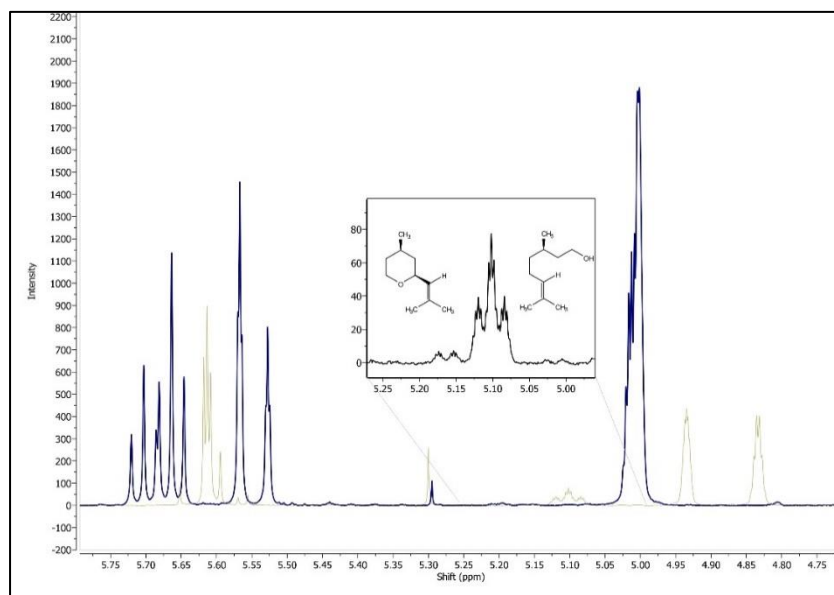


Figure 4.33: Stacked  $^1\text{H}$  NMR in  $\text{CDCl}_3$  of the unquenched hydroperoxide photoproduct and the diols after quenching with the stream of  $\text{PPh}_3$ . The change in appearance and shift of the peaks after quench with  $\text{PPh}_3$  indicates that the quench has occurred successfully in flow. The zoomed in view of the citronellol and rose oxide peak of the quenched solution is also shown.

Following on from the successful quenching of the hydroperoxides in flow, a preliminary investigation into achieving the cyclisation in flow was also initiated. The Jasco® HPLC pump was added after the quench reaction coil to deliver the acid stream. The subsequent solution exhibited a deep green colour, indicating protonation of the TPP and good mixing of the constituents in which no colour gradients were observed. However, no signals for **13** were determined through  $^1\text{H}$  NMR analysis of the resulting solution.

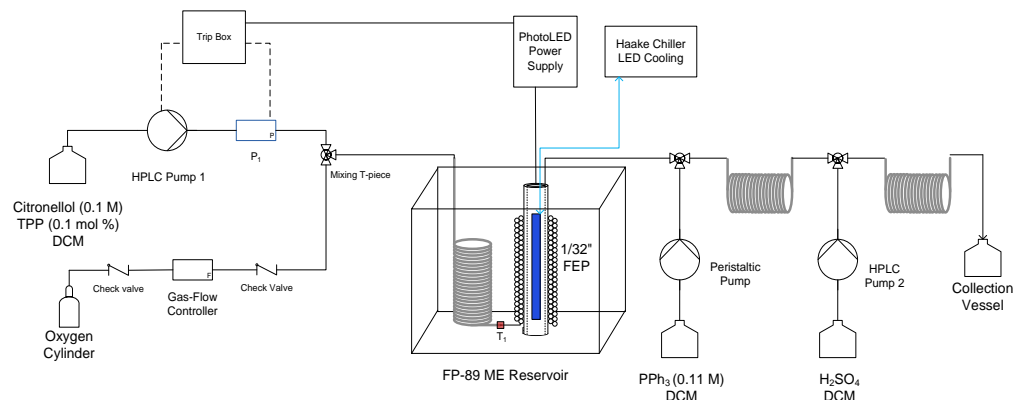


Figure 4.34: Schematic of the reactor set-up for the preliminary investigations into the full continuous synthesis of rose oxide. Photo-oxidation is carried out using the narrow diameter double-layer FEP (1/16" o.d., 1/32" i.d., volume 7.54 cm<sup>3</sup>) low temperature photoreactor. A quench solution of  $\text{PPh}_3$  was delivered at an equivalence of 1.1 M via a peristaltic pump set to 8 rpm, while a stream of sulphuric acid in DCM was provided by a HPLC pump at 1.0  $\text{mL min}^{-1}$ .

To follow the Dragoco synthesis of **13** more closely, methanol replaced DCM.<sup>156</sup> This also prompted a switch of photosensitiser to rose bengal, due to TPP's insolubility in methanol. The photo-oxidation was carried out under ambient conditions. An aqueous solution of sodium sulphite was used for the quench stream while an aqueous solution of  $\text{H}_2\text{SO}_4$  (5% v/v) initiated the cyclisation of **9** to **13**. HPLC analysis of the product revealed the peaks of *trans*- and *cis*-**13**, Figure 4.35, indicating that the quench and cyclisation were successful.

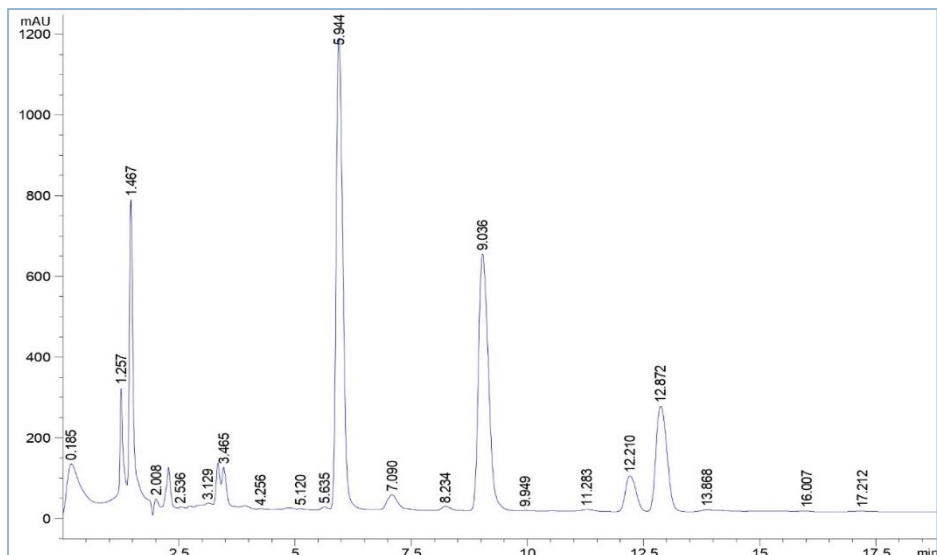


Figure 4.35 HPLC-210nm chromatogram of the product from the continuous synthesis of rose oxide in methanol. The product was collected before the appropriate equilibrium time had been completed due to significant increases in back-pressure as the reaction progressed, until a point in which the reagent solution leaked from the pump head of Jasco HPLC Pump 1. Despite the equilibrium time not being completed, the chromatogram indicates that rose oxide has been formed, via the peaks at 12.210 and 12.872 minutes, corresponding to *trans*- and *cis*-rose oxide respectively. The large peak at 5.944 minutes belongs to trimethoxybenzene, used as an internal NMR standard.

#### 4.8.3. Development of the Automated System for the Continuous Synthesis of **13**.

The previous investigations showed that the fully continuous synthesis of **13** in the low-temperature reactor were successful. The next stage of the investigation was to produce internal standard calibrations for the quantification of **8** and *cis*- and *trans*-**13**. The development of the internal standard calibration, with TMB, is discussed in detail in Chapter 5.

The set up for the automated synthesis of **13** is shown in Figure 4.36, includes the addition of the manually controlled peristaltic pump for the addition of the quench stream, as well as the computer controlled third HPLC pump for the delivery of acid. The control of the acid pump required an additional device driver to be added to the Labview reactor controller, along with the addition of two new control parameters, 14 and 15, in the indep2ctrl.m script. Control parameter 14 determines the flow rate of the pump depending on: i) the acid molar ratio, set within the experiment file, ii) the acid concentration of the acid feed, set in indep2ctrl.m, and iii) the concentration of the substrate and the substrate flow rate. Control parameter 15 simply turns on or off the pump depending on whether a reaction is running or not. Independent variable 5, the

molar ratio of acid, has been added into the script file and can be set within the experiment file.

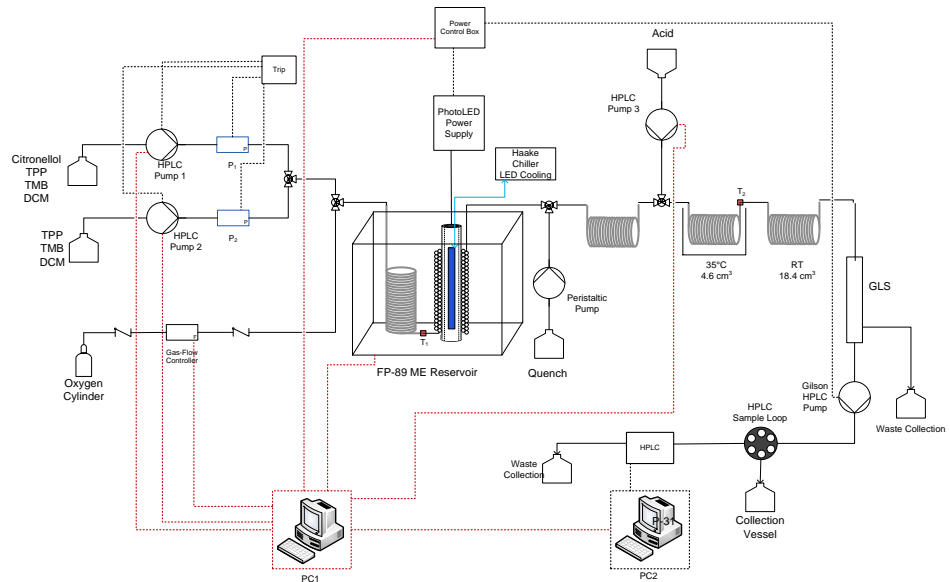


Figure 4.36: Schematic of the reactor set-up for the fully automated continuous flow synthesis of rose oxide using the low temperature photoreactor.

#### 4.8.4. Computer Controlled List Run to Test Calibration

To test the automated system, a List sequence was initiated, the parameters and outcomes of which are found in Table 4.17. The reaction was performed in methanol using rose bengal (1 mol %) with the second-generation white PhotoLED.

Table 4.17: List experiment independent variables and corresponding reaction outcomes as measured by HPLC-210 nm.

Run	Independent Variable					conversion /	trans-RO /	cis-RO /%
	1 / °C	2 / mL min <sup>-1</sup>	3/ mol dm <sup>-3</sup>	4	5			
1	10	1	0.1	2	1	61.8	0.7	-1.8
2	0	1	0.1	2	1	70.4	1.6	-1.8
3	-10	1	0.1	2	1	78.0	0.8	-2.3
4	-20	1	0.1	2	1	-	-	-

The reaction was performed with citronellol (0.1 M) in methanol using rose bengal (1 mol %) as the photosensitiser and a second-generation white PhotoLED (500 mA) as the light source. Aqueous sodium sulphite delivered by the peristaltic pump (17 rpm) at 1 mL min<sup>-1</sup> acted as the quench reagent, while 5 % sulphuric acid was delivered by the computer controlled HPLC pump.

Runs 1-3 were completed successfully, with reasonable levels of conversion of citronellol, albeit, with very low yields for the two isomers of rose oxide. A similar phenomenon occurred to that found during the synthesis of **18**, in which a number of

peaks with short retention times and significant areas were observed. These are potentially polar intermediate compounds in the formation of rose oxide.

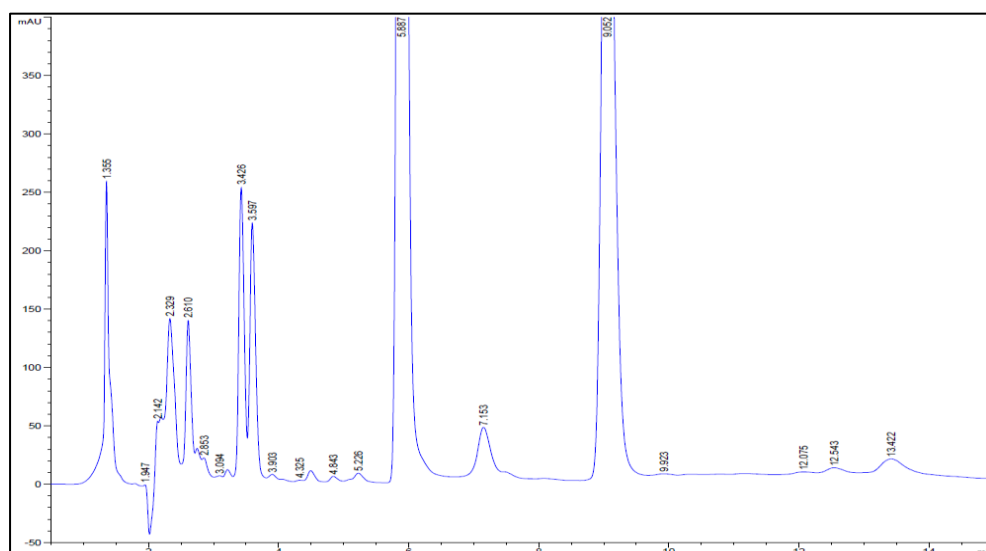


Figure 4.37: 210 nm chromatogram of Run 3. Small peaks can be observed for *cis*-rose oxide at 13.422 mins, and *trans*-rose oxide at 12.543 minutes. A number of early eluting peaks are also found which likely belong to intermediate compounds in the formation of rose oxide.

Due to the lack of reaction completion, the peak areas of *trans*- and *cis*-**13** are negligible, with the *cis* producing areas between 219 and 379 which result in negative calculated yield due to the size of the intercept of the calibration equation. Due to the fact that low concentrations are being measured for the isomers of **13**, the calibration curves were forced through zero and the yields recalculated. This process, although not ideal, is acceptable when measuring peaks at the low end of the concentration range, but has a major impact on the accuracy of the calibration at higher analyte concentrations. Recalculating slightly reduced the yield of the *trans*- isomer, while the *cis*- increases.

Table 4.18: Yields of **13** recalculated using calibration equations forcing the straight line through zero to improve the analysis of the rose oxide isomers at low concentrations.

Run	conversion / %	trans-RO / %	cis-RO / %
1	61.8	0.3	1.8
2	70.4	1.2	1.9
3	78.0	0.4	1.4

Disruption to the Taylor flow equilibrium was experienced during Run 4. The lower photoreactor temperature of -20°C resulted in a slight increase in the back-pressure ( $P_1$  20 psi), however, due to the increased length and additional flow from the third HPLC

pump, this increase was enough to disrupt the flow. The reaction solvent, methanol, possesses a viscosity of 0.545 cP at 25°C, compared to 0.41 cP for DCM.<sup>224,309</sup> Switching to the latter can allow the photo-oxidation to be conducted at temperatures down to -80°C as achieved for photo-oxidations of **14**, while, the use of TFA, successful in the fully continuous synthesis of **18** in DCM, can replace the aqueous H<sub>2</sub>SO<sub>4</sub> used in the Dragoco synthesis.

The switch to DCM as the reaction solvent also prevents the use of the previously used photosensitiser, rose bengal; due to its low solubility. Therefore, TPP was reinstated. The absorbance maximum of TPP matches poorly with the emission spectrum of the white PhotoLED; therefore, the light source was replaced with the first-generation 424 nm blue PhotoLED. The improvement in absorbance and emission overlap is the first of two benefits of using this photosensitiser/light source combination, the second being the increased emission intensity of the light source when compared to the white PhotoLED.

To test the adapted set-up, an automated List experiment was performed; the independent variables along with the experimental results are shown in Table 4.19. The experiment was completed without error, each run was successfully initiated with the correct reaction parameters after analysis and quantification of the preceding run had completed. Firstly, the results of the automated reactions show the improvements due to the adaptations of the photoreactor, with high levels of conversion, > 90%, being achieved. The previous set-up produced a conversion high of just 78%. Second, the results highlight the effect of the acid concentration on the yield of rose oxide. The lowest yields are found when using 1 molar acid equivalent. At this concentration (0.1 M) the reaction is not complete at the point of sampling; as the acid concentration is increased, the reaction profile is driven further towards completion at the time of analysis, resulting in far higher observed yields. Increasing the acid concentrations seems to reach a yield plateau at 3 molar equivalents, at which the highest total yield for rose oxide at 48.30 % is found. At this molarity, the effect of the reaction temperature can also be assessed, with a large reduction in yield being observed at the lower photoreactor temperature of -80°C compared to -40°C. The levels of conversion are, however, nearly identical. It appears that the lower temperature of the reagent stream upon exiting the photoreactor hampers the subsequent quenching and cyclisation steps, lowering the rate of reaction. Thus, for reactions carried out at the lowest temperatures, an increase in the heated coil temperature and length may improve the formation of **13**.

Table 4.19: Automated continuous flow synthesis of rose oxide in DCM in the low temperature photoreactor with the 424 nm PhotoLED.

Run	Independent Variable					Conversion / %	Trans-RO / %	Cis-RO / %	Total RO / %
	1 / °C	2 / mL min <sup>-1</sup>	3 / mol dm <sup>-3</sup>	4	5				
1	-40	0.5	0.1	2	1	91.3	1.4	2.4	3.8
2	-40	0.5	0.1	2	5	96.3	11.1	36.1	47.2
3	-40	1.0	0.1	2	5	98.2	11.7	36.1	47.8
4	-40	1.0	0.1	2	3	99.3	12.7	35.7	48.3
5	-80	1.0	0.1	2	3	99.6	5.2	14.9	20.0
6	-40	1.0	0.1	2	3	92.0	12.0	36.9	48.9

#### 4.8.5. CCF DoE for the Synthesis of Rose Oxide

The test of the automated set-up showed that successful implementation of the continuous synthesis of **13** and of the On-line analysis had been achieved. To further develop the reactor towards full self-optimisation, a Design of Experiments (DoE) based List sequence was set-up. This would allow for testing of the reactor over a long time span, indicating the viability of conducting self-optimised reactions. Furthermore, the outcome of the DoE was expected to show reaction factors that have a negligible impact on the reaction outcome. Thereby, allowing for the removal of these factors to reduce the computational cost of self-optimisation.

A 4 factor, 3-level CCF design approach was adopted. The concentration of the substrate was excluded as a factor to reduce the number of experiments required. Fortunately, the Julabo FP89-ME control unit had been repaired at this point and adapted to prevent loss to the communication board from occurring again. This allowed for the reactor to be brought down to the low of -80°C. The experimental bounds of the remaining factors were set as follows:

Table 4.20: 4 factor, 3-level CCF design for the preliminary DoE to test the automated reactor for the 3 step synthesis of rose oxide.

Factor	-1	0	+1
Temperature / °C	-80	-40	0
Substrate Flow Rate / mL min <sup>-1</sup>	0.5	1	2
Oxygen Molar Equivalents	2	5	8
Acid Molar Equivalents	2	3	5

A total of 26 conditions were generated and subsequently initiated; the factors and the reaction outcomes are shown in Table 4.21. While most DoE methods perform runs in a randomly assigned order to prevent external factors from affecting the experiments,

the logistics and time cost of repeatedly chilling and heating the photoreactor chiller forced the grouping of runs by temperature for convenience and efficiency.<sup>310</sup>

A variety of issues were identified and solved in order to allow seamless running of the reaction controller for future experiments. While in an ideal world, all runs would have been performed without interruption, frequent debugging of the MatLab scripts marred this set of experiments and forced frequent interruption. Despite taking considerable time and resource, this process allowed the successful “real-world” testing and proving of the newly adapted script and built a groundwork for future self-optimisation.

Of the initial 27 proposed DoE experiments, 20 were completed successfully. Despite the reduced viscosity of DCM, backpressure still presented a large issue and caused the failure of a handful of runs at -80°C. Four additional runs at -60 °C were planned, to assess the ability of the reactor to perform at this higher temperature. Three of the four extra experiments were completed, yet still displayed some of the same flow issues observed at -80 °C. It is unclear whether this is an inherent issue with DCM at temperatures lower than -40 °C, as at this temperature the issues were not observed, or a sporadic effect observed in only this instance. Further disruptions to the runs occurred due to the loss of connection from the Reactor Controller to the Bronkhorst® gas flow controller.

Increased equivalents of acid significantly increased the yield, with the highest yield of 55.1% achieved using five equivalents. While increasing from 2 equivalents of acid to 3 seemed to increase yields, a plateau of sorts can be observed, and yields did not increase appreciably with 5 equivalents of acid when compared with 3.

The starting material flow rate also affected the yield. An overall downward trend was observed with respect to increasing starting material flow rate. This is expected and due to lower residence time in the reactor and, as such, decreased reaction progression post-photo-oxidation.

Another important factor to consider is the productivity of the reactor – an experimental run at 0.5 ml min<sup>-1</sup> would have 4 times less throughput and have a run time 4 times longer than that of a 2.0 ml min<sup>-1</sup> run. This would make optimisation at this low flow rate time consuming and likely result in poor productivity. In terms of productivity of the reactor setup overall, while the highest yield was obtained with a 0.5 ml min<sup>-1</sup>, the

highest productivity was obtained with the conditions of Run 28 at 2 ml min<sup>-1</sup>: 22 g day<sup>-1</sup>. This productivity could, however, be optimised by the reactor autonomously with relative ease using equation 4.5, and aiming to maximise the productivity variable, where c is the concentration of starting material, y is the yield percentage and V is the starting material flow rate (in mL min<sup>-1</sup>)

$$\text{Productivity (g day}^{-1}) = c \times \frac{y}{100} \times \frac{V}{1000} \times 154.25 \times 1440 \quad 4.5$$

The ratio of gas appeared to have little effect on the overall yield of the reaction with only a very slight negative trend observed. This is certainly due to the simultaneous reduction in residence time with increasing gas ratio, rather than a direct impact of the concentration of oxygen itself. Increased flow positively impacted the flow dynamics and often a high gas ratio enabled more consistent and repeatable Taylor flow conditions. It was later determined that for the previously failed runs at -80°C with 2 gas equivalents, an increase to 3 equivalents resulted in far more desirable Taylor flow patterns and disruption to the flow occurred less frequently.

Table 4.21: The value of each of the factors (independent variables) of the 4 factor, 3-level CCF design of experiments, along with the reaction outcomes.

Run	Independent Variable					Conv. / %	Trans-RO / %	Cis-RO / %	Total RO / %	trans-/cis-ratio / %
	1 /°C	2 / mL min <sup>-1</sup>	3 / mol dm <sup>-3</sup>	4	5					
1	0	0.5	0.098	2	2	99.9	6.1	16.9	23.0	35.9
2	0	0.5	0.098	2	5	99.8	12.3	34.4	46.7	35.7
3	0	0.5	0.098	8	2	99.5	6.4	17.3	23.6	36.9
4	0	0.5	0.098	8	5	99.3	10.6	31.3	42.0	34.0
5	0	2.0	0.098	2	2	99.3	5.0	11.5	16.4	43.3
6	0	2.0	0.098	2	5	95.6	11.3	33.7	45.0	33.6
7	0	2.0	0.098	8	2	99.3	4.7	11.1	15.9	42.3
8	0	2.0	0.098	8	5	99.9	12.4	36.9	49.3	33.7
9	0	1.0	0.098	5	3	100.0	13.3	37.1	50.4	35.7
10	0	1.0	0.098	5	3	99.8	13.2	36.7	49.9	36.0
11	-40	0.5	0.098	5	3	99.9	11.6	33.4	45.0	34.8
12	-40	2.0	0.098	5	3	98.6	12.5	34.6	47.1	35.9
13	-40	1.0	0.098	2	3	97.5	12.7	35.9	48.6	35.4
14	-40	1.0	0.098	8	3	99.8	12.5	34.5	47.0	36.2
15	-40	1.0	0.098	5	2	99.8	3.9	8.8	12.7	44.9
16	-40	1.0	0.098	5	5	99.8	13.7	39.6	53.3	34.5
17	-40	1.0	0.098	5	3	99.7	13.9	38.8	52.7	35.8
18	-40	1.0	0.098	5	3	99.7	13.8	38.7	52.5	35.7
19	-80	0.5	0.098	2	5	98.2	6.2	21.6	27.7	28.5
20	-80	0.5	0.098	8	2	99.9	0.5	10.9	11.4	4.9
21	-80	0.5	0.098	8	5	-	-	-	-	-
22	-80	2.0	0.098	2	2	-	-	-	-	-
23	-80	2.0	0.098	2	5	-	-	-	-	-
24	-80	2.0	0.098	8	2	-	-	-	-	-
25	-80	2.0	0.098	8	5	-	-	-	-	-
26	-80	1.0	0.098	2	3	-	-	-	-	-
27	-80	0.5	0.098	2	2	-	-	-	-	-
28	-60	2.0	0.098	8	5	98.1	4.1	11.9	15.9	34.5
29	-60	2.0	0.098	2	5	94.1	13.0	37.2	50.2	34.9
30	-60	2.0	0.098	2	2	99.4	7.8	21.3	29.1	36.9
31	-60	1.0	0.098	2	2	-	-	-	-	-

## 4.9. Summary

Good progress was made in relation to the initial aims set out at the beginning of this Chapter. However, due to numerous complexities discovered during the development of the automated reactor, not all of the aims were achieved.

Significant efforts were made to produce robust HPLC methods for the On-line analysis of i) artemisinin and DHAA, ii) rose oxide and citronellol, these are detailed in Chapter 5.

In the case of artemisinin, the intricacies of interfacing On-line analysis with the automation of such a complex reaction, which involves sequential photo-oxidation and thermal steps, proved to be a challenge. Throughout the investigation a great deal of insight was acquired into the interdependencies between reactor, reaction and analytical method development. Modifications to the reactor or the reaction profile often required adaptations to the analysis method. For example, the use of toluene to enhance the formation of artemisinin had the subsidiary effect of initially preventing UV analysis and affecting detection with the ELSD. Adaptations of both stationary and mobile phases were eventually implemented to achieve reliable detection in this solvent. This provides an example of how careful considerations have to be made when developing reactions in tandem with On-line analysis, where, unlike typical Off-line HPLC analysis, preparative steps cannot be facilitated. Nevertheless, valuable knowledge was gained about the complexities and limitations of HPLC analysis and, specifically, ELS detection, as discussed further in Chapter 5.

The use HPLC-ELSD and -UV analysis also provided an insight into the reaction profile at the time of sampling and exhibits the potential to advance the understanding of the route to photochemically-produced artemisinin. This information aided in the iterative development of the automated low temperature photoreactor and highlighted the impact of reactor design, in particular the sections facilitating the secondary reactions, on the formation of artemisinin. The addition of the Vortex reactor showed the importance of providing sufficient oxygen and superior mixing for the secondary reaction by improving the formation of artemisinin and preventing the formation of the 6-lactone. Insights were also gained into the potential reason for the discrepancies observed between <sup>1</sup>H NMR and HPLC analysis, with evidence of the cause of the variation in the <sup>1</sup>H NMR yields of artemisinin and the 6-lactone.

The development of the HPLC method for citronellol and rose oxide was a far simpler task, partly due to the absence of an ELS signal for the analytes and, thus, development was necessarily focused on UV detection. As discussed further in Chapter 5, this method was found to be routinely more reliable than ELS.

The implementation of the On-line analysis into the self-optimisation framework was successful. However, a number of issues arose: as with the automated syntheses of artemisinin, the formation of rose oxide was hampered by disruption to the substrate-oxygen flow equilibrium at low reactor temperatures, highlighting the difficulties of performing multi-step flow syntheses at low temperature. Connection issues to the Bronkhorst® gas flow controller were also experienced during the DoE sequence. The latter is easily solved, but the flow issues experienced in both reactions require significant further investigation.

Ultimately, On-line analysis methods were developed for the synthesis of artemisinin and rose oxide using HPLC-UV analysis. These were implemented into the self-optimisation framework and both successfully performed automated reaction sequences, showing that with further reactor development, the self-optimisation of these photo-oxidative reactions is likely to be feasible.

# Chapter 5. Experimental

## 5.1. Materials

Unless otherwise stated, all reagents, gases and solvents were of reagent grade and obtained from commercial suppliers. Maleimide, propargyl alcohol (99%), deuterated chloroform and dimethyl sulfoxide and the glass beads used were obtained from Sigma Aldrich. 1-hexyne (97 %) was obtained from Acros Organics. Tetrahydrophthalic acid anhydride had been previously synthesised within our group. Citronellol (95 %) and meso-TPP (97 %) were purchased from Acros Organics. Rose oxide (mix of isomers, > 98 %), TFA (99%) and TCA (99%) and Rose Bengal were purchased from Sigma Aldrich. Dihydroartemisinic acid and artemisinin (97 %) were kindly provided by Huvepharma.

## 5.2. General Analysis

### 5.2.1. NMR Analysis

All NMR spectra were obtained using either a Bruker 400 MHz or HD-400 MHz spectrometer at the University of Nottingham NMR facility. Quantitative  $^1\text{H}$  NMR was used to determine analyte yields using biphenyl or trimethoxybenzene as either external or internal standards. The chemical shifts of the protons were reported in parts per million (ppm). Sample preparation followed a general procedure – 0.5 mL of sample was dried under  $\text{N}_2$  and, if analysing *via* external standard, combined with a known mass of the standard, and finally dissolved in approximately 0.70 mL  $\text{CDCl}_3$ . Use of internal standards did not require the addition of the standard to the dried sample. The  $^1\text{H}$  shift values were determined relative to residual  $^1\text{H}$  nuclei in  $\text{CDCl}_3$  ( $\delta$  7.26 singlet) using Mnova<sup>TM</sup> software from Mestrelab®. The starting standard integral values,  $I_{std}$ , are determined through the equation (1.2).

$$I_{std} = n_{std} \times \frac{\text{No. protons in standard peak}}{n_{SM}} \quad (5.1)$$

Where:  $n_{std}$  is the moles of the standard and  $n_{SM}$  is the moles of starting material based on the concentration and volume of sample collected (concentration based on the mass of starting material used). The corresponding integral value of the standard is then set for the standard peak within each of the starting material NMRs. The mean integral of

the starting material is then calculated, and the starting concentration adjusted to reflect this value. The updated concentration is then used to re-calculate the standard integral value which is then carried forward for the determination of the analyte integrals in the photoproduct samples.

### 5.2.2. Statistical Analysis

Outliers in each data set were determined using the Grubbs test, performed using RStudio software. The Grubbs test detects single outliers in a univariate data set that is assumed to come from a normally distributed population.<sup>311</sup> Grubbs' P-values of less than 0.05 (95 % confidence interval) signified the presence of an outlier within a particular data set.

Mean values of HPLC and NMR data sets with outliers removed were calculated and reported with the corresponding uncertainty, determined using a two-tailed distribution to a 95 % confidence interval. The relative standard deviations, RSD %, of the data sets were also reported. An inherent uncertainty within the NMR measurements of 1.5 % was applied to peaks with signal to noise ratios >100, and an error of 5 % applied to peaks with S/N < 100, in accordance with the findings of Malz *et al.* and Schoenberger.<sup>312,313</sup>

## 5.3. Development of a Low Temperature Continuous-Flow Photoreactor

This section describes the reactions performed during the development of the HPR (high pressure reactor). First, the UV initiated [2+2]-cycloadditions of; (i) maleimide, **1**, with 1-hexyne, **2**; and (ii) 3,4,5,6-tetrahydrophthalic anhydride, **4**, with propargyl alcohol, **5**, were performed to assess the capabilities of the reactor. Following this, the reactor was adapted to undertake photo-oxidation reactions at reduced temperature. The photo-oxidations of  $\beta$ -citronellol, **8**, and dihydroartemisinic acid, **14**, to their corresponding hydroperoxides were then performed.

### 5.3.1. UV Initiated [2+2]-cycladditions

#### 5.3.1.1. [2+2] Photo-Cycloadditions of Maleimide and 1-Hexyne

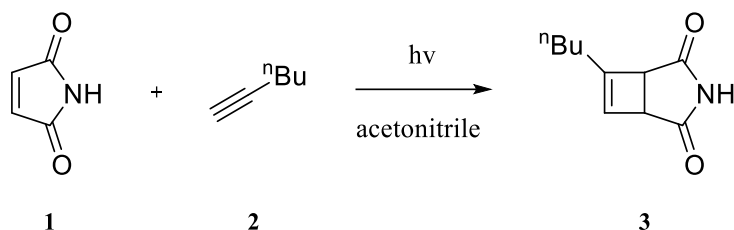


Figure 5.1: Reaction scheme of the [2+2] photocycloaddition of maleimide (1) and 1-hexyne (2) in acetonitrile.<sup>101</sup>

#### Reaction in Batch

Maleimide (874 mg, 9 mmol) and 1-hexyne (1.55 mL, 13.5 mmol) were combined in acetonitrile (90 mL) and the solution degassed. Under an inert atmosphere, the solution was irradiated with a UV light source ( $\lambda_{\text{max}} = 366 \text{ nm}$ ). 1 mL aliquots were taken every 15 minutes until full conversion was achieved. 0.2 mL of each aliquot was subsequently dried under nitrogen and biphenyl added as an external standard to allow semi quantitative NMR to be carried out. The remaining solution was dried under reduced pressure and purified by passing through a silica column with a 1:3 v/v ratio of ethyl acetate to cyclohexane as the eluent, to yield the product as an orange oil.  $^1\text{H}$  NMR (400 MHz,  $\text{CDCl}_3$ );  $\delta$  0.91 (t, 3H), 1.34 (m, 2H), 1.48 (m, 2H), 2.18 (m, 2H), 3.62 (m, 1H), 3.69 (dd, 1H), 6.08 (d, 1H). These values correspond well to the literature values:<sup>114</sup>  $^1\text{H}$  NMR (400 MHz,  $d^6\text{-DMSO}$ );  $\delta$  0.86 (t, 3H), 1.29 (qt, 2H), 1.42 (tt, 2H), 2.10 (t, 2H), 3.53 (s, 1H), 3.65 (d, 1H), 6.13 (s, 1H).

#### Continuous-Flow Reaction in an FEP Coil

Maleimide (1.748 g, 18 mmol) and 1-hexyne (3.1 mL, 27 mmol) were combined in acetonitrile (180 mL) and the solution degassed. The solution was pumped through a one-layer FEP coil reactor at varying flow rates of 1.5, 2 and 3  $\text{mL min}^{-1}$ . Samples were taken after an equilibrium time equal to the time taken for at least two reactor volumes to pass through the entire set-up. Samples were taken in triplicate and prepared for  $^1\text{H}$  NMR analysis in  $\text{CDCl}_3$  with biphenyl as an external standard.

#### Continuous-Flow Reaction in the HPR

Maleimide (1.748 g, 18 mmol) and 1-hexyne (3.1 mL, 27 mmol) were combined in acetonitrile (180 mL) and the solution degassed. The solution was degassed with nitrogen for 5 minutes before being pumped at various flow rates through the HPR reactor at ambient temperature and pressure. Photochemistry was carried out using a medium pressure Hg arc lamp (125 W). Samples were taken after an equilibrium time equal to the time taken for at least two reactor volumes to pass through the entire set-up. Samples were taken in triplicate (3 x 0.5 mL) and subsequently dried with nitrogen; a known amount of biphenyl was added to each sample before dissolution in  $\text{CDCl}_3$ .

### 5.3.2. [2+2] Photo-cycloadditions of THPA and propargyl alcohol

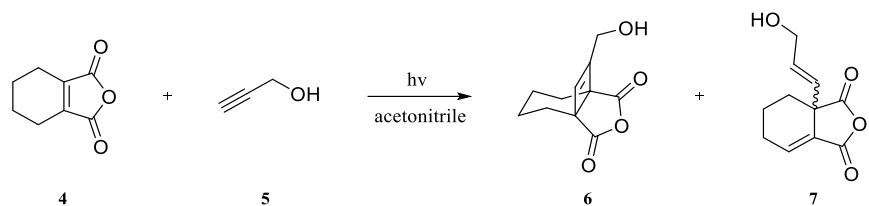


Figure 5.2. Reaction scheme of the [2+2] cycloaddition of THPA and propargyl alcohol forming the major bridged product and the minor product. Adapted from Booker-Milburn et al.<sup>206</sup>

### Continuous-Flow Reaction in the HPR

3,4,5,6-tetrahydropthalic anhydride (THPA, 0.1 M, 1.52 g) and propargyl alcohol (0.15 M, 0.87 mL) were combined with thioxanthone (1 mol %) in acetonitrile (100 mL). The solution was degassed with nitrogen for 5 minutes before being pumped at various flow rates through the HPR reactor at ambient temperature and pressure. Photochemistry was carried out using a medium pressure Hg arc lamp (125 W). Samples were taken after an equilibrium time equal to the time taken for at least two reactor volumes to pass through the entire set-up. Samples were taken in triplicate (3 x 0.5 mL) and subsequently dried with nitrogen; a known amount of biphenyl was added to each sample before dissolution in  $\text{CDCl}_3$ .

### 5.3.3. Photo-Oxidations in the HPR

#### 5.3.3.1. Photo-oxidations of Citronellol

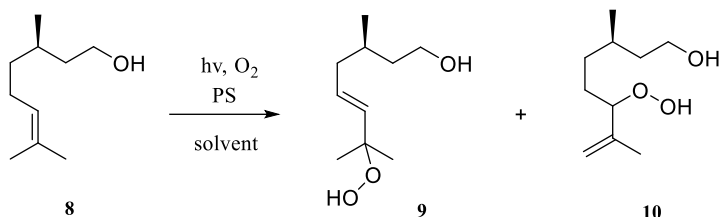


Figure 5.3. Scheme for the photo-oxidation of citronellol, **8**, the reaction proceeds via an ene-oxidation to the corresponding hydroperoxides, **9** and **10**.

The standard procedure for the photo-oxidations of citronellol to the corresponding hydroperoxides in the HPR is as follows: Citronellol (0.1 M) was combined with  $[\text{Ru}(\text{bpy})_3][\text{PF}_6]$  (0.5 mM, 0.5 mol %) in methanol and the solution sonicated and degassed for 5 minutes. The solution was then pumped at various flow rates towards the HPR where it was combined with an oxygen stream at a flow rate of value 10 times the substrate flow rate. Taylor flow between the substrate and the oxygen formed and the flow was directed through the pre-cooling coil and then into the reactor where it was irradiated with 424 nm light. The solution passed through the reactor via the spiralled inner and exited through the top outlet. Samples were taken after an equilibrium time equal to the time taken for at least two reactor volumes to pass through the entire set-up. Samples (0.5 mL each) were collected in triplicate and analysed by  $^1\text{H}$  NMR ( $\text{CDCl}_3$ ) using biphenyl as an external standard. The reaction was repeated at various photoreactor temperatures.

#### $^1\text{H}$ NMR Analysis

The crude reaction product collected from the photo-oxidation of citronellol, **8**, to hydroperoxide **9** (7-hydroperoxy-3,7-dimethyloct-5-en-1-ol) and **10** (6-hydroperoxy-3,7-dimethyloct-5-en-1-ol) was analysed by  $^1\text{H}$  NMR. The reaction conversion and product yields were quantified *via* integration of the relevant peaks corresponding to **8** ( $\delta = 5.11$  ppm), **9** and **10**. Purification of the reaction products was not required for an understanding of the reaction conversion or yields to be obtained.<sup>203</sup> The characterisation of **8** has been reported:<sup>314</sup> (S)-Citronellol (**8**):  $^1\text{H}$  NMR (400 MHz,  $\text{CDCl}_3$ )  $\delta = 5.10\text{--}5.05$  (m, 1H, H6), 3.71–3.60 (m, 2H, H1), 2.02–1.90 (m, 2H, H5), 1.66 (s, 3H, H7), 1.64–1.50 (m, 5H, H3/H4/H8), 1.43–1.28 (m, 3H, H2/H4/OH), 1.20–1.11 (m, 1H, H2), 0.88 (d, 3H, H9).

Literature values for the hydroperoxides as determined by Lumley *et al.* and Tung *et al.*:<sup>315,316</sup>

(3S)-(E)-7-hydroperoxy-3,7-dimethyloct-5-en-1-ol (**9**): <sup>1</sup>H-NMR (CDCl<sub>3</sub>, 400 MHz) δ: 1.28 (s, 6H, C7-Me<sub>2</sub>), **5.49-5.62** (m, 2H, CH=CH).

(3S)-(E)-6-hydroperoxy-3,7-dimethyloct-5-en-1-ol (**10**): <sup>1</sup>H-NMR (CDCl<sub>3</sub>, 400 MHz) δ = 1.65 (s, 3H, 7-Me), 4.17-4.21 (m, 1H, CH-OOH), **4.90** (m, 2H, C=CH<sub>2</sub>)

Experimentally found:

<sup>1</sup>H-NMR of **9** (300 MHz, CDCl<sub>3</sub>): δ = 0.93 to 0.95 (d, 3H, J = 6.8 Hz, CH<sub>3</sub>), 1.35 (s, 6H, (CH<sub>3</sub>)<sub>2</sub>), 1.94 to 2.15 (m, 2H, CH<sub>2</sub>), 3.63 to 3.77 (m, 2H, CH<sub>2</sub>OH), **5.54 - 5.75** (m, 2H, HC=CH).

<sup>1</sup>H-NMR of **10** (300 MHz, CDCl<sub>3</sub>): δ = 0.91 to 0.93 (d, 3H, J = 6.8 Hz, CH<sub>3</sub>), 1.75 to 1.76 (m, 3H, CH<sub>3</sub>), 4.28 to 4.32 (t, 1H, J = 6.7 Hz, CHOOH), **5.00 - 5.05** (m, 2H, C=CH<sub>2</sub>).

### 5.3.3.2. Photo-oxidations of DHAA

The standard procedure for the photo-oxidations of DHAA to the corresponding hydroperoxides in the HPR is as follows:

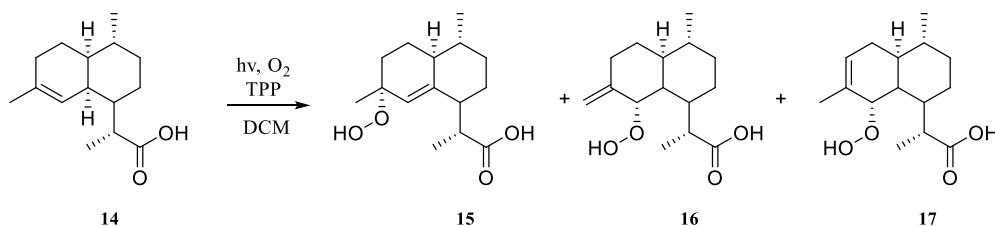


Figure 5.4: Simplified synthesis of artemisinin through the photo-oxidation of DHAA, **14**, to the corresponding hydroperoxides, **15**, **16** and **17**.

DHAA (0.05 M) was combined with TPP (0.25 mM, 0.5 mol %) in dichloromethane and the solution sonicated and degassed for 5 minutes. The solution was then pumped at various flow rates towards the HPR where it was combined with an oxygen stream at a flow rate of value 5 times the substrate flow rate. Taylor flow between the substrate and the oxygen formed and the flow was directed through the pre-cooling coil and then into the reactor where it was irradiated with 424 nm light. The solution passed through the reactor around the spiralled inner and through the top outlet. Samples were taken after an equilibrium time equal to the time taken for at least two reactor volumes to pass through the entire set-up. Samples (0.5 mL each) were collected in triplicate and

analysed by  $^1\text{H}$  NMR ( $\text{CDCl}_3$ ) using biphenyl as an external standard. The reaction was repeated at various photoreactor temperatures.

### 5.3.3.3. $^1\text{H}$ NMR Analysis

As hydroperoxide **17** is only a trace compound, analysis was focussed on the yields and ratios of **15** and **16**. Literature values for the  $^1\text{H}$ -NMR of **14** and **15**, as determined by Wallaart *et al.*, are given below:<sup>176,317</sup>

Dihydroartemisinic acid, DHAA (**14**):  $^1\text{H}$  NMR ( $\text{CDCl}_3$ , 300 MHz)  $\delta$  **5.12** (1H, s), 2.5 (1H, m), 2.5 (1H, m), 1.95 and 1.56 (2H, m), 1.92 and 1.80 (2H, m), 1.64 (3H, s), 1.64 (1H, m), 1.60 and 0.96 (2H, m), 1.43 (1H, m), 1.37 (1H, m), 1.19 (3H, d) 1.11 (1H, q of d, ), 0.87 (3H, d)

Tertiary DHAA hydroperoxide (**15**):  $^1\text{H}$  NMR ( $\text{CDCl}_3$ , 300 MHz)  $\delta$  **5.26** (1H, s); 2.74 (1H, m); 2.15 (1H, m); 1.92 and 1.48 (4H, m); 1.83 and 1.21 (2H, m); 1.77 and 1.22 (2H, m); 1.58 (1H, m); 1.30 (3H, s); 1.28 (3H, d); 1.24 (1H, m) 0.93 (3H, d).

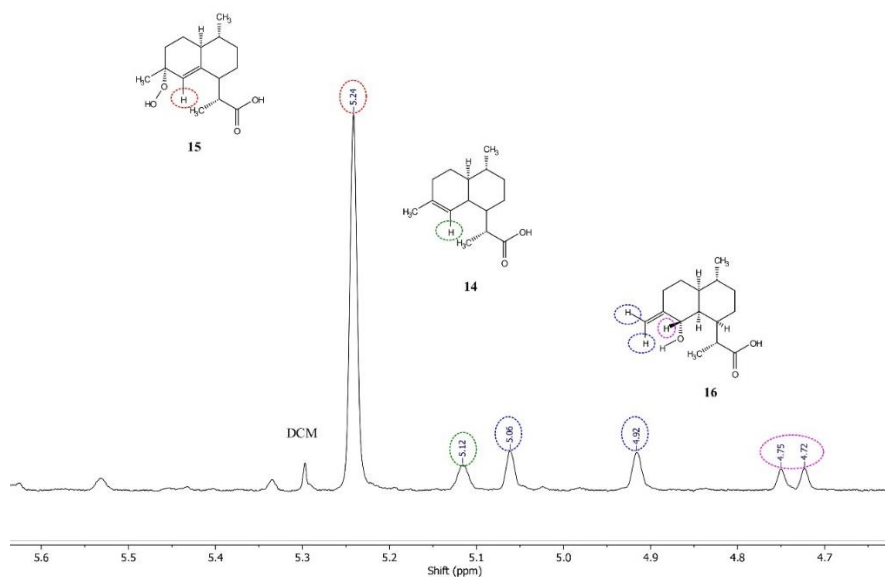


Figure 5.5:  $^1\text{H}$  NMR of the product after photo-oxidation of DHAA under standard conditions. The peaks are labelled according to literature values as determined by Wallaart *et al.*,<sup>176,317</sup> and Amara *et al.*<sup>189</sup> Determination of the yields is performed through the integration of the peaks at  $\delta$  5.12, 5.24 and 5.06 ppm for **14**, **15** and **16** respectively.

Yields of the allylic hydroperoxides were calculated via integration of the peaks at  $\delta$  = 5.24 ppm and  $\delta$  = 5.06 ppm for peroxides **15** and **16** respectively, and compared to biphenyl (external standard). Characteristic shift of hydroperoxide **16** based upon work conducted by Amara *et al.* which determined the identifying shifts of **15** and **16** in acetone- $d_6$ .<sup>189</sup> Conversion was calculated *via* the integration of the signal at  $\delta$  5.12 ppm corresponding to **14**.

### **Calculation of the Ratio of Hydroperoxides**

The ratio of hydroperoxide **15** to hydroperoxide **16** was calculated using the integration values of the relevant peaks as found in the Mnova NMR software. The integral of **15** ( $\delta$  5.24 ppm) was set to a value of 1000 and divided by the corresponding integral of **16** ( $\delta$  5.06 ppm). The mean and associated error to a 95 % confidence interval were calculated for samples in triplicate.

## 5.4. Development of a Continuous-Flow Reactor for Low Temperature Photo-Oxidations

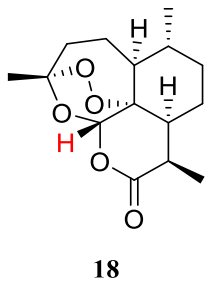
This section describes the reactions performed to first, aid in the development of the low temperature continuous flow photoreactor and, second, to exploit potential improvements in the synthesis of artemisinin, **18**, at low temperature.

### 5.4.1. $^1\text{H}$ NMR Analysis

As with Chapter 2, quantification was achieved using  $^1\text{H}$  NMR analysis, with biphenyl as an internal standard.  $^1\text{H}$  NMR analysis of the products of the photo-oxidations of **14** along with products from the subsequent synthesis of artemisinin, **18**, were conducted using the same preparative and quantification methods described earlier.

#### Artemisinin, **18**

The  $^1\text{H}$  NMR characterisation of **18** has been reported:<sup>189</sup>



**18**

$^1\text{H}$  NMR (300 MHz,  $\text{CDCl}_3$ ):  $\delta$  5.87 (s, 1H), 3.41 (dq, 1H), 2.44 (td, 1H), 2.09–1.98 (m, 2H), 1.91–1.86 (m, 1H), 1.81–1.74 (m, 2H), 1.56–1.34 (m, 3H), 1.46 (s, 3H), 1.22 (d, 3H), 1.11–1.04 (m, 2H), 1.01 ppm (d, 3H).

### 6-lactone, **19**

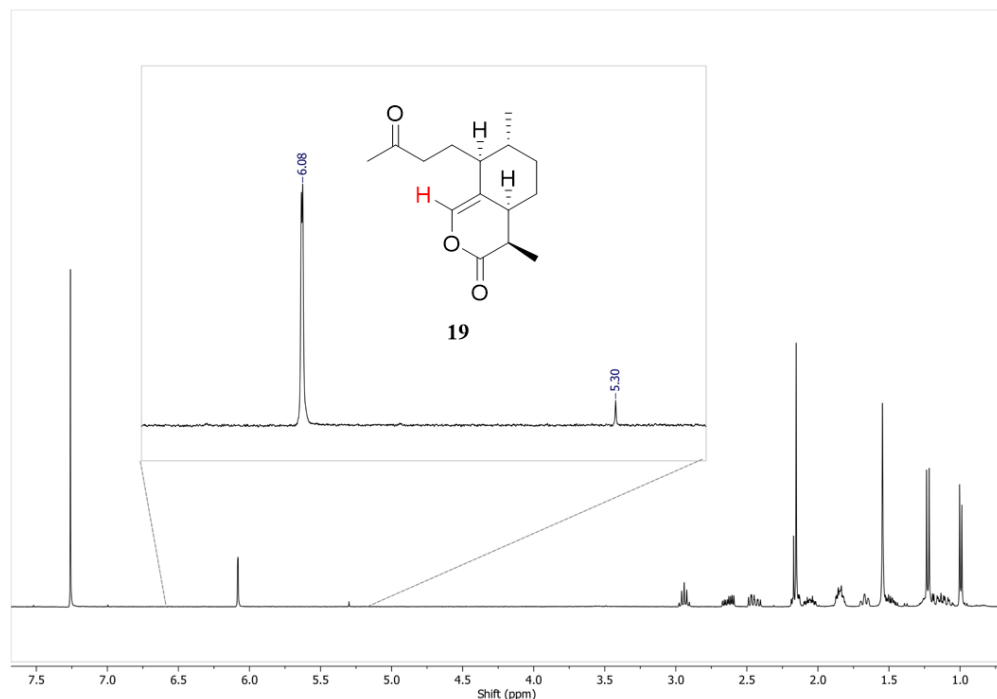


Figure 5.6:  $^1\text{H}$  NMR spectra of isolated 6-lactone, **19**, the characteristic peak used for identification in photoproducts is highlighted with a shift of  $\delta$  6.08 ppm.

The  $^1\text{H}$  NMR characterisation of **19** has been reported.<sup>143</sup>

$^1\text{H}$  NMR (400 MHz,  $\text{CDCl}_3$ )  $\delta$  **6.10** (d,  $J$ = 1.5 Hz, 1H), 2.96 (p,  $J$ = 7.1 Hz, 1H), 2.66 (ddd,  $J$ = 17.8, 9.2, 4.9 Hz, 1H), 2.47 (ddd,  $J$ = 17.9, 8.8, 6.7 Hz, 1H), 2.18 (s, 2H), 2.23 – 2.01 (m, 1H), 1.93 – 1.79 (m, 2H), 1.69 (ddt,  $J$ = 10.7, 9.2, 1.9 Hz, 1H), 1.59 (s, 2H), 1.54 – 1.43 (m, 1H), 1.25 (d,  $J$ = 7.0 Hz, 3H), 1.25 – 1.13 (m, 1H), 1.17 – 0.94 (m, 3H).

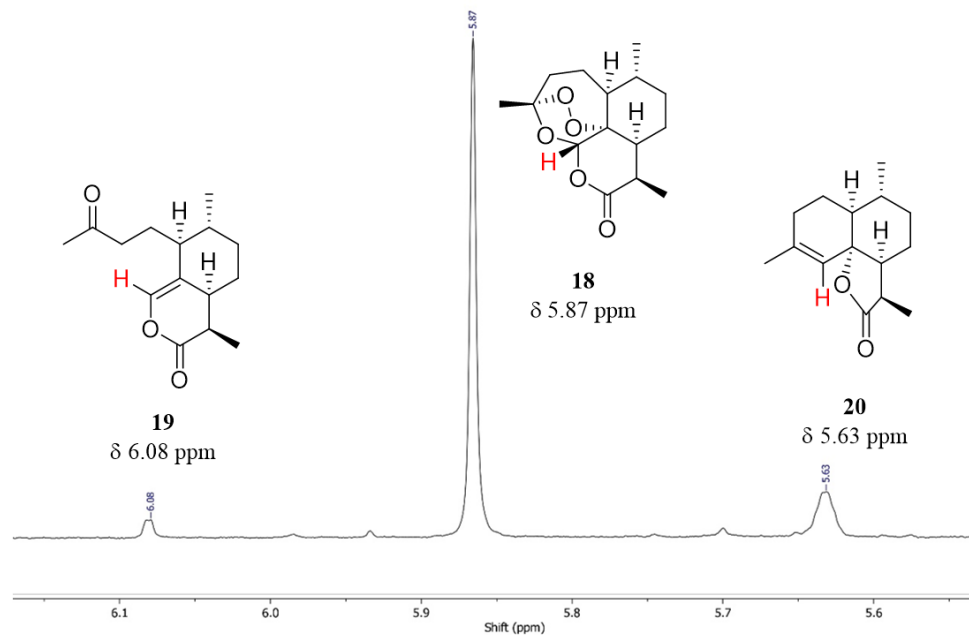
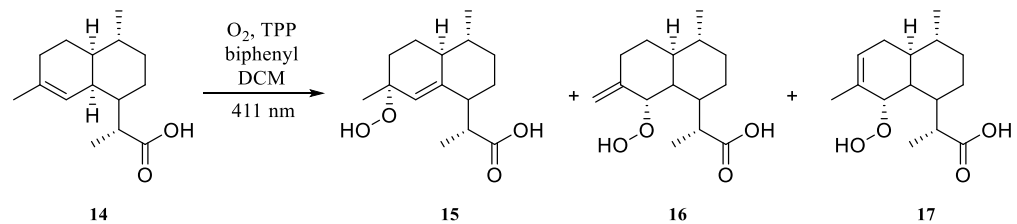


Figure 5.7:  $^1\text{H}$  NMR spectra of product collect after the ‘two-pot’ synthesis of **18**, the peak of which possesses a shift of  $\delta$  5.87 ppm. Also present are signals corresponding to the main side-products of the reaction, **19** and **20** with shifts of  $\delta$  6.08 ppm and  $\delta$  5.63 ppm respectively.

## 5.4.2. General Reaction Procedures

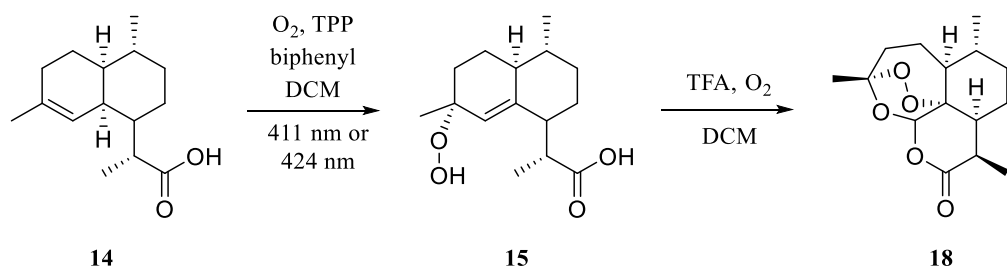
### 5.4.2.1. Photo-Oxidations of 14



Dihydroartemisinic acid, **14**, (DHA, 0.05 M) was combined with tetraphenylporphyrin (0.25 mM, 0.5 mol %) and biphenyl (known amount  $\sim$ 10% w/w) in dichloromethane (volume varied) and the solution degassed. After degassing, the solution was pumped at a stipulated flow rate between 1-20 mL min $^{-1}$  and combined with an oxygen flow (at a flow rate ratio of 1:2.5 or 1:5 mL min $^{-1}$  substrate: $\text{O}_2$  corresponding to delivering either 2.1 or 4.2 molar equivalents of oxygen to DHA) at a mixing T-piece to produce Taylor flow. The gas/liquid flow then entered the photoreactor at a set temperature. The photo-oxidation was initiated using a PhotoLED (424 nm or 411 nm) light source. The photoproduct was then collected: samples were taken in triplicate (0.5 mL each) after an equilibrium time equivalent to the time taken

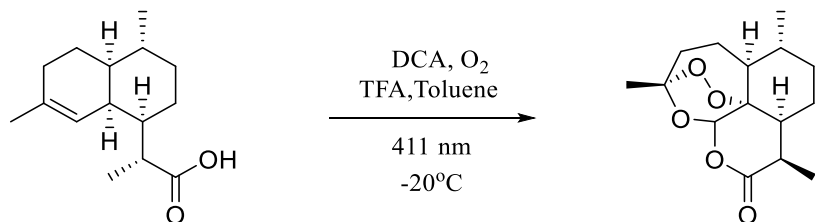
for two reactor volumes to pass through the full set-up. The samples were analysed by  $^1\text{H}$  NMR ( $\text{CDCl}_3$ , biphenyl external standard).

#### 5.4.2.2. Semi-Continuous ‘Two-Pot’ Synthesis of Artemisinin



DHAA (0.05 M) was combined with TPP (0.25 mM, 0.5 mol %) and biphenyl (known amount  $\sim 10\%$  w/w) in dichloromethane (volume varied) and the solution degassed. After degassing, the solution was pumped (Gilson HPLC pump) at a stipulated flow rate and combined with an oxygen flow (at a flow rate ratio of 1:2.5 or 1:5  $\text{mL min}^{-1}$  liquid: $\text{O}_2$  corresponding to delivering either 2.1 or 4.2 molar equivalents of oxygen to DHAA) at a mixing T-piece to produce Taylor flow. The gas/liquid flow then entered the photoreactor at a set temperature. The photo-oxidation was initiated using a PhotoLED (424 nm or 411 nm) light source. The photoproduct was then collected after an equilibrium time equivalent to the time taken for two reactor volumes to pass through the full set-up. Samples were taken in triplicate (0.5 mL each) and analysed by  $^1\text{H}$  NMR ( $\text{CDCl}_3$ , biphenyl external standard). A portion of the remaining photoproduct (20 mL) was then added to the secondary vessel. To the stirred solution was added a stream of oxygen ( $2.0 \text{ mL min}^{-1}$ ) and TFA (0.25 M, 0.50 equivalents). The reaction was allowed to proceed for 20 minutes before samples were taken in triplicate and analysed by  $^1\text{H}$  NMR.

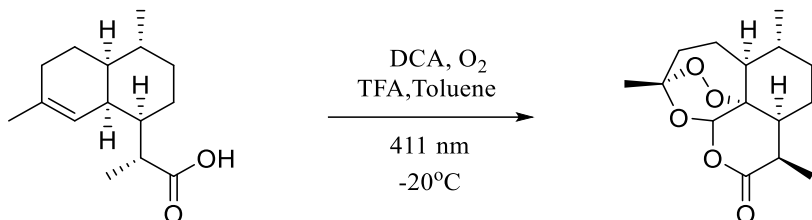
#### 5.4.2.3. Continuous ‘One-Pot’ Synthesis of Artemisinin with TPP in DCM



DHAA (0.05 M) was combined with TPP (0.25 mM, 0.5 mol %), TFA (0.025 mM, 0.5 equivalents) and biphenyl (known amount  $\sim 10\%$ ) in DCM (volume varied) and the solution degassed. After degassing, the solution was pumped (Gilson HPLC pump) at a stipulated flow rate and combined with an oxygen flow (at a flow rate ratio of 1:2.5

or 1:5 mL min<sup>-1</sup> liquid:O<sub>2</sub> corresponding to delivering either 2.1 or 4.2 molar equivalents of oxygen to DHAA) at a mixing T-piece to produce Taylor flow. The gas/liquid flow then entered the photoreactor at a set temperature. The photo-oxidation was initiated using the 411 nm PhotoLED. The photoproduct was then collected, after an equilibrium time equivalent to the time taken for two reactor volumes to pass through the full set-up. Samples were taken in triplicate (0.5 mL each) and analysed by <sup>1</sup>H NMR (CDCl<sub>3</sub>, biphenyl external standard).

#### 5.4.2.4. Continuous ‘One-Pot’ Synthesis of Artemisinin with DCA in Toluene



DHAA (0.05 M) was combined with DCA (2.5 mM, 5 mol %), TFA (0.025 mM, 0.5 equivalents) and biphenyl (known amount ~10% w/w) in toluene (volume varied) and the solution degassed. After degassing, the solution was pumped (Gilson HPLC pump) at a stipulated flow rate and combined with an oxygen flow (at a flow rate ratio of 1:2.5 or 1:5 mL min<sup>-1</sup> liquid:O<sub>2</sub> corresponding to delivering either 2.06 or 4.16 molar equivalents of oxygen to DHAA) at a mixing T-piece to produce Taylor flow. The gas/liquid flow then entered the photoreactor at a set temperature. The photo-oxidation was initiated using the 411 nm PhotoLED. The photoproduct was then collected, after an equilibrium time equivalent to the time taken for two reactor volumes to pass through the full set-up. Samples were taken in triplicate (0.5 mL each) and analysed by <sup>1</sup>H NMR (CDCl<sub>3</sub>, biphenyl external standard). The remaining photoproduct was added to a secondary container, to which O<sub>2</sub> was passed through and samples taken and analysed by NMR after 20 minutes.

#### 5.4.2.5. Semi-Continuous ‘Two-pot’ Reaction to Test the PFA Photoreactor

DHAA (1.18 g, 0.05 M) was combined with TPP (0.0154g, 0.5 mol %) and biphenyl (110.9 mg) in DCM (100 mL) and the solution degassed. The substrate stream was pumped at a flow rate of 3.0 mL min<sup>-1</sup> and mixed with an oxygen stream at 15 mL min<sup>-1</sup> at a T-piece. The resulting Taylor flow enters the low-temperature photoreactor at a measured T<sub>1</sub> of -80°C. The photoproduct was collected after 20 minutes of reaction time. Three samples (0.5 mL each) were prepared for <sup>1</sup>H NMR analysis and while 10

mL of the remaining solution was combined with TFA (0.19 mL, 0.025 M, 0.5 equivalents) and an additional stream of oxygen ( $2 \text{ mL min}^{-1}$ ) was passed through the stirred solution for 20 minutes before sample were collected for  $^1\text{H}$  NMR analysis.

#### 5.4.2.6. Semi-Continuous ‘Two-pot’ Reaction using DHA Ethylcarbonate

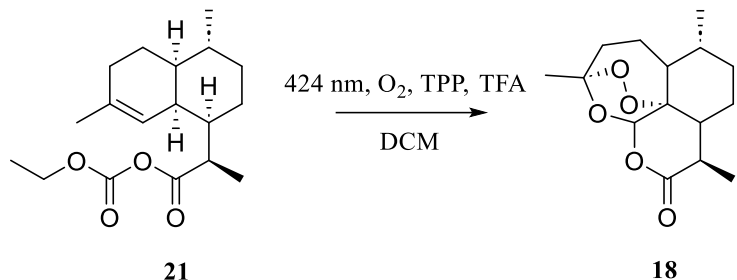


Figure 5.8: Schematic for the 'two-pot' synthesis of 18 from DHAA ethylcarbonate, 21.

DHA ethylcarbonate (0.05 M) was combined with TPP (0.5 mol %), TFA (0.025 M, 0.5 equivalents) and biphenyl (known amount ~10% w/w) in DCM. The solution was pumped at 2.0 mL min<sup>-1</sup> to combine with an O<sub>2</sub> flow of 10.0 mL min<sup>-1</sup>. The resulting Taylor flow then entered the ‘thick-walled’ FEP (1/8” o.d, 1/16” i.d) low temperature photoreactor. The solution was irradiated with 424nm light. Photoproduct was collected after the equilibration time, and analysed *via* <sup>1</sup>H NMR.

The characterisation of DHA ethyl carbonate, **21**, has been reported:<sup>143</sup>

<sup>1</sup>H NMR (400 MHz, CDCl<sub>3</sub>) δ 5.10 (h, J = 1.4 Hz, 1H), 4.34 (q, J = 7.1 Hz, 2H), 2.60 (dq, J = 11.0, 6.9 Hz, 1H), 2.52 (d, J = 5.2 Hz, 1H), 2.02 – 1.88 (m, 1H), 1.82 (dd, J = 17.7, 7.0 Hz, 0H), 1.77 – 1.35 (m, 10H), 1.35 – 1.20 (m, 4H), 1.16 (qd, J = 12.7, 3.2 Hz, 1H), 0.99 (tdd, J = 13.0, 11.7, 3.4 Hz, 1H), 0.89 (d, J = 6.5 Hz, 3H).

## 5.5. Development towards a Self-Optimising Reactor for the Synthesis of 18

This Section describes:

- The iterative development of the HPLC method for On-line analysis of artemisinin, 18, and DHAA, 14, including the issues encountered and subsequent adjustments made.
- A description of the automated reactor - including modifications to the hardware and software to facilitate On-line analysis and automated reaction control.
- An overview of the general experimental procedures performed.

### 5.5.1. Description of the Automated Reactor

#### 5.5.1.1. Reactor Hardware

The automated reactor builds upon the continuous flow low temperature FEP reactor developed and discussed in Chapter 3.

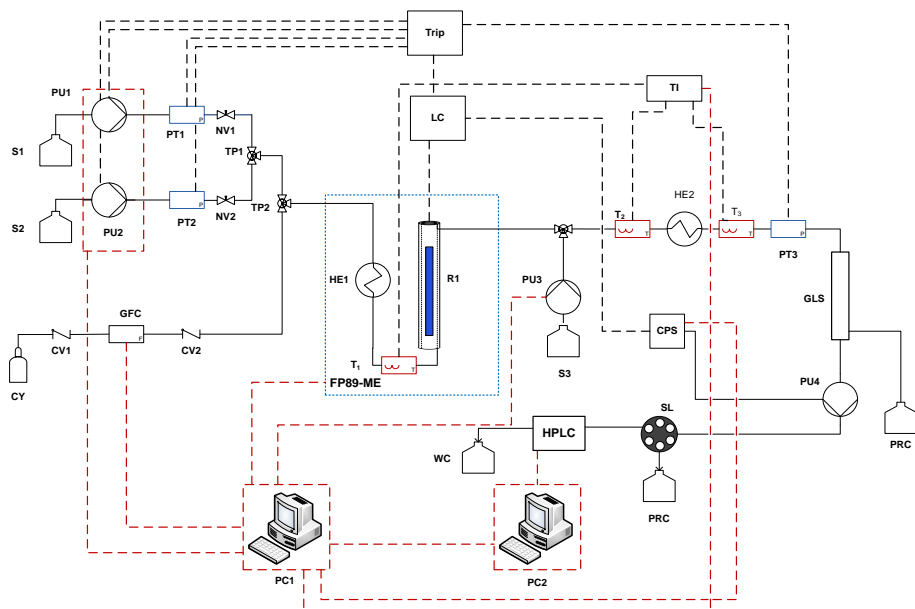


Figure 5.9: Schematic of the self-optimising rig set-up for low temperature photo-oxidative synthesis of artemisinin. Trip cables are indicated by black dashed lines. Computer connections are indicated as red dashed lines. Key: CPS – computer controlled power supply, CV – check valve, CY – gas cylinder ( $O_2$ ), HE – heat exchanger, HPLC – Agilent 1260 Infinity HPLC, GLS – gas-liquid separator, LC –LED controller, GFC – Gas flow controller, PT – pressure transducer, PC – personal computer, PRC – product collector, PU – HPLC pump, R – photo-reactor, S – sample reservoir, SL – HPLC sample loop, T – thermocouple, TI – temperature indicator, TP – T-piece, WC – waste collector.

## Pumps

All starting reagents were pumped using Jasco dual piston HPLC pumps (PU-980). These pumps were connected to the controller via RS-232 connection. A Cole Palmer Masterflex peristaltic pump was used to pump solution towards the gas-liquid separator (GLS). A Gilson HPLC pump was used to pump solution from the GLS to the sample loop of the HPLC injector. All pump heads were routinely dismantled and cleaned with isopropanol. Pump heads were also primed with isopropanol when left idle.

## Sample Injectors

On-line HPLC samples were injected onto the HPLC column using a VICI Valco 6-port internal sample injector. Samples were switched to the analytical mobile phase without prior dilution. Sample loops of sizes 1, 2 and 5  $\mu$ L have been used for analysis. The valve rotor is able to rotate relative to a stationary component (the stator); it is therefore able to switch from the load configuration, where the fluid passes through the sample loop, to the inject position which allows the sample to be injected into the instrument and analysed.

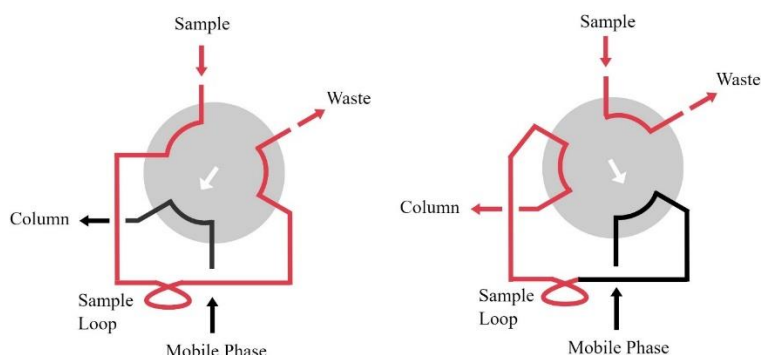


Figure 5.10: Six-port rotary valve with a single sample loop. Left: Load configuration, reaction mixture is pumped from the reactor and through the sample loop towards the waste. Right: Inject configuration – the injector is rotated and connects the sample loop to the HPLC mobile phase. Schematic adapted from manufacturer's website.<sup>48</sup>

## Tubing and Fittings

PTFE tubing (1/8" o.d. 1/16" i.d. or 1/16" o.d. 1/32" i.d.) was used throughout the reactor, prior to and post the FEP photoreactor section. All connections and fittings to equipment were of the specific brand (Agilent, Jasco, VICI etc.); all other connections were Swagelok 316 stainless steel. Reagent and gas streams were mixed in tee joints (Swagelok) unless otherwise stated. PEEK HPLC tubing (1/16" o.d.) was used to connect the Gilson pump with the 6-port injector.

## Automated Sampling Device

Photo-oxidations require the addition of oxygen or air to the reagent stream to form effective Taylor flow before entering the photoreactor. At the outlet of the reactor, the stream will consist of a biphasic gas-liquid flow. The gas phase must be separated from the product stream before the liquid phase can be injected into the HPLC for analysis.

A simple gas-liquid separator (GLS) has been constructed from stainless steel tubing and Swagelok® fittings. The biphasic flow enters the top of the GLS, the liquid drips into the liquid collector and is pulled from the bottom of the GLS *via* a HPLC pump (PU4, Figure 5.9). Since the HPLC sample loop has a very small bore size and is a relatively long distance from the outlet of the GLS (approximately 30 cm), the liquid cannot flow through the sample loop without the use of the pump. Therefore, a sampling pump (Gilson) is used to force the product stream from the GLS through the HPLC sample loop. To ensure no gas bubbles appear in the sample loop, the flow rate of PU4 is set lower than the combined flow rates of PU1-3. However, it is also preferential for the flow rate of PU4 to be as high as possible to quickly refresh the liquid inside the collector, sampling pump, transferring lines and the sample loop. The excess liquid coming out of the liquid collector is accumulated in the bottom of the GLS and eventually discarded through the waste side-arm once the volume has reached the limit.

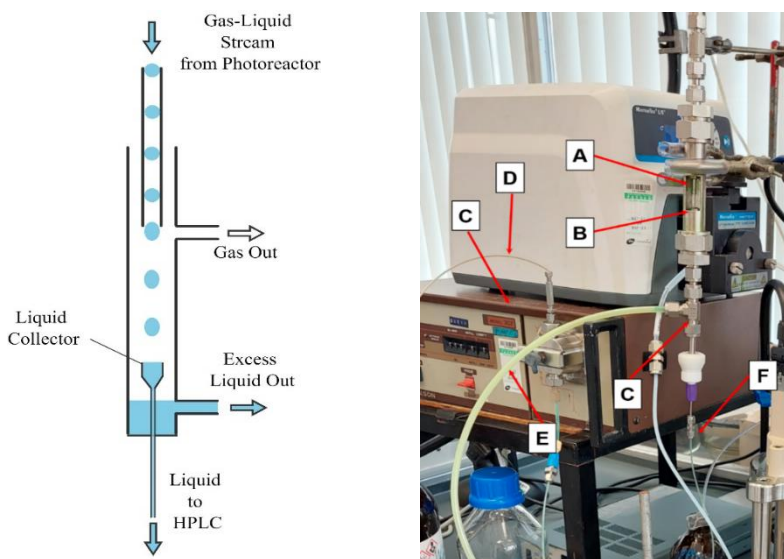


Figure 5.11: Left: Schematic of the Gas-Liquid Separator (GLS) for HPLC sampling. Right: Annotated photo of the GLS. A: The needle B: The well C: Gilson HPLC pump D: PEEK tubing leading to HPLC E: Tubing for excess solvent runoff to waste F: FEP Tubing into Gilson pump

### On-Line HPLC

On-line HPLC analysis was carried out on an Agilent 1260 Infinity II system, using Agilent ChemStation control software. All tubing between the pump head and the UV detector was green stainless steel Agilent capillary tubing (ID 0.17 mm); red PEEK tubing (1/16" o.d. 0.005" i.d.) was used from the outlet of the UV detector to the ELSD. Nitrogen was used as the evaporation gas in the ELSD; the delivery pressure was kept constant for all analysis at 4 bar. The flow rate, recorded as Standard Litre per Minute (SLM), was adjusted depending on the method used.

### Reactor Software and Communications

To facilitate automated reactions, each reactor device is required to be connected to a control computer. In the case of the reactor schematic shown in Figure 5.9, two computers are used. The first, PC1, controls all the reactor devices through the ‘Reactor Controller’ and ‘Self Optimisation Client (SOClient)’ programmes controlled by LabView and MatLab, developed by Dr. Jie Ke of our group. The second, PC2, controls the HPLC software and is also connected to PC1 through the LabView software; this connection allows for the HPLC analysis to be triggered once a reaction has been completed and to transfer the resulting data file to PC1 for interpretation by the SOClient.

The three Jasco® PU-980 HPLC pumps and the Bronkhorst® gas flow controller are directly connected and controlled by PC1 *via* RS232 connections. A fourth Gilson® HPLC pump is used to flow the solution from the outlet of the Gas-Liquid Separator continuously through the HPLC sample loop. This pump, and the PhotoLED controller, do not possess an RS232 connection. To allow for automated control, both are powered through a computer controlled ‘Arduino’ trip box. Once a reaction is triggered, the trip box is activated, sending power to the LED and the pump. Both are kept in ‘on’ mode such that they are automatically turned on when the power is supplied. The HPLC was connected *via* Ethernet connection to PC2.

### Reactor Controller

The Reactor Controller server (“Rig08-Server.exe”) has been created using LabVIEW™ software. The reactor controller is the interface that allows for each of the ‘real’ or ‘virtual’ reactor devices to be controlled. A virtual device is a combined unit consisting of more than one real device. For example, the virtual device of <LT Photo-

Reactor> consists of two pumps, the gas-flow controller and the FP89-ME and the lamp power box as real devices.

Each device driver has two modes - Auto and Manual. Auto mode is used for operating the reactor for self-optimisation experiments. In this mode, the Reactor Controller will be controlled by a MatLab programme which sends instructions to the controller. Manual mode is employed when initiating or stopping optimisation experiments, and is a useful method for assessing the behaviour of each device.

### **Self-Optimisation Client**

The optimisation programme is written in MatLab. The programme has three main functional units: i) user interface, ii) optimisation algorithms, iii) chromatography processing. The Self-Opt Client sends commands to the Reactor Controller, which executes the commands and returns the logged data (ie reactor temperature), and returns the results of the HPLC analysis to the Self-Opt Client.

For any optimisation process, the factors define a multi-dimensional parameter space of interest. Typical examples of factors are: the substrate concentration, flow rate, and reaction temperature etc. The factors and the response (e.g yield, productivity) are not necessarily the parameters directly sent to, or received from, the Reactor Controller. Therefore, two customised MatLab scripts are required to convert the factors to the parameters to be sent to the Reactor Controller and to convert the information received from the controller to the response. There is a third script which processes the HPLC spectrum. The names of the MatLab scripts are shown in Table 5.1.

*Table 5.1: Scripts used by the Self-Optimisation Client.*

Script Name	Function
indep2ctrl.m	Convert the factors to the parameters to be sent to the controller
status2target.m	Convert the information received from the controller to the response
hplcimport.m	Process HPLC data

The Self-Opt Client has a number of run methods, allowing for the processes to be run in partial or full automation. Full automation adheres to processes controlled by algorithms, such as SNOBFIT or Simplex. Partial processes follow a list style approach where the parameters for each iteration are input by the user; the computer runs through

the script, adjusting the parameters accordingly. List runs allow for testing of the scripts after alteration and for Design of Experiment (DoE) runs to be carried out. The method type and all of the parameters (e.g the lower and upper bounds of each factor) are defined within the ‘Experiment File’.

### **Experiment File**

The Experiment File is Text file that is loaded into the Self-Optimisation Client and allows the user to input various descriptions and details of the automated experiment and, most importantly, allows the user to specify the type of experiment to be performed. Within Section 1 of the Experiment file, shown in Figure 5.12, the operator can define the ‘real’ devices attached to the rig, along with the ‘virtual’ devices that are controlled by the RigController. The virtual device ‘RigCtrlVirtualDevice8’ corresponds to <LT Photo-Reactor> and is composed of attached devices 1, 2, 3, 5 and 6. The Gilson HPLC does not possess an RS232 connection and as such is defined as a manually controlled device. Highlighted in Section 2 is the ‘RunMethod’. This allows the user to specify the experimental method to be performed. Methods can either be semi-automated such as the List method, or fully automated self-optimising such as SNOBFIT or Modified Simplex methods. The independent variables are also set in this section. Here four variables are set:

1. Photoreactor Temperature - Julabo FP-89 ME temperature in °C
2. The liquid flow rate in mL min<sup>-1</sup>
3. The substrate concentration in mol dm<sup>-3</sup>
4. The molar gas ratio

Section 3 allows the user to define the constraints of each of the independent variables for automated methods such as Ramp, SNOBFIT and Simplex. Within the [Range] of each independent variable, the first, second and third values define the start, end and the step-size respectively. The fourth value defines the starting value for Simplex experiments. Within Section 2 the run method is set as a LIST method, in Section 4 the number of Runs to be performed is set along with the values of each of the four independent variables, with **1 – 4** set from left to right.

Section 1	Section 3
<pre> RigName = Rig04 # Devices attached to the rig AttachedDevice1 = Jasco pump PU-980(Pump A, COM21) AttachedDevice2 = Jasco pump PU-2085Plus(Pump B, COM22) AttachedDevice3 = BH gas flow meter (COM23) AttachedDevice4 = Picologger USB-TC08 (USB) AttachedDevice5 = Julabo low temperature water bath(COM28) AttachedDevice6 = Power switch for lamp (COM31) AttachedDevice7 = HPLC (Agilent 1260 II with UV and ELSD, HPLC3Server IP = 192.168.254.100:25030) AttachedDevice8 = Gilson HPLC pump # Virtual Devices controlled by RigController (LabView application) RigCtrlVirtualDevice1 = AttachedDevice1 RigCtrlVirtualDevice2 = AttachedDevice2 RigCtrlVirtualDevice3 = AttachedDevice3 RigCtrlVirtualDevice4 = AttachedDevice4 RigCtrlVirtualDevice5 = AttachedDevice5 RigCtrlVirtualDevice6 = AttachedDevice6 RigCtrlVirtualDevice7 = AttachedDevice7 RigCtrlVirtualDevice8 = AttachedDevice1+2+3+5+6 # Devices operated manually ManuallyOperatedDevice1 = AttachedDevice8 (set flow rate to 0.7 ml/min) </pre>	<pre> # Define the range etc. used for [Ramp]/[Snobfit]/[SuperModSimplex]/[SuperModSimplex3]/[MSimplex]/[MSimplex2]/[MSimplex3]. # All independent variables must be a number (DBL or U32). # The first, second and third parameters are start, end and stepsize, respectively. # The fourth parameter in the [Range] section is the starting point for [SuperModSimplex]/[MSimplex]/[MSimplex2]/[MSimplex3]. # The fifth parameter TolXI for each independent variables. [Range]  IndepVar1 = -80.0 0.0 10.0 -35.0 10.0 IndepVar2 = 0.5 2.0 0.05 1.25 0.05 IndepVar3 = 0.01 0.10 0.01 0.055 0.01 IndepVar4 = 1.0 5.0 0.1 3.0 0.1 </pre>
Section 2	Section 4
<pre> [Run] ExpNoToStart = 1 AllowToReDoExp = 1 RunMethod = List RunOptSimulator = 0 ExpInfo.PlotAnalysisData = 1 OptSimulationFunctionName = default SingleExpTimeOutinHour = 8.0 ProcQueuePeroidinSecond = 10.0 # DelayOfSamplingInMinute = 43.0 DelayOfSamplingInMinute = 2.0 NumIndependentVar = 4 IndepVarName1 = Bath Temp IndepVarName2 = Liq FR IndepVarName3 = Conc IndepVarName4 = Gas ratio </pre>	<pre> [List]  Run1 = 20 1.0 0.05 1.0 Run2 = 20 2.0 0.05 1.0 Run3 = 20 1.0 0.05 2.0 </pre>

Figure 5.12: Four sections taken from an example Experiment File. This does not depict the full file.

### Indep2ctrl.m

The indep2ctrl.m script converts the reaction factors (that are set within the experiment file as the independent variables) to control parameters that are sent to the reactor controller. Within this script, the operator can define metrics that will adjust these parameters and, hence, the controller output. There are 13 control parameters, as shown below and in Figure 5.13:

1. Trigger a new experiment, set to 1 to trigger an experiment and 0 for no experiment to be run.
2. Julabo FP89 ME Recirculating chiller temperature. Defined by independent variable **1**.
3. Maximum allowed deviation of the FP89-ME temperature from the set value, measured in °C. The default value is 2°C.
4. Standard deviation limit of the FP89-ME temperature. The default is 1.0 °C. If the standard deviation of the measure temperature in a given period, defined by control parameter 9, is less than set standard deviation limit then the system temperature is considered stable and an experiment will be triggered.
5. Flow rate of Jasco Pump 1, in  $\text{mL min}^{-1}$
6. Flow rate of Jasco Pump 2, in  $\text{mL min}^{-1}$
7. Gas flow rate
8. A waiting period between the devices acquiring the parameters for the new experiment and the experiment starting. Defined in seconds.
9. The minimum wait time for the system temperature to reach a steady state in which the measured temperature standard deviation remains below the limit set in control parameter 4. The default value is 600 s
10. The wait time for the reaction to reach a steady state, i.e. the reaction equilibration time. This parameter depends on the total flow rate, independent variable **2**, and the volume of the reactor, which is set within ctrlpara(10), as shown in Figure 5.13., and is defined in seconds. It essentially provides a steady state wait time equal to the time taken for two reactor volumes of material to pass through the reactor.
11. The wait period after reaction equilibration time has been completed before the HPLC triggers analysis. It gives extra time for the HPLC sample loop to reach a steady state.
12. Once all the previous control parameters have been completed, control parameter 12 triggers the HPLC rotor valve to switch from the ‘waste’ position

to the ‘external’ and hence injecting the contents of the sample loop into the HPLC.

13. Control parameter 13 assesses whether the HPLC analysis result has been successfully received by the Self Optimisation Client. If the report has been received and the analytes successfully detected and quantified then the next experiment will be triggered. If an issue occurs with the SOClient being unable to interpret the HPLC results, then the experiment will be automatically restarted.

The first two lines of code that are of interest to the operator in Figure 5.13 are – ‘SubstrateConc\_high = X’ and ‘SubstrateConc\_low = Y’. These allow the user to set the substrate concentration in each of the reagent feeds for the input HPLC Pumps 1 and 2. These values are then used along with the value of independent variables **2** and **3**, to define Control Parameters (ctrlpara) 6 and 7, the individual flow rates of Pumps 1 and 2 respectively, such that the correct level of dilution can occur to deliver the set substrate concentration during the reaction.

The delivery of the appropriate oxygen flow rate by the Bronkhorst ® gas flow controller is defined by Control Parameter 7, equation 5.2. The ‘GasConvertFactor’ converts the gas delivery from units of  $\text{mol min}^{-1}$  to a percentage, a unit that can be interpreted by the gas flow controller. To calculate the ‘GasConvertFactor’ the molar volume of the gas under ideal conditions,  $24.05 \text{ dm}^3 \text{ mol}^{-1}$  equal to  $24050 \text{ mL mol}^{-1}$ , is divided by the value of 1 % of the ‘FullScaleGasController’, the maximum (100 %) flow rate of the gas controller. In Figure 5.13 this value is set to  $30 \text{ mL min}^{-1}$ . 1 % of this value is  $0.3 \text{ mL min}^{-1}$ ; therefore, the GasConvertFactor is defined as equation 5.3 in units of  $\text{min mol}^{-1}$ . Following through the units of equation 5.2, they each cancel out producing a percentage value to deliver to the gas flow controller.

```
ctrlpara{7} =  
SubstrateConc*TotalFlowRate*0.001*GasRatio*GasConvertFactor      5.2
```

```
GasConvertFactor = 24050/0.3                                         5.3
```

```

function ctrlpara = indep2ctrl(indepvar)

global ExpInfo;

SubstrateConc_high = 0.25;
SubstrateConc_low = 0.00;
FullScaleGasController = 30;
GasConvertFactor = 24050/0.3;

ReactorTemp = indepvar(1);
TotalFlowRate = indepvar(2);
SubstrateConc = indepvar(3);
GasRatio = indepvar(4);

ctrlpara{1} = 1;
ctrlpara{2} = ReactorTemp;
ctrlpara{3} = 3.0;
ctrlpara{4} = 1.5;
ctrlpara{5} = round(TotalFlowRate*(SubstrateConc-SubstrateConc_low)/(SubstrateConc_high-SubstrateConc_low),3);
ctrlpara{6} = round(TotalFlowRate*(SubstrateConc_high-SubstrateConc)/(SubstrateConc_high-SubstrateConc_low),3);
ctrlpara{7} = SubstrateConc*TotalFlowRate*0.001*GasRatio*GasConvertFactor;
ctrlpara{8} = 60;
ctrlpara{9} = 60;
ctrlpara{10} = round(2*('Reactor Volume'/TotalFlowRate*60,1);
ctrlpara{11} = round(5/TotalFlowRate*60,1);
ctrlpara{12} = 1;
ctrlpara{13} = 0;

WaitforExtraTimeInMinutesBeforeStartingAnaly = 2.0/60.0;

if ExpInfo.AllowToReDoExp == 0
    DelayOfSamplingInMinute = 120.0/60.0;
else
    DelayOfSamplingInMinute = ExpInfo.DelayOfSamplingInMinute;
end
ThisRow = ExpInfo.QueueTable.NumRowTableHead+ExpInfo.QueueTable.ExpNoLastAvailable+1;
ExpInfo.QueueTable.List{ThisRow,12} = num2str(WaitforExtraTimeInMinutesBeforeStartingAnaly);
ExpInfo.QueueTable.List{ThisRow,13} = num2str(DelayOfSamplingInMinute);
end

```

Figure 5.13: Example of the *indep2ctrl.m* MatLab script file.

### Status2target.m

The *status2target.m* script file analyses the HPLC data from each completed experiment. The HPLC data is received in the form of a Text File as shown in Figure 5.15. It is from this file that the data is interpreted by the *status2target.m* script within the Self Optimisation Client.

First, in Section 1 of *status2target.m*, Figure 5.14, the user inputs the gradient coefficient and intercept of the analyte calibration equations into *HPLCLinearEqCoeff(IDComp,X)*. Where ‘IDComp’ identifies the analyte, and is expressed later within the script. The value of X indicates the identity of the coefficient of the calibration equation, with the intercept and gradient indicated by X=1 and X=2, respectively. The starting material, DHAA, is defined as *IDComp* = 1 and the product, artemisinin is defined as *IDComp* = 2.

Section 2 of the script is where the methods of detection of each of the analytes is input. This is done simply by defining the start and end search tags,

‘HPLCProcOptions.SectionStartTag’ and ‘HPLCProcOptions.SectionEndTag’, of the received data text file; this instructs the script to analyse a specific section of the data file. In Section 2 of Figure 5.14, the start and end tags for the analysis of the starting material are set to ‘SignalDAD1 C’ and ‘SignalELS1 A’ respectively. Relating this to the example data file of Figure 5.14, the script has been instructed to begin the search of the compound from the line of text ‘SignalDAD1 C’ and scan until it reaches ‘SignalELS1 A’. This results in the script analysing just the data output from the UV spectrometer at 210 nm. Further within the section, the retention time and allowed margin of error of the analyte are set as ‘HPLCProcOptions.CompRT’ and ‘HPLCProcOptions.CompRTError’ respectively. If a signal retention time is found within the window, the corresponding area is analysed as HPLCAnalysisResults (IDComp). Further lines, ‘HPLCProcOptions.AreaUpperLimit’ and ‘HPLCProcOptions.AreaLowerLimit’ allow for maximum and minimum peak area limits to be set. This is of use where there may be the presence of interfering compound peaks of relatively low area. If the area of these peaks falls below the limit, they will not be analysed, hence improving the selectivity of the detection to the target analyte. The remaining lines for each analyte analysis refer to the column number of the data text file in which to find the retention times, peak areas and peak heights.

In Section 3 the concentrations of the starting material and product are calculated from the determined peak areas, as HPLCAnalysisResults(IDComp) and the calibration equation coefficients. The analyte concentration is denoted as ‘ConcList(IDComp)’. Hence, the starting material concentration is calculated using equation 5.4, while equation 5.5 determines the product concentration. The yield is calculated by equation 5.6, in which Figure 5.13 ‘ConcReactant’ is the starting material concentration and is defined within the Experiment File.

$$\text{ConcList}(1) = \text{HPLCLinearEqCoeff}(1,1) \quad 5.4$$

$$+ \text{HPLCLinearCoeff}(1,2) \times \text{HPLCAnalysisResults}(1)$$

$$\text{ConcList}(2) = \text{HPLCLinearEqCoeff}(2,1) \quad 5.5$$

$$+ \text{HPLCLinearCoeff}(2,2) \times \text{HPLCAnalysisResults}(2)$$

$$\text{YieldFromHPLC} = (\text{ConcList}(2) / \text{ConcReactant}) \times 100 \quad 5.6$$

<b>Section 1</b>
<pre>% Compound1 (starting material) (y = mx + c) Conc(mol/L) = HPLCLinearEqCoeff(1,1)+HPLCLinearEqCoeff(1,2)*Area     HPLCLinearEqCoeff(1,1) = c;     HPLCLinearEqCoeff(1,2) = m; % Compound2 (product) (y = mx + c) Conc(mol/L) = HPLCLinearEqCoeff(2,1)+HPLCLinearEqCoeff(2,2)*Area     HPLCLinearEqCoeff(2,1) = c;     HPLCLinearEqCoeff(2,2) = m;</pre>
<b>Section 2</b>
<pre>IDComp = 1; fprintf('Look at Coumpound %d in HPLC report file (status2target.m)\n', IDComp); HPLCProcOptions.SectionStartTag = 'SignalDAD1 C,'; HPLCProcOptions.SectionEndTag = 'SignalELS1 A,'; HPLCProcOptions.SectionHeadLineTag = 'Area'; HPLCProcOptions.SectionExcludingTag = 'Sum'; HPLCProcOptions.CompRT = X; HPLCProcOptions.CompRTError = X; HPLCProcOptions.AreaLowerLimit = 0.0; HPLCProcOptions.AreaUpperLimit = 1e6; HPLCProcOptions.ColNumForRT = 1; HPLCProcOptions.ColNumForArea = 3; HPLCProcOptions.ColNumForHeight = 4; HPLCProcOptions [PeakRT,PeakArea,PeakHeight,ErrorCode,ErrorMsg] = hplcimport(ResultFileNameArray{1},HPLCProcOptions); HPLCAalysisResults(IDComp) = UpdateHPLCInfo(NoCalled,IDComp,PeakRT,PeakArea,PeakHeight,ErrorCode); IDComp = 2; fprintf('Look at Coumpound %d in HPLC report file (status2target.m)\n', IDComp); HPLCProcOptions.SectionStartTag = 'SignalELS1 A,'; HPLCProcOptions.SectionEndTag = 'Short_Area_SelfOpt1.rdl'; HPLCProcOptions.SectionHeadLineTag = 'Area'; HPLCProcOptions.SectionExcludingTag = 'Sum'; HPLCProcOptions.CompRT = Y; HPLCProcOptions.CompRTError= Y; HPLCProcOptions.AreaLowerLimit = 0.0; HPLCProcOptions.AreaUpperLimit = 1e6; HPLCProcOptions.ColNumForRT = 1; HPLCProcOptions.ColNumForArea = 3; HPLCProcOptions.ColNumForHeight = 4; HPLCProcOptions; [PeakRT,PeakArea,PeakHeight,ErrorCode,ErrorMsg] = hplcimport(ResultFileNameArray{1},HPLCProcOptions); HPLCAalysisResults(IDComp) = UpdateHPLCInfo(NoCalled,IDComp,PeakRT,PeakArea,PeakHeight,ErrorCode); catch     ErrorCode = -1000;    ErrorMsg = 'Invalid AnalysisResult Data File (status2target.m)'; end</pre>
<b>Section 3</b>
<pre>ConcList(1) = (HPLCAalysisResults(1)- HPLCLinearEqCoeff(1,1))/HPLCLinearEqCoeff(1,2); ConcList(2) = (HPLCAalysisResults(2)- HPLCLinearEqCoeff(2,1))/HPLCLinearEqCoeff(2,2);  ConcReactantStr = ExpInfo.QueueTable.List{ExpInfo.QueueTable.NumRowTableHead...     +ExpInfo.ThisExpNum,ExpInfo.QueueTable.LastColExpQueueSection+3}; ConcReactant = sscanf(ConcReactantStr, '%f'); ConvFromHPLC = ((ConcReactant-ConcList(1))/ConcReactant)*100.0; YieldFromHPLC = (ConcList(2)/ConcReactant)*100.0; TargetFunc = 200.0-YieldFromHPLC; else</pre>

Figure 5.14: Example of status2target.m script file. The file has been reduced to show only the features that are of interest to the operator.

Area Percent Report					
SignalDAD1 C, Sig=210,4 Ref=off					
:					
RT [min]	Width [min]	Area	Height	Area%	Name
0.512	0.08	7.865	1.322	0.02	
0.880	0.06	12.004	2.846	0.03	
1.213	0.07	83.494	18.217	0.22	
1.499	0.06	149.978	34.388	0.40	
1.607	0.06	1108.337	271.205	2.94	
1.974	0.10	1089.484	150.530	2.89	
2.205	0.05	25.932	8.086	0.07	
2.293	0.12	13642.734	1541.640	36.19	
3.088	0.13	16499.654	2084.312	43.77	
3.555	0.13	18.454	2.212	0.05	
3.811	0.12	11.042	1.513	0.03	
4.212	0.17	31.885	2.930	0.08	
4.628	0.17	260.853	23.863	0.69	
5.066	0.27	136.364	7.703	0.36	
5.652	0.29	275.084	14.443	0.73	
7.026	0.23	21.642	1.345	0.06	
7.585	0.27	196.223	10.768	0.52	
8.052	0.26	943.856	56.683	2.50	
9.118	0.33	2154.358	104.013	5.72	
11.272	0.19	12.070	1.038	0.03	
12.080	0.52	849.073	25.821	2.25	
13.157	0.42	164.212	6.047	0.44	
		Sum	37694.5972		
SignalELSD1 A, ELSD Signal					
:					
RT [min]	Width [min]	Area	Height	Area%	Name
1.975	0.08	71.642	13.195	3.23	
2.338	0.10	941.989	135.401	42.51	
2.653	0.07	593.758	125.670	26.79	
3.554	0.11	21.234	3.130	0.96	
5.003	0.13	275.439	32.831	12.43	
12.494	0.24	311.943	16.520	14.08	
		Sum	2216.0054		
Short_Area_SelfOpt1.rdl		Printed: 2/10/2022	Page 2 of 2		
[Rev.		5:03:31			
9]		PM			

Figure 5.15: Section of a HPLC data Text File, downloaded after successful completion of an automated reaction and HPLC method and interpreted by the status2target.m script file of the SOClient.

## Automated Sequence of Events

Upon initiation of an automated reaction sequence:

1. Signals are sent from the ‘Reactor Controller’ to each of the devices, setting the initial reaction parameters.
2. The Julabo® FP89-ME recirculating chiller, is activated and attempts to reach the initial target temperature. The Jasco® PU-980 HPLC pumps receive the initial flow rate information that corresponds to the total flow rate and concentration of the substrate. The pumps and all other devices remain in standby until the chiller has remained at the target temperature within a set deviation window for a defined period. These are specified within the indep2ctrl.m script file detailed later.
3. Once the temperature has reached a steady state the reaction is triggered, activating the Jasco® HPLC pumps and the gas flow controller. The Arduino

trip box is also activated, turning on the PhotoLED and the Gilson HPLC sampling pump.

4. The reaction proceeds for a defined equilibrium time, dependent on the substrate flow rate and the total reactor volume. These parameters are specified within the ‘Experiment File’ and the indep2ctrl.m script.
5. Once the reaction has reached a steady state, additional time is allocated to ensure the filling of the HPLC sample loop has also reached a steady state.
6. Upon completion of all the equilibrium times, the reactor devices are deactivated and the HPLC analysis sequence is triggered. The HPLC analysis method is initiated simultaneously with the rotation of the 6-port valve, switching the sample loop position from ‘waste’ to ‘external’ and, hence, introducing the sample solution into the HPLC.
7. During the HPLC analysis the <LT photoreactor> is in idle mode waiting for a return signal from the HPLC computer. During the idle mode, all devices are switched off except for the FP89-ME which remains at the set reaction temperature.
8. The resulting HPLC data is sent to PC1 in the form of a text file. The SOClient interprets the data. If an issue occurs such as a ‘missing’ analyte peak the run will have failed and the process will be automatically restarted. If all analytes are successfully quantified, the subsequent reaction parameters will be sent to the appropriate devices, and the process repeated from that point.

### 5.5.2. Issues with RS232 Connection to FP89-ME Control Unit

During multiple automated experiments, connection between the control computer and the FP89-ME control unit was lost mid-sequence. Diagnostic tests found that the RS232 communication board of the unit was damaged. This occurred despite there being a surge protector attached to the RS232 connection cable and a protector attached to the unit’s power lead. The unit was returned to the manufacturer for replacement of the communication board. The replacement of the board resolved the connection issue. However, damage to the board occurred on two subsequent occasions, after the first of which the unit was once again sent to the manufacturer for repair. The unit was eventually repaired and modified to prevent the damage from occurring again; however, the period of FP-89ME controller head downtime was significant. During this time two alternative set-ups were used to allow testing to continue on the automated reactor.

First, a Julabo F25-HE circulator was connected to the system. The driver developed for the control of the FP-89 ME was also compatible with the F25-HE. Due to the size of the fluid reservoir and serious reduction in cooling capacity compared to the original chiller, the photoreactor was not placed within this recirculator and instead remained with the FP-89 ME. As such, the photoreactor was at ambient temperature and under no control. The connection to the F25-HE simply allowed for all of the drivers in the system to be detected and therefore allow for automated reactions to occur. For tests using this set up the photoreactor temperature was set to 20°C. Second, the control head of a similar unit FP50-ME was used as a replacement for the FP-89 ME. The replacement allowed for the whole chiller to be used with cooling down to -50°C.

### 5.5.3. HPLC Method Development for the Quantification of **18**

Investigations were made using an Agilent 1260 Infinity II HPLC with UV and ELS detection allowing for simultaneous analysis *via* the two techniques, thereby increasing the capability of the system. ELS (Evaporative Light Scattering) is a destructive technique and must be, therefore, placed after the UV detector. As discussed in Chapter 4, the weak UV absorption of **18** resulted in the ELSD being used initially as the primary form of detection, with efforts focussed on the optimisation of the detector parameters to enhance the quantification of **18**.

The ELSD has several key parameters that can be altered. These include the nebuliser temperature, evaporation tube temperature, nitrogen gas flow, and the LED intensity. Each of these affects the sensitivity of the detector, as does the composition of the mobile phase. Therefore, the aim of the HPLC method development was to find the optimum combination of mobile and stationary phases along with ideal ELSD parameters, such that sufficient analyte separation occurs with highly sensitive detection of **18**.

The use of HPLC-ELSD for the detection of plant extracted **18** has been reported previously. Lapkin *et al.* opted for an isocratic mobile phase system of 50:30:20 (% v/v) acetonitrile : water : methanol with a reverse-phase octadecylsilyl (C18) column (Betasil™ 5µm, 100Å, 250 x 4.6 mm) at a column temperature of 40°C and a flow rate of 1.0 mL min<sup>-1</sup>. The ELSD was set to a nitrogen flow rate of 3.6 SLM (Standard Litre per Minute) and an evaporator temperature of 55°C. There is no information on a nebulisation temperature.<sup>295</sup> In this work, a comparison was made between the triphasic mobile phase and a biphasic mixture of 65:35 (% v/v) acetonitrile : water, finding that

the former eluted artemisinin earlier (ca. 7 minutes *versus* 9 minutes) with a sharper peak. The decrease in retention time and, hence, overall method time, is important in the context of self-optimised reactions that contain large numbers of experiment iterations. Liu *et al.* instead used a more typical isocratic biphasic system of 60:40 (% v/v) acetonitrile : water, with a reverse-phase C18 column (Agilent 5 $\mu$ m, 100 $\text{\AA}$ , 150 x 4.6 mm) at a temperature of 30°C and a flow rate of 1.0 mL min<sup>-1</sup>. The optimal ELSD conditions were a N<sub>2</sub> flow rate of 2 SLM and an evaporator temperature of 70°C. The nebuliser temperature was not specified.<sup>293</sup>

#### 5.5.3.1. Preliminary HPLC Conditions

The initial HPLC and ELSD parameters used in this work are based on these two studies. ELS performance is highly sensitive to detector parameters: mobile phase composition, the warm-up and stabilisation times, the stability of the gas pressure, and gas flow rate, all influence detection.<sup>295,301,318</sup> Response also increases with eluent volatility; the increase in volatility reduces condensation on the wall of the nebulisation chamber and more product travels through the drift tube to be detected.<sup>319</sup> This effect works in tandem with the nitrogen flow rate; larger droplets are formed at lower N<sub>2</sub> flow rates, resulting in excessive signal noise. Therefore, increasing the flow rate decreases the signal response.<sup>320</sup> There is a compromise between noise reduction and gas consumption; thus, it was decided that the lower N<sub>2</sub> flow rate of 2.0 SLM should be used initially as opposed to 3.6 SLM, as suggested by Lapkin *et al.* Detector response is also reduced at higher drift tube temperatures; therefore, the lower evaporation temperature of 55°C was selected as opposed to 70°C. If the sensitivity was found to be too high, indicated by detector saturation, this could be alleviated by increasing gas flow rate and/or increasing evaporator temperature. The preliminary HPLC and ELSD conditions used for the following investigations are outlined in Table 5.2.

Table 5.2. HPLC conditions for the preliminary investigations into the detection of artemisinin using UV and ELS detection.

HPLC	Column	Phenomenex Luna C18, 5 $\mu$ m, 250 x 4.6 mm
	Mobile Phase	50:30:20 (% v/v) acetonitrile : water : methanol
	Sample Loop / $\mu$ L	5
	Temperature / °C	40
	Flow Rate / mL min <sup>-1</sup>	1.0
	UV / nm	210 nm
ELSD	Nebuliser Temperature / °C	40
	Evaporator Temperature / °C	55
	N <sub>2</sub> Flow Rate / SLM	2
	N <sub>2</sub> Inlet Pressure / bar	4.0
	LED intensity / %	100
	Gain	1

## Mobile Phase Testing

### Sample Solvent

Typically, HPLC analysis is conducted using the same solvent mixture as the mobile phase. However, to reduce potential variation, all analyses and calibrations employed the reaction solvent. Dichloromethane (DCM) is the most frequently used reaction solvent in this research. A blank DCM injection produced large signal at 210 nm, with a retention time of approximately 3.5 minutes; no signal was observed in the ELSD.

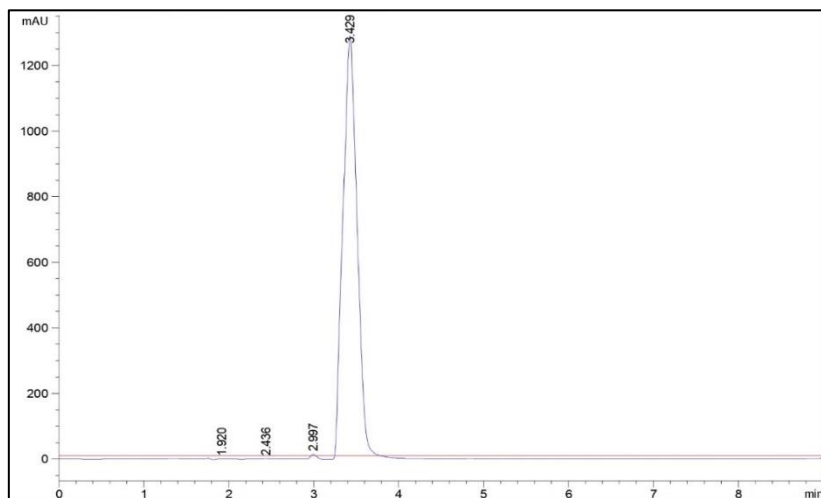


Figure 5.16: DCM analysed via the initial HPLC and ELSD conditions. No peak observed in the ELSD, shown in red, but a strongly absorbing peak shown in 210 nm at 3.43 minutes, in blue.

Biphenyl has been commonly used within this work as an internal standard for NMR analysis. The aromatic structure of biphenyl results in a high degree of absorption of low wavelength UV light. Biphenyl therefore presents a potential risk to the quantification of analyte compounds using low wavelength 210 nm UV detection. To assess this impact, biphenyl, at a standard concentration of 6.5 mM in DCM, was analysed by HPLC. Figure 5.17 indicates that biphenyl does indeed produce a strong signal with 210 nm eluting at 11.91 minutes, while no peak is present for the ELSD, likely due to the low concentration and moderate volatility of the compound.

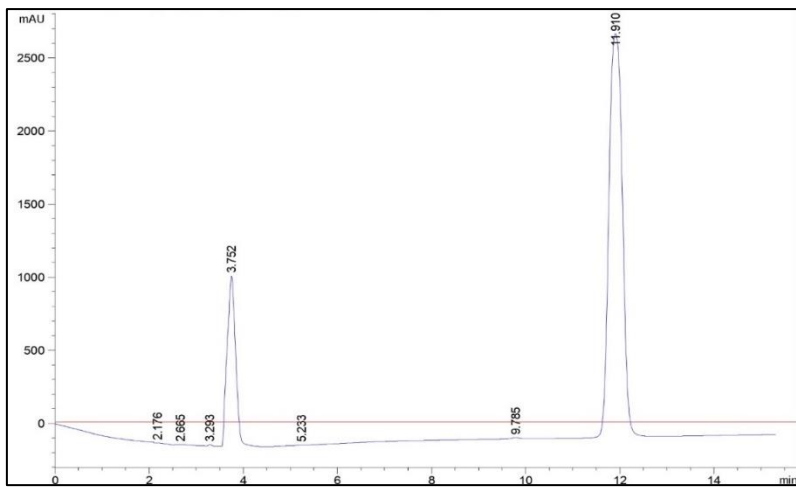


Figure 5.17: *HPLC-ELSD* and *HPLC-210nm* analysis of biphenyl in DCM under preliminary mobile phase and ELSD conditions. A strong signal is found for biphenyl under UV detection with an elution time of 11.910 minutes, no corresponding signal is found in the ELSD, due to the low concentration of the compound.

### Synthesis of **18** to Test HPLC Conditions

Successful On-line analysis of **18** is dependent on the resolution of the analyte peak from the other compounds present. The mobile phase outlined in Table 5.2 was developed for the separation of plant extracted compounds; not all of these are present in the photochemical reaction, whereas several other compounds of varying structures are. To assess the separation, a solution of photochemically produced **18** was injected onto the HPLC. The UV and ELSD spectra of the injection are shown superimposed in Figure 5.18, highlighting the peaks attributed to **18**, **14** as well as DCM and biphenyl. These peaks were determined by comparing the retention times to those observed from isolated injections of each compound. NMR analysis of the photoproduct indicated a yield of 61 % (0.0305 M) for **18** and 96 % (0.002 M) conversion. At these concentrations, only **18** is detected in the ELSD. There is no indication of significant side products eluting in areas that would cause issues for detection.

Table 5.3. Compound elution times for the injection of photochemically synthesised artemisinin, shown in Figure 5.18. The HPLC and ELSD conditions are outlined in Table 5.2.

Compound	UV Retention Time / min	ELSD Retention Time / min
Artemisinin	7.11	7.37
DHAA	17.71	-
Biphenyl	11.27	-

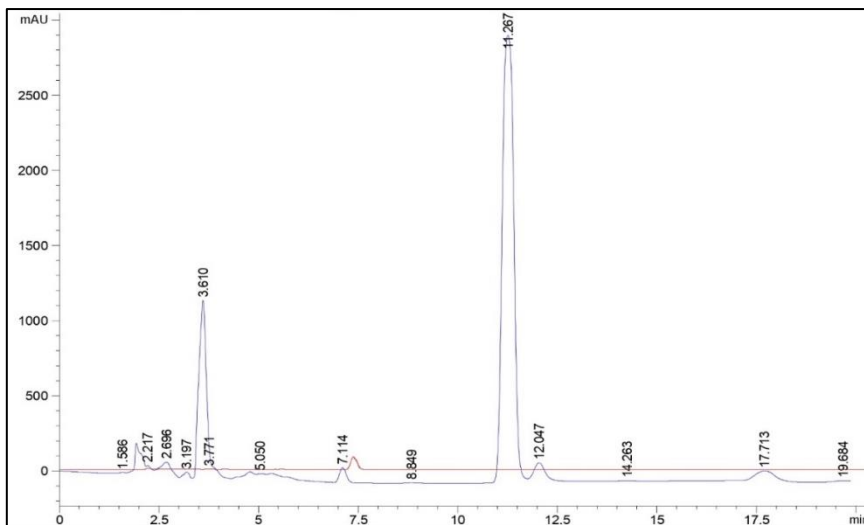


Figure 5.18: *HPLC-210 nm* and *HPLC-ELSD* chromatograms of the photochemically produced artemisinin. Mobile phase - 50:30:20 (% v/v) acetonitrile:water:methanol, 40°C at 1.0 mL min<sup>-1</sup>.

#### 5.5.4. ELSD Parameter Optimisation

The analysis of photochemically produced **18** indicated that on the scale of the concentrations produced, only **18** elicited a response in the ELSD, albeit very small. Therefore, the next stage of the development was to find the optimum ELSD parameters to maximise the sensitivity of the detector for **18**.

##### Sensitivity Testing

The typical concentration of DHAA used for the synthesis of artemisinin in this work is 0.05 M and therefore a concentration of 0.05 M was used as the upper limit to determine the detection capabilities of the ELSD.

A standard of 0.05 M artemisinin (0.1412 g) in DCM (10 mL) was injected under the preliminary HPLC conditions (Table 5.2), resulting in a truncated peak in the ELSD with a residence time of 7.6 minutes. The truncation is an indication of detector saturation. A corresponding peak was also observed in the UV at 7.215 minutes. The difference in time reflects the physical distance between the UV detector and the ELSD.

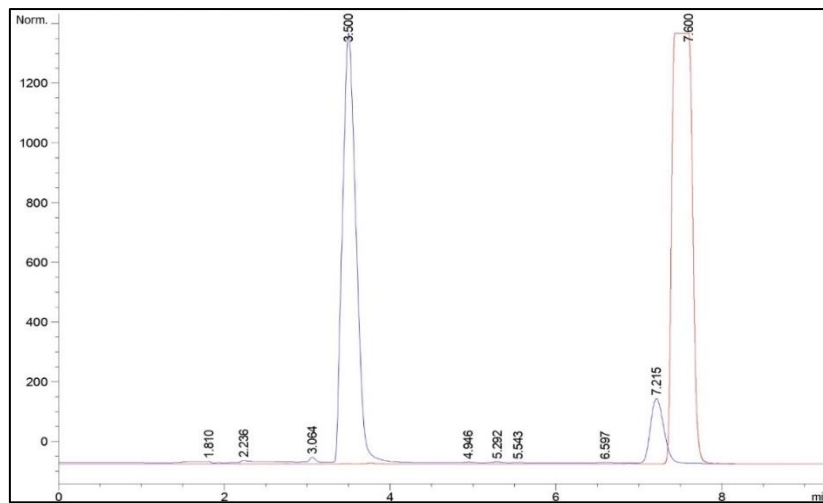


Figure 5.19: Overlaid HPLC chromatograms from the initial analysis of 0.05 M artemisinin in DCM. The 210 nm is depicted in blue exhibiting a strong signal for the solvent, DCM with an elution time of 3.500 minutes and a smaller signal for artemisinin eluting at 7.215 minutes. The ELSD signal is shown in red and exhibits a single signal corresponding to artemisinin with an elution time of 7.600 minutes. The ELSD signal is truncated, an indication that the concentration has led to detector saturation.

The concentration of **18** was reduced to quantify the upper threshold value where saturation is no longer observed. The saturation limit was determined to be a peak height value around 1210 mV; peaks that exhibit this height or greater were deemed to be saturated. As shown in Table 5.4, both 0.025 M and 0.02 M resulted in saturation. The detector response limit was not reached when 0.01 M artemisinin was analysed.

Table 5.4. Artemisinin concentrations and corresponding peak areas and heights while the LED intensity is set to 100 %.

Concentration / M	Peak Area	Peak Height
0.050	19900	1210
0.025	15900	1211
0.020	13673	1212
0.010	6727	718

The LED intensity was reduced and the 0.05 M artemisinin analysed. The highest intensity that did not result in detector saturation was 20 %, resulting in a peak height of 956 mV. Under these parameters a solution of DHAA (0.05 M in DCM) produced a weak signal in the ELSD, eluting at 17.93 minutes with a height of 43 mV. The UV response was far larger and, therefore, more appropriate for detection.

Table 5.5. Peak areas and heights of 0.05 M artemisinin while varying the ELSD LED intensity. A peak height around 1210 mV is regarded to saturate the detector.

LED intensity / %	Peak Area	Peak Height
100	19900	1210
25	12491	1218
20	9727	956
15	6819	667

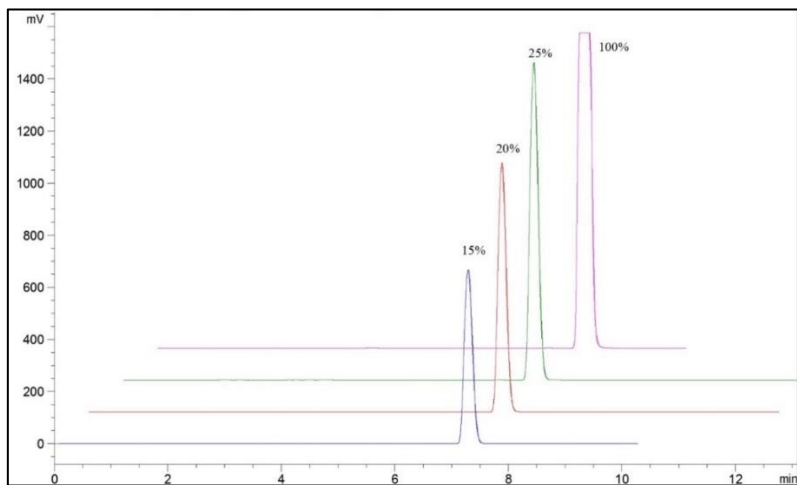


Figure 5.20: HPLC-ELSD chromatograms of the 0.05 M artemisinin standard analysed with varying LED intensity. ELSD parameters – nebuliser temperature 40°C; evaporator temperature 55°C, N<sub>2</sub> flow at 2 SLM.

### 5.5.5. External Artemisinin Calibration 1

The HPLC and ELSD parameters for the first external calibration of **18** are outlined in Table 5.6; the LED intensity was reduced to 20 % to avoid saturation of the detector.

Table 5.6. HPLC and ELSD parameters for the initial artemisinin calibration.

HPLC	Column	Phenomenex Luna C18, 5µm, 250 x 4.6 mm
	Mobile Phase	50:30:20 (% v/v) acetonitrile : water : methanol
	Sample Loop / µL	5
	Temperature / °C	40
	Flow Rate / mL min <sup>-1</sup>	1.0
	UV / nm	210 nm
ELSD	Nebuliser Temperature / °C	40
	Evaporator Temperature / °C	55
	N <sub>2</sub> Flow Rate / SLM	2
	N <sub>2</sub> Inlet Pressure / bar	4.0
	LED intensity / %	20
	Gain	1

## Calibration Standards

Through the serial dilution from a stock artemisinin standard of concentration 0.0484 M, a series of seven standards were prepared. Injections were performed manually through the attachment of a syringe to the inlet port of the 6-valve rotor. Each sample was injected a minimum of three times. For sample sets that contained more than three sets of data, however, the Grubb's test was performed thereby allowing the presence of outliers ( $p$ -value  $< 0.05$ ) to be detected and removed from the data. The relative standard deviation (RSD) was calculated for both the mean retention time and mean artemisinin area within each sample set.

## ELSD Calibration

As discussed in section **Chapter 4**, the relationship between the ELSD response and the analyte concentration is non-linear and is expressed by equation 5.7. To generate a linear response, the peak areas and the analyte concentration are  $\log_{10}$ -transformed, forming equation 5.8).

$$A = \alpha M^b \quad 5.7$$

$$\log(A) = b \cdot \log(M) + \log(\alpha) \quad 5.8$$

Table 5.7 HPLC-ELSD Calibration data. Conditions outlined in Table 5.6.

Standard	Concentration / mol dm <sup>-3</sup>	Peak Area		Log <sub>10</sub>	
		Mean	RSD / %	Concentration	Mean Area
1	0.048	9711	1.18	-1.315	3.987
2	0.039	7158	0.80	-1.412	3.855
3	0.029	4844	0.50	-1.536	3.685
4	0.019	2753	1.31	-1.712	3.440
5	0.010	920	0.90	-2.014	2.964
6	0.005	271	0.58	-2.315	2.432
7	0.002	78	9.10	-2.616	1.895

Concentrations of artemisinin standards for seven point calibration curve. Stock solution A was prepared through the dissolution of 0.274 g of artemisinin in 20 mL of DCM. The subsequent six standards were prepared through serial dilution of standard A.

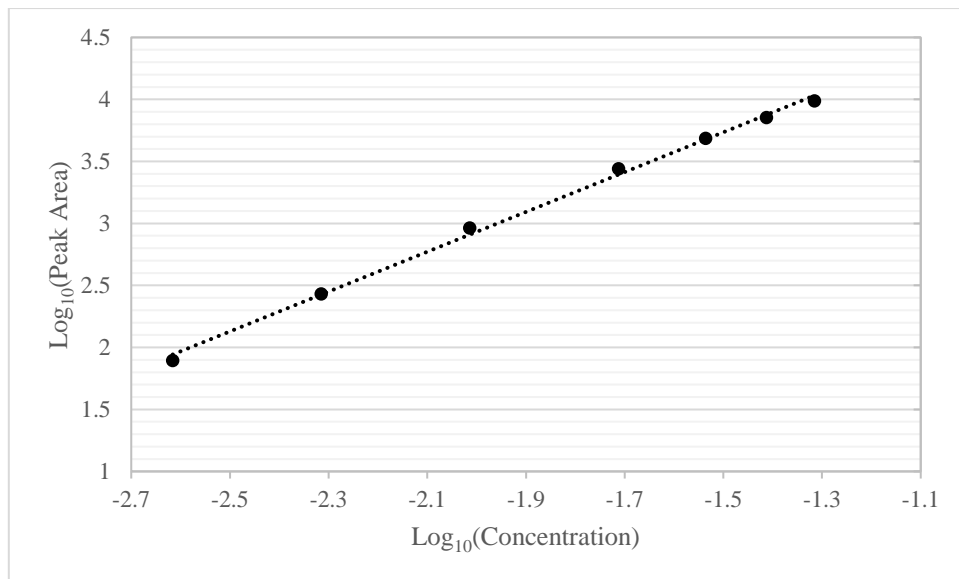


Figure 5.21 Calibration curve for the ELSD. The graph is generated by plotting the log values of the mean peak area against the concentration. The line of best fit produced a straight line equation of  $y = 1.6063x + 6.1447$  (Equation 5.9) with an  $R^2$  value of 0.9973.

The corresponding ELSD calibration curve produced a straight line of equation (5.9) which exhibited a good correlation between the log-transformations of the detector response and the artemisinin concentration, giving a coefficient of determination value ( $R^2$ ) of 0.997.

$$y = 1.61x + 6.14 \quad 5.9$$

The data for the peak area exhibits low RSD values between 0.5 and 1.3 % for samples down to Standard 6. It is only at the very lowest concentration of Standard 7 where the RSD increases significantly to a value of 9.1 %, giving an indication that the ELSD may not be appropriate for precise quantification at low concentrations.

## 210 nm Calibration

Unlike the ELSD, UV detection exhibits a linear response with analyte concentration. As with the ELSD, the variances within the peak areas of Standards 1-5 are low with RSD values below 1 %. However, Standard 6 and 7 exhibit RSD values 2.44 % and 11.12 % respectively. This is not unexpected due to artemisinin being a weak chromophore. Overall, the 210 nm detector exhibits lower RSD values than the ELSD. The seven point calibration curve generated a straight line equation exhibited in equation (1.2) and in Figure 5.22.

$$y = 43157x + 12.1$$

5.10

Table 5.8 HPLC-210 nm artemisinin calibration data. Conditions outlined in Table 5.6.

Standard	Peak Area	
	Mean	RSD /%
1	2069	0.84
2	1706	0.59
3	1275	0.33
4	852	0.33
5	430	0.52
6	218	2.44
7	109	11.12

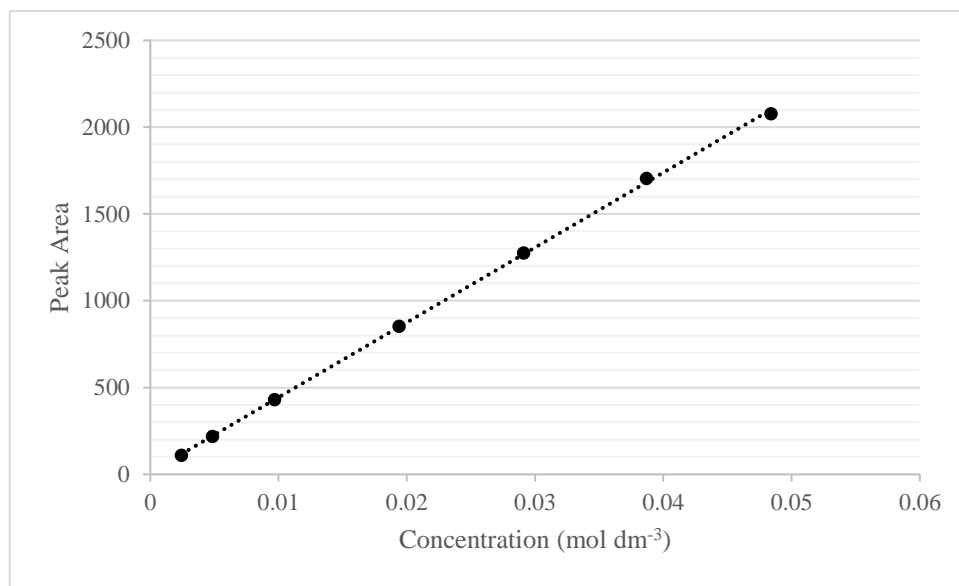


Figure 5.22. Seven point calibration of artemisinin using the 210 nm UV detector. This produced straight line equation (1.2) with good fitting of  $R^2 = 0.9996$ .

### LOQ and LOD

The limit of detection (LOD) and limit of quantification (LOQ) were calculated based on the calibration curve using the formulae:

$$LOD = \frac{3.3\sigma}{S} \quad 5.11$$

$$LOQ = \frac{10\sigma}{S} \quad 5.12$$

Where  $\sigma$  represents the standard deviation of the response and  $S$  is the slope of the calibration curve. In general, the LOD is defined as the lowest concentration of an analyte in a sample that can be detected, but not necessarily quantified. The LOQ is the

lowest concentration of an analyte that can be determined with acceptable precision and accuracy.<sup>321</sup> The LOD and LOQ of the 210 was determined to be lower than that for the ELSD, as shown in Table 5.9; this is in agreement with the finding of Lapkin *et al.*<sup>295</sup>

Table 5.9. LOQ and LODs for the ELSD and 210 nm

Instrument	ELSD	210 nm
LOD(mM)	0.07	0.05
LOQ(mM)	0.21	0.14

## Intra- and Inter-day Precision

### Retention Time Precision

Analysis of the standards was repeated on two subsequent days to assess the inter- and intra-day accuracy and precision. The samples were stored at -20°C when not being used. The retention times of artemisinin showed low intra- and inter- day variation. The highest intra-day RSD value was found for the ELSD on Day 1 with a value of 1.53 %. The inter- day precisions were lower at 1.16 % and 1.14 % for the ELSD and UV respectively.

Table 5.10: Intra- and inter-day precision of the artemisinin retention time in the 210 nm and the ELSD.

Day	ELSD		210 nm	
	Mean RT / min	RSD / %	Mean RT / min	RSD / %
1	7.154	1.53	6.873	1.28
2	7.158	0.97	6.860	1.30
3	7.156	0.81	6.850	1.23
Overall	7.151 (n = 59)	1.16	6.863 (n = 58)	1.14

### Detector Response Precision

The ELSD exhibited reasonably good intra-day precision, with RSD values generally below 2 %; the largest intra-day variation occurred on day 1 Standard 7, the lowest concentration of artemisinin with an RSD of 9.10 %. Larger variation was expected at the lower concentrations, as was observed in the calibration data.

Despite the good intra-day precision of the ELSD, significant variation was found when comparing the inter-day peak areas, with the detector response decreasing from Day 1 to Day 2, with the area remaining relatively constant on Day 3. At first, this

phenomenon may appear to be due to partial decomposition of the standard between Days 1 and 2; however, the UV analysis reveals more precise, consistent peak intra- and inter-day peak areas, where the peak area tends to increase with the day. Decomposition of the product was therefore ruled out; the inconsistency of the ELSD is due to the detector itself.

Table 5.11. Intra- and inter-day RSD calculations of ELSD peak area.

Standard	Day 1		Day 2		Day 3		Inter-day	
	Mean Peak Area	RSD /%	Mean Peak Area	RSD /%	Mean Peak Area	RSD /%	Mean Peak Area	RSD / %
1	9710	1.18	9336	1.86	7988	1.84	9011	10.05
2	7158	0.80	6805	0.94	6078	1.64	6680	8.24
3	4844	0.50	4075	0.37	4094	1.05	4337	10.11
4	2753	1.31	2262	1.34	2322	2.54	2446	10.96
5	920	0.90	768	0.51	789	0.41	826	9.95
6	271	0.58	223	1.63	227	1.45	240	11.02
7	78	9.10	59	0.81	60	1.07	66	16.85

Table 5.12. Intra- and inter-day RSD calculations of 210 nm peak area. Grubbs's outlier tests were carried out on each sample set, a statistical outlier is present if  $p < 0.05$  (95 % confidence interval).

Standard	Day 1		Day 2		Day 3		Inter-day	
	Mean Peak Area	RSD /%	Mean Peak Area	RSD /%	Mean Peak Area	RSD /%	Mean Peak Area	RSD / %
1	2069	0.84	2146	1.36	2136	0.80	2117	1.97
2	1706	0.59	1709	0.50	1741	0.23	1719	1.14
3	1275	0.33	1293	0.67	1309	0.40	1292	1.32
4	852	0.33	863	0.29	883	1.32	866	1.77
5	430	0.52	434	0.09	435	0.69	433	0.62
6	218	2.43	219	0.49	225	3.76	221	1.79
7	109	11.12	111	0.49	108	1.08	109	1.42

## Known Concentration Analysis

Three standards of known artemisinin concentration were analysed in triplicate. The results in Table 5.13 indicate similar results to those of the intra- and inter-day precision calculations - the ELSD exhibited larger deviation from the known concentration of **18**, with values ranging from 6.83 to 16.53 %. The 210 nm UV produced a far narrower range of 1.38 to 2.1 %. The variation along with the >1% deviation can, in part, be attributed to the small sample size which does not allow for statistically irrelevant data

to be omitted from the calculations; hence, mean values are more susceptible to deviation due to the inclusion of outliers.

Along with the intra- and inter-day precision, the analysis of the known concentration samples also highlighted the inadequacy of the ELSD under the current conditions. UV analysis, however, provided acceptable levels of variation and accuracy.

*Table 5.13: Standards of known artemisinin concentration, analysed by HPLC-UV and ELSD. Equations*

Conc. / mM	ELSD				210 m			
	Mean Peak area	RSD /%	Calculated Conc. / mM	Deviation / %	Mean Peak area	RSD /%	Calculated Conc. / mM	Deviation / %
37.8	5808	3.2	33.0	-12.88	1675	2.33	38.6	2.1
18.9	2647	3.6	20.2	6.83	816	4.43	18.7	-1.38
7.6	409	2.45	6.3	-16.53	344	1.18	7.7	1.41

### 5.5.6. External Artemisinin Calibration 2

Due to the unacceptable levels of variation and deviation found with the ELSD, a second calibration was completed. The HPLC and ELSD parameters were identical to the initial calibration conditions as shown in Table 5.6. The artemisinin standards for this calibration were prepared in methanol, rather than DCM. Methanol is less volatile than DCM and therefore less likely to evaporate between analyses. The volatility of DCM may have been a factor affecting the inter-day precision of the previous calibration.

#### Calibration Standards

A stock artemisinin standard (Standard 1) was prepared with a concentration of 0.0502 mol dm<sup>-3</sup>. Through serial dilution a further six standards were produced; concentrations are shown in Table 5.14.

Each standard was analysed five times. Grubb's outlier tests were performed to detect the presence of outliers in each of the data sets. If an outlier was detected (  $p < 0.05$  ) this was removed from the data and the mean value and standard deviation subsequently adjusted to omit this result.

### ELSD and 210 nm Calibration

The initial injection of Standard 1 led to saturation of the ELSD. The LED intensity was reduced by half to 10 %; however, a subsequent injection also led to peak truncation. This issue was alleviated by flushing the column with a 70:30 (v/v %) mixture of acetonitrile : water before increasing the ELSD evaporator and nebulising temperatures to 120°C and 90°C respectively along with increasing the N<sub>2</sub> flow to 2.8 SLM for 30 minutes. This highlighted the importance of proper cleaning of the ELSD between days, especially when water is being used in the HPLC mobile phase.

A seven point calibration curve formed by injecting each standard five times and plotting the log<sub>10</sub> (Mean Peak Area) against log<sub>10</sub> (artemisinin concentration). The plot produced a straight line expressed by equation 5.13, with good linearity, albeit poorer than that of equation 5.9, with a coefficient of determination value (R<sup>2</sup>) of 0.9965.

$$y = 1.533x + 6$$

5.13

Table 5.14: ELSD Peak areas and corresponding RSD values for the second external calibration of 18. Standards produced in methanol. HPLC conditions are outlined in Table 5.6.

Standard	Conc. / mol dm <sup>-3</sup>	ELSD Peak Area		210 nm Peak Area	
		Mean	Mean	Mean	RSD /%
1	0.050	8877	2181	2181	0.41
2	0.040	6853	1760	1760	0.19
3	0.030	4662	1323	1323	0.35
4	0.020	2743	893	893	0.33
5	0.010	970	445	445	0.98
6	0.005	302	223	223	1.19
7	0.003	90	115	115	2.67

The seven point calibration using the 210 nm detector again produced good data with RSD values typically being below 1 %, although increasing to 1.19 % and 2.67 % for the standards containing lowest concentrations of artemisinin, Standards 6 and 7 respectively. The linear response of peak area against concentration produced a straight line of equation 5.14 with a coefficient of determination value of 0.999 indicating a high level of correlation.

$$y = 43405x + 10$$

5.14

## Retention Time Precision

The standards were stored at -20°C and analysed the next day. The first observation of note, as seen in Table 5.15, is the significant reduction in retention times from the previous day and the first artemisinin calibration, despite HPLC conditions remaining constant. On Day 1, for example, over the 35 injections the average retention time of the ELSD is determined to be 6.77 minutes with a relatively low RSD of 0.83 %, far shorter than the 7.15 minutes average of the first calibration. Unexpectedly, the retention times of Day 2 are far shorter than Day 1, with an average of 5.86 minutes for the ELSD.

Table 5.15: Intra- and inter-day precision of the artemisinin retention time in the 210 nm and the ELSD.

Day	ELSD		210 nm	
	Mean RT / min	RSD / %	Mean RT / min	RSD / %
1	6.77 (n = 35)	0.83	6.48 (n=35)	0.86
2	5.86 (n = 21)	1.21	5.55 (n=21)	1.88
Overall	6.43 (n = 56)	7.00	6.13 (n = 56)	7.16

There are two possible explanations for this phenomenon. The first may be a reduction in secondary interactions between the analyte and underderivatised silanol groups of the column. Underderivatised silanol groups in the column interact with the analyte, slowing down their elution and often resulting in peak tailing.<sup>322</sup> A new column requires several priming injections for sample constituents to irreversibly bind to the most active silanol groups. Each subsequent injection becomes exposed to fewer silanol species, reducing the number of secondary interactions and hence shortening retention times. However, this is not expected over the lifetime of the column used.

Second, the decrease in retention time could be indicative of a malfunction with the HPLC pump and mixing, thus altering the composition of the mobile phase. This would not only lead to a change in analyte retention times, but would also affect the sensitivity of the ELSD. A shorter retention time is indicative of a higher organic content within the mobile phase; an increase in acetonitrile would lead to an increase in ELSD response. A change in solvent composition would not result in an adverse effect in the 210 nm analysis. The increase in ELSD peak area is indeed observed on Day 2, along with the significant reduction in retention time as shown in Table 5.16.

## Detector Response

The inter-day deviation observed in the 210 nm data is far lower than that of the ELSD, corresponding to the findings of the initial artemisinin calibration. The ELSD response was found to increase from Day 1 to Day 2. This could be linked to the potential reason for reduced retention times discussed above; increased levels of acetonitrile will increase the volatility of the eluent and, hence, increase the analyte peak area.

Table 5.16: Intra- and inter-day precision of ELSD calibration.

Standard	Peak Area				Peak Area Difference / %	
	Day 1		Day 2			
	Mean	RSD / %	Mean	RSD / %		
1	8877	0.35	9672	0.87	8.22	
2	6853	1.03	7278	3.71	5.84	
3	4662	0.76	5108	1.96	8.73	
4	2743	1.08	3036	1.38	9.65	
5	970	1.96	1084	2.00	10.49	
6	302	1.24	357	0.85	15.35	
7	90	1.41	105	1.25	15.04	

Table 5.17 Intra- and inter-day precision of 210 nm calibration.

Standard	Peak Area				Peak Area Difference / %	
	Day 1		Day 2			
	Mean	RSD / %	Mean	RSD / %		
1	2181	0.41	2176	0.54	0.23	
2	1760	0.19	1737	2.30	1.32	
3	1323	0.35	1325	0.62	0.21	
4	893	0.33	893	0.40	0.01	
5	445	0.98	443	0.48	0.63	
6	223	1.19	227	5.15	1.97	
7	115	2.67	113	1.20	2.48	

## Known Concentration Analysis

Three standards of artemisinin were prepared, analysed by HPLC with five injections each, and the calculated concentration compared to the known value. Again, the data for the 210 nm revealed concentrations close to that of the actual value, at least within error of the standard preparation step. In respect to the 210 nm UV data, equation 5.13 returned more accurate artemisinin concentrations than equation 5.9, a testimony to the use of a larger number of sample injections, reducing the variation within the data.

However, the ELSD did not produce accurate results, with the previous calibration (equation 5.9) exhibiting less varied data. The ELSD retention time over the fifteen injections was determined to be 5.83 minutes with a low RSD of 0.61 %. This is still lower than the retention time of the data used to produce the artemisinin calibration and is, therefore, a likely explanation of the deviation of the ELSD, while the UV remains consistent.

*Table 5.18 Known artemisinin concentration analysis using the ELSD ad 210 nm. The deviation of the calculated concentration from the actual value was determined and the multiple calibrations of the detectors compared.*

210 nm							
				Equation 5.14		Equation 5.10	
Standard	Conc. / mM	Mean Peak Area	RSD / %	Calculated Conc. / mM	Deviation / %	Calculated Conc. / mM	Deviation / %
1	28.3	1243	0.33	28.4	0.30	28.6	0.91
2	16.4	2231	0.28	16.1	-1.85	16.1	-1.50
3	3.8	225	3.43	3.7	-0.85	3.7	-2.32
ELSD							
				Equation 5.13		Equation 5.9	
Standard	Conc. / mM	Mean Peak Area	RSD / %	Calculated Conc. / mM	Deviation / %	Calculated Conc. / mM	Deviation / %
1	28.3	4797	0.95	31.1	9.64	29.3	3.41
2	16.4	2231	0.59	18.9	15.23	18.2	9.90
3	3.8	225	2.52	4.4	16.05	4.4	13.64

### 5.5.7. Issues with ELSD Detection

It became clear that there was an issue with the precision of the ELSD; not only was this observed in the inter-day calibration results but also in the known concentration analysis. Furthermore, seemingly random saturation of the detector was a constant occurrence, often despite the sample not causing saturation during the previous day or even the previous run.

The use of the ELSD LED at 20 % was a potential cause for the observed variation. The reduction in the intensity of the light could lead to a wider fluctuation than when being used at full capacity. However, as previously discussed, the use of the ELSD at full intensity leads to saturation of the peak of **18**. Saturation did not occur at an LED intensity of 20 %, with the 5  $\mu$ L sample loop; therefore, the use of a 1  $\mu$ L sample loop in combination with the LED at 100% was investigated.

To test the new set-up, a 0.05 M solution of **18** was injected onto the column under the typical HPLC and ELSD conditions, Table 5.6, with the LED now set to 100 %. The first observation was the significant increase in pressure within the system when the sample loop is switched to the ‘external’ direction; in this position the eluent is flowing through the sample loop and towards the column. The increase in pressure is due to the very narrow bore of the 1  $\mu$ L PEEK (Vici®) sample loop. The pressure exceeded 300 bar, the pressure limit set for this method, at a flow rate of 1.0 mL min<sup>-1</sup>. The typical pressure of the method using the 5  $\mu$ L loop was around 150 bar. On exceeding the pressure limit, the pump reduces flow rate to a value that brings the pressure below 300 bar; it does not shut down as with other HPLC systems. The sample loop was removed and sonicated in an attempt to remove any blockage; this reduced the pressure when set in ‘external’ mode to 250 bar.

Under the preliminary HPLC and ELSD conditions the detection of 0.05 M artemisinin did not lead to detector saturation, giving an area and height values of 3942 and 470 mV respectively.



Figure 5.23 PEEK Vici® 1 $\mu$ L sample loop with PEEK end fittings. The length of the 1 $\mu$ L sample loop is far longer than that of the 5 $\mu$ L, the corresponding bore diameter is therefore significantly smaller for the 1 $\mu$ L volume, hence the increased pressure in the system.

The ELSD parameters were adjusted to increase the sensitivity towards **18**. A number of parameters led to saturation despite being only minor adjustments from previously working parameters. After many such failed analyses, the original parameters were returned to. These too, however, resulted in detector saturation; the signal for the 210 nm remained consistent and so it was concluded that the anomaly was not due to a change in the sample composition. The saturation issue was only rectified after shutting down the detector and switching back on.

Table 5.19: ELSD parameters and corresponding artemisinin retention time, peak area and peak height for a standard of 0.05 M in DCM. HPLC mobile phase of 50:30:20 acetonitrile : water : methanol at a flow rate of 1.0 mL min<sup>-1</sup> and 40°C column temperature.

Injection	Neb. / °C	Evap. / °C	N <sub>2</sub> / SLM	LED / %	RT / min	Height / mV	Area
1	40	55	2	100	6.53	453	4130
2	40	45	2	100	6.72	692	5747
3	40	45	2	100	7.00	661	5770
4	30	45	2	100	6.99	654	5834
5	30	40	2	100	6.89	1210	14296
6	35	40	2	100	6.63	1210	13597
7	35	45	2	100	6.62	1211	13299
8	35	50	2	100	6.49	1211	13234
9	40	55	2	100	6.62	1211	12663
10	40	55	2	100	6.69	1211	12550
11	40	55	2	100	6.28	1211	12078
ELSD Restarted							
12	40	55	2	100	6.61	548	4070
13	40	50	2	100	6.55	577	4808
14	40	45	2	100	6.59	660	5615
15	40	40	2	100	6.62	879	7197

The parameters of Injection 15, outlined in Table 5.19, were selected for further analysis. The HPLC mobile phase and column conditions remained the same as previously discussed. The height value of 879 mV is expected to be sufficiently large such that the low concentration of **18** is detected, while reducing the chance of saturation.

Due to the change in HPLC conditions, a new calibration was required. During initial injections of a solution of DHAA, **14**, (0.052 M in DCM) with the typical mobile phase of acetonitrile:water:methanol 50:30:20 (v/v %, 1 mL min<sup>-1</sup>, 40°C) a small peak was detected around 6.5 minutes in the UV but not in the ELSD. On first observation, this peak appeared to be residual material from previous runs. However, after column cleaning and injection of the standard, the peak remained. An alternative is that the peak corresponds to artemisinin which typically elutes between 6 and 6.5 minutes under the current HPLC parameters. The spontaneous conversion of dried **14** to **18** and dihydro-*epi*-deoxyartemisinin B, **20**, has been previously reported and discussed *vide supra*.<sup>177,183,184</sup> The conversion occurred after storage of **14** at -20°C in the absence of light for six months, occurring more readily in the presence of ambient light. It is therefore conceivable that through improper storage of **14**, **18** could form on a scale large enough to be detected in the HPLC. However, the lack of a signal in the ELSD disputed the

presence of **18**. Furthermore, a later injection of **14** resulted in no unknown peak. It was later discovered that this peak was due to plasticiser leaching from the injection syringe, the discovery of which is discussed later.

The presence of the plasticiser peak presented a severe issue for the UV analysis of **18**. Attempts were made to adjust the mobile phase to sufficiently separate the plasticiser peak from **18**. However, it proved difficult to find a composition that provides sufficient separation while giving an acceptable peak shape for the later eluting **14**. The plasticiser peak was continuously found to interfere with the peak of **18**; therefore, due to the absence of the plasticiser peak in the ELSD, this was selected as the primary detection method.

**18** was photochemically synthesised and the product solution was injected into the HPLC. The composition of the mobile phase was adjusted to improve the separation and shape of product peaks. Due to quantitative conversion occurring, **14** was added to the product solution such that the effect of the mobile phase composition could be made. A mobile phase composition of 70:30 (v/v %) acetonitrile : 0.1 % acetic acid resulted in a significantly lower retention time for **14**, consequently improving the peak shape. While these metrics were also improved at the less polar composition of 80:20, the significant reduction in retention times of both **18** and **14** can result in peak overlap with other reaction by-products. Therefore, 70:30 was selected as the composition of choice, improving peak shape while maintaining enough selectivity for the product and starting material peaks. The effect of the column temperature at this composition was also briefly investigated, in general the retention times decreased with temperature as expected. 40°C, the typical column temperature used in previous experiments was maintained for future work. Due to the adjustment in mobile phase composition and the use of the 1  $\mu$ L sample loop an external calibration curve was developed. However, during the analysis of **18** a number of previously addressed issues arose once again; oversaturation of the ELSD occurred regularly for the first **18** standard (0.0505 M). This was resolved by restarting the ELSD; however, subsequent injections of the standard gradually increased in peak size towards saturation. The ELSD was cleaned, after which analysis of the standard produced a non-truncated peak of area 9019 and height of 867 mV. The subsequent run, however, under the same conditions resulted in detector saturation. Restarting the ELSD again briefly resolved the issue with the next injection producing a peak of an area and height of 7174 and 682 mV respectively. However, once again the subsequent injection led to saturation.

The ELSD detection issues were constantly encountered in following investigations along with the pressure of the system exceeding the limit of 300 bar. The use of the 1  $\mu\text{L}$  sample loop did not improve the analysis of **18** and regularly led to over-pressure of the system. Therefore, the 5  $\mu\text{L}$  loop was reintroduced.

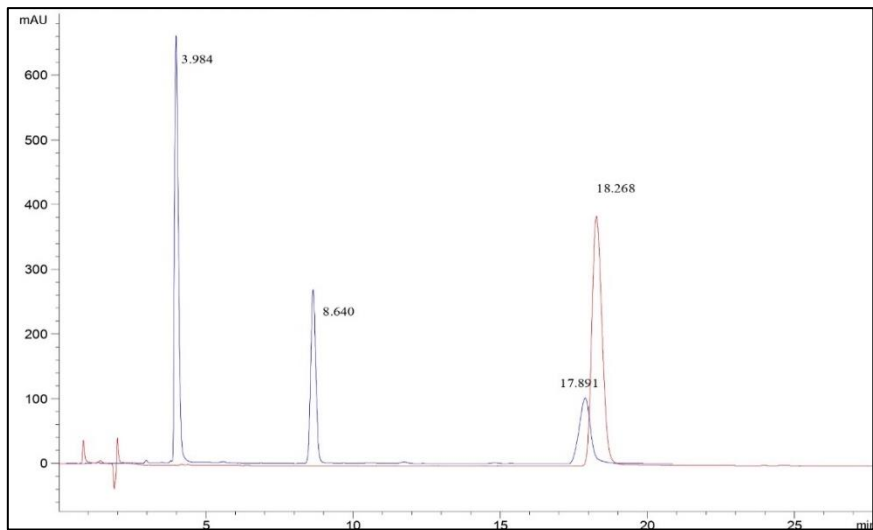


Figure 5.24: DHAA in DCM with a mobile phase composition of 60:40 acetonitrile: 0.1% acetic acid, the plasticiser peak elutes in the 210 nm at 8.64 minutes. Injection of **DHAA** in MeOH, with a mobile phase composition of 60:40 acetonitrile: 0.1% acetic acid. The plasticiser peak is not observed in this injection.

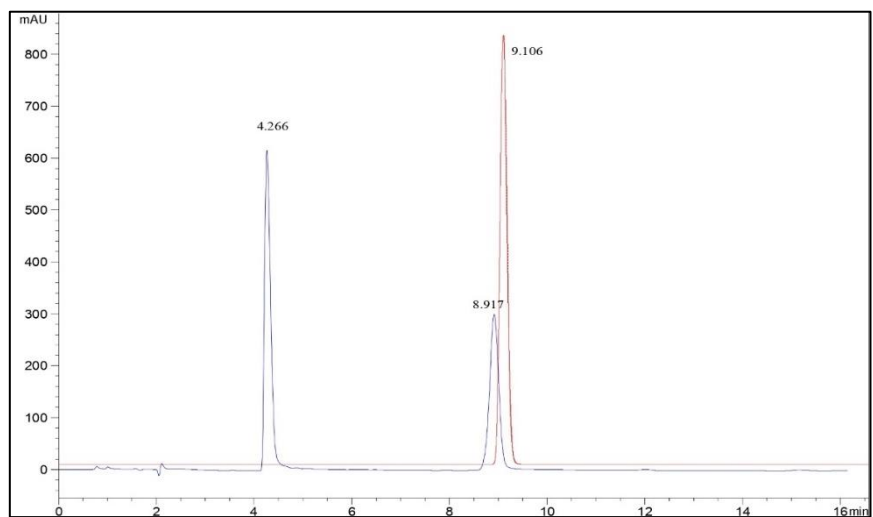


Figure 5.25: Spectra of artemisinin standard, with a mobile phase composition of 60:40 acetonitrile: 0.1% acetic acid. No signal for the unknown peak is observed in the 210 nm or **ELSD** spectra.

Table 5.20 Comparison of artemisinin and DHAA retentions times and peak widths at various mobile compositions.

Mobile phase Composition			Artemisinin		DHAA	
MeCN /%	0.1 % AcOH /%	MeOH / %	Retention Time / min	Width / min	Retention Time / min	Width / min
80	20	-	4.50	0.09	7.21	0.18
70	30	-	6.13	0.11	11.07	0.19
60	40	-	9.16	0.14	19.15	0.24
50	40	10	10.35	0.16	27.19	0.32
50	30	20	7.16	0.12	16.95	0.21

Table 5.21. Effect of column temperature on the retention times of artemisinin and DHAA with a mobile phase of 70:30 (v/v %) acetonitrile : 0.1 % acetic acid at a flow rate of 1.0 mL min<sup>-1</sup>.

Column Temperature /°C	Artemisinin		DHAA	
	Retention Time / min	Width / min	Retention Time / min	Width / min
25	6.76	0.12	12.61	0.16
30	6.7	0.1	12.39	0.18
35	5.96	0.11	11.26	0.21
40	6.09	0.11	10.99	0.19

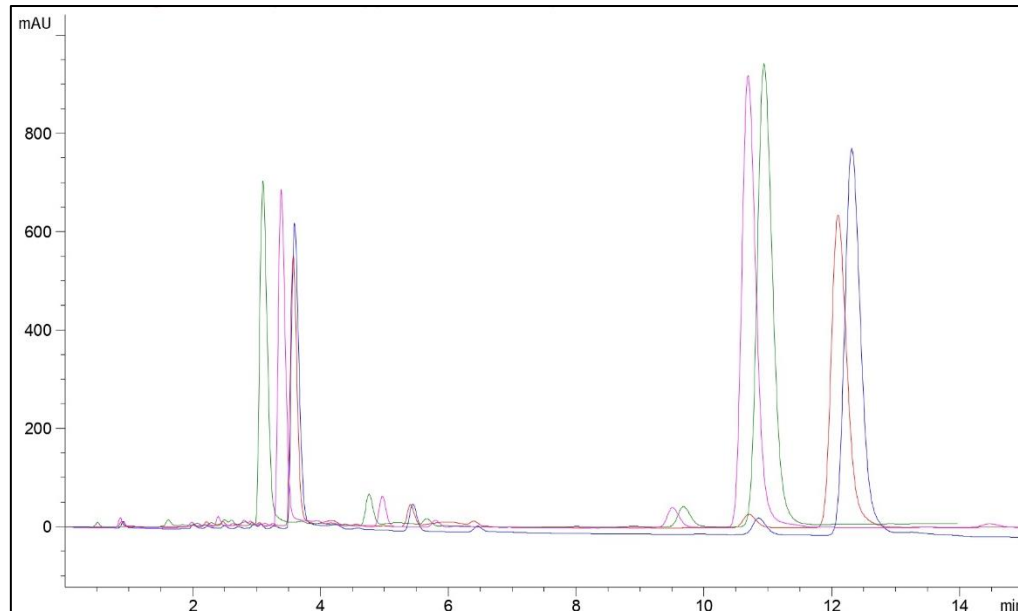


Figure 5.26: HPLC-210 nm chromatograms of the combined artemisinin and DHAA standard injected with a mobile phase of 70:30 (v/v %) acetonitrile : 0.1 % acetic acid at a flow rate of 1.0 mL min<sup>-1</sup>. The column temperature was adjusted from 25°C, 30°C, 35°C, 40°C.

### 5.5.8. External Standard Calibration 3

Table 5.22 HPLC and ELSD conditions for the external calibration of artemisinin and DHAA.

HPLC	Column Mobile Phase Sample Loop / $\mu$ L Temperature / $^{\circ}$ C Flow Rate / mL min $^{-1}$ UV / nm	Phenomenex Luna C18, 5 $\mu$ m, 250 x 4.6 mm 60:40 (% v/v) acetonitrile:0.1% acetic acid 5 40 1.0 210 nm
ELSD	Nebuliser Temperature / $^{\circ}$ C Evaporator Temperature / $^{\circ}$ C N <sub>2</sub> Flow Rate / SLM N <sub>2</sub> Inlet Pressure / bar LED intensity / % Gain	40 40 2 4.0 20 1

#### DHAA Calibration

To reduce the sensitivity of the ELSD the eluent composition was reverted back to 60:40 (v/v %) acetonitrile: 0.1 % acetic acid along with a reduction in the LED intensity to 20%. External calibration curves for **14** and **18** were produced using the regime outlined in Table 5.22, with no issues of system overpressure or of detector saturation. A series of five standards of **14** in DCM were analysed in triplicate.

Table 5.23: ELSD and 210 nm data for the external calibration of **14**.

Standard	Concentration / mol dm $^{-3}$	ELSD Peak Area		210 nm Peak Area	
		Mean	RSD / %	Mean	RSD / %
1	0.0503	4492	2.42	30858	0.89
2	0.0383	2274	2.37	24158	1.70
3	0.0316	2025	1.24	20561	0.54
4	0.0188	734	1.41	12300	0.82
5	0.0085	152	6.84	5885	4.65

Table 5.24: DHAA mean retention time as determined by both detectors. The value is averaged over the 15 injections of all standards and RSD values calculated to be relatively low at 1.24 % and 1.07 % for the ELSD and UV respectively. Grubbs analysis revealed the presence of no statistical outliers.

Detector	Retention Time / min	RSD / %
ELSD	19.25	1.24
210 nm	18.97	1.07

The ELSD quantification of DHAA yielded reasonable data with 4 of the 5 standards exhibiting RSD values below 2.5%. Unfortunately, the RSD of the lowest concentration standard increases to 6.84 %; this is of a particular concern as it is expected that the majority of the photo-oxidation reactions of DHAA to artemisinin will result in near full conversion and, therefore, the accurate detection of DHAA at low concentrations is

essential. The ELSD calibration produced a straight line graph of equations (5.15) and, both with good coefficient of determination of values of 0.999.

$$y = 1.914x + 6 \quad (5.15)$$

The UV analysis of the DHAA standards also resulted in somewhat better data than with the ELSD, with each standard showing improved RSD values than the ELSD counterpart, with 4 of the 5 values being 1.70 % or below, while the largest value, again for the lowest concentration, was below 5% at 4.65%. The calibration plot produced a straight line of equation (5.16), with a strong correlation with  $R^2$  of 0.9986.

$$y = 601100x - 1020 \quad (5.16)$$

### Artemisinin Calibration

Seven artemisinin standards were prepared through a combination of serial dilution and dissolution of a measured amount of artemisinin in the particular volumetric flask. Each standard was injected onto the HPLC column five times and analysed by the ELSD and 210 nm.

Table 5.25. ELSD and 210 nm data for the external calibration of 18.

Standard	Conc. / mol dm <sup>-3</sup>	ELSD Peak Area		210 nm Peak Area	
		Mean	RSD /%	Mean	RSD /%
1	0.051	8692	2.50	2144	2.20
2	0.042	6638	2.48	1789	1.66
3	0.033	4694	2.09	1416	1.17
4	0.021	2344	1.84	900	2.13
5	0.010	752	3.13	450	2.98
6	0.026	3336	1.90	1143	1.05
7	0.004	151	8.00	211	1.61

Table 5.26: Artemisinin mean retention time as determined by both detectors. The value is averaged over the 35 injections of all standards and RSD values calculated to be relatively low at 1.24 % and 1.07 % for the ELSD and UV respectively. Grubbs analysis revealed the presence of no statistical outliers.

Detector	Retention Time / min	RSD / %
ELSD	9.331	0.98
210 nm	9.040	1.01

The ELSD produced relatively good data for the analysis of artemisinin, with all but one of the standards RSD values being below 3.20 %. As with the analysis of DHAA the RSD value of the lowest concentration gave rise to the largest RSD value of 8.00 %. The retention times remained stable exhibiting little drift with a retention time of 9.33 minutes averaged over the 35 samples, with a corresponding RSD of 0.98 %. The calibration produced a straight line of equation (5.17). A high coefficient of determination value of 0.997 was measured.

$$y = 1.56x + 6 \quad (5.17)$$

Similar to the analysis of **14**, the UV detector response led to generally lower RSD values for **18** compared to the ELSD. A point of significance in this detection is the low RSD value of 1.61 % associated with standard 7, the lowest concentration of **18**. As seen with the ELSD analysis of **14** and **18** the variance increases significantly at these lower concentrations. The external calibration plot of the 210 nm detector produced a straight line of equation (5.18), with a strong correlation ( $R^2 = 0.999$ ).

$$y = 41200x + 50 \quad (5.18)$$

### Calibration Precision Test

Following on from the calibrations of **14** and **18** under the new mobile phase composition, three artemisinin standards were analysed in triplicate to determine the accuracy of the calibration.

The precision calculations indicate a good accuracy for the calibration despite the deviation of the middle concentration for which both the ELSD and the 210 nm give the largest deviations of 4.54 and 3.52 % respectively.

Table 5.27: Artemisinin standard concentrations along with the calculated mean peak areas with the corresponding RSD value. The artemisinin concentrations were calculated and the deviation from the actual concentration measured.

Standard	Conc. / mol dm <sup>-3</sup>	ELSD				210 nm			
		Mean Peak Area	RSD / %	Calculated Conc. / mol dm <sup>-3</sup>	Deviation / %	Mean Peak Area	RSD / %	Calculated Conc. / mol dm <sup>-3</sup>	Deviation / %
1	0.024	2856	1.09	0.024	0.87	1036	1.22	0.0239	0.70
2	0.011	770	2.73	0.011	4.54	487	5.04	0.0106	3.52
3	0.007	398	2.10	0.0071	0.45	348	2.29	0.0072	1.86

### 5.5.9. Gradient Mobile Phase to Aid the Elution of DHAA

During the synthesis of **18** it was found that the peak of **14** was often not identified in the ELSD despite a signal appearing. To aid the detection by reducing the retention time and, hence, increasing the peak height, a gradient mobile phase was investigated. The aim of the gradient phase was to keep the analysis of **18** unchanged from the previous method, while decreasing the elution time of **14**. Therefore, the composition was kept isocratic with - acetonitrile : 0.1 % acetic acid 60:40 (v/v %) for the first 10 minutes of the analysis. The preliminary gradient composition is shown in Table 5.28. The resulting spectra, Figure 5.27, showed a much improved peak shape for **14**.

Table 5.28: Mobile phase gradient regime for reducing the retention time of DHAA and hence improving peak shape and detection.

Time / min	acetonitrile / %	0.1 % acetic acid / %
0	60	40
10	60	40
11	80	20
17	80	20
18	100	0
25	100	0
30	60	40
35	60	40

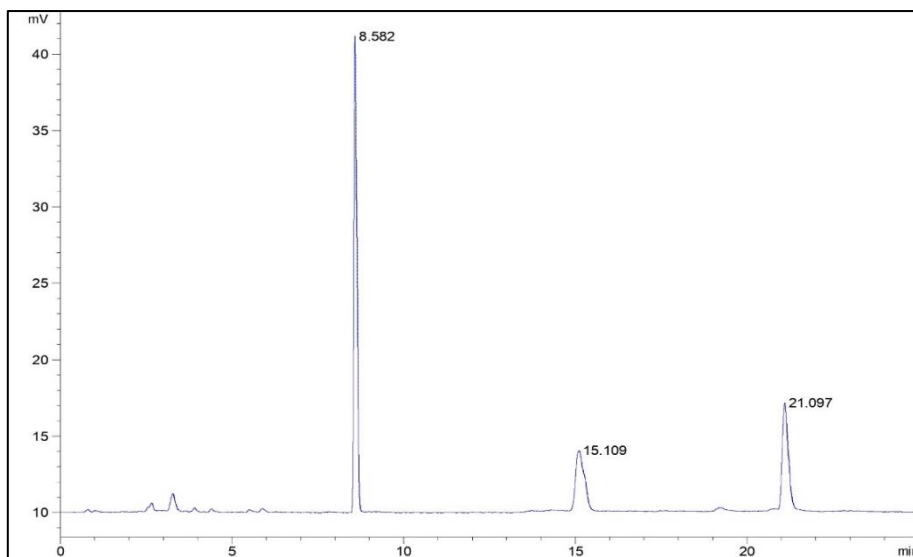


Figure 5.27: HPLC-ELSD chromatograms after changing to the gradient mobile phase, the peak shape of DHAA (21.097 mins) has greatly improved.

### 5.5.10. Internal Standard Calibration of DHAA and Artemisinin in Toluene

In efforts to drive the formation of **18** to completion within the continuous flow reactor, a switch to toluene as the reaction solvent was made, as discussed in Chapter 4. The use of toluene allows for higher temperatures to be used during the thermal Hock Cleavage and secondary oxidation, and was found to accelerate the reaction. HPLC analysis of toluene determined a strong signal in the 210 nm UV, with no corresponding signal in the ELSD, Figure 5.28. The isolated UV peak possessed a similar elution time to **18**. Upon analysis of a solution of photochemically synthesised **18** a severe issue with the use of toluene was discovered. Toluene and **18** co-eluted, with the strong signal of the solvent completely masking the weaker signal of **18**. Furthermore, toluene was observed to possess a very large tail, spanning an elution time of around 7 minutes, hence overlapping with other compound peaks, as shown in Figure 4.20. The comparison between the isolated toluene analysis and the photo-product indicates that some potential secondary interactions are occurring - first, the significant tailing shows that the retention of toluene is greatly increased when in the photo-product mixture, and that the solvent could be flushing previously retained compounds from the column; second, the strength of the signal in the photo-product is approximately an order greater than the isolated peak. Both of these points are potentially caused by the toluene forming a complex with TPP, exhibiting greater UV absorption properties. Moreover, TPP is likely to be strongly retained on the C18 column when using a combination of water and acetonitrile. A study conducted by Saitoh *et al.* on the separation of metal centred TPPs and H<sub>2</sub>TPP using C18-bonded silica found the retention of TPP is greatly

reduced when toluene was used as the developer solvent.<sup>323</sup> It is therefore possible that toluene is aiding in the elution of TPP, resulting in the strong and broad signal observed.

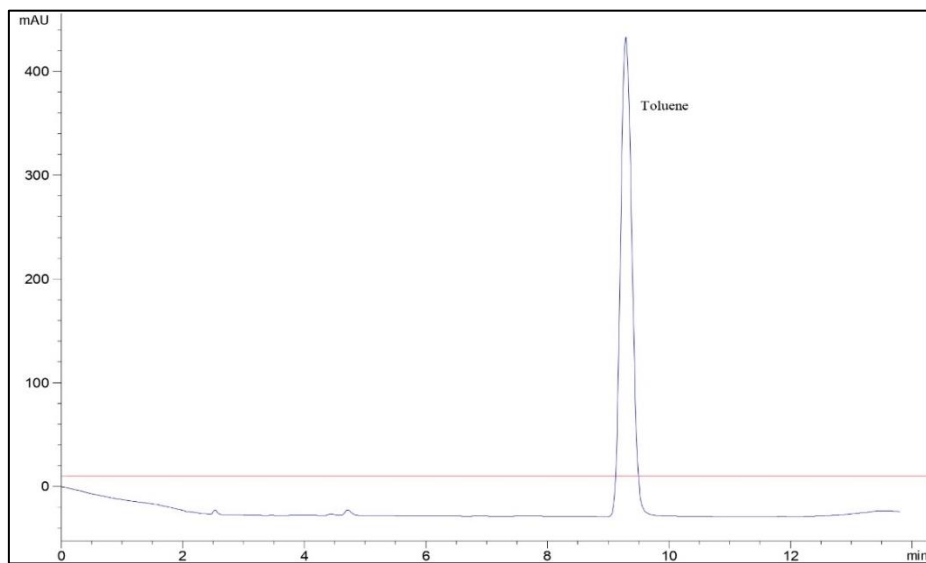


Figure 5.28: HPLC-210 nm chromatogram of toluene injected using the 5 $\mu$ L sample loop, onto the Luna C18 5 $\mu$ m 250 x 4.6 mm column, under the conditions for artemisinin quantification, 60:40 acetonitrile : 0.1% acetic acid (v/v %) at a flow rate of 1.0 mL min<sup>-1</sup> and column temperature of 40 °C. Toluene possesses an elution time of 9.30 minutes and absorbs strongly at this wavelength. Potentially presenting an issue with quantification of artemisinin. No signal is present in the *ELSD*.

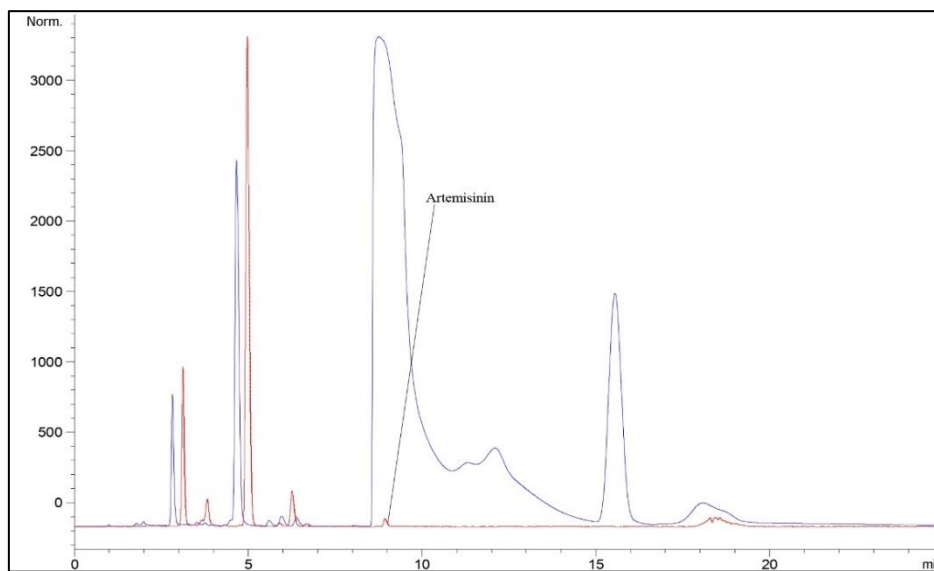


Figure 5.29: HPLC-210 nm chromatograms of the solution sampled immediately after the addition of TCA to the photoproduct. Toluene elutes slightly earlier than previously and overlaps the region of artemisinin elution with a strong tailing peak. The strong peak of biphenyl is found around 15.5 minutes. A number of early eluting peaks can also be observed. The corresponding *ELSD* signal also shows these early eluting peaks along with a small peak attributed to artemisinin, clearly showed co-eluting with toluene.

The change in concentration of the reagent stream at the outlet of the continuous reactor renders the use of an external standard calibration obsolete. The change in concentration is due to two factors: the addition of the acid after the photoreactor dilutes the product; while evaporation of the solvent, enhanced by the increased temperature of the thermal

reactor section, will concentrate the solution. With these two opposing effects in play it was crucial to develop an analysis that utilised an internal standard. As biphenyl was often used as the internal NMR standard, this would have provided a convenient option as a HPLC standard. However, biphenyl does not produce a signal in the ELSD under the typical parameters and overlaps with the toluene peak tail in the UV spectra, while **18** is fully masked.

As the UV detector has been frequently found to be the more accurate and reliable of the detectors, efforts were made to adapt the HPLC mobile phase to separate the artemisinin and biphenyl peaks from toluene to allow for biphenyl to be used as an internal standard for the UV detection of artemisinin.

Photochemically produced **18** was analysed with the mobile phase gradient outlined in Table 5.29. The ELSD parameters were adjusted to allow for a high level of sensitivity such that the presence of biphenyl could be detected in the ELS. The nebuliser and evaporation chamber were both set to 25 °C, while the nitrogen flow was decreased to 1 SLM and the LED intensity increased to 100 %. With these less than ideal conditions for the quantification of artemisinin, a negligible peak at 15.26 minutes with an area of 49 was measured for biphenyl. These results made it apparent that if biphenyl were to be used as an internal standard and analysed with the ELSD a much greater quantity would be required; however, this would not be possible as it would greatly diminish its ability as an NMR standard. Furthermore, biphenyl in the negligible concentration required as an NMR standard already exhibits a large peak in the UV detector; increasing its concentration would likely saturate the UV detector.

*Table 5.29: Mobile phase gradient regime previously developed for reducing the retention time of DHAA and hence improving peak shape and detection.*

Time / min	acetonitrile / %	0.1 % acetic acid / %
0	60	40
10	60	40
11	80	20
17	80	20
18	100	0
25	100	0
30	60	40
35	60	40

The remaining solution was analysed using a series of isocratic conditions, shown in Table 5.30. The UV spectra of each of the isocratic methods showed complete overlap of **18** with toluene, it appears that the two had equal affinity to the C18 stationary phase.

*Table 5.30: Isocratic mobile phases investigated to separate the HPLC peaks of artemisinin and the reaction solvent, toluene.*

Acetonitrile	0.1% Acetic Acid	Methanol	Flow Rate / mL min <sup>-1</sup>	Sample loop / $\mu$ L
60	40	0	1	5
70	30	0	1	5
80	20	0	1	5
50	30	20	1	5
60	40	0	1	1

The lack of separation between **18** and toluene meant that analysis of the former would not be possible using the UV detector. To facilitate accurate analysis attention was turned to finding an appropriate compound to be used as an internal standard for ELS detection. The ELSD was returned to the original parameters, while the gradient mobile phase shown in Table 5.29 was used. First, the long chain alkanes, dodecane and octadecane, were analysed; however, neither produced a signal in the ELSD for run times exceeding 60 minutes. ELS detection is often used for the analysis of fatty acids; hence, these were the next group of compounds analysed.<sup>324</sup>

Lauric acid (dodecanoic acid, LA) provided the most promising peak shape and elution time. Longer chain acids possessed high retention times and, consequently, poor peak shape. LA is weak acid, with a pKa of 5.30, compared to 0.30 and 0.51 for TFA and TCA respectively.<sup>325</sup> However, to assess whether lauric acid would catalyse the Hock Cleavage, a standard continuous photo-oxidation of **14** was performed with lauric acid and no other acid present. The first observation was the lack of protonation of the TPP in the starting material. HPLC analysis of the photo-product revealed no peak for **18**. Furthermore, the level of lauric acid remains relatively constant, at least within the error of the detector. There is a slight decrease in the area of the LA peak through the samples, but the area of **14** also decreases in this time; therefore it is likely due to variation within the sensitivity of the detector.

To further improve the peak shape of lauric acid, a new gradient phase was created. The new phase used the added feature of the Agilent HPLC that allows for the column temperature to be adjusted during the course of a run. As such, the column temperature

was increased from 40°C to 50°C after 10 minutes. The first 10 minutes were left isocratic with the 60:40 (v/v %) composition of acetonitrile: 0.1 % acetic acid in order to maintain the normal elution of **18**. The organic composition was subsequently increased after this first period to 90:10 to aid in the elution of the hydrophobic standard. The mobile phase regime, expressed in Table 5.31, provided sufficient separation, with a resolution of 7.03 between DHAA (14.530 minutes, area 8563, width 0.15 minutes) and LA (15.549 minutes, area 1061, width 0.14 minutes), for the gradient mobile phase to be adopted.

*Table 5.31: Gradient mobile phase composition to improve the elution of the internal standard, lauric acid. The increase in the organic composition of acetonitrile will aid with the solubility of the hydrophobic lauric acid into the mobile phase while the column temperature ramp will also aid in the mobility of the compound.*

Time /min	Acetonitrile / %	0.1 % Acetic Acid / %	Column Temperature / °C	Flow Rate / mL min <sup>-1</sup>
0 - 10	60	40	40	1.0
10 - 11	90	10	40	1.0
11 - 20	90	10	50	1.0
20 - 21	60	40	50	1.0
21 - 25	60	40	40	1.0

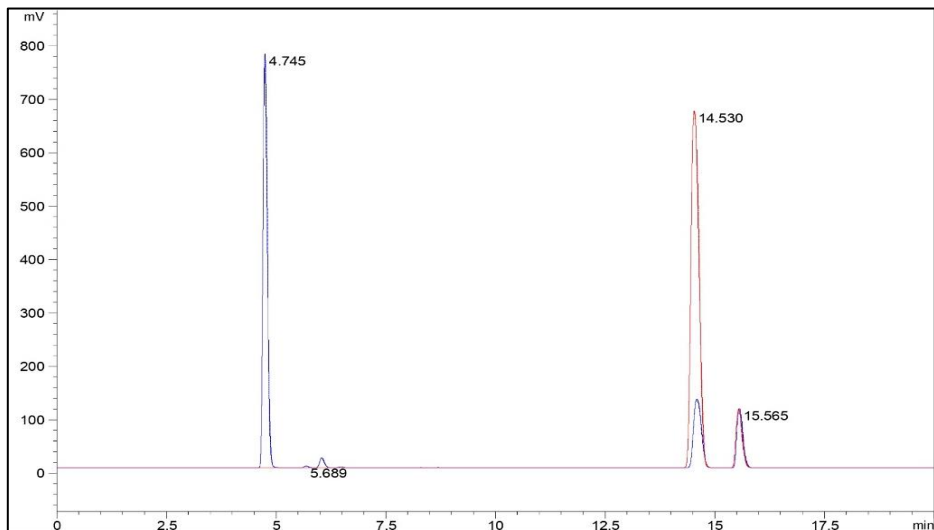


*Figure 5.30: Red: HPLC-ELSD of the starting material, **14** (14.53 mins) and lauric acid (15.57 mins) run under a gradient mobile phase with a column temperature ramp. Blue: HPLC-ELSD chromatogram of the initially injection after the photo-oxidation of **14** in the presence of TPP and lauric acid in toluene. The DHAA peak eluting at 14.53 has decreased in peak area from 8726 to 1602, while the lauric acid peak (15.57 mins) has remained relatively constant at 1072 from an original value of 1089. The large peak originating at 4.745 minutes is attributed to tertiary hydroperoxide **15**.*

The remaining photoproduct was acidified and stirred with O<sub>2</sub> to complete the synthesis of **18**. The corresponding HPLC-ELSD spectrum, Figure 5.31, indicates that lauric acid is stable with respect to the acidification of the solution. The peak area increases compared to those after the photo-oxidation; however, this is in line with a similar increase in the peak area of **14**.

*Table 5.32: DHAA and lauric acid ELSD peak areas at various stages during the initial investigation in to the viability of lauric acid as the internal HPLC standard. The lauric acid peak area remains relatively stable for all samples except the final analysis after the acidification of the solution, this increase however also occurs for DHAA and is therefore likely due to a variation in the sensitivity of the detector rather than due to changes in the composition of the solution.*

Sample	DHAA	Lauric acid
Starting material	8564	1061
S.M with TPP	8726	1089
0 minutes	1602	1072
50 minutes	1573	1059
85 minutes	1536	1055
After addition of TFA	1829	1312

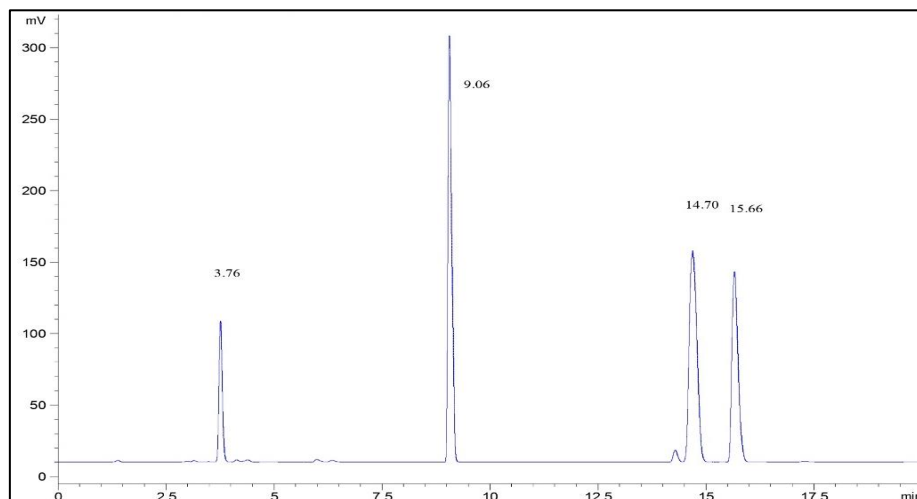


*Figure 5.31: HPLC-ELSD chromatogram of the photo-product after the addition of TFA. The lauric acid peak (15.66 minutes) has increased in value but as too has the **14** peak (14.70 minutes), despite this compound being further formed into **18** (9.06 minutes).*

After determining the suitability of LA as an internal ELSD standard, the parameters were re-investigated to find the optimum conditions for the detection of **18**, **14** and LA. First, the original parameters of the ELSD (nebuliser and evaporation temperatures of 40°C, Nitrogen at 2 SLM, LED at 20 %, 5 µL sample loop) were used to analyse 0.05 M artemisinin in toluene. It was observed that the corresponding **18** peak saturated the detector. Furthermore, it was noted that the peak appeared narrower than was typically seen when injections of similar concentration were made in DCM. A sharper peak will

result in a greater height and increased likelihood of detector saturation. The shape of the peak can be put down to the change of injection solvent. The co-elution of toluene and **18** along with the higher volatility of toluene compared to the mobile phase, which contains a considerable amount of water, will have a significant effect on the evaporation of the solvent in the ELSD drift tube, increasing the sensitivity of the detector during the elution of toluene.

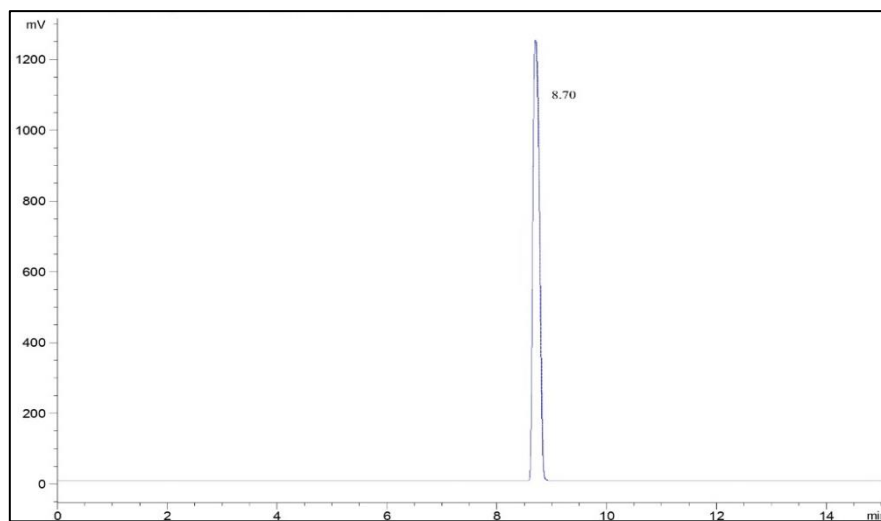


Figure 5.32: ELSD chromatogram of 0.05 M **18**. Mobile phase gradient outlined in Table 5.31. Injection using the 5  $\mu$ L sample loop. ELSD parameters of: Nebuliser 40°C, Evaporator 40°C,  $N_2$  2 SLM, LED 20 %. Detector saturation, peak height of 1245 mV

The standard was re-analysed while the ELS light intensity was gradually reduced. The nebuliser, evaporation tube and nitrogen flow were kept constant. The response of **18** continually saturated the detector, even with the intensity set to 10 %. Therefore, the nebuliser and evaporation chamber temperatures were gradually increased while the LED intensity was kept at 10 %; however, at 50°C for both parameters the response was still saturated. The ELSD was subsequently cleaned. After the cleaning process, the 5  $\mu$ L sample loop was replaced with the 1  $\mu$ L and the ELS parameters returned to the original values. The standard was once again analysed. The corresponding response was negligible with an area of 32 and a height of 3 mV. At an LED intensity of 100 %, **18** produced a reasonable area and height with values of 2684 and 359 mV respectively. The repeated oversaturation highlighted the importance of regular cleaning of the ELSD, the detector has already been shown to be temperamental and, therefore, great efforts were made to reduce any potential factors that may diminish the accuracy of the detector.

The standard of **18**, along with **14** (0.051 M) and lauric acid (0.02 M) was then analysed and the ELSD parameters adjusted to optimise detection. However, during these efforts

saturation occurred under conditions that had previously not resulted in saturation. After cleaning and further adjustments the settled parameters consisted of a slight adjustment with the N<sub>2</sub> increased to 2.15 SLM, while the nebuliser and evaporation chamber remained at 40°C with the LED intensity at 100 %. The 5 µL sample loop was replaced with the 1 µL for analysis in toluene. However, subsequent injections of the standard resulted in seemingly random saturation, shown in Table 5.33. The detector was put through the cleaning regime. This alleviated the issue with the next injection exhibiting an artemisinin peak height of 302. The standard was then injected multiple times however the response of **18** varied considerably until it ultimately saturated the detector despite the ELS and mobile phase parameters remaining constant. The seemingly random saturation of the ELS was unexplained with large variations occurring for subsequent injections of the same standard under identical conditions. The variation was not limited to the co-elution of **18** and toluene, the response of lauric acid was also severely affected.

*Table 5.33: ELSD artemisinin peak areas. Mobile phase gradient and ELSD parameters outlined in Error! Reference source not found.. <sup>a</sup>N<sub>2</sub> 2.20 SLM. <sup>b</sup>N<sub>2</sub> 2.10 SLM. <sup>c</sup>N<sub>2</sub> 2.15 SLM. Height values in bold indicate saturation of the detector.*

Injection	Artemisinin		Lauric Acid	
	Area	Height	Area	Height
1	11695	1208	757	81
2	2501	302	176	18
3	1993	265	191	21
4	2828	352	169	19
5	2842	356	170	16
6	2248	277	174	19
7	3402	437	130	14
8	11546	1208	762	82
9	11295	1208	715	79
10	11982	1208	891	104
11 <sup>a</sup>	7837	1071	80	16
12 <sup>b</sup>	10739	1208	36	3
13 <sup>c</sup>	8615	1118	101	11

### 5.5.11. Internal Standard Calibration of **14** and **18** in DCM

Due to the severe variation experienced with the ELSD, the development of an internal standard calibration using 210 nm UV was investigated. The use of UV detection required reverting back to DCM as the reaction solvent. An appropriate UV standard was needed. Biphenyl was already shown to be too absorbent. An alternative, also

commonly used as an internal NMR standard, is trimethoxybenzene (TMB). A solution of TMB was analysed using an isocratic mobile phase of 60:40 (v/v %) acetonitrile : 0.1 % acetic acid with a constant column temperature of 40°C; the previously developed gradient, Table 5.33, exhibited a sloping baseline in the 210 nm UV, deeming it unsuitable for such analysis. Due to the weak UV absorption of artemisinin, injections of standards and samples were performed with the 5  $\mu$ L sample loop.

Under the isocratic conditions, TMB was found to elute with a strong signal at a retention time of 5.63 minutes with sufficient separation from other photoproducts, Figure 5.33. As with biphenyl, TMB did not elicit an ELS response under the current parameters. The need for an isocratic mobile phase resulted in a flow rate ramp being employed to reduce the retention time of the more hydrophobic compounds. During the analysis of a mixed standard of **18**, **14**, and TMB, an unknown peak observed in 210 nm UV arose just prior to the peak of **18**. This peak is similar to that discussed earlier and was eventually identified as belonging to a plasticiser compound. The unknown peak's retention time shifted between injections and eventually overlapped with **18**, presenting an issue for the quantification.

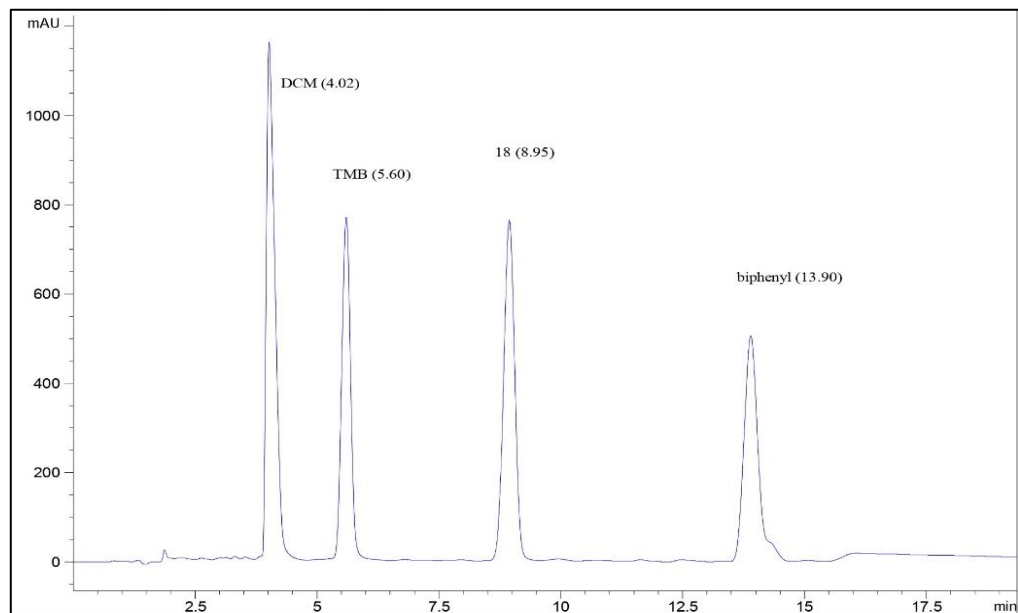


Figure 5.33: HPLC-210 nm UV chromatogram of a solution of photochemically produced **18** with added TMB (5.60 minutes). Sufficient separation is achieved with an isocratic mobile phase of 60:40 (v/v %) acetonitrile : 0.1 % acetic acid, column temperature of 40 °C, and 1.0 mL min<sup>-1</sup>.

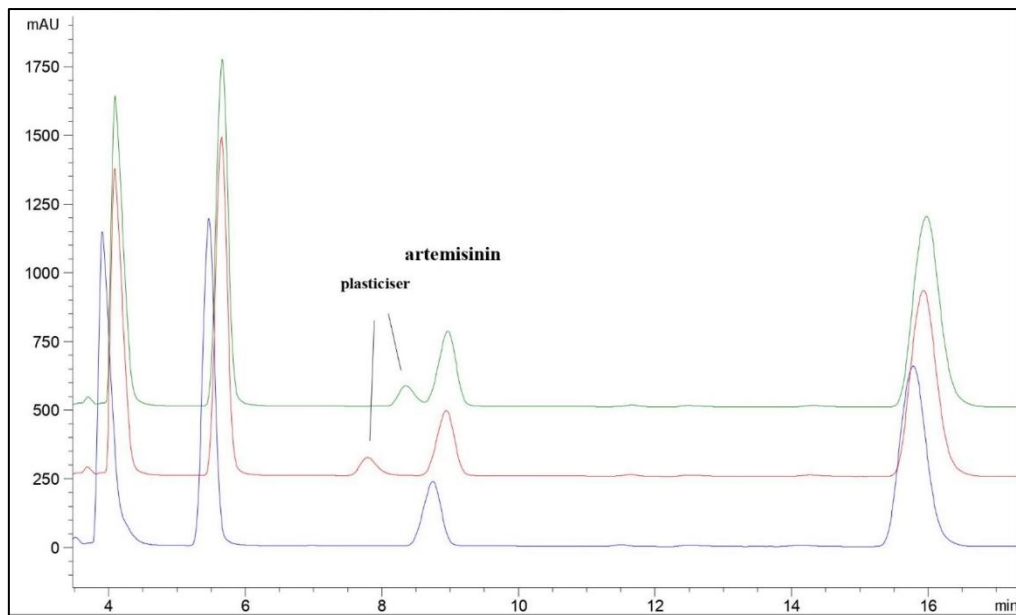


Figure 5.34: Stacked HPLC-210 nm UV chromatograms of the mixed standard. The plasticiser peak was found to increase in area and drift in retention time, eventually eluting at 8.35 minutes and slightly overlapping with the artemisinin peak (8.97 minutes).

### 5.5.12. Investigations into the Source of the Unknown Peak in UV

To investigate the source of the unknown peak a solution of TMB (27 mM) in DCM was analysed a total of five times on the HPLC. Initially the unknown peak exhibited a large peak with an elution time around 8.61 minutes. The compound possessed no corresponding ELSD signal and was therefore ruled out as a carryover peak of **18** from previous injections. Over the successive injections both the retention time and the area of the unknown peak varied significantly, while these metrics for TMB remained relatively stable, as shown in Table 5.34. The unknown peak did not appear in the final injection of the standard, indicating that the source of the peak was not a contaminant of TMB.

Table 5.34: 210 nm data from the injections of the solution of TMB in DCM to assess the prevalence of the unknown peak.

Injection	TMB		Unknown	
	Retention time / min	Area	Retention time / min	Area
1	5.61	17993	8.62	1312
2	5.66	17830	8.54	475
3	5.70	18030	8.40	230
4	5.64	17360	8.48	190
5	5.65	17467	-	-

Blank injections of DCM after column and sample loop cleaning and on an alternative column (Phenomenx Prodigy C185  $\mu\text{m}$ , 250 mm x 4.6 mm) also produced the unknown peak. Injections using acetonitrile, and the mobile phase also resulted in the appearance of the peak. Finally, DCM was extracted directly from the Winchester bottle using a glass syringe and injected into the HPLC sample loop through a metal inlet fitting. This and subsequent injections did not produce the unknown peak. This provided strong evidence that the signal belonged to plasticiser from the plastic syringe leaching into the solvent prior to injection. DCM was then injected from a plastic syringe (B. Braun Injekt®-F), all previous manual injections had been made using this type of syringe. The injections occurred after 1, 30, and 60 minutes of the DCM being in the syringe. The area of the peaks increased upon the first injection, Table 5.35. Injections of DCM made from the glass syringe using a plastic sample loop inlet fitting, this also gave rise to the unknown peak. The peak was absent when the same glass syringe of DCM was injected with a metal sample loop inlet fitting. An indication that the leaching of plasticiser occurs from even brief contact between the solvent and the plastic and therefore may not solely occur from the plastic injection syringes but potentially from all plastics within the reactor that come into contact with DCM.

*Table 5.35: 210 nm Peak areas for DCM and the unknown peak. DCM was left in the syringe for a total of 60 minutes.*

Time in Syringe / min	DCM Area	Unknown Area
1	13131	814
30	12939	1370
60	13429	1226

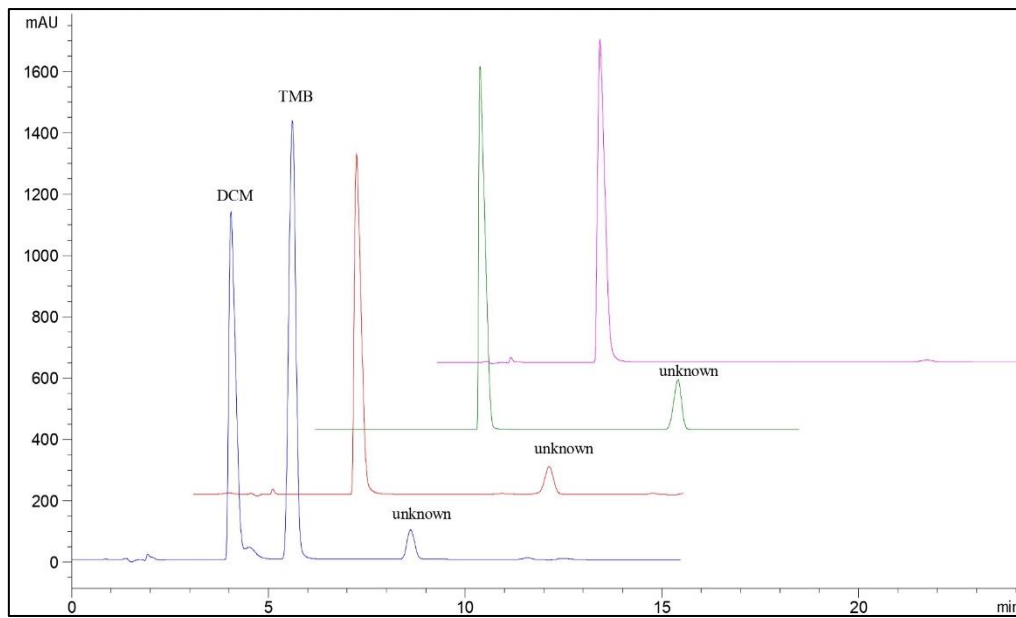


Figure 5.35: Stacked HPLC-210 nm UV chromatograms. **Blue:** TMB in DCM, unknown peak is observed at 8.62 minutes. **Red:** Blank DCM after column cleaning, the unknown peak is still present with a retention time of 9 minutes. **Green:** Blank DCM injected onto a second column (Phenomenex Prodigy). Unknown peak still observed at 8.76 minutes, therefore unlikely to be an issue of column contamination/residual compound build up. **Purple:** DCM extracted directly from Winchester using glass syringe, the unknown peak is not present. This finding led to the identification of the unknown peak likely being a plasticiser leaching from the plastic injection syringe into the DCM.

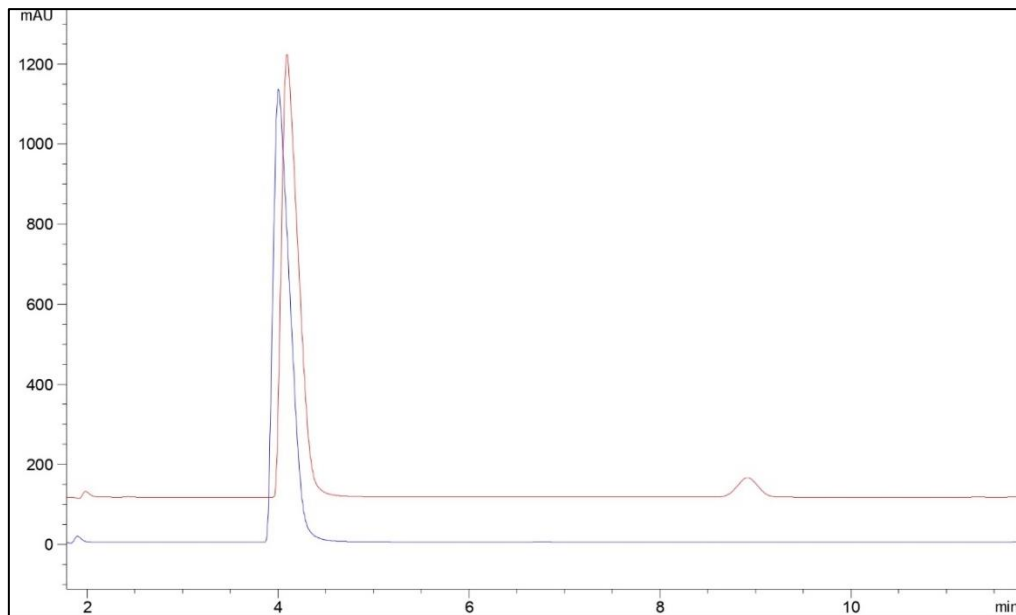


Figure 5.36: **Red:** DCM injected from glass syringe via plastic fitting to sample loop. **Blue:** DCM injected from glass syringe via metal fitting to sample loop. The plasticiser peak does not appear.

DCM was pumped through the photo-reactor section using a peristaltic pump (Cole Parmer Masterflex™) this produced no peak indicating that the FEP and PTFE tubing does not leach into the solvent. The full reactor was then set up with the Vortex, GLS and Gilson® pump, and Jasco® HPLC pumps. Analysis of DCM passed through the full system showed the unwanted peak. Next, just the photoreactor section without the

Vortex or GLS was flushed with DCM using a Jasco® HPLC, also giving rise to the plasticiser peak. This section of the reactor did not produce the plasticiser peak when flushed using the peristaltic pump, it was therefore likely that the plasticiser peak also originates from a component within the Jasco® HPLC pump section. As this is a vital component that cannot be easily replaced, the alternative was to adjust the mobile phase to better enhance the separation between the plasticiser peak and that of **18**.

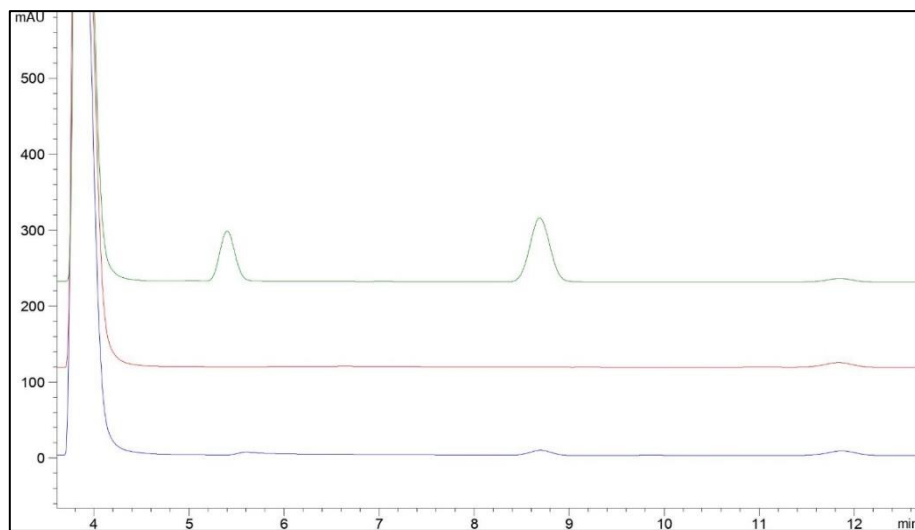


Figure 5.37: Stacked 210 nm UV chromatograms. *Blue*: DCM pumped through the photoreactor section of the reactor, collection before entering the Vortex reactor. Pumped using Jasco HPLC pump 1. *Red*: DCM pumped through the photoreactor section of the reactor, collection before entering the Vortex reactor. Pumped using peristaltic pump. No indication of the plasticiser peak between 8-9 minutes. *Green*: Full system (photoreactor, vortex, GLS and Gilson pump) flushed with DCM using Jasco HPLC pumps. Gilson Pump attached to HPLC sample loop, sample collected from waste stream of sample loop in a glass syringe. Plasticiser peak appears with an elution time of 8.688 minutes.

The composition of the mobile phase was kept isocratic at 60:40 (v/v %) acetonitrile: 0.1 % acetic acid at a column temperature of 40°C, while the flow rate was adjusted through the run. A number of conditions were explored with the final protocol being outlined in Table 5.36. The slow ramp of the flow rate from 0.5 to 1.0  $\text{mL min}^{-1}$  over 10 minutes prevents the column from being shocked by a significant sudden increase in pressure which was occurring in the previous protocol whereby the flow rate increased

by 0.5 mL min<sup>-1</sup> over 1 minute. Despite the increased retention time of each of the analytes, the peak shapes remained sharp and highly symmetrical.

*Table 5.36: HPLC protocol for injections in DCM to separate the plasticiser peak from artemisinin.*

Time / minutes	acetonitrile / %	0.1 % acetic acid / %	Flow Rate / mL min <sup>-1</sup>
0	60	40	0.5
10	60	40	0.5
20	60	40	1.0
25	60	40	1.5
30	60	40	1.5
35	60	40	0.5

During the initial injections of a mixed standard under the conditions outlined in Table 5.36, it was noticed that the plasticiser peak still appeared despite minimisation of plastic interaction with the standard. Furthermore, the peak elution time again drifted over subsequent runs, eventually overlapping with the peak of **18**. As this phenomenon appeared to be uncontrollable it was decided that using the UV for detection of **18** would not be appropriate. The reduction in the variation of the ELSD was then investigated to allow this to be a suitable detector for analysis of **18**. The mobile phase protocol was further adjusted to maximise the sensitivity of the ELSD for all analytes, while ideally producing a flat baseline in the UV for the regions in which each of the analytes elute such that UV detection can also be used secondary to the ELS. Several mobile phases were tested; the eventual composition is shown in Table 5.37.

*Table 5.37: HPLC protocol for the detection of artemisinin, DHAA, lauric acid and TMB in the ELS and UV detectors.*

ELSD			
Evaporator /°C	Nebuliser /°C	N <sub>2</sub> / SLM	LED /%
40	40	2.0	20
Mobile Phase			
Time / minutes	acetonitrile / %	0.1 % acetic acid / %	Flow Rate / mL min <sup>-1</sup>
0	65	35	1
5	65	35	1
9	65	35	1.5
11	65	35	1.5
12	80	20	1.5
15	80	20	1.5
16	65	35	1.5
20	65	35	1.5

### 5.5.13. Internal Standard Calibration in DCM using ELSD

A stock internal standard solution of TMB (0.0325 g, 1.93 mM) was prepared in DCM (100 mL). A stock solution of artemisinin (0.363 g, 0.0514 M) was then prepared in 25 mL of the internal standard solution. Lauric acid (0.0500 g – 0.0506 g) was added to eight volumetric flasks (Standards 1-7 in 5 mL, Standard 8 in 10 mL). Working standards were prepared by adding varying amounts of the stock solution along with a measured amount of DHAA to each flask. Injections were made using a glass syringe with a stainless steel fitting connected to the stainless steel 5  $\mu$ L sample loop.

Table 5.38: Calibration standard concentrations of artemisinin, **18**, DHAA, **14**, lauric acid and TMB in DCM.

Standard	18 / mol dm <sup>-3</sup>	14 / mol dm <sup>-3</sup>	LA / mol dm <sup>-3</sup>	TMB / mol dm <sup>-3</sup>
1	0.0514	-	0.0504	0.0014
2	0.0206	0.0619	0.0504	0.0014
3	0.0411	0.0377	0.0502	0.0014
4	0.0309	0.0148	0.0504	0.0014
5	0.0103	0.0052	0.0505	0.0014
6	0.0051	0.0253	0.0499	0.0014
7	0.0257	0.0478	0.0505	0.0014
8	0.0026	0.0014	0.0499	0.0014

Seven injections of Standard 1 produced unacceptable levels of error in the ELSD, with RSD values of 12.32 %, 3.41 %, and 17.13 % for artemisinin, DHAA and LA respectively. The use of the gradient mobile phase, Table 5.37, and lack of column re-equilibration to the starting composition was likely to be the cause of the variation. As has been shown, minor changes in mobile phase composition can greatly affect the sensitivity of the ELSD. Furthermore, the time required for column re-equilibration at the end of the method negated any time reductions from the flow rate ramp or the increase in the organic composition. Therefore, for achieving high precision a return to an isocratic mobile phase was made, albeit slightly different from the previous isocratic method.

The new method contained a higher proportion of organic phase at 65:35 (v/v %) acetonitrile : 0.1% acetic acid at a constant flow rate of 1.50 mL min<sup>-1</sup>. These parameters were chosen to reduce the overall run time while producing sharp peaks for all analytes. The higher proportion of volatile organic phase also increases the sensitivity of the ELSD for each of the analytes. Standard 1 was again analysed *via* five injections and

exhibited improved precision for all analytes with RSD values for artemisinin, DHAA and LA of 2.50 %, 1.51 % and 3.68 % respectively. Each standard was analysed a minimum of five times under isocratic conditions. The calibration of **18** with LA was made using the ELSD, while the calibration of **14** with TMB was performed using the 210 nm UV detector.

*Table 5.39: Comparison of the ELSD artemisinin data from the initial injections of Standard 1 using the gradient mobile phase outlined in Table 5.37 and isocratic mobile phase.*

Retention Time				Area			
Gradient		Isocratic		Gradient		Isocratic	
Mean	RSD /%	Mean	RSD /%	Mean	RSD /%	Mean	RSD /%
6.93	10.19	4.87	0.32	8254	12.32	7657	2.50

*Conditions: isocratic mobile phase of 65:35 (v/v %) acetonitrile: 0.1 % acetic acid at a flow rate of 1.5 mL min<sup>-1</sup>, column temperature of 40°C. Injections were made using the 5 µL sample loop. ELSD parameters: nebuliser temperature of 40°C, evaporator temperature of 40°C, Nitrogen flow rate of 2.0 SLM, and an LED intensity of 20 %. The use of the isocratic mobile phase at a higher flow rate has reduced variation in both the retention time and the artemisinin peak area with corresponding RSD values of 0.32 and 2.50 % respectively. Grubbs' outlier tests were performed on the retention time and area data, producing a p-value of 0.0026 for the retention time indicating the first value of 4.642 minutes is an outlier and was hence omitted from the mean calculation.*

For each injection, the peak areas of artemisinin and Lauric acid are first log<sub>10</sub> transformed. The ratio between the log<sub>10</sub> values is then calculated for **18** against LA. Grubbs' outlier tests are performed on each Standard sample set and values determined to be outliers with a p-value < 0.05, are omitted from the calculations of the mean values, Table 5.40. The mean log<sub>10</sub> area ratio is then plotted against the log<sub>10</sub> ratio of the analyte concentrations. The calibration graph was plotted, producing a straight line of equation (5.19), with a strong coefficient of determination of 0.994. This value is very slightly lower than previous calibrations with the ELSD. The reduction can be attributed to the additional error associated with the detection of two analytes with respect to the internal standard calibration, previous external calibration require the quantification of just one analyte.

$$y = -0.7355x + 2.0881 \quad (5.19)$$

The quantification of DHAA was assessed with both the ELS and UV. It was determined that for each standard sample set, the variation, reflected in the RSD values, was generally lower for the UV detection. The superior precision of UV detection over ELS has been regularly observed during this investigation. Furthermore, the ELS was unable to detect and quantify the standard containing the lowest concentration of DHAA (Standard 8, 0.0014 M,), this did not occur with 210 nm detection. Therefore DHAA

calibration was undertaken using the 210 nm UV detector with TMB as the internal standard.

*Table 5.40: ELSD data for the quantification of artemisinin and lauric acid. For each standard injection the  $\log_{10}$  value of the artemisinin and lauric acid peaks are determined. The ratio of the two  $\log_{10}$  values is calculated and Grubbs' test is performed to remove any outliers ( $p < 0.05$ ) from the calculations of the mean values.*

Standard	Mean <b>18</b> :LA Ratio	RSD /%	Mean <b>14</b> : TMB Ratio	RSD /%
1	1.342	0.27		
2	1.147	0.40	2.940	0.29
3	1.302	0.31	1.879	0.19
4	1.237	0.33	0.763	0.20
5	0.996	0.05	0.275	0.39
6	0.814	0.12	1.230	0.36
7	1.178	0.29	2.322	0.16
8	0.600	0.50	0.089	2.62

Unlike the ELSD, the UV response is linear with concentration. Therefore, to generate the straight line calibration of DHAA with TMB, the ratio of peak areas is plotted against the ratio of the concentrations. The calibration graph was plotted, giving a straight line of equation (5.20), with a high coefficient of determination value of 0.999.

$$y = 0.0917x + 0.0414 \quad (5.20)$$

#### 5.5.14. Internal Standard Calibration in Toluene

The reactions performed in the automated flow reactor, under both the ‘one-pot’ and continuous ‘two-pot’ regimes, discussed in Chapter 4, highlighted the limitations of using DCM with regards to driving the formation of **18** to completion. Therefore, the use of toluene within the automated reactor was investigated. This required the development of an internal standard calibration using the ELSD.

The previous calibration in DCM highlighted the positive effect of using an isocratic mobile phase on the reliability and precision of the method. However, attempts to use an increased flow rate to reduce the retention time of **14** and Lauric acid led to system over-pressure, due to the use of the 1  $\mu$ L sample loop. The lower volume sample loop was required to avoid detector saturation of the **18** peak; this is due to the co-elution with toluene greatly increasing the sensitivity of the detector.

A stock solution of the internal standards was prepared by dissolving lauric acid (0.49 g, 0.0489 M) and TMB (28.6 mg, 0.0034 M) in toluene (50 mL). A starting standard of **18** (0.047 M) and **14** (0.050 M) was prepared with 5 mL of the stock internal standard solution. Attempts were made to reduce the retention time of lauric acid and hence improve the peak shape. The eventual ELSD parameters and mobile phase composition used are shown in Table 5.40. However, analysis of the starting standard produced unacceptable levels of variation with regards to the **18** and lauric acid ELS peak areas with RSD values of 16.76 % and 27.99 % respectively, over 5 injections. The ratio between the two peaks for each run was calculated to assess whether the variation was on a run-by-run basis affecting both analytes and would be balanced in their ratio; however, these values too produced unacceptable variation with an RSD of 19.52 %.

*Table 5.41: ELSD parameters and gradient mobile phase protocol for the elution and detection of artemisinin, DHAA, lauric acid and TMB with the ELSD and UV. 1  $\mu$ L sample loop used.*

ELSD			
Evaporator /°C	Nebuliser /°C	N <sub>2</sub> / SLM	LED /%
40	40	2.15	100
Mobile Phase			
Time / minutes	acetonitrile / %	0.1 % acetic acid / %	Flow Rate / mL min <sup>-1</sup>
0	65	35	1.0
13	65	35	1.0
14	80	20	1.0
18	80	20	1.0
19	65	35	1.0
25	65	35	1.0

Similarly, the individual UV data of **14** and TMB also exhibited uncharacteristically varied data with RSD values of 11.16 % and 9.99 % respectively. The ratios, however, were far more precise than the ELSD, with an RSD value of 1.32 %. Through serial dilution, a further 4 standards were produced and analysed. These standards also exhibited poor results with unexpected values being observed. The first and second standard exhibited lauric acid height values around 50 mV. After the second standard was stored at -20°C overnight the lauric acid peak exhibited a signal of 250 mV. The artemisinin and DHAA peak areas on the other hand were far smaller than the previous injections. To investigate, a solution of 0.496 g lauric acid in 50 mL toluene was analysed; this also produced the unusually large lauric acid peaks. TMB peak areas in the 210 nm remained consistent while ELSD LA peak areas were varying, ruling out evaporation of solvent as the causative factor.

Repeated variations in the data prompted another change to the mobile phase, reverting back to an isocratic method, as shown in Table 5.42. This protocol was used for the calibration of **18** in toluene.

*Table 5.42: HPLC and ELSD parameters for artemisinin internal standard calibration in toluene. 2  $\mu$ L sample loop.*

ELSD			
Evaporator /°C	Nebuliser /°C	N <sub>2</sub> / SLM	LED /%
40	40	2.15	100
Mobile Phase			
Time / minutes	acetonitrile / %	0.1 % acetic acid / %	Flow Rate / mL min <sup>-1</sup>
0	65	35	1.5
20	65	35	1.5

#### 5.5.14.1. Automated Calibration

To reduce variation due to manual handling, an automated calibration system was set up. This involved separating the HPLC and the rest of the photoreactor, such that the mixed standards were passed in a continuous loop through the HPLC sample loop using a peristaltic pump, as shown in Figure 5.38. The photoreactor was set up with acetone flowing in a continuous loop. The Self Opt Client was set-up to run a ‘List’ method with equilibrium and waiting times reduced to minimum values, allowing for short waiting times between analyses of the standard. This method reduces the impact of errors that can occur when manually injecting standards, such as improper filling of the sample loop. As the sample loop is continuously being filled in the automated set-up, this phenomenon is practically diminished. Furthermore, the time between the run initiating and switching the rotor valve to injection can have a degree of variance when in manual mode, as both operations have to be selected in order by the user, which can result in delayed injections and, hence, potential variation in the analyte retention times. Within the automated system the time between the HPLC method being initiated and the injection of the sample is essentially constant, producing far greater consistency in analyte retention times.

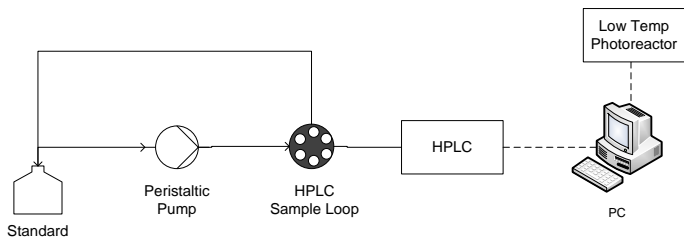


Figure 5.38: Schematic of the set-up for the automated standard analysis. The standard is pumped using the Gilson HPLC pump through the HPLC sample loop in a continuous loop. The reactor is set up to pump acetone in a continuous loop, after the specified equilibrium times of the 'reaction' have been completed the HPLC rotor valve is triggered from 'waste' to 'external' injecting the standard in the sample loop into the HPLC for analysis. Once appropriate HPLC results have been returned to the control computer the next set of conditions are activated and the equilibrium stage is repeated. For standard analysis the equilibrium times are set to a minimum to allow for rapid analysis.

During the calibration, however, it was noticed that on multiple occasions lauric acid was identified as two peaks by the HPLC software. As the script file will only detect a single peak for each compound it will only identify the first 'peak' as that of the standard, therefore effectively reducing the peak value by a half. This results in overinflated yields. Furthermore, if this phenomenon occurs during a self-optimised experiment it would invalidate the data and require restarting of the experimental sequence.

Changes to the smoothing factor of the ELSD were investigated to determine whether this was a contributing factor to the identification of multiple peaks. The smoothing factor is used to average the output data to achieve a smoother response and reduce noise - a lower smoothing factor will increase sensitivity, producing sharper, more resolved peaks albeit with higher levels of noise.<sup>318</sup> The original smoothing factor that was used throughout the investigations with the ELSD was 30 (3 seconds). There appeared to be no correlation between the smoothing value and the determination of multiple peaks. The lauric acid peak and the artemisinin peak were both detected as two peaks for smoothing values above and below 30. It was therefore determined that the observed phenomenon was unlikely to be related to the smoothing factor. An alternative option was to stipulate a minimum expected value for the lauric acid peak within the status2target.m script. Lauric acid is added to the reaction medium in a known, consistent quantity, and should therefore produce a consistent peak area. The setting of the 'HPLCProcOptions.AreaLowerLimit' allows areas below the typical peak value to be discarded, invalidating the run and causing a restart.

### 5.5.15. Alternative Column for the Separation of **18** and Toluene

The variation of the ELSD data, along with the software detecting the analyte peaks as multiplets, again led to a reversion to the use of 210 nm UV. In an attempt to separate the **18** and toluene a number of alternative columns were tested. Eventually the use of a C-8 (Phenomenex Luna 5 $\mu$  250 x 4.6 mm), was found to separate the two compounds, with elution of **18** observed prior to that of toluene in the UV. The mobile phase composition was then adjusted to 65:35 (v/v %) acetonitrile : 0.1% acetic acid to improve the separation, with a flow rate of 0.5 mL min<sup>-1</sup> over the first 10 minutes increasing to 1.5 mL min<sup>-1</sup> over the next five minutes.

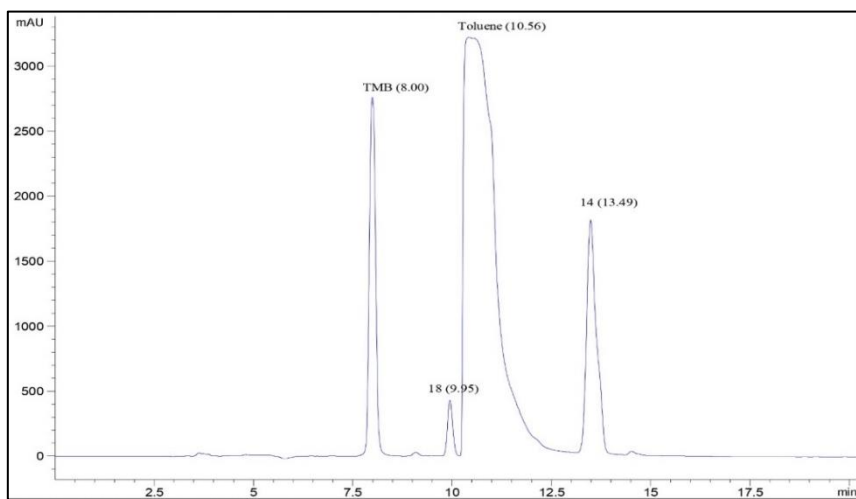


Figure 5.39: HPLC-210 nm UV chromatograms of the mixed standard of **18**, **14**, and TMB in toluene, separation achieved using a C-8 column with an isocratic mobile phase of 65:35 acetonitrile:0.1 % acetic acid with a flow rate ramp.

### 5.5.16. Internal Standard Calibration in Toluene using UV

The separation of **18** from toluene allowed for a calibration to be conducted using 210 nm UV detection. A solution of **18** (0.4521 g, 0.0641 M) and **14** (0.04542 g, 0.0769 M) was prepared in a stock solution of TMB (0.0029 M) and lauric acid (0.0541 M) in toluene (25 mL). Through serial dilution a further six standards were produced, each standard was injected a minimum of five times, with additional injections being made for samples that provided inconsistent results.

Table 5.43: Isocratic mobile phase with a flow rate ramp to accelerate the elution of the hydrophobic analytes. The 5 $\mu$ L sample loop was used.

Mobile Phase			
Time / minutes	acetonitrile / %	0.1 % acetic acid / %	Flow Rate / mL min <sup>-1</sup>
0	65	35	0.5
10	65	35	0.5
15	65	35	1.5
25	65	35	1.5

Table 5.44: Concentration of standard used for the internal standard calibration of **18** and **14** with TMB in toluene using 210 nm UV detection.

Standard	18 / mol dm <sup>-3</sup>	14 / mol dm <sup>-3</sup>
1	0.0641	0.0769
2	0.0512	0.0615
3	0.0256	0.0308
4	0.0205	0.0246
5	0.0384	0.0461
6	0.0128	0.0154
7	0.0064	0.0077

Detection was performed with 210 and 194 nm UV light. The 194 nm was chosen in an attempt to increase the analyte signals. The variation within each of the analyte sample sets for each wavelength was calculated and expressed as the RSD values as shown in Table 5.45. The ratios of **18** to TMB and **14** to TMB for each injection were calculated, with Grubb's outlier tests removing outliers ( $p < 0.05$ ). The mean values and corresponding RSD values were then calculated from the remaining data, and expressed in **Error! Reference source not found.**. The RSD values of these ratios were then compared and a weighting produced based on equation 5.21.

$$Weight = RSD_{210\text{ nm}} - RSD_{194\text{ nm}} \quad 5.21$$

Table 5.45: Comparison of the RSD % values for the mean ratios of artemisinin to TMB and DHA to TMB as analysed by the 210 nm and 194 nm UV detection. The weight of the RSD values were calculated

in relation to the 210 nm value to indicate which wavelength produced the overall lower RSD for each analyte.

Artemisinin:TMB Ratio			
Standard	210 nm RSD/%	194 nm RSD / %	Weight
1	1.34	0.63	0.71
2	2.56	1.58	0.99
3	3.09	2.68	0.40
4	0.94	1.85	-0.91
5	1.99	3.99	-2.00
6	4.25	2.01	2.24
7	1.21	0.52	0.67
<b>Total</b>			2.12
DHAA:TMB Ratio			
Standard	210 nm RSD/%	194 nm RSD / %	Weight
1	1.36	2.41	-1.05
2	1.08	2.38	-1.30
3	1.39	2.17	-0.78
4	1.32	2.93	-1.61
5	1.66	2.46	-0.80
6	2.92	1.99	0.93
7	0.10	3.13	-3.02
<b>Total</b>			-7.64

The RSD weightings indicate more precise data is produced for **18** when 194 nm detection is used, while for **14**, the 210 nm UV produced overall lower RSD values. The fact that the **18** peak areas are larger with 194 nm detection will also improve the sensitivity, reducing the LOD and LOQ of the analysis. The calibrations produced straight lines of equations (5.22) and (5.23), for **18** and **14** respectively. Both calibrations exhibited  $R^2$  values of 0.99.

$$y = 0.038x + 0.01 \quad (5.22)$$

$$y = 0.039x + 0.05 \quad (5.23)$$

Table 5.46: The isocratic method with a flow rate ramp produced reasonably low levels of variation in the retention times of the analytes.

Analyte	Mean Residence Time / min	RSD / %
Artemisinin (n = 45)	10.15	1.16
DHAA (n = 44)	13.70	0.66
TMB (n = 45)	8.09	1.28

The residence times and associated RSD for the 194 nm data for each analyte is shown in Table 5.46. The majority of the injections were made manually, although three injections of Standard 2 were performed under automated control. An experiment file was produced to run a LIST method with shortened equilibration times. The reactor and HPLC were separated with the reactor set up to recirculate acetone, while the HPLC sample loop was connected to a peristaltic pump to flow the standard in a continuous manner. Three standard injections were made under automated control exhibiting initiation and completion of each ‘run’ with successful detection of the analytes triggering the start of the subsequent run. The 210 nm data from the automated injections is shown in Table 5.47. What is clear from this data is the low variation within the residence times and the peak areas of each of the analytes, with maximum values being observed in the artemisinin data with a retention time and area RSD of 0.10 % and 0.59 % respectively. Despite this only being a small sample set, it gave an indication into the beneficial effects of using automation when injecting the analyte standards for calibration. The continuous flow of standard through the sample loop prevents errors in loop filling that can occur when under manual operation, while the triggering of the HPLC injection *via* the automated system reduces time variations that occur when the operator switches the injector position from waste to the column, hence producing more far more consistent residence times.

Table 5.47: Automated injections of Standard 2. The retention time variation is greatly reduced.

Injection			Retention Time		Peak Area	
	Retention Time / min	Area	Mean	RSD /%	Mean	RSD /%
<b>Artemisinin</b>						
<b>1</b>	10.395	2359				
<b>2</b>	10.377	2379	10.383	0.10	2364	0.59
<b>3</b>	10.376	2352				
<b>DHAA</b>						
<b>1</b>	13.892	19234				
<b>2</b>	13.872	19296	13.880	0.07	19250	0.21
<b>3</b>	13.877	19221				
<b>TMB</b>						
<b>1</b>	8.309	21796				
<b>2</b>	8.3	21737	8.302	0.08	21731	0.31
<b>3</b>	8.296	21660				

### 5.5.17. General Procedures for the Synthesis of 18

All starting materials were produced in brown glass vessels and degassed with nitrogen to avoid unwanted reactions prior to the experiment.

#### Photo-Oxidation of DHAA and Semi-continuous Synthesis of Artemisinin in Toluene

DHAA (1.18 g, 0.05 M) was combined with TPP (0.0154 g, 0.5 mol %) and biphenyl (internal nmr standard, 0.1182 g) in toluene (100 mL). The solution was pumped at a flow rate of  $1.0 \text{ mL min}^{-1}$ . Simultaneously,  $\text{O}_2$  was flowed at  $10.0 \text{ mL min}^{-1}$  to meet the substrate flow at a union to form a Taylor flow pattern. The subsequent Taylor flow passed through the photoreactor (double layer FEP, 1/32" i.d., volume  $7.54 \text{ cm}^3$ , 424 nm PhotoLED) housed in the cooling bath at  $-50^\circ\text{C}$  ( $T_1 = -48^\circ\text{C}$ ). Photoproduct was collected after an equilibration time of 30 minutes. A sample was prepared and analysed *via* NMR. 10mL of the photoproduct was heated to  $50^\circ\text{C}$ , whereupon TCA (0.04 g, 0.5 equivalents) was added, and the solution stirred with a flow of oxygen at  $2.0 \text{ mL min}^{-1}$ . An aliquot was taken 1 minute after acidification and analysed *via* HPLC. The solution was maintained under these conditions with samples being taken and analysed with the HPLC after 40 and 60 minutes.

#### Initial Continuous ‘Two-Pot’ Synthesis of 18

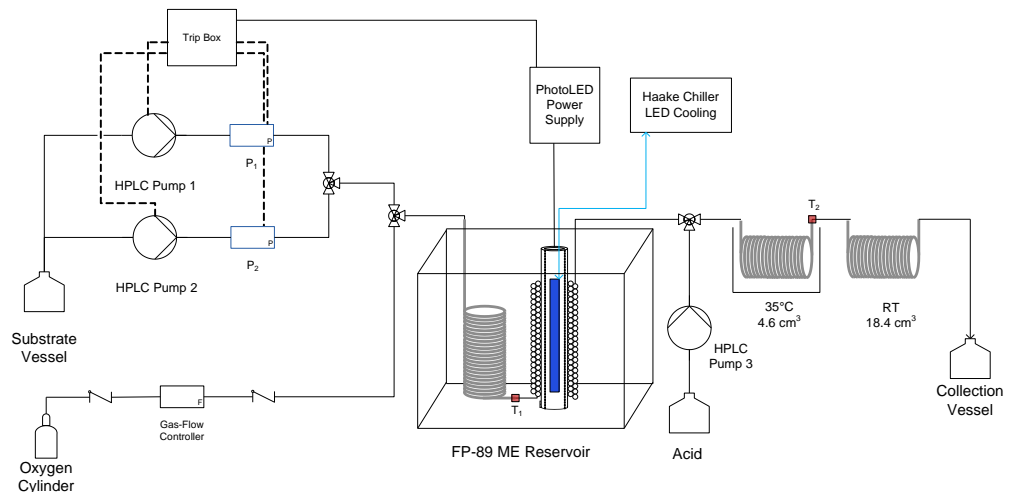


Figure 5.40: Schematic of the reactor set-up for the fully continuous ‘two-pot’ synthesis of artemisinin. A third HPLC pump has been added after the photoreactor to deliver the acid after the photo-oxidation has taken place.

DHAA (1.18 g, 0.05 M) was combined with TPP (0.015 g, 0.5 mol %) and biphenyl (0.121 g) in DCM (100 mL). The solution ( $1.0 \text{ mL min}^{-1}$ ) was mixed with an  $\text{O}_2$  stream ( $10.0 \text{ mL min}^{-1}$ ) to form a Taylor flow pattern. The resulting flow entered the low temperature FEP (1/16" o.d., 1/32" i.d.,  $7.54 \text{ cm}^3$ ) photoreactor ( $T_1 = 20^\circ\text{C}$ , 424 nm

PhotoLED). The photoproduct then met a stream of TFA ( $1.0 \text{ mL min}^{-1}$ , 0.19 mL, 0.025 M) in DCM (100 mL) to provide an acid equivalence of 0.50 (0.025 mol  $\text{dm}^{-3} \text{ min}^{-1}$ ). A colour change from purple ( $\text{H}_2\text{TPP}$ ) to green ( $\text{H}_4\text{TPP}^{2+}$ ) of the photoproduct was observed upon mixing with the acid stream. The solution passed through the secondary coils and into the collection vessel. The reactor was not connected directly to the HPLC sample loop, and so samples were manually collected *via* syringe after an equilibration time of 70 minutes and injected onto the HPLC for analysis. Yield quantification was not carried out on the HPLC data as a result of the significant level of dilution due to the additional acid stream. Internal HPLC calibration had not been completed at this stage. The use of biphenyl as an internal NMR standard allows quantification of this data.

### Fully-Continuous Synthesis of Artemisinin in Toluene

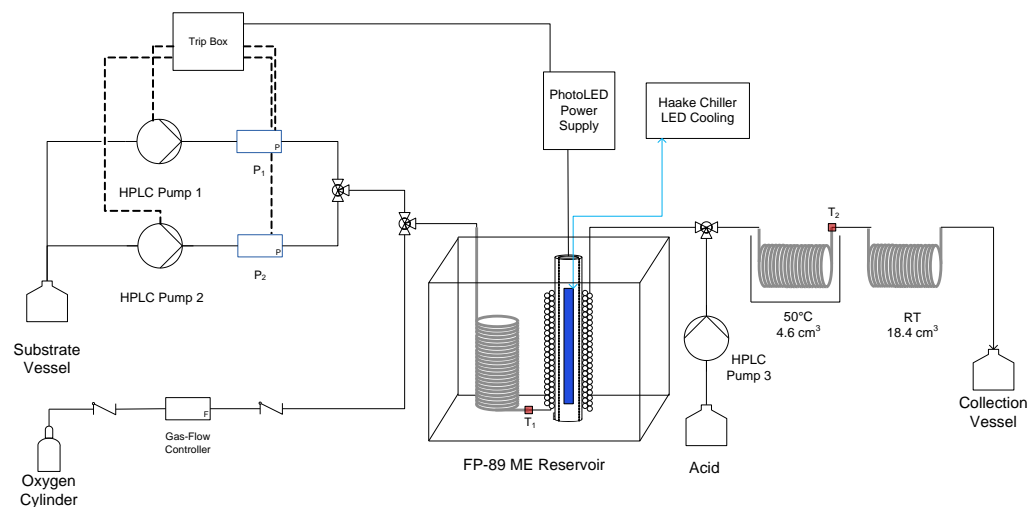


Figure 5.41: Schematic of the reactor set-up for the continuous synthesis of artemisinin in toluene. A second HPLC pump was placed after the photoreactor to deliver TCA in toluene at an equivalence of 0.5. The acid and photoproduct streams intersect at a Swagelok® T-union where they would combine. Good levels of mixing were observed by the colour change of the TPP from purple (unprotonated) to green (protonated). The stream would then enter a coil ( $4.60 \text{ cm}^3$ ) heated in an oil bath set to  $50^\circ\text{C}$  then into an ambient coil ( $18.40 \text{ cm}^3$ ).

DHAA (1.18 g, 0.05 M) was combined with TPP (0.0154 g, 0.5 mol %) and biphenyl (internal nmr standard, 0.1182 g) in toluene (100 mL). The solution was pumped at a flow rate of  $1.0 \text{ mL min}^{-1}$ . Simultaneously,  $\text{O}_2$  was flowed at  $10.0 \text{ mL min}^{-1}$  to meet the substrate flow at a union to form a Taylor flow pattern. The subsequent Taylor flow passed through the photoreactor (FEP, 1/32" I.D,  $7.54 \text{ cm}^3$ , 424 nm PhotoLED) housed in the cooling bath at  $-50^\circ\text{C}$  ( $T_1 = -47^\circ\text{C}$ ). After exiting the photoreactor the product was combined with a second stream of TCA (0.42 g) in toluene (50 mL) at a flow rate of  $0.50 \text{ mL min}^{-1}$  delivering 0.50 equivalents of acid, and mixed in a T-piece. After mixing with acid, the solution flowed through a section of PTFE tubing filled with glass

beads to enhance mixing, then into a stainless steel coil (1/8" o.d, 0.055 i.d, length 3 m, volume 4.60 cm<sup>3</sup>) placed in an oil bath held at 50°C. A thermocouple placed at the outlet of the heated coil, T<sub>2</sub>, measured the solution temperature to be 25°C. The solution then passed through another stainless steel coil (1/8" o.d, 0.055 i.d, length 12 m, volume 18.40 cm<sup>3</sup>) without heat control before collection. Samples were collected for NMR and HPLC analysis after a reaction time of 45 minutes. Subsequent HPLC injections were made with the remaining sample in the syringe after the previous runs were completed.

### Fully-Continuous Synthesis of Artemisinin in Toluene

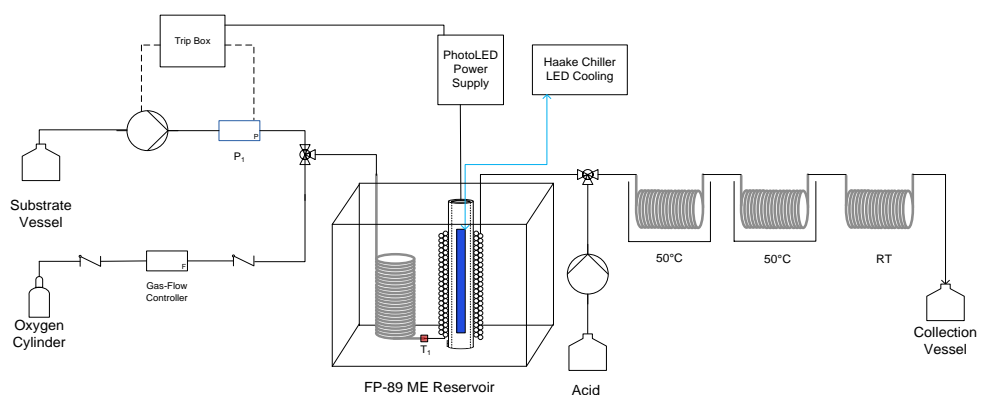


Figure 5.42: Schematic of the reactor set-up for the continuous synthesis of artemisinin in toluene, a second heated coil was added to further drive the reaction to completion.

DHAA (3.54 g, 0.05 M) was dissolved in toluene (300 mL) along with TPP (0.046 g, 0.5 mol %) and biphenyl (0.335 g). This solution was pumped at a flow rate of 1 mL min<sup>-1</sup> and mixed with an oxygen flow of 10 mL min<sup>-1</sup>. The corresponding 'slug' flow entered a cooling coil to allow for the solution to reach a temperature of - 47°C before entering the FEP photoreactor. A stream of TCA ( 1.23 g) dissolved in toluene (150 mL) was delivered at a flow rate of 0.5 mL min<sup>-1</sup> to allow 0.5 equivalents of acid to be mixed with the outlet stream of photoproducts. On mixing with acid a clear colour change from purple (H<sub>2</sub>TPP) to green (H<sub>4</sub>TPP<sup>+</sup>) was observed. The mixture, still exhibiting slug flow, then entered a section of glass beads to enhance mixing, followed by two stainless steel coils (each: 1/8" o.d, 0.055 i.d, length 3 m, volume 4.60 cm<sup>3</sup>) placed in oil baths held at 50°C. The heated mixture then entered a coil (1/8" o.d, 0.055 i.d, length 12 m, volume 18.40 cm<sup>3</sup>) before collection. An initial sample was collected and injected immediately onto the HPLC, with subsequent injections following from the sample remaining in the syringe. The above reaction was repeated with each of the pump flow rates at half the value and with the same starting material.

## Continuous ‘One-pot’ Synthesis of Artemisinin with the Vortex Reactor

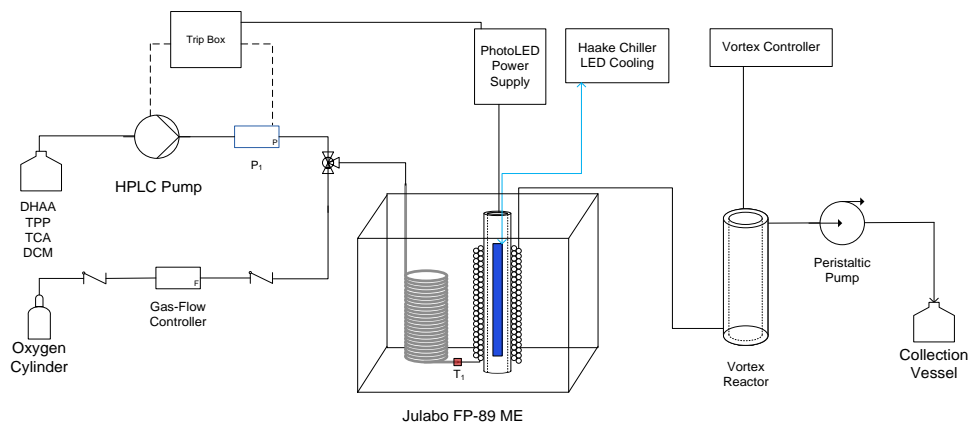


Figure 5.43: Schematic of the reactor set-up for the continuous synthesis of artemisinin. The heated coils have been replaced by a small vortex reactor to aid in the Hock cleavage and oxidation of the tertiary hydroperoxide. Upon exiting the photoreactor the photoproduct stream enters the bottom of the vortex reactor through a 1/8" o.d screw fitting. To prevent the solution from leaking out of the top seal of the reactor, a peristaltic pump is attached to the outlet to effectively pull the solution out.

A solution of DHAA (1.18 g, 0.05 M), TPP (0.0154 g, 0.5 mol %), TCA (0.41 g, 0.025 M) and biphenyl (0.106 g) in DCM (100 mL) was pumped at a flow rate of  $1.0 \text{ mL min}^{-1}$  before mixing with an  $\text{O}_2$  flow ( $10.0 \text{ mL min}^{-1}$ ) and forming a Taylor flow pattern. The stream then entered a cooling coil ( $T_1 = -77^\circ\text{C}$ ) before entering the FEP photoreactor (1/32" i.d., volume  $7.54 \text{ cm}^3$ , 424 nm PhotoLED). Upon exiting the photoreactor the solution enters the Vortex reactor (4000 rpm), the solution is removed from the Vortex via a peristaltic pump (17 rpm, measured to be  $1.09 \text{ mL min}^{-1}$ ). A sample (2 mL) was collected after 70 minutes and immediately injected onto the HPLC. Subsequent samples were injected from the same syringe. An aliquot (0.5 mL) of the sample was prepared for  $^1\text{H}$  NMR analysis ( $\text{CDCl}_3$ ).

## Continuous ‘Two-pot’ Synthesis of Artemisinin with the Vortex Reactor

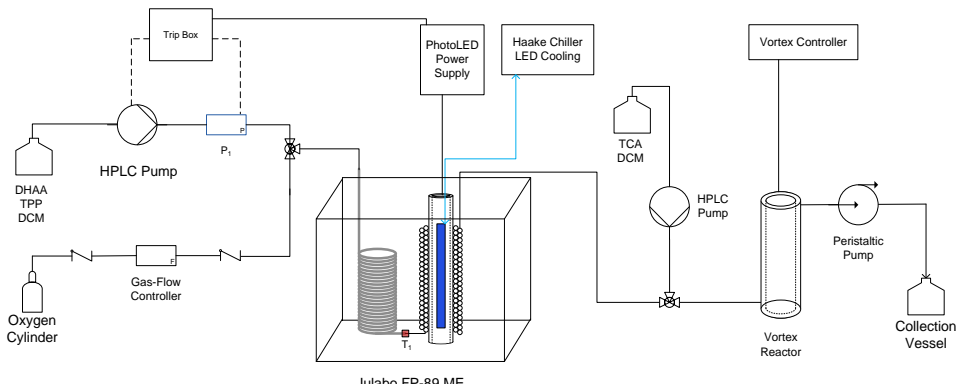


Figure 5.44: (Figure 4.28) Schematic of the reactor set-up for the continuous ‘two-pot’ synthesis of artemisinin. The addition of the second HPLC delivers TCA in DCM before the vortex reactor.

A solution of DHAA (3.36 g, 0.05 M), TPP (0.0308 g, 0.5 mol %) in DCM (200 mL) was pumped at a flow rate of  $1.0 \text{ mL min}^{-1}$  before mixing with an  $\text{O}_2$  flow ( $10.0 \text{ mL min}^{-1}$ ) and forming a Taylor flow pattern. The stream then entered a cooling coil ( $T_1 = -77^\circ\text{C}$ ) before entering the FEP photoreactor (1/32" i.d., volume  $7.54 \text{ cm}^3$ , 424 nm PhotoLED). Upon exiting the photoreactor the plug flow mixed with a flow of TCA (0.82 g) in DCM (100 mL) at a flow rate of  $0.5 \text{ mL min}^{-1}$  giving 0.5 equivalents of acid to each plug. The streams enter the Vortex (4000 rpm). The solution is removed from the outer of the Vortex *via* a peristaltic pump set to 25 rpm (measured to be  $1.60 \text{ mL min}^{-1}$ ). Sample was collected after 70 minutes and immediately injected onto the HPLC. Subsequent samples were injected from the same initial syringe. With the system still flowing, the vortex was then set to 3000 RPM and further samples were collected after the 70 minute equilibrium time and analysed by HPLC.

#### Photo-Oxidation of DHAA with Lauric Acid

DHAA (0.59 g, 0.05 M) and lauric acid (0.25 g, 0.025 M) were combined in toluene (50mL). The solution was pumped at a flow rate of  $1.0 \text{ mL min}^{-1}$  and combined with an oxygen flow of  $5.0 \text{ mL min}^{-1}$ . The resulting Taylor flow was then directed into the photoreactor maintained at a temperature of  $20^\circ\text{C}$ . Product was collected after an equilibrium time of 35 minutes and analysed *via* HPLC.

#### Automated ‘One-Pot’ List Method with Vortex Rotation Adjusted

DHAA (2.95 g) was combined with TCA (1.02 g, 0.025 M), TPP (0.25 mM) in 250 mL of a stock solution of Lauric acid (0.05 M) and TMB (3.3 mM) in DCM. HPLC analysis of the starting material revealed a DHAA concentration of 0.047 M, this value was then set as the concentration in the Experiment File and as a constant value for each of the Run’s independent variable **3**. The automated List method was performed over 3 Runs; the independent variables are outlined in Table 5.48.

Table 5.48: Automated List run parameters for the ‘one-pot’ synthesis of artemisinin using the Vortex reactor.

Run	Independent Variable				Vortex /rpm
	<b>1</b> /°C	<b>2</b> / mL min <sup>-1</sup>	<b>3</b> / mol dm <sup>-3</sup>	<b>4</b>	
1	10	1.0	0.047	2	2000
2	10	1.0	0.047	2	3000
3	10	1.0	0.047	2	4000

Within the indep2ctrl.m script, the concentration of the starting material, 0.047 M, was set as the ‘SubstrateConc\_high’. The combination of this setting with each independent variable **3** also being set to 0.047, results in only Jasco® HPLC Pump 1 working at the set flow rate (independent variable **2**), Pump 2 is not active as no dilution of the substrate feed is required. With this set up, the outlet tubing from Pump 2 is replaced with a cap on the mixing T-piece to prevent the reagent feed from flowing towards Pump 2.

## 5.6. Developing the Automated Synthesis of Rose Oxide, **13**.

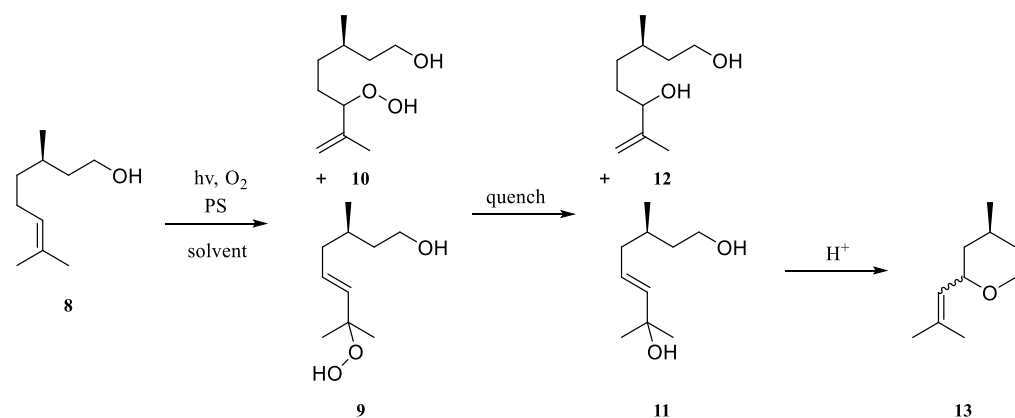


Figure 5.45. Scheme for the photo-oxidation of citronellol to the corresponding hydroperoxides. Followed by subsequent quenching to the relevant diols and acidification to produce the commercially relevant molecule rose oxide.

### 5.6.1. HPLC Method Development

The initial HPLC analysis of citronellol, **8**, and rose oxide, **13**, used conditions similar to those previously developed by Meyer *et al.*: reverse-phase C18 column (5  $\mu$ m, 100 $\text{\AA}$ , 250 x 4.6 mm) with a mobile phase composition of 70:30 (v/v %) acetonitrile: 0.1 % acetic acid, at a flow rate of 1 mL  $\text{min}^{-1}$  and a column temperature 40°C, with 210 nm UV detection.<sup>154</sup>.

**8** in DCM under the conditions outlined above produced a signal for the solvent dichloromethane at 3.3 minutes, a major citronellol peak at 5.8 minutes with a minor peak at 4.8 minutes. Commercially available (-)-**13** was then analysed on the HPLC indicating two peaks in the UV with retention times of 11.36 minutes and 12.05 minutes, corresponding to the two stereoisomers. Due to its relatively high volatility, **13** did not elicit a response with the ELSD. To determine the identity of each of the peaks the rose oxide was also analysed by  $^1\text{H}$  NMR in  $\text{CDCl}_3$ . The subsequent NMR was compared to the literature values for both *cis*-(-) - and *trans*-(-)-rose oxide and corresponded accordingly.<sup>326</sup> The olefinic hydrogens originating from carbon-7,

produced clear multiplets that allow for ease of identification. The olefinic hydrogen *cis*-(-)-rose oxide gives rise to a multiplet with a shift of 5.15 ppm, while the *trans*- form gives a signal at 5.28 ppm. Integration of these peaks reveals a ratio of around 8.60:1 of *cis:trans*. This aids with the identification of the two peaks in the HPLC, revealing that the smaller peak that elutes first belongs to the *trans*- isomer, while the larger, later peak is of the *cis*- form. This separation is potentially very beneficial, as it can aid in the process development to prioritise the formation of the *cis*- isomer.

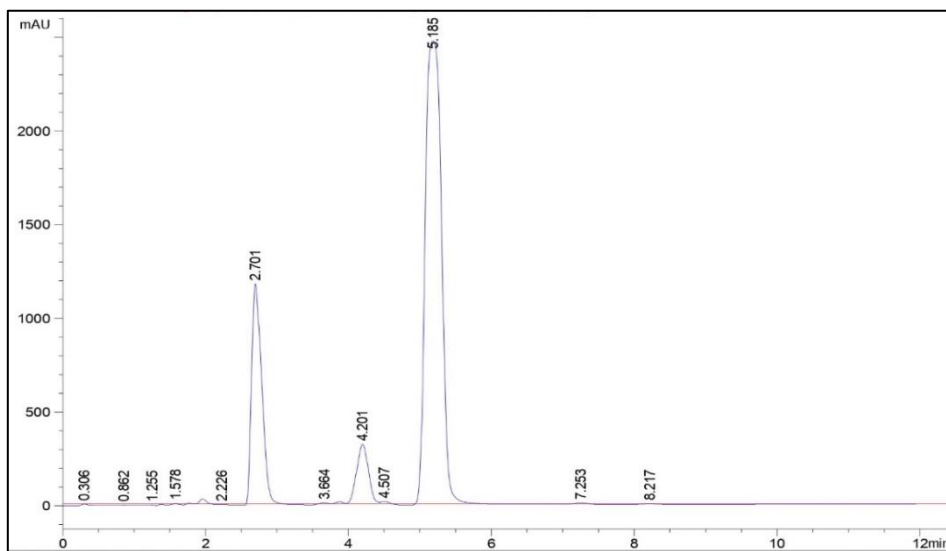


Figure 5.46: HPLC-210 nm and ELSD chromatograms of citronellol in DCM. No response is observed with the ELSD. A strong major peak is present for citronellol in the 210 nm with a retention time of 5.185 minutes, along with a minor peak at 4.201 minutes. Mobile Phase 70:30 MeCN/0.1% AcOH 1mL min<sup>-1</sup> 40°C Column temperature.

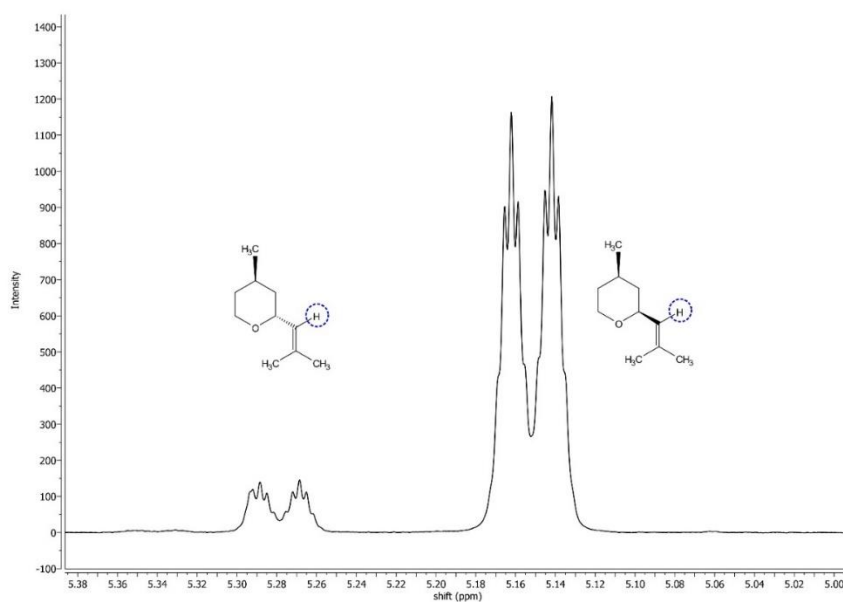


Figure 5.47: <sup>1</sup>H NMR shifts of the olefinic hydrogen on *trans*-(-)-rose oxide ( $\delta$  5.26 – 5.30 ppm) and *cis*-(-)-rose oxide ( $\delta$  5.12 – 5.18 ppm).

HPLC showed the *trans*- isomer to elute at 11.36 minutes with a peak area of 12878, while the *cis*- form elutes after 12.05 minutes with an area of 58301. The area ratio is 4.5:1, far lower than that found through NMR, indicating that the *cis*- and *trans*- isomers possess different electronic properties and hence differences in their UV absorbance. Therefore, the ratio between the isomers was obtained through  $^1\text{H}$  NMR analysis.<sup>327</sup>

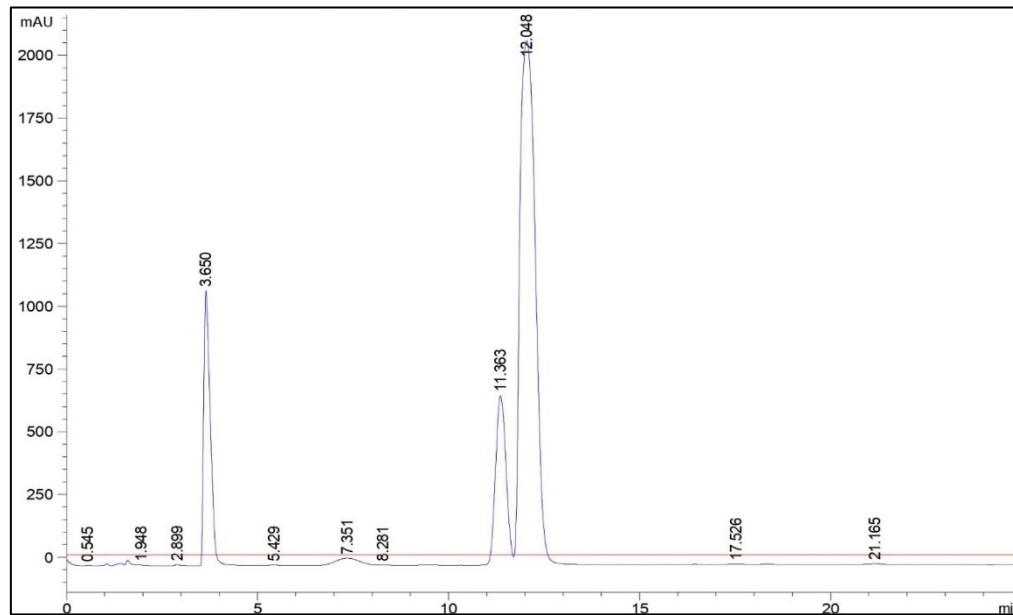


Figure 5.48: HPLC-210 nm and ELSD analysis of rose oxide. No response is observed with the ELSD. Two peaks corresponding to *trans*-rose oxide (11.363 minutes) and *cis*-rose oxide (12.048 minutes) are present in the 210 nm. Mobile phase 60:40 acetonitrile: 0.1 % acetic acid, 1.0 mL min<sup>-1</sup> at a column temperature of 40°C.

Rose oxide was photo-chemically synthesised in a semi-continuous ‘two-pot’ approach in DCM, described in 5.6.3, using the low-temperature double-layer FEP (1/16” o.d, 1/32” i.d, volume 7.54 cm<sup>3</sup>) photoreactor developed for the photo-oxidative synthesis of **18**. HPLC analysis was conducted at each stage of the reaction.

The consumption of citronellol after the photo-oxidation was observed along with the formation of a prominent peak at 2.60 minutes. The early elution of this peak indicates that the compound is relatively polar, and is therefore attributed to the hydroperoxides formed after the photo-oxidation, analogous to the observed hydroperoxide formation in the oxidation of **14**. The hydroperoxides were then quenched with triphenylphosphine to produce the corresponding diols. After the reduction, the corresponding HPLC signal is reduced while the signal typically attributed to the reaction solvent, DCM appears to be larger, this indicates that the diols and DCM co-elute. A similar phenomenon was observed with the hydroperoxides of **14** co-eluting with DCM. The stacked 210 nm and ELSD spectra of the quenched hydroperoxides,

Figure 5.50, shows two truncated ELSD peaks corresponding to the two prominent peaks in the 210 nm with retention times of 2.40 and 3.25 minutes. The UV peak at 3.25 minutes is indicative of DCM, however DCM has been shown to not exhibit a peak in the ELSD; therefore, the observed peak is attributed to one of the citronellol diols, while the earlier eluting peak is attributed to the other.

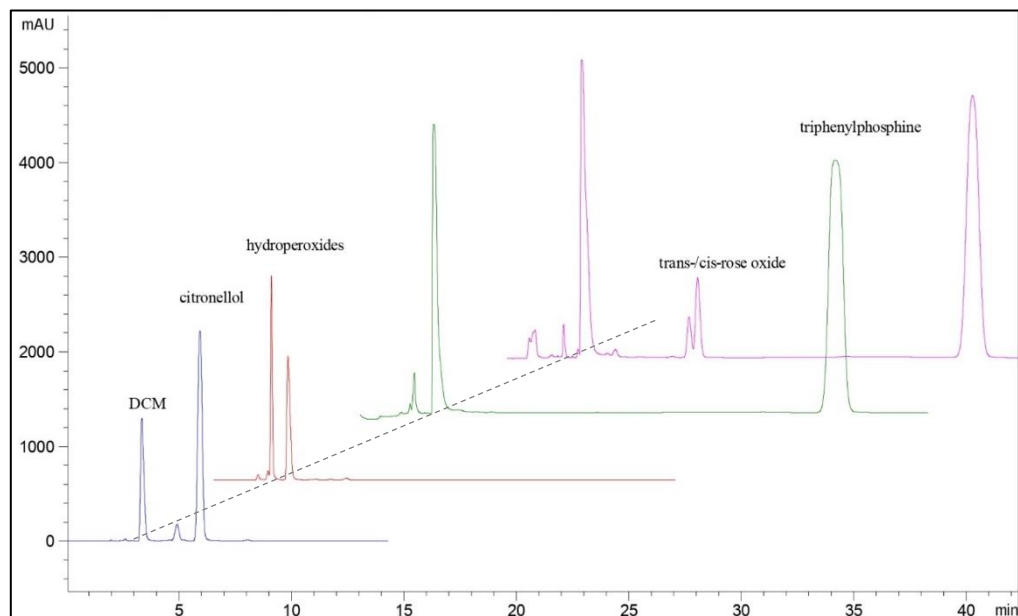


Figure 5.49: HPLC-210 nm stacked chromatograms of the substrate composition during subsequent stages of the semi-continuous photo-oxidative synthesis of rose oxide. The spectra depict as follows; *starting material*; *after photo-oxidation*; *after quench with  $PPh_3$* ; *after acidification*. Mobile Phase 70:30 MeCN/0.1% AcOH  $1\text{mL min}^{-1}$ ,  $40^\circ\text{C}$  Column temperature.

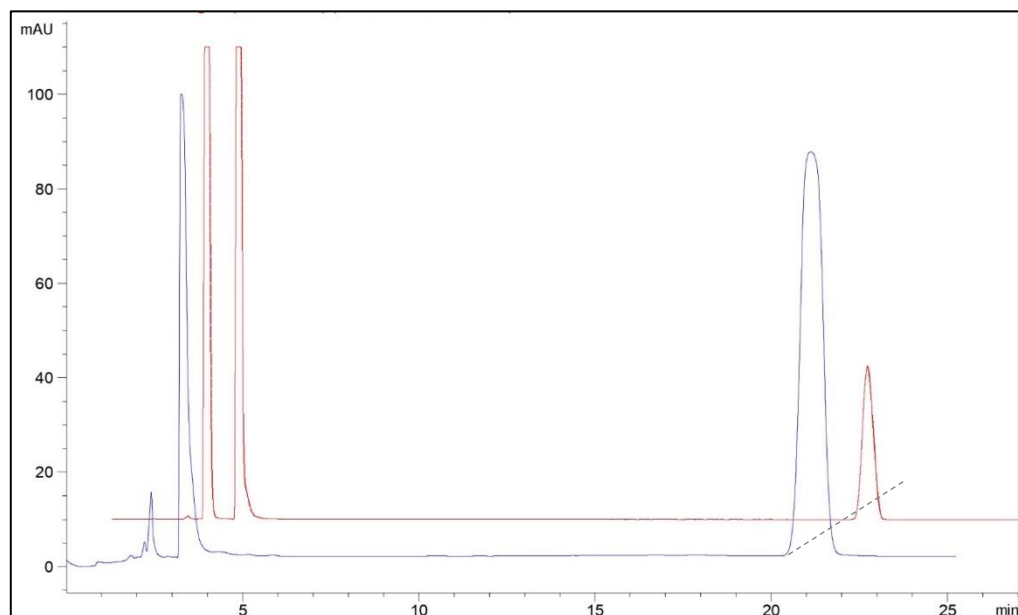


Figure 5.50: HPLC-210 nm and ELSD chromatograms of the photo-product after quenching with  $PPh_3$ . Two truncated peaks are observed in the ELSD corresponding to the 210 nm peaks with elution times of 2.40 and 3.25 minutes. The later eluting signals in both detectors are due to  $PPh_3$ .

After quenching,  $\text{H}_2\text{SO}_4$  was added to cyclise the diols to rose oxide. The peaks of *trans*- and *cis*-rose oxide are present after the acidification, with retention times of 8.09 and 8.47 minutes respectively. The resolution between the two isomer peaks was calculated to be 1.81, using equation (5.24) where  $t_{Ri}$  is the peak retention time and  $W_i$  is the peak width. At this resolution the peaks are not fully separated. The retention times are shorter than the previously analysed sample of rose oxide shown in Figure 5.48 due to the adjustment of the mobile phase composition, from 60:40 (v/v %) acetonitrile : 0.1 % acetic acid for the rose oxide analysis to 70:30 (v/v %) for the reaction product analysis.

$$R = \frac{t_{R2} - t_{R1}}{\frac{1}{2}(W_1 + W_2)} \quad (5.24)$$

The reaction product was then analysed using various mobile phase compositions to determine optimum conditions for the separation of the isomers of **13**. The composition of 60:40 (v/v %) acetonitrile : 0.1 % acetic acid allowed for full separation of the peaks, with a resolution of 2.39, and a relatively short method time. A gradient mobile phase, Table 5.49, was then developed to appropriately separate the isomers and to reduce the retention of the high affinity non-polar adjuncts. The mobile phase is isocratic at 60:40 for the first 15 minutes, resulting in a flat baseline and good separation of all the peaks of interest. The proportion of acetonitrile was then increased to increase the affinity of the non-polar compounds to the mobile phase. The increase in acetonitrile, however, causes a slope in the baseline. Although the UV cut-off point of acetonitrile is 190 nm, a proportion of the 210 nm light will still be absorbed; hence; as the phase composition changes, so too does the absorption.<sup>309</sup>

Table 5.49: Mobile phase gradient for the elution of separated rose oxide isomers and to reduce the retention time of the non-polar compounds present such as  $\text{PPh}_3$ .

Time/ min	Acetonitrile/ %	Acetic acid (0.1%) / %	Flow Rate/ mL min <sup>-1</sup>	Column Temperature/ °C
0	60	40	1.0	40
15	60	40	1.0	40
17	80	20	1.0	40
22	80	20	1.0	40
25	60	40	1.0	40

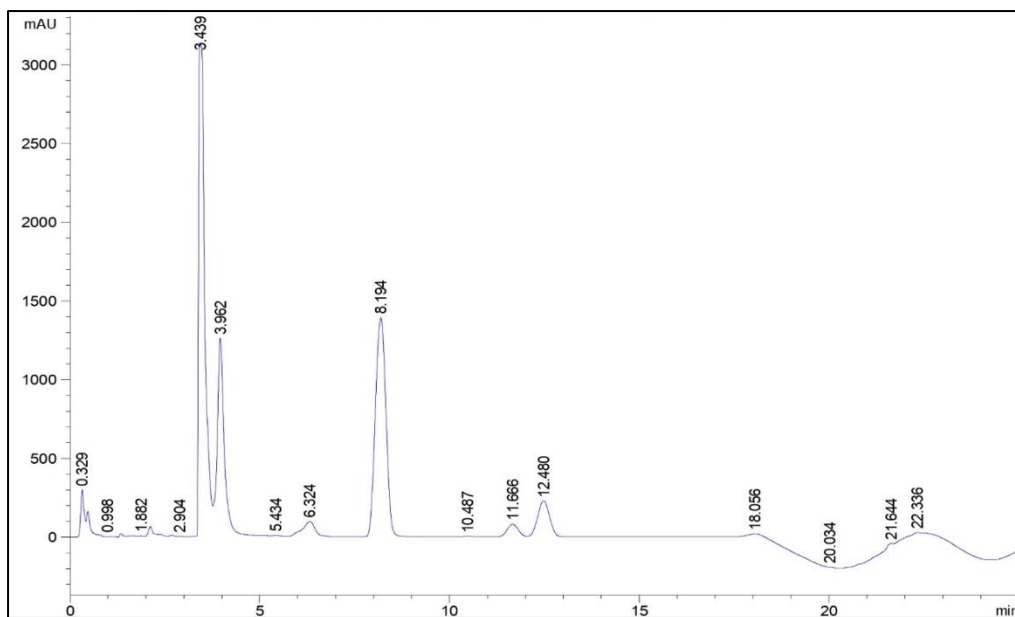


Figure 5.51: HPLC-210 nm chromatogram of the photoproduct with added citronellol to highlight the separation of the analyte peaks. Mobile Phase 60:40 MeCN/0.1% AcOH.  $1\text{mL min}^{-1}$ ,  $40^\circ\text{C}$  column temperature. Citronellol is found with an elution of 8.194 minutes. Trans-rose oxide at 11.666 minutes and cis-rose oxide at 12.480 minutes. The increase in the proportion of acetonitrile causes the dip in the baseline.

### 5.6.2. Internal Standard Calibration of Citronellol, trans- and cis-rose oxide

The development towards the self-optimisation of **18** highlighted the requirement for internal standard calibrations, to negate the dilution effects that will occur in a multi-step continuous flow reaction.

Trimethoxybenzene, TMB, was found to be a good standard for UV detection, with a strong UV response and early elution. This compound had been previously added to a starting reagent solution and used in the synthesis of **13**. Under the gradient conditions of Table 5.49, TMB, added to a solution of photo-product, possessed a retention time of 5.94 minutes, with no significant peaks around it.

The **13** used for the standard was prepared for NMR analysis as 12 samples. The *cis*- to *trans*- ratio was found to be 8.63:1 with a low RSD of 0.21 %. In total, nine standards of **8** and **13** were prepared through serial dilution from a stock solution of TMB (0.0031 M) in methanol, the concentrations of which are shown in Table 5.50. Each standard was analysed a minimum of five times. Outliers from each sample set were identified by the Grubbs' outlier test and subsequently removed before the mean value and

corresponding relative standard deviation were calculated. Table 5.50 reveals overall acceptable levels of variation within each standard set, especially for the isomers of **13**. The ratio of **8** to TMB exhibits slightly higher variation at the high and low end of the concentration range. The variation within an internal standard calibration is expected to be slightly higher than for an external equivalent due to the measurement of two analytes, the error of each peak area can effectively superimpose, potentially exacerbating the level of variation.

The residence times of each analyte were measured over all injections; again outliers were removed giving a total of 36, from which the mean values and corresponding RSD values were calculated, Table 5.51. The RSD values were typically around 2 %, slightly higher than is usually observed when an isocratic mobile phase is used, which is likely due to a slight change in the level of the mobile and stationary phase equilibrium between subsequent runs.

*Table 5.50: Concentrations along with the calculated mean ratio of the analyte peak area to the TMB area of each injection of the nine combined standards of citronellol and rose oxide. The standards were prepared from the same stock solution of TMB in methanol, hence each possess the same concentration of the standard.*

Standard	citronellol			cis-rose oxide			trans-rose oxide		
	Conc. / mol dm <sup>-3</sup>	Area Ratio	RSD /%	Conc. / mol dm <sup>-3</sup>	Area Ratio	RSD /%	Conc. / mol dm <sup>-3</sup>	Area Ratio	RSD /%
1	0.204	2.577	3.51	0.1835	2.558	0.18	0.0213	0.499	0.32
2	0.152	2.119	0.71	0.1358	2.041	0.26	0.0157	0.370	0.24
3	0.102	1.641	0.28	0.0906	1.424	0.11	0.0105	0.239	0.33
4	0.081	1.384	0.06	0.0725	1.173	0.11	0.0084	0.192	0.17
5	0.061	1.092	0.15	0.0543	0.911	0.07	0.0063	0.145	0.27
6	0.051	0.752	0.22	0.0453	0.622	0.08	0.0052	0.097	0.54
7	0.025	0.382	1.35	0.0226	0.314	0.38	0.0026	0.047	1.17
8	0.010	0.239	6.43	0.0091	0.164	0.60	0.0010	0.024	0.58
9	0.006	0.108	2.99	0.0057	0.083	0.07	0.0007	0.012	0.44

*Table 5.51 Mean residence times (n=36) of each analyte with RSD values.*

Analyte	Mean Residence Time / min	RSD / %
TMB	5.81	1.99
citronellol	8.97	1.86
trans-rose oxide	12.46	1.85
cis-rose oxide	13.24	2.01

The analysis of the nine standards produced linear responses of the analyte area to TMB area ratio to the concentration area. Firstly, for **8**, the calibration produced a straight line of equation 5.14. The corresponding graph, Figure 5.52, shows a small degree of deviation from the straight line, this being quantified as an  $R^2$  value of 0.9734. The slightly lower than ideal  $R^2$  can be partially attributed to the increased RSD values of Standards 1, 8 and 9.

$$y = 0.0390x + 0.16 \quad 5.25$$

The calibrations of the isomers of rose oxide on the other hand exhibit good linearity with  $R^2$  values of 0.9917 and 0.9975 for *trans*- (equation 5.26) and *cis*-rose oxide (equation 5.27) respectively.

$$y = 0.0731 - 0.01 \quad 5.26$$

$$y = 0.0437 + 0.0499 \quad 5.27$$

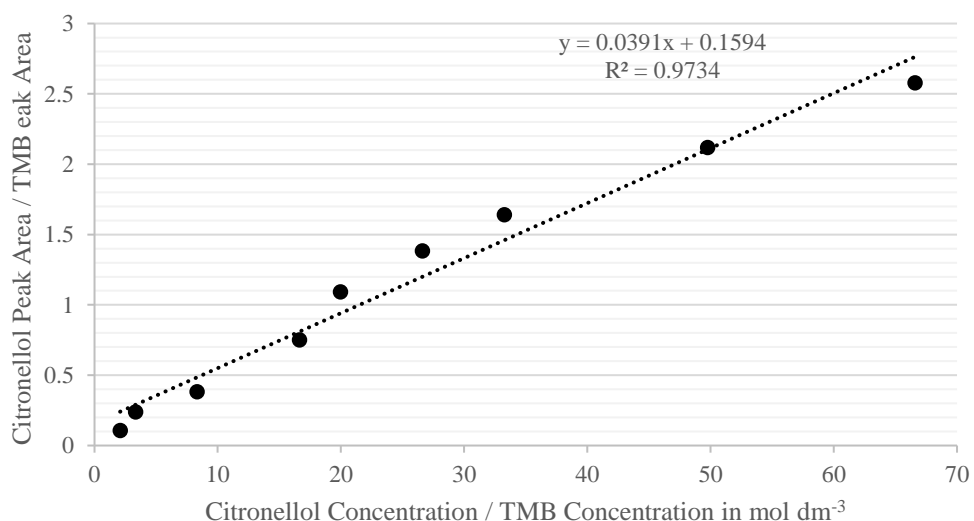


Figure 5.52: HPLC-210 nm internal standard calibration of citronellol and trimethoxybenzene. The straight line is generated by plotting the ratio of the citronellol to TMB peak area against the ratio of the concentrations. The straight line generated has an equation of  $y = 0.0391x + 0.1594$  with an  $R^2$  value of 0.9734, indicating a slight degree of deviation from the trend line. The concentrations were measured in mol dm⁻³.

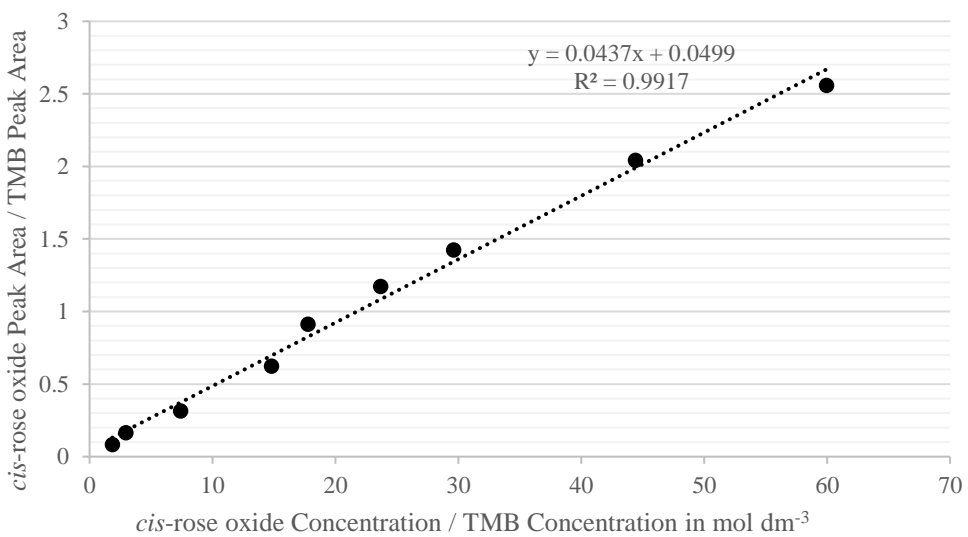
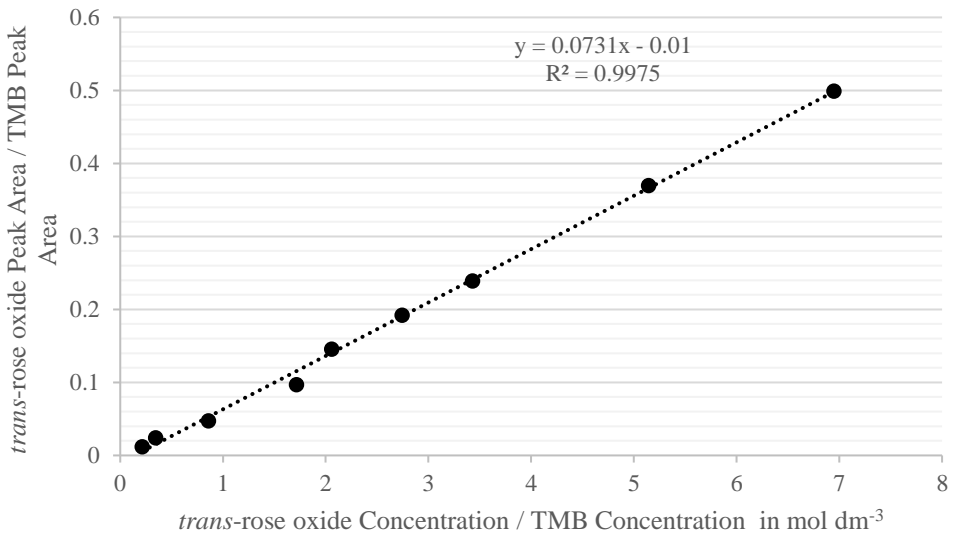


Figure 5.54: HPLC-210 nm internal standard calibration of trans-rose oxide and trimethoxybenzene. The straight line generated has an equation of  $y = 0.0437x + 0.0499$  with a good degree of linearity indicated by the  $R^2$  value of 0.9917. The concentrations were measured in  $\text{mol dm}^{-3}$

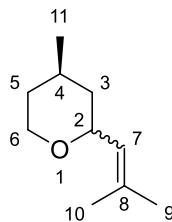
### 5.6.2.1. $^1\text{H}$ NMR Analysis

The  $^1\text{H}$  NMR data for (s)-citronellol (**8**) and the corresponding hydroperoxides, **9** and **10** are outlined earlier in this Chapter. The characteristic  $^1\text{H}$  shifts used for identification and quantification of the following literature shift values are highlighted in bold. The  $^1\text{H}$  NMR characterisation of diols **11** and **12** have been reported as:<sup>328</sup>

(3S)-(E)-3,7-dimethyloct-5-en-1,7-diol (**11**)  $^1\text{H}$  NMR (400 MHz,  $\text{CDCl}_3$ ),  $\delta$  = 1.32 (6H, s, 2Me-C7), **5.59** (1H, ddd, H5), **5.61** (1H, d, H6)

(3S)-(E)-3,7-dimethyloct-5-en-1,6-diol **(12)** (400 MHz,  $\text{CDCl}_3$ ),  $\delta$  = 1.72 (3H, s, Me-C7), 4.05 (1H, t, H6), **4.84** (1H, d, H8a), **4.91** (1H, d, H8b)

The  $^1\text{H}$  NMR characterisation of *cis*-**13** and *trans*-**13** have been reported as:<sup>326</sup>



*Cis*-**13** (500 MHz,  $\text{CDCl}_3$ ),  $\delta$  = 0.92 (3H, d, Me-11), 1.0 (1H, ddd, H3<sub>ax</sub>), 1.19 (1H, dddd, H5<sub>ax</sub>), 1.47 – 1.65 (3H, m, H-3<sub>eq</sub>/-4/-5<sub>eq</sub>) 1.67 (3H, d, Me-9), 1.70 (3H, d, Me-10), 3.44 (1H, ddd, H6<sub>ax</sub>), 3.96 (2H, m, H-2/-6<sub>eq</sub>), **5.14** (1H, d, H-7).

*trans*-**13** (500 MHz,  $\text{CDCl}_3$ ),  $\delta$  = 1.06 (3H, d, Me-11), 1.24 (1H, dddd, H5<sub>eq</sub>), 1.36 (1H, ddd, H3<sub>eq</sub>), 1.60 (1H, ddd, H3<sub>ax</sub>), 1.69 (3H, d, Me-9), 1.72 (3H, d, Me-10), 1.76 (1H, dddd, H5<sub>ax</sub>), 2.02 (1H, m, H-4), 3.69 (1H, ddd, H6<sub>ax</sub>), 3.75 (1H, m, H6<sub>eq</sub>), 4.36 (1H, m, H2), **5.28** (1H, d, H-7).

### 5.6.3. Reactions Conducted during the Development of the Automated Synthesis of 13

All starting materials were produced in brown glass vessels and degassed with nitrogen to avoid unwanted reactions prior to the experiment.

#### Photo-Oxidation of Citronellol to Hydroperoxides

Citronellol (3.65 mL, 0.1 M) was combined with TPP (0.12 g, 1 mol %) and trimethoxybenzene (0.207 g, internal NMR standard) in dichloromethane (200 mL), degassed with N<sub>2</sub> and the solution pumped at a flow rate of 1.0 mL min<sup>-1</sup>. Simultaneously, O<sub>2</sub> was flowed at 10.0 mL min<sup>-1</sup> to meet the substrate flow at a union to form a Taylor flow pattern. The subsequent Taylor flow passed through the photoreactor (FEP 1/16" o.d., 1/32" i.d., 7.54 cm<sup>3</sup>, 424 nm PhotoLED) housed in the cooling bath at -50°C (T<sub>1</sub> = -48°C). Samples (3 x 0.5 mL) were collected after an equilibration time of 30 minutes, these samples were subsequently prepared in CDCl<sub>3</sub> and analysed with NMR. This procedure was then repeated at cooling bath temperatures of -20°C and 10°C.

#### Semi-Continuous Synthesis of Rose Oxide to Test the HPLC mobile phase

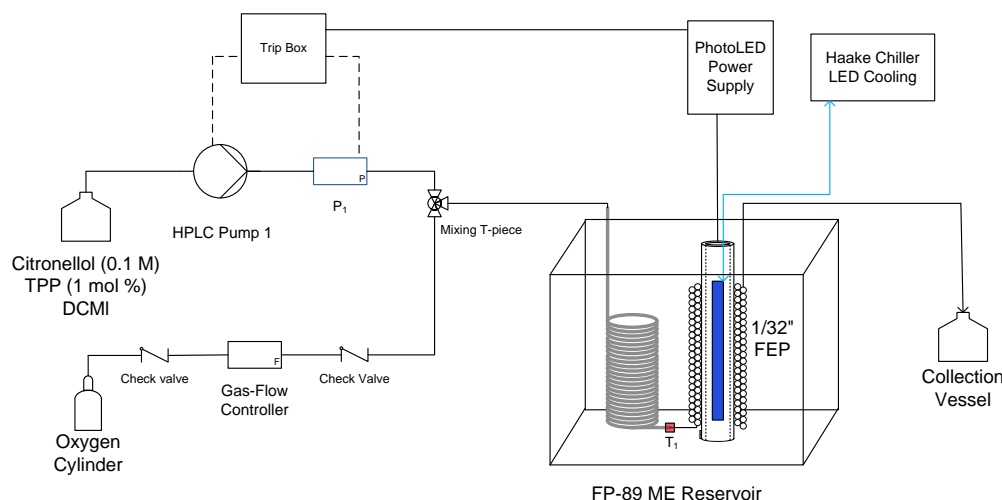


Figure 5.55: Schematic of the low-temperature photoreactor used for the semi-continuous synthesis of rose oxide. Citronellol (0.1 M) was photo-oxidised using TPP (0.1 mol %) in DCM under ambient conditions, T<sub>1</sub> = 17°C, with substrate and oxygen flow rates of 1.0 and 10.0 mL min<sup>-1</sup> respectively. The first-generation 424 nm PhotoLED was used as the light source.

Citronellol (1.56 g, 0.1 M) and TPP (0.061 g, 1 mol %) were combined in DCM (100 mL) and pumped at 1 mL min<sup>-1</sup> with a corresponding oxygen flow rate of 10 mL min<sup>-1</sup>. The subsequent Taylor flow of the reagents passed through the double-layer FEP coiled reactor (1/16" o.d., 1/32" i.d., 7.54 cm<sup>3</sup>) where the mixture was illuminated by a 424 nm PhotoLED light source at a reactor temperature of 17°C (T<sub>1</sub>). After an equilibrium time of 90 minutes, sample was collected and run on the HPLC. To the remaining sample (6.5 mL), triphenylphosphine (PPh<sub>3</sub>, 0.19 g, 1.1 eqv) was added and the solution stirred for 20 minutes. A sample was then collected and analysed by HPLC. H<sub>2</sub>SO<sub>4</sub> (0.032 mL, 1 eqv) was added dropwise to the stirred solution and allowed to continue stirring for 15 minutes. A sample was then collected and analysed by HPLC. Subsequent samples were then analysed while the mobile phase was adjusted.

### **Semi-Continuous Synthesis of Rose Oxide with Sodium Sulphite**

Citronellol (1.56 g, 0.1 M) and TPP (0.061 g, 1 mol %) were combined in DCM (100 mL) and pumped at 1 mL min<sup>-1</sup> with a corresponding oxygen flow rate of 10 mL min<sup>-1</sup>. The subsequent Taylor flow of the reagents passed through the double-layer FEP coiled reactor (1/16" o.d., 1/32" i.d., 7.54 cm<sup>3</sup>) utilising a 424 nm PhotoLED light source; T<sub>1</sub> was measured to be steady at 17°C during the reaction. After an equilibrium time of 45 minutes, a sample (0.5 mL) was collected, dried down, dissolved in CDCl<sub>3</sub> and submitted on NMR to assess the hydroperoxide formation. A further aliquot of photoproduct was collected (20 mL) to which Na<sub>2</sub>SO<sub>3</sub> (0.28 g, 0.11 M) was added and the mixture stirred for 30 minutes before H<sub>2</sub>SO<sub>4</sub> (95%, 0.1 mL) was added dropwise to complete the cyclisation to rose oxide. The reaction mixture appeared dark and possessed dark green precipitate around the round bottom flask.

#### 5.6.4. Continuous Synthesis of the Citronellol Diols

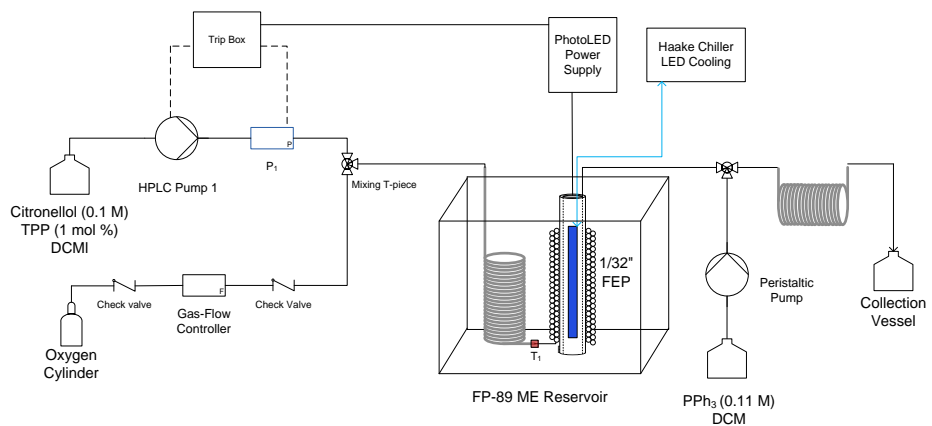


Figure 5.56: Schematic of the reactor set-up for the continuous synthesis of the citronellol diols. A peristaltic pump was connected to the outlet of the photoreactor to quench the hydroperoxides.

Citronellol (1.56 g, 0.1 M) and TPP (0.061 g, 1 mol %) were combined in DCM (100 mL) and pumped at  $1 \text{ mL min}^{-1}$  with a corresponding oxygen flow rate of  $10 \text{ mL min}^{-1}$ . The subsequent Taylor flow of the reagents passed through the double-layer FEP coiled reactor at ambient temperature (1/16" O.D, 1/32" I.D, 7.54 cm<sup>3</sup>) utilising the 424 nm PhotoLED. After an equilibrium time of 45 minutes, a sample (0.5 mL) was collected, dried down and dissolved in CDCl<sub>3</sub> and submitted on NMR. The pump and oxygen flow were then stopped and the quench line (peristaltic) was attached. The quench line fed a solution of PPh<sub>3</sub> (5.78 g in 100 mL DCM, 0.22 M) at  $0.5 \text{ mL min}^{-1}$  (1.1 eq) to mix with the photo-product in a T-piece before entering a section of glass beads and a stainless-steel coil (3 m, 1/8" o.d.). A sample of this solution (0.5 mL) was collected and analysed by NMR to assess whether sufficient quenching of the hydroperoxides had taken place.

#### Fully Continuous Synthesis of Rose Oxide in Methanol

Citronellol (1.56 g, 0.1 M) was combined with Rose Bengal (0.195 g, 2 mol %) in methanol (100 mL). This solution was pumped at a flow rate of  $1 \text{ mL min}^{-1}$ , mixing with an O<sub>2</sub> flow at a rate of  $10 \text{ mL min}^{-1}$  at a T-piece, resulting in Taylor flow through the FEP (1/32" I.D) photoreactor (424 nm Blue PhotoLED). After photo-oxidation, the solution was met with an aqueous stream of sodium sulphite (2.8 g in 100 mL at  $1 \text{ mL min}^{-1}$ ) to quench the hydroperoxides into the corresponding diols. The mixture of diols was then combined with a stream of 5% H<sub>2</sub>SO<sub>4</sub> (aq) at  $1 \text{ mL min}^{-1}$ . Upon addition of the acid it was observed that the colour was stripped from the solution. High levels of back pressure were observed, especially noted from the internal transducer of pump 1; subsequently, the increased pressure led to a leak within the pump head. Product solution was then collected, substantially before the ideal equilibrium time, before the

reaction was shut off. It was found that the increased pressure within the pump was due to the outlet frit; following cleaning and sonication the observed pressure was not sufficiently reduced.

### Automated Continuous Synthesis of 13 in Methanol

Citronellol (0.1 M) was combined with Rose Bengal (0.1 mol %) and TMB (3 mM) in methanol (500 mL). The reaction proceeded with the reaction parameters outlined in Table 5.52. Photo-oxidation was conducted in the double-layer FEP (1/16" o.d., 1/32" i.d., 7.54 cm<sup>3</sup>) reactor using the white PhotoLED. Quenching of the hydroperoxides was carried out by combining the photoproduct stream with a flow of sodium sulphite in water. This was provided by a peristaltic pump set of 17 RPM, which translates approximately to a flow rate of 1 mL min<sup>-1</sup>. The quenched solution was then combined with a flow of H<sub>2</sub>SO<sub>4</sub> at a T-piece before the solution entered a steel coil submerged and maintained at 30°C in an oil bath, before reaching the gas-liquid separator to allow only liquid flow to be passed through the HPLC sample loop.

Table 5.52: List experiment independent variables and corresponding reaction outcomes as measured by HPLC-210 nm.

Run	Independent Variable					conversion / %	trans-RO / %	cis-RO / %
	1 / °C	2 / mL min <sup>-1</sup>	3/ mol dm <sup>-3</sup>	4	5			
1	10	1	0.1	2	1	61.8	0.7	-1.8
2	0	1	0.1	2	1	70.4	1.6	-1.8
3	-10	1	0.1	2	1	78.0	0.8	-2.3
4	-20	1	0.1	2	1	-	-	-

The reaction was performed with citronellol (0.1 M) in methanol using rose bengal (1 mol %) as the photosensitiser and a second-generation white PhotoLED (500 mA) as the light source. Aqueous sodium sulfite delivered by the peristaltic pump (17 rpm) at 1 mL min<sup>-1</sup> acted as the quench reagent, while 5 % sulphuric acid was delivered by the computer controlled HPLC pump.

## Automated continuous synthesis of rose oxide in DCM

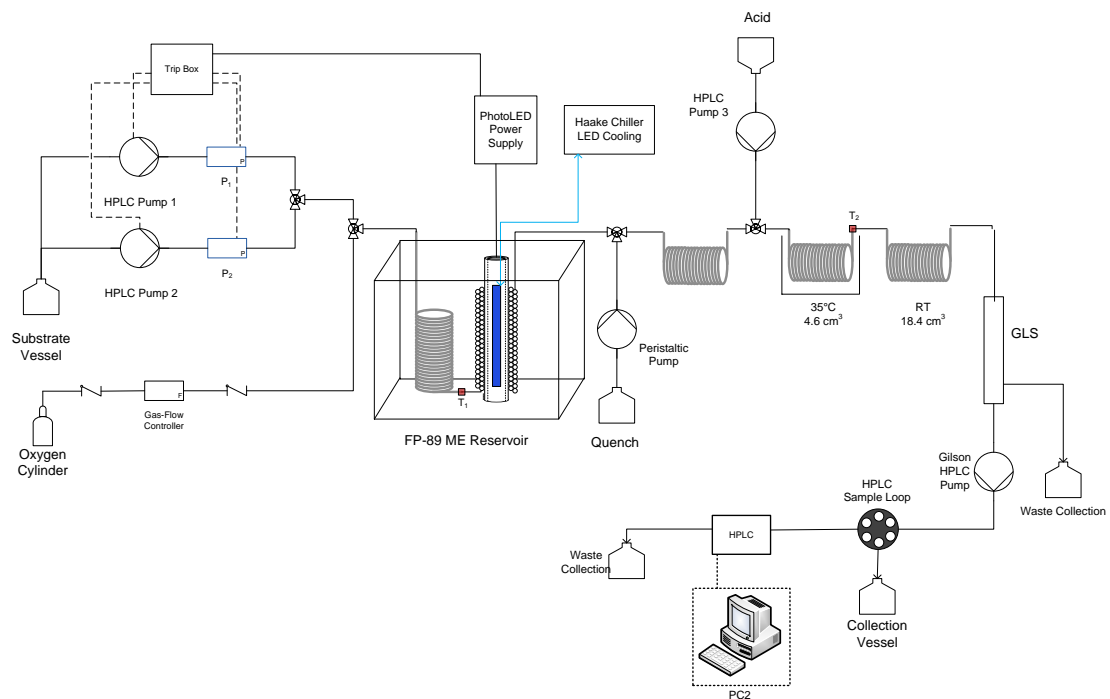


Figure 5.57: Schematic of the automated reactor for the continuous synthesis of rose oxide.

Citronellol (7.97 g, 0.102 M) was combined with TPP (0.1536 g, 0.5 mM, 0.5 mol %) and TMB (0.2611 g, 3.1 mM) in DCM (500 mL). The reaction proceeded with the reaction parameters outlined in Table 5.53. Photo-oxidation was conducted in the double-layer FEP (1/16" o.d., 1/32" i.d., 7.54 cm<sup>3</sup>) reactor using the white PhotoLED. Quenching of the hydroperoxides was carried out by combining the photoproduct stream with a flow of triphenylphosphine (5.77 g, 0.11 M) in DCM (200 mL). This was provided by a peristaltic pump set of 17 RPM, (ca. 1 mL min<sup>-1</sup>). The quenched solution was then combined with a flow of TFA (11.4 g, 0.50 M) in DCM (200 mL) at a T-piece before the solution entered a steel coil submerged and maintained at 30°C in an oil bath,

before reaching the gas-liquid separator to allow only liquid to be passed through the HPLC sample loop.

Table 5.53: Automated continuous flow synthesis of rose oxide in DCM in the low temperature photoreactor with the 424 nm PhotoLED.

Run	Independent Variable					Conversion / %	Trans-RO / %	Cis-RO / %	Total RO / %
	1 /°C	2 / mL min <sup>-1</sup>	3 / mol dm <sup>-3</sup>	4	5				
1	-40	0.5	0.1	2	1	91.3	1.4	2.4	3.8
2	-40	0.5	0.1	2	5	96.3	11.1	36.1	47.2
3	-40	1.0	0.1	2	5	98.2	11.7	36.1	47.8
4	-40	1.0	0.1	2	3	99.3	12.7	35.7	48.3
5	-80	1.0	0.1	2	3	99.6	5.2	14.9	20.0
6	-40	1.0	0.1	2	3	92.0	12.0	36.9	48.9

### CCF DoE List Run for the Synthesis of Rose Oxide

To facilitate the 4-factor, 3-level, CCF design of experiments List run a starting material was produced with citronellol (15.3255 g, 0.098 M), TPP (0.2913g, 0.474 mM) and TMB (0.00355 M) in DCM (1000 mL). The substrate concentration as independent variable 3 was kept constant at the starting material concentration of 0.098 M throughout all the runs; thus, the experiment file and indep2ctrl.m script files were updated to reflect this. Only Pump 1 was required to deliver the reagent feed. The reagent and oxygen mixture was irradiated with 424 nm light in the narrow diameter FEP photoreactor (1/16" o.d, 1/32" i.d, volume 7.54 cm<sup>3</sup>). PPh<sub>3</sub> (7.2125 g, 0.11 M) in DCM (250 mL) quenched *via* the peristaltic pump, the flow rate of which was manually adjusted to correspond to the flow rate of the reagent solution to provide equal quench solution for all runs. The delivery of the acid, TFA (14.414 g, 0.506 M) in DCM (250 mL), was performed by the 3<sup>rd</sup> Jasco® HPLC pump and controlled by the computer.

## Chapter 6. Thesis Conclusions and Future Directions

### 6.1. Aim 1

‘To develop robust design(s) of flow reactors that can be used at low temperature, overcoming the issues of dissipating heat from the light sources without compromising the low temperature operation of the reactor.’

#### Rationale

Performing photochemical reactions at low temperature can enhance reaction selectivity; this has been exhibited in both enantioselective and oxidative photochemistry.<sup>8,329,330</sup> As discussed in Chapter 1, continuous-flow photochemistry is superior in terms of reaction control, dynamics and output compared to the traditional batch approach,<sup>22,100,101,240,331</sup> and naturally, the benefits of flow methodologies should be exploited when developing a system for low temperature photochemistry. In terms of photo-oxidations, the combination of continuous flow and reduced temperature provides an added safety benefit, which is of great importance when considering the scale up of such reactions.

There are significant challenges associated with the design and implementation of these reactors: First, and most critical, involves designing a system that provides high levels of light-substrate interaction while minimising the effect of heat emitted from the light source. The second challenge involves physical changes to the reaction solution at low temperature, affecting substrate solubility, solvent viscosity and, hence, flow dynamics. These challenges are worth addressing: the development of robust reactors that can achieve ultra-low temperatures while also performing continuous flow photochemistry has the potential to greatly improve the larger scale synthesis of important molecules, including the anti-malarial drug, artemisinin, which has been the main focus of this study.

#### Progress

Chapter 2 outlined the design and subsequent modifications to a previously developed reactor, the HPR, to facilitate photo-oxidations down to -45°C. The adaptation that had the most significant effect on performance was the replacement of the Hg arc lamp by the PhotoLED. During this process the significant effect of heat absorption became

apparent, both during the transportation of the coolant and from ambient sources in any part of the reactor that was not sufficiently insulated. These factors were addressed in the design of the secondary reactor. Through numerous iterations, the ‘near-micro’ FEP reactor was produced, which proved to be capable of performing photo-oxidative reactions down to -80°C.

The low temperature reactor typically exhibited good flow dynamics during low temperature photo-oxidations, in particular when conducting reactions in DCM. However, the liquid-oxygen flow was occasionally disrupted at the lowest temperatures; this effect was exacerbated when solvents of higher viscosity, such as toluene, were used and when the reactor required additional reagent streams, creating high levels of back-pressure within the system. Considerations of several parameters, including the combination of the temperature, solvent and reactor size/set-up showed themselves to be of paramount importance when performing photo-oxidations.

## 6.1. Aim 2

‘To apply the photoreactor to the specific photo-oxidation reactions of DHAA and citronellol by  $^1\text{O}_2$ , where in both cases it is known that the yields of the desired photo-products are favoured by low temperature’

### Rationale

Selectivity of the photo-oxidation of dihydroartemisinic acid, a precursor to artemisinin, can be enhanced through application of the reactor.<sup>8</sup> The reactor provides the dual benefit of lower reaction temperature and improved reaction dynamics. These factors are likely to increase the formation of the desired DHAA hydroperoxide, which translates into an improved synthesis of artemisinin, via the primary aim of increasing yield and subsidiary aim of improving the productivity of the synthesis.

The synthesis of rose oxide, a valuable fragrance compound, involves a similar photo-oxidative step to that of artemisinin, forming two hydroperoxides – only one of which can form the product. It is, therefore, expected that improvements to the selectivity of the photo-oxidation, via low temperature, can improve the overall yield of rose oxide.

## Progress

The application of low temperature to the photo-oxidations of DHAA and citronellol was first investigated using the HPR and discussed in Chapter 2. These preliminary reactions showed a strong temperature dependence on selectivity in the case of DHAA, with the ratio of the hydroperoxides **15:16** typically increasing from around 8:1 at 20°C to 10:1 at -45°C. The effect on the oxidation of citronellol was negligible with the observed increase on the ratio of **9:10** mostly likely due to the reduction in conversion rather than a sole effect of the temperature.

Chapter 3 then detailed the elaboration of these findings, with the selectivity towards hydroperoxide **15** being further improved at lower temperature, with ratios around 11:1 being achieved at -60°C, as shown in Table 3.3. Full progression to the synthesis of artemisinin was completed. The improved selectivity towards **15** was found to translate into increased yields of **18**; the highest yield of 68 ± 2% achieved using the semi-continuous ‘two-pot’ regime at a photoreactor temperature of -80°C.

Further work also detailed the effect of low temperature on the formation of other reaction constituents within the two reaction methods, the ‘one-pot’ and ‘two-pot’ regimes. The more laborious semi-continuous ‘two-pot’ regime was found to be superior in terms of conversion and yield of **18**, along with reduced levels **19**, due to the higher concentration of dissolved oxygen compared to the ‘one-pot’. These findings encouraged the development of a fully continuous ‘two-pot’ reactor that facilitated the photo-oxidation of DHAA to quantitative levels of conversion, followed by the continuous delivery of acid to complete the synthesis of **18**. The nature of the two-part system enabled improvements in the dynamics of both the photochemical and thermal steps of the synthesis. The photo-oxidation had been previously optimised within the semi-continuous reactor and is in fact facile and highly selective. The thermal step was found to be the crux of the synthesis, with conversion from **15** to **18** occurring slowly with typical yields of **18** of 0% being measured at the initial point of sampling. Adaptations were, therefore, made to increase the kinetics of the secondary steps. Heated coils were added after the photoreactor to lengthen the residence time and to enhance the thermal steps through the addition of heat, however, these only led to minor improvements. The addition of the Vortex reactor resulted in the initial yield of **18** increasing from 0% to around 20%, a significant improvement that can form the basis of the progression of the reactor with the aim of optimising this step.

## 6.2. Aim 3

‘To interface the photoreactor with self-optimisation techniques so that process development can be accelerated, particularly for complex reactions with costly starting materials.’

### Rationale

As previously described, the traditional ‘one variable at a time’ optimisation of chemical reactions is inefficient and rarely converges on the global maxima.<sup>256–258</sup> In the case of artemisinin, the complexities of the sequential photochemical and thermal steps, combined with the number of potential variables, presents a significant challenge to optimisation. A Design of Experiment style approach was adopted to achieve efficiently the following aims: (i) identification of synergistic and antagonistic variables, (ii) removal of redundant variable combinations to reduce the potential ‘reaction space’ (iii) identification of an appropriate starting position for optimisation. These three goals all aim to improve the outcome and efficiency for single objective self-optimisation, thereby reducing material and computational cost. The application of multi-objective optimisation of antagonistic reaction outcomes, such as environmental (E-factor) and economic (productivity) objectives, can then be applied to give a more holistic approach to the synthesis of artemisinin.<sup>332</sup>

### Progress

Chapter 4 details the development of the reactor and reactions towards self-optimisation. The first essential requirement to realise this aim was the development of a reliable method for ‘On-line’ analysis. As discussed in Chapters 4 and 5, the development of the analytical technique proved to be a significant challenge. However, good progress was made and a great deal of experience was gained dealing with the many nuances of linking a complex flow reaction with automated analysis.

Through the development of the fully continuous reactor along with the HPLC-UV and ELSD methods for the quantification of **18**, a good level of insight was provided not only into the progress of the reaction, but also into the influence of the reactor design and thus how both aspects needed to be adapted to improve the overall process. On-line HPLC was found to greatly reduce variation in the data that arose due to manual handling of samples and also provided an accurate snapshot of the reaction composition

at the point of sampling. This allowed for an improved understanding of the reaction, highlighting incomplete formation of **18** within the reactor; an outcome that could not be determined with  $^1\text{H}$  NMR analysis. The implementation of On-line analysis, therefore, provided information that greatly influenced the modifications made to the reactor. As discussed in Section 6.1, the incomplete formation of **18** showed the requirement for increased residence time for the thermal reaction to take place. However, it was determined that if using the standard approach of a coiled reactor, the length and, hence, residence time required to achieve full completion would not be practical. Therefore, a Vortex reactor was used, and its introduction highlighted the importance of efficient mixing, leading to the synergistic effect of increasing the yield of **18** and preventing the formation of **19**.

Ultimately, the challenges associated with producing reliable quantification of **18** and **14** held back the development of the self-optimising system, although automated reactions were completed. Overwhelmingly, the main challenge was to establish a reliable and stable detection regime: if the analytical method is not reliable, then the resulting optimisation is redundant. These challenges highlighted factors that must be carefully considered when implementing On-line analysis with a complex reaction and reactor system. The approach to development must first address the requirement of a robust analytical method. The ideal HPLC method will provide good separation of all analyte peaks, while maintaining good peak shape, but for the case of self-optimisation must also possess a relatively short run time. The detection method must be reproducible and sensitive to each analyte with an appropriate dynamic range; furthermore, detection of the analytes must not be affected by the presence of the reaction solvent.

### 6.3. Future Directions

To achieve the aim of single objective self-optimisation, it is clear that the functioning of the many parameters encountered and subsequently addressed in this Thesis must all align successfully. This includes the performance of the reactor, the analytical method and the self-optimisation framework, which together must act to deliver consistent, reliable outcomes.

The On-line analysis is central to the success of any self-optimisation system. During this research, it was found that HPLC-UV was a more reliable and sensitive detector for the quantification of artemisinin than ELSD. However, for the reasons discussed earlier, it was necessary to change the solvent to toluene, but under the existing reaction conditions, it was not possible to use this detector for analysis. Later developments in this Thesis showed a method that does allow for the use of UV for reactions conducted in toluene and, thus, progress was achieved.

However, this highlights the primary importance of establishing an effective and reliable detection method at the outset of any future work: A larger screening of stationary and mobile phases should be made to further improve the separation of all analytes: products, reactants, intermediates and the reaction medium itself, and, in particular, to ensure reliable quantification of those compounds which will be the targets for optimisation. For future work with the current system and reactants, this will enable automated reactions in toluene, with HPLC-UV

Additionally, further adaptation of the reactor is required to alleviate the pressure issues that have been experienced when using toluene (and DCM in the fully-automated system). These issues arise due to disruptions of the oxygen-liquid flow equilibrium and may be addressed by installing a gas-flow controller capable of delivering oxygen at elevated pressures; however, caution is advised when using oxygen at pressure in the presence of toluene.

The addition of the Vortex reactor greatly enhanced the formation of artemisinin while adding a relatively small volume to the overall system. The reactions were still, however, incomplete. Therefore, future reactions should make use of a larger volume Vortex, with prior heating of the solution to drive the thermal reaction towards completion. Furthermore, developments should be made to enable automated control of the Vortex reactor so that it may be used within a fully optimised system. Although the optimisation of the rotation can be done manually and is likely to be consistent across many conditions, there is a requirement for the Vortex to be switched off in-between reactions. The reactor could be further modified, therefore, to incorporate multiple FEP coiled reactors with multiple PhotoLEDS. This would greatly increase the through-put of the reactor compared to the rudimentary design of the original.

To further exploit the insights provided into the intermediate stage of the reaction, the analysis of the prevalent side-product, 6-lactone and dihydro-*epi*-deoxyarteannuin B, should be facilitated using HPLC-UV. Furthermore, analysis with HPLC-MS should be investigated. Mass spectrometry will provide a greater understanding of the identities of the intermediate compounds as well as insights into the kinetics and mechanism of the formation of artemisinin in the flow reactor.

Use of DoE on the synthesis of artemisinin should help to identify synergistic and antagonistic variables efficiently, and highlight redundant variables, whose removal will reduce the computational cost of self-optimising experiments. Once a reliable automated reactor is developed, DoE should be applied to reduce variables and exploration space. Single-objective optimisation can then be performed to find the optimum conditions for metrics such as yield, productivity and selectivity. The next stage is then to apply multi-objective optimisation, providing a more holistic approach to the synthesis of artemisinin which can then be translated into significant improvements for the industrial synthesis of this important molecule.

This reactor system can then be applied to the synthesis of other photochemically produced molecules, in which lower reaction temperatures may enhance selectivity. The advancement of enantioselective photochemistry could be further exploit through the use of this low temperature reactor. Many enantioselective photochemical reactions rely on the complexation of the substrate to a chiral catalyst through hydrogen-bonding, or other intermolecular interactions.<sup>329,333</sup> The strength of these interactions increases at reduced temperature, therefore, the yield and selectivity of these reactions are too expected to increase.<sup>334</sup> This effect has already been explored by Alonso *et al.* who improved the enantiomeric excess of a chiral [2+2] cyclisation by lowering the reaction temperature to -25°C.<sup>329</sup>

The ability of the HPR to achieve internal temperatures down to -46°C and maintain relatively high pressure, potentially up to 100 bar, could facilitate photochemical reactions in unconventional solvents such as liquid ammonia, liquid CO<sub>2</sub> and supercritical CO<sub>2</sub> or other solvents that require low temperature and pressure to remain in the liquid phase.

## Bibliography

- 1 *World Malaria Report 2019*, World Health Organisation, 2019.
- 2 *Guidelines for the Treatment of Malaria.*, World Health Organisation, 2010, vol. 2.
- 3 A. B. Hogan, P. Winskill and A. C. Ghani, *PLoS Med*, 2020, **17**, 1–19.
- 4 M. B. Laurens, *Hum Vaccin Immunother*, 2020, **16**, 480–489.
- 5 J. Turconi, F. Griolet, R. Guevel, G. Oddon, R. Villa, A. Geatti, M. Hvala, K. Rossen, R. Göller and A. Burgard, *Org. Process Res. Dev*, 2014, **18**, 417–422.
- 6 R. J. Roth and N. Acton, *J Nat Prod*, 1989, **52**, 1183–1185.
- 7 N. Acton and R. J. Roth, *J. Org. Chem*, 1992, **57**, 3610–3614.
- 8 D. Kopetzki, F. Lévesque and P. H. Seeberger, *Chem. Eur. J*, 2013, **19**, 5450–5456.
- 9 F. Lévesque and P. H. Seeberger, *Angew. Chem. Int. Ed.*, 2012, **51**, 1706–1709.
- 10 H. Trommsdorff, *Annalen der Pharmacie*, 1834, **11**, 190–207.
- 11 S. Cannizzaro and G. Fabris, *Berichte der deutschen chemischen Gesellschaft*, 1886, **19**, 2260–2265.
- 12 G. Ciamician, *The Photochemistry of the Future*, 1912, vol. 36.
- 13 H. Stobbe, *Zeitschrift für Elektrotechnik und Elektrochemie*, 1908, **14**, 473–483.
- 14 A. Albini, *Photochemistry*, Springer Berlin Heidelberg, Berlin, Heidelberg, 2016.
- 15 A. Albini and M. Fagnoni, *Green Chem.*, 2004, **6**, 1–6.
- 16 D. A. DiRocco and D. M. Schultz, *Science of Synthesis*, 2019, **6**, 611–635.
- 17 T. Noël, *J Flow Chem*, 2017, **7**, 87–93.
- 18 T. H. Rehm, *ChemPhotoChem*, 2020, **4**, 235–254.
- 19 A. Dzebo, H. Janetschek, C. Brandi and G. Iacobuta, *Connections between the Paris Agreement and the 2030 Agenda: the case for policy coherence*, Stockholm Environment Institute , Stockholm, 2019.
- 20 P. T. Anastas and J. Charles. Warner, *Green chemistry: theory and practice*, Oxford University Press, 1998.
- 21 D. Ravelli, D. Dondi, M. Fagnoni and A. Albini, *Chem. Soc. Rev.*, 2009, **38**, 1999–2011.
- 22 J. P. Knowles, L. D. Elliott and K. I. Booker-Milburn, *Beilstein J. Org. Chem*, 2012, **8**, 2025–2052.
- 23 T. Noël, M. Escriba Gelonch and K. Huvaere, in *Photochemical Processes in Continuous-Flow Reactors*, World Scientific (Europe), 2017, pp. 245–267.
- 24 K. Loubière, M. Oelgemöller, T. Aillet, O. Dechy-Cabaret and L. Prat, *Chem. Eng. Proc*, 2016, **104**, 120–132.
- 25 K. H. Pfoertner, *J Photochem Photobiol A Chem*, 1990, **51**, 81–86.
- 26 N. Hoffmann, *Chem Rev*, 2008, **108**, 1052–1103.
- 27 N. Hoffmann, *Photochem. Photobiol. Sci*, 2012, **11**, 1613.

28 N. J. Turro, V. Ramamurthy and J. C. (Juan C. ) Scaiano, *Modern molecular photochemistry of organic molecules*, University Science Books, 2010.

29 J. Twilton, C. C. Le, P. Zhang, M. H. Shaw, R. W. Evans and D. W. C. MacMillan, *Nat. Rev. Chem*, 2017, **1**, 1–19.

30 B. Wardle, *Principles and applications of photochemistry*, John Wiley & Sons, Ltd, 2009.

31 H. E. Bonfield, T. Knauber, F. Lévesque, E. G. Moschetta, F. Susanne and L. J. Edwards, *Nat. Comm*, 2020, **11**, 1–4.

32 S. D. A. Zondag, D. Mazzarella and T. Noël, *Annu Rev Chem Biomol Eng*, 2023, **14**, 5.1-5.18.

33 A. G. Griesbeck and J. Mattay, *Synthetic Organic Photochemistry*, Marcel Dekker, 2005.

34 P. Klán and J. Wirz, *Photochemistry of Organic Compounds*, John Wiley & Sons, Ltd, Chichester, UK, 2009.

35 L. Buglioni, F. Raymenants, A. Slattery, S. D. A. Zondag and T. Noël, *Chem Rev*, 2022, **122**, 2752–2906.

36 Jack. Simons, *An Introduction to Theoretical Chemistry*, Cambridge University Press, 2003.

37 Michael Kasha, *Discuss Faraday Soc*, 1950, **9**, 14–19.

38 S. E. Braslavsky, *Pure and Applied Chemistry*, 2007, **79**, 293–465.

39 E. Coyle, PhD Thesis, Dublin City University, 2010.

40 H. E. Avery, *Basic Reaction Kinetics and Mechanisms*, Macmillan Education UK, London, 1974.

41 A. Arrhenius, *Zeitschrift für Physikalische Chemie*, 1889, **4**, 226–248.

42 T. van Gerven and A. Stankiewicz, *Ind Eng Chem Res*, 2009, **48**, 2465–2474.

43 P. Anastas and N. Eghbali, *Chem. Soc. Rev.*, 2010, **39**, 301–312.

44 A. Albini, M. Fagnoni and M. Mella, *Pure Appl. Chem.*, 2000, **72**, 1321–1326.

45 J. Z. Bloh, *Front. Chem*, 2019, **7**, 1–13.

46 A. U. Khan and M. Kasha, *J. Chem. Phys*, 1963, **39**, 3133.

47 M. C. DeRosa and R. J. Crutchley, *Coord Chem Rev*, 2002, **233–234**, 351–371.

48 G. Herzberg and S. Mrozowski, *Am J Phys*, 1951, **19**, 390–391.

49 J. R. Hurst and G. B. Schuster, *J. Am. Chem. Soc.*, 1983, **105**, 5756–5760.

50 R. M. Badger, A. C. Wright and R. F. Whitlock, *J. Chem. Phys*, 1965, **43**, 4345.

51 Michael. A. J. Rodgers, *J. Am. Chem. Soc.*, 1983, **105**, 6201–6205.

52 E. Afshari and R. Schmidt, *Chem Phys Lett*, 1991, **184**, 128–132.

53 C. Schweitzer and R. Schmidt, *Chem Rev*, 2003, **103**, 1685–1757.

54 D. R. Worrall, A. A. Abdel-Shafi and F. Wilkinson, *J. Phys. Chem. A*, 2001, **105**, 1270–1276.

55 E. S. Nyman and P. H. Hynninen, *J Photochem Photobiol B*, 2004, **73**, 1–28.

56 S. Lacombe and T. Pigot, *New materials for sensitised photo-oxygenation*, Royal Society of Chemistry, 2011.

57 R. C. Kanner and C. S. Foote, *J Am Chem Soc*, 1992, **114**, 678–681.

58 S. M. Linden and D. C. Neckers, *Photochem Photobiol*, 1988, **47**, 542–550.

59 M. I. Gutiérrez, C. G. Martínez, D. García-Fresnadillo, A. M. Castro, G. Orellana, A. M. Braun and E. Oliveros, *J. Phys. Chem. A*, 2003, **107**, 3397–3403.

60 R. Costa E Silva, L. Oliveira Da Silva, A. De Andrade Bartolomeu, T. J. Brocksom and K. Thiago De Oliveira, *Beilstein J. Org. Chem*, 2020, **16**, 917–955.

61 M. Prein and W. Adam, *Angew. Chem. Int. Ed. Engl*, 1996, **35**, 477–494.

62 P. Bayer, R. Pérez-Ruiz and A. Jacobi von Wangelin, *ChemPhotoChem*, 2018, **2**, 559–570.

63 G. O. Schenck, *Naturwissenschaften*, 1948, **35**, 28–29.

64 A. Schonberg, *Preparative Organic Photochemistry*, Springer, Berlin, 1958.

65 G. Ohloff, in *Organic Synthesis*, Elsevier, 1975, pp. 481–502.

66 H. H. Wasserman and J. L. Ives, *Tetrahedron*, 1981, **37**, 1825–1852.

67 W. Adam, M. Braun, A. Griesbeck, E. Staab, B. Will and V. Lucchini, *J Am Chem Soc*, 1989, **111**, 203–212.

68 W. Adam and M. J. Richter, *Acc Chem Res*, 1994, **27**, 57–62.

69 E. D. Mihelich and D. J. Eickhoff, *J. Org. Chem*, 1983, **48**, 4135–4137.

70 A. G. Davies and C. H. Schiesser, *Tetrahedron*, 1991, **47**, 1707–1726.

71 L. B. Harding and W. A. Goddard, *J Am Chem Soc*, 1980, **102**, 439–449.

72 S. Inagaki and K. Fukui, *J Am Chem Soc*, 1975, **97**, 7480–7484.

73 M. N. Alberti and M. Orfanopoulos, *Chem. Eur. J*, 2010, **16**, 9414–9421.

74 C. S. Foote, *Acc Chem Res*, 1967, **1**, 104–110.

75 A. A. Gorman and M. A. J. Rodgers, *Chem Soc Rev*, 1981, **10**, 205–231.

76 L. B. Harding and W. A. Goddard, *Tetrahedron Lett*, 1978, **19**, 747–750.

77 C. W. Jefford, *Chem Soc Rev*, 1993, **22**, 59–66.

78 B. Grdina, M. Orfanopoulos and L. Stephenson, *J Am Chem Soc*, 1979, **101**, 3111–3112.

79 A. A. Gorman, I. Hamblett, C. Lambert, B. Spencer and M. C. Standen, *J. Am. Chem. Soc*, 1988, **110**, 8053–8059.

80 A. A. Gorman, I. R. Gould and I. Hamblett, *J. Am. Chem. Soc*, 1982, **104**, 12105–68.

81 D. R. Kearns, *J Am Chem Soc*, 1969, **91**, 6554–6563.

82 A. A. Frimer, *Chem Rev*, 1979, **79**, 359–387.

83 J. R. Hurst, S. L. Wilson and G. B. Schuster, *Tetrahedron*, 1985, **41**, 2191–2197.

84 A. A. Gorman, I. R. Gould and I. Hamblett, *J Am Chem Soc*, 1982, **104**, 7098–7104.

85 A. A. Gorman, I. Hamblett, C. Lambert, B. Spencer and M. C. Standen, *J Am Chem Soc*, 1988, **110**, 8053–8059.

86 C. W. Jefford and A. F. Boschung, *Helv Chim Acta*, 1974, **57**, 2242–2257.

87 K. N. Houk, J. C. Williams and P. A. Mitchell, *J Am Chem Soc*, 1981, **103**, 949–951.

88 M. Orfanopoulos and C. S. Foote, *Tetrahedron Lett*, 1985, **26**, 5991–5994.

89 E. L. Clennan, X. Chen and J. J. Koola, *J Am Chem Soc*, 1990, **112**, 5193–5199.

90 M. Orfanopoulos, M. Stratakis and Y. Elemes, *Tetrahedron Lett*, 1989, **30**, 4875–4878.

91 M. Stratakis and M. Orfanopoulos, *Synth Commun*, 1993, **23**, 425–430.

92 M. Sender and D. Ziegenbalg, *Chemie Ingenieur Technik*, 2017, **89**, 1159–1173.

93 *Immersion Well Reactors*, .

94 A. M. Braun, M. Maurette and E. Oliveros, *Photochemical Technology*, Wiley, Chichester, 1991.

95 T. Q. Khanh, P. Bodrogi, Q. T. Vinh and H. Winkler, *LED Lighting*, Wiley-VCH Verlag, Weinheim, Germany, 2014.

96 C. G. Bochet, *Synlett*, 2004, **2004**, 2268–2274.

97 Ü. Taştan, P. Seeber, S. Kupfer and D. Ziegenbalg, *React Chem Eng*, 2021, **6**, 90–99.

98 D. F. Swinehart, *J Chem Educ*, 1962, **39**, 333.

99 A. M. Braun, L. Jakob, E. Oliveros and C. A. O. do Nascimento, in *Advances in Photochemistry*, John Wiley & Sons, Ltd, 1993, vol. 18, pp. 235–313.

100 K. Gilmore and P. H. Seeberger, *Chem. Rec*, 2014, **14**, 410–418.

101 L. D. Elliott, J. P. Knowles, P. J. Koovits, K. G. Maskill, M. J. Ralph, G. Lejeune, L. J. Edwards, R. I. Robinson, I. R. Clemens, B. Cox, D. D. Pascoe, G. Koch, M. Eberle, M. B. Berry and K. I. Booker-Milburn, *Chem. Eur. J.*, 2014, **20**, 15226–15232.

102 I. R. Baxendale, J. Deeley, C. M. Griffiths-Jones, S. V. Ley, S. Saaby and G. K. Tranmer, *Chem. Commun*, 2006, 2566–2568.

103 B. P. Mason, K. E. Price, J. L. Steinbacher, A. R. Bogdan and D. T. McQuade, *Chem Rev*, 2007, **107**, 2300–2318.

104 H. P. L. Gemoets, Y. Su, M. Shang, V. Hessel, R. Luque and T. Noël, *Chem Soc Rev*, 2016, **45**, 83–117.

105 E. E. Coyle and M. Oelgemöller, *Photochem. Photobiol. Sci.*, 2008, **7**, 1313.

106 M. Oelgemöller and O. Shvydkiv, *Molecules*, 2011, **16**, 7522–7550.

107 Y. Su, N. J. W. Straathof, V. Hessel and T. Noël, *Chem. Eur. J.*, 2014, **20**, 10562–10589.

108 Y. Su, K. Kuijpers, V. Hessel and T. Noël, *React Chem Eng*, 2016, **1**, 73–81.

109 F. Zhao, D. Cambié, J. Janse, E. W. Wieland, K. P. L. Kuijpers, V. Hessel, M. G. Debije and T. Noël, *ACS Sustain. Chem. Eng.*, 2018, **6**, 422–429.

110 I. Rossetti and M. Compagnoni, *Chem. Eng. J.*, 2016, **296**, 56–70.

111 J. D. Williams, M. Nakano, R. Gérardy, J. A. Rincón, Ó. de Frutos, C. Mateos, J.-C. M. Monbaliu and C. O. Kappe, *Org Process Res Dev*, 2019, **23**, 78–87.

112 S. D. Halperin, D. Kwon, M. Holmes, E. L. Regalado, L.-C. Campeau, D. A. DiRocco and R. Britton, *Org Lett*, 2015, **17**, 5200–5203.

113 E. B. Corcoran, F. Lévesque, J. P. McMullen and J. R. Naber, *ChemPhotoChem*, 2018, **2**, 931–937.

114 B. D. A. Hook, W. Dohle, P. R. Hirst, M. Pickworth, M. B. Berry and K. I. Booker-Milburn, *J. Org. Chem.*, 2005, **70**, 7558–7564.

115 M. T. Musser, *Ullmann's Encyclopedia of Industrial Chemistry*, Wiley-VCH, 2012.

116 M. L. Campbell, *Ullmann's Encyclopedia of Industrial Chemistry*, Wiley-VCH, 2012.

117 J.-R. Chen, H.-H. Yang and C.-H. Wu, *Org. Res. Process Dev*, 2004, **8**, 252–255.

118 A. K. Suresh, M. M. Sharma and T. Sridhar, *Ind Eng Chem Res*, 2000, **39**, 3958–3997.

119 C. J. Mallia and I. R. Baxendale, *Org Process Res Dev*, 2016, **20**, 327–360.

120 V. Tukač, J. Vokál and J. Hanika, *J. Chem. Tech. Biotech.*, 2001, **76**, 506–510.

121 T.-C. Chou and F.-S. Lin, *Can J Chem*, 1983, **61**, 1295–1300.

122 T. A. Kletz, *J Hazard Mater*, 1975, **1**, 165–170.

123 J.-R. Chen, *Process Safety Process* 2004, 2004, **23**, 72–81.

124 G. R. Astbury, *Org Process Res Dev*, 2002, **6**, 893–895.

125 T. Sato, Y. Hamada, M. Sumikawa, S. Araki and H. Yamamoto, *Ind. Eng. Chem. Res.*, 2014, **53**, 19331–19337.

126 N. Kockmann, P. Thenée, C. Fleischer-Trebes, G. Laudadio and T. Noël, *React Chem Eng*, 2017, **2**, 258–280.

127 Y. Su, G. Chen, Y. Zhao and Q. Yuan, *AIChE Journal*, 2009, **55**, 1948–1958.

128 J. Yue, L. Luo, Y. Gonthier, G. Chen and Q. Yuan, *Chem Eng Sci*, 2009, **64**, 3697–3708.

129 T. Cubaud, M. Sauzade and R. Sun, *Biomicrofluidics*, 2012, **6**, 022002.

130 J. W. Bolk and K. R. Westerterp, *AIChE Journal*, 1999, **45**, 124–144.

131 N. B. Siccama and K. R. Westerterp, *Ind. Eng. Chem. Res*, 1993, **32**, 1304–1314.

132 N. B. Siccama and K. Roel Westerterp, *Modeling of the Ignition of Ethene-Air Mixtures with a Hot Surface under Flow Conditions*, 1995, vol. 34.

133 R. C. R. Wootton, R. Fortt and A. J. De Mello, *Org Process Res Dev*, 2002, **6**, 187–189.

134 K. Jähnisch and U. Dingerdissen, *Chem Eng Technol*, 2005, **28**, 426–427.

135 O. Shvydkiv, C. Limburg, K. Nolan and M. Oelgemöller, *J Flow Chem*, 2012, **2**, 52–55.

136 A. Yavorskyy, O. Shvydkiv, C. Limburg, K. Nolan, Y. M. C. Delauré and M. Oelgemöller, *Green Chem*, 2012, **14**, 888.

137 K. Barberis and C. R. Howarth, *Ozone Sci Eng*, 1991, **13**, 501–519.

138 T. Van Gerven, G. Mul, J. Moulijn and A. Stankiewicz, *Chem. Eng. Proc.*, 2007, **46**, 781–789.

139 A. Chaudhuri, K. P. L. Kuijpers, R. B. J. Hendrix, P. Shivaprasad, J. A. Hacking, E. A. C. Emanuelsson, T. Noël and J. van der Schaaf, *Chem. Eng. J.*, 2020, **400**, 125875.

140 F. Lévesque and P. H. Seeberger, *Org. Lett.*, 2011, **13**, 5008–5011.

141 D. S. Lee, Z. Amara, C. A. Clark, Z. Xu, B. Kakimpa, H. P. Morvan, S. J. Pickering, M. Poliakoff and M. W. George, *Org Process Res Dev*, 2017, **21**, 1042–1050.

142 D. S. Lee, M. Sharabi, R. Jefferson-Loveday, S. J. Pickering, M. Poliakoff and M. W. George, *Org Process Res Dev*, 2020, **24**, 201–206.

143 N. Sharif, PhD Thesis, The University of Nottingham, 2021.

144 R. A. Bourne, X. Han, M. Poliakoff and M. W. George, *Angew. Chem. Int. Ed.*, 2009, **48**, 5322–5325.

145 X. Han, R. A. Bourne, M. Poliakoff and M. W. George, *Chem Sci*, 2011, **2**, 1059.

146 G. I. Ioannou, T. Montagnon, D. Kalaitzakis, S. A. Pergantis and G. Vassilikogiannakis, *ChemPhotoChem*, 2017, **1**, 173–177.

147 J. Schachtner, P. Bayer and A. Jacobi von Wangelin, *Beilstein J. Org. Chem.*, 2016, **12**, 1798–1811.

148 M. Meeuwse, J. van der Schaaf and J. C. Schouten, *Ind Eng Chem Res*, 2010, **49**, 1605–1610.

149 M. Meeuwse, J. van der Schaaf, B. F. M. Kuster and J. C. Schouten, *Chem Eng Sci*, 2010, **65**, 466–471.

150 C. F. Seidel and M. Stoll, *Helv Chim Acta*, 1959, **42**, 1830–1844.

151 T. Yamamoto, H. Matsuda, Y. Utsumi, T. Hagiwara and T. Kanisawa, *Tetrahedron Lett*, 2002, **43**, 9077–9080.

152 P. L. Alsters, W. Jary, V. Nardello-Rataj and J.-M. Aubry, *Org Process Res Dev*, 2010, **14**, 259–262.

153 J. Panten and H. Surburg, in *Ullmann's Encyclopedia of Industrial Chemistry*, eds. K.-G. Fahlbusch, F.-J. Hammerschmidt, W. Pickenhagen, D. Schatkowski, K. Bauer, D. Garbe, H. Surburg and J. Panten, John Wiley & Sons, Ltd, 2015, pp. 1–9.

154 S. Meyer, D. Tietze, S. Rau, B. Schäfer and G. Kreisel, *J Photochem Photobiol A Chem*, 2007, **186**, 248–253.

155 M. Oelgemöller, C. Jung, J. Ortner, J. Mattay and E. Zimmermann, *Green Chem.*, 2005, **7**, 35–38.

156 United States Patent, 5892059, 1999.

157 D. Ravelli, S. Protti, P. Neri, M. Fagnoni and A. Albini, *Green Chem*, 2011, **13**, 1876–1884.

158 D. Wöhrle, M. W. Tausch and W. D. Stohrer, *Photochemie: Konzepte, Methoden, Experimenta*, Wiley-VCH, Weinheim, 1998.

159 J. van Houten and R. J. Watts, *Inorg Chem*, 1978, **17**, 3381–3385.

160 K. Mendis, B. J. Sina, P. Marchesini and R. Carter, in *American Journal of Tropical Medicine and Hygiene*, American Society of Tropical Medicine and Hygiene, 2001, vol. 64, pp. 97–106.

161 A. E. Greenberg, M. Ntumbanzondo, N. Ntula, L. Mawa, J. Howell and F. Davachi, *Bull World Health Organ*, 1989, **67**, 189–96.

162 *World Malaria Report 2021*, 2021.

163 WHO recommends groundbreaking malaria vaccine for children at risk  
- <https://www.who.int/news-room/detail/06-10-2021-who-recommends-groundbreaking-malaria-vaccine-for-children-at-risk>.

164 *The Lancet*, 2015, **386**, 31–45.

165 D. M. Opsenica and B. A. Šolaja, *J. Serb. Chem. Soc.*, 2009, **74**, 1155–1193.

166 R. D. Slack, A. M. Jacobine and G. H. Posner, *Medchemcomm*, 2012, **3**, 281–297.

167 D. J. Weiss, T. C. D. Lucas, M. Nguyen, A. K. Nandi, D. Bisanzio, K. E. Battle, E. Cameron, K. A. Twohig, D. A. Pfeffer, J. A. Rozier, H. S. Gibson, P. C. Rao, D. Casey, A. Bertozzi-Villa, E. L. Collins, U. Dalrymple, N. Gray, J. R. Harris, R. E. Howes, S. Y. Kang, S. H. Keddie, D. May, S. Rumisha, M. P. Thorn, R. Barber, N. Fullman, C. K. Huynh, X. Kulikoff, M. J. Kutz, A. D. Lopez, A. H. Mokdad, M. Naghavi, G. Nguyen, K. A. Shackelford, T. Vos, H. Wang, D. L. Smith, S. S. Lim, C. J. L. Murray, S. Bhatt, S. I. Hay and P. W. Gething, *The Lancet*, 2019, **394**, 322–331.

168 D. L. Klayman, *Science (1979)*, 1985, **228**, 1049–1055.

169 M. M. Nyunt and C. V. Plowe, *Clin Pharmacol Ther*, 2007, **82**, 601–605.

170 I. Fernández and A. Robert, *Org Biomol Chem*, 2011, **9**, 4098–4107.

171 N. J. White, *Science (1979)*, 2008, **320**, 330–334.

172 K. J. Arrow, C. Panosian and H. Gelband, in *Saving Lives, Buying Time: Economics of Malaria Drugs in an Age of Resistance*, National Academies Press (US), 2004.

173 G. Schmid and W. Hofheinz, *J Am Chem Soc*, 1983, **105**, 624–625.

174 D. K. Ro, E. M. Paradise, M. Quellet, K. J. Fisher, K. L. Newman, J. M. Ndungu, K. A. Ho, R. A. Eachus, T. S. Ham, J. Kirby, M. C. Y. Chang, S. T. Withers, Y. Shiba, R. Sarpong and J. D. Keasling, *Nature*, 2006, **440**, 940–943.

175 J. A. Dietrich, Y. Yoshikuni, K. J. Fisher, F. X. Woolard, D. Ockey, D. J. McPhee, N. S. Renninger, M. C. Y. Chang, D. Baker and J. D. Keasling, *ACS Chem Biol*, 2009, **4**, 261–267.

176 T. E. Wallaart, N. Pras and W. J. Quax, *J Nat Prod*, 1999, **62**, 1160–1162.

177 G. D. Brown and L. K. Sy, *Tetrahedron*, 2004, **60**, 1125–1138.

178 L. K. Sy and G. D. Brown, *Tetrahedron*, 2002, **58**, 897–908.

179 J. N. Cumming, D. Wang, S. B. Park, T. A. Shapiro and G. H. Posner, *J Med Chem*, 1998, **41**, 952–964.

180 L. Bryant, B. Flatley, C. Patole, G. D. Brown and R. Cramer, *BMC Plant Biol*, 2015, **15**, 1–13.

181 S. S. A. Soetaert, C. M. F. van Neste, M. L. Vandewoestyne, S. R. Head, A. Goossens, F. C. W. van Nieuwerburgh and D. L. D. Deforce, *BMC Plant Biol*, 2013, **13**, 1–14.

182 Y.-S. Zhang, L. Ben-Ye, Z.-Q. Li, Y. E. He-Chun, H. Wang, G.-F. Li and H. Jun-Li, *Acta Bot Sin*, 2004, **46**, 1338–1346.

183 K. Varela, H. D. Arman and F. K. Yoshimoto, *J Nat Prod*, 2021, **84**, 1967–1984.

184 K. Varela, H. D. Arman and F. K. Yoshimoto, *J Nat Prod*, 2020, **83**, 66–78.

185 L. K. Sy, G. D. Brown and R. Haynes, *Tetrahedron*, 1998, **54**, 4345–4356.

186 L. K. Sy, N. Y. Zhu and G. D. Brown, *Tetrahedron*, 2001, **57**, 8495–8510.

187 L. K. Sy, K. S. Ngo and G. D. Brown, *Tetrahedron*, 1999, **55**, 15127–15140.

188 G. D. Brown, *J Nat Prod*, 1992, **55**, 1756–1760.

189 Z. Amara, J. F. B. Bellamy, R. Horvath, S. J. Miller, A. Beeby, A. Burgard, K. Rossen, M. Poliakoff and M. W. George, *Nat Chem*, 2015, **7**, 489–495.

190 A. J. Lin, D. L. Klayman and J. M. Hoch, *J. Org. Chem.*, 1985, **50**, 4504–4508.

191 C. J. Paddon, P. J. Westfall, D. J. Pitera, K. Benjamin, K. Fisher, D. McPhee, M. D. Leavell, A. Tai, A. Main, D. Eng, D. R. Polichuk, K. H. Teoh, D. W. Reed, T. Treynor, J. Lenihan, H. Jiang, M. Fleck, S. Bajad, G. Dang, D. Dengrove, D. Diola, G. Dorin, K. W. Ellens, S. Fickes, J. Galazzo, S. P. Gaucher, T. Geistlinger, R. Henry, M. Hepp, T. Horning, T. Iqbal, L. Kizer, B. Lieu, D. Melis, N. Moss, R. Regentin, S. Secret, H. Tsuruta, R. Vazquez, L. F. Westblade, L. Xu, M. Yu, Y. Zhang, L. Zhao, J. Lievense, P. S. Covello, J. D. Keasling, K. K. Reiling, N. S. Renninger and J. D. Newman, *Nature*, 2013, **496**, 528–532.

192 S. H. Kung, S. Lund, A. Murarka, D. McPhee and C. J. Paddon, *Front Plant Sci*, 2018, **9**, 1–7.

193 D. Ravelli, S. Protti, P. Neri, M. Fagnoni and A. Albini, *Green Chemistry*, 2011, **13**, 1876–1884.

194 A. Burgard, T. Gieshoff, A. Peschl, D. Hörstermann, C. Keleschovsky, R. Villa, S. Michelis and M. P. Feth, *Chem. Eng. J.*, 2016, **294**, 83–96.

195 R. Bonnett and G. Martō Áñez, *Tetrahedron*, 2001, **57**, 9513–9547.

196 V. S. Chirvony, A. Van Hoek, V. A. Galievsy, I. V Sazanovich, T. J. Schaafsma and D. Holten, *J. Phys. Chem. B*, 2000, **104**, 9909–9917.

197 J. A. S. Cavaleiro, H. Görner, P. S. S. Lacerda, J. G. MacDonald, G. Mark, M. G. P. M. S. Neves, R. S. Nohr, H. P. Schuchmann, C. Von Sonntag and A. C. Tomé, *J Photochem Photobiol A Chem*, 2001, **144**, 131–140.

198 R. Petrucci, W. Harwood, G. Herring and J. Madura, *General Chemistry Principles and Modern Applications*, Pearson Prentice Hall, 9th edn., 2007.

199 W. Wagner and A. Prüß, *J Phys Chem Ref Data*, 2002, **31**, 33102.

200 N. Simsek Kus, *Tetrahedron*, 2012, **68**, 949–958.

201 A. Adeyemi, J. Bergman, J. Bra, J. Sa and M. Larhed, *Org Process Res Dev*, 2017, **21**, 947–955.

202 M. Charaschanya, A. R. Bogdan, Y. Wang and S. W. Djuric, *Tetrahedron Lett*, 2016, **57**, 1035–1039.

203 J. Bellamy, PhD Thesis, The University of Nottingham, 2014.

204 X. Han, PhD Thesis, The University of Nottingham, 2010.

205 fused quartz properties, <http://www.h-baumbach.co.uk/Quartzproperties.htm>, <http://www.h-baumbach.co.uk/Quartzproperties.htm>, (accessed 20 May 2019).

206 K. I. Booker-Milburn, J. K. Cowell, F. Delgado Jiménez, A. Sharpe and A. J. White, *Tetrahedron*, 1999, **55**, 5875–5888.

207 Y. N. Ahn, K. do Kim, G. Anoop, G. S. Kim and J. S. Yoo, *Sci Rep*, 2019, **9**, 1–10.

208 M. V. Tsurkan, C. Jungnickel, M. Schlierf and C. Werner, *J Am Chem Soc*, 2017, **139**, 10184–10187.

209 M. Song, H. Ma, M. Ren, Z. Ai and M. Li, *Synlett*, 2016, **28**, 445–450.

210 L. M. Tedaldi, A. E. Aliev and J. R. Baker, *Chem. Commun.*, 2012, **48**, 4725.

211 S. I. A. Shah, L. W. Kostiuk and S. M. Kresta, *Int. J. Chem. Eng.*, 2012, **2012**, 1–16.

212 *Engineering and Operating Guide for DOWTHERM SR-1 and DOWTHERM 4000 Inhibited Ethylene Glycol-based Heat Transfer Fluids*, .

213 L. Wu, Z. Abada, D. S. Lee, M. Poliakoff and M. W. George, *Tetrahedron*, 2018, **74**, 3107–3112.

214 L. Wu, D. S. Lee, H. Boufroura, M. Poliakoff and M. W. George, *ChemPhotoChem*, 2018, **2**, 509–509.

215 Z. E. Hamami, L. Vanoye, P. Fongarland, C. de Bellefon and A. Favre-Réguillon, *ChemPhotoChem*, 2019, **3**, 122–128.

216 R. W. Redmond and J. N. Gamlin, *Photochem Photobiol*, 1999, **70**, 391–475.

217 E. N. D. C. Andrade, *Nature*, 1930, **125**, 309–310.

218 *Philos Trans R Soc Lond*, 1803, **93**, 29–274.

219 D. W. Green and R. H. Perry, *Perry's Chemical Engineers' Handbook*, Eighth Edition, McGraw-Hill Education, 2008.

220 S. Black and F. Muller, *Org Process Res Dev*, 2010, **14**, 661–665.

221 B. Tambasco, K. Segura, C. Seyrig, D. Cabrera, M. Port, C. Ferroud and Z. Amara, *ACS Catal*, 2018, **8**, 4383–4389.

222 J. Alagy, P. Trambouze and H. Van Landeghem, *Ind. Eng. Chem. Process Des. Develop.*, 1974, **13**, 317–323.

223 J. Hao, H. Cheng, H. Wang, S. Cai and F. Zhao, *J Mol Catal A Chem*, 2007, **271**, 42–45.

224 B. González, N. Calvar, E. Gómez and Á. Domínguez, *J Chem Thermodyn*, 2007, **39**, 1578–1588.

225 D. R. Lide, *Handbook of Chemistry and Physics*, CRC, Boca Raton, 85th edn., 2004.

226 C. Reichardt, *Solvents and Solvent Effects in Organic Chemistry*, Wiley-VCH Publishers, Third., 2003.

227 G. W. Kauffman and P. C. Jurs, *J Chem Inf Comput Sci*, 2001, **41**, 408–418.

228 J. A. Riddick, W. B. Bunger and T. K. Sakano, 1986.

229 S. Blanc, T. Pigot, C. Cugnet, R. Brown and S. Lacombe, *Phys. Chem. Chem. Phys.*, 2010, **12**, 11280–11290.

230 P. M. Osterberg, J. K. Niemeier, C. J. Welch, J. M. Hawkins, J. R. Martinelli, T. E. Johnson, T. W. Root and S. S. Stahl, *Org. Res. Process Dev.*, 2014, **19**, 1537–1543.

231 W. E. Baker, P. A. Cox, J. J. Kulesz, R. A. Strehlow and P. S. Westine, *Explosion Hazards and Evaluation*, Elsevier Scientific Publishing Company, Amsterdam, Oxford, New York, 1981, vol. 5.

232 M. G  dde, C. Liebner and H. Hieronymus, *Chemie Ingenieur Technik*, 2009, **81**, 73–78.

233 J. P. McMullen and K. F. Jensen, *Org Process Res Dev*, 2010, **14**, 1169–1176.

234 B. J. Reizman and K. F. Jensen, *Acc Chem Res*, 2016, **49**, 1786–1796.

235 M. Rasheed and T. Wirth, *Angew. Chem. Int. Ed.*, 2011, **50**, 357–358.

236 V. Sans and L. Cronin, *Chem Soc Rev*, 2016, **45**, 2032–2043.

237 A. D. Clayton, J. A. Manson, C. J. Taylor, T. W. Chamberlain, B. A. Taylor, G. Clemens and R. A. Bourne, *React Chem Eng*, 2019, **4**, 1545–1554.

238 S. V. Ley, D. E. Fitzpatrick, R. J. Ingham and R. M. Myers, *Angewandte Chemie - International Edition*, 2015, **54**, 3449–3464.

239 M. Rodriguez-Zubiri and F. X. Felpin, *Org Process Res Dev*, 2022, **26**, 1766–1793.

240 M. B. Plutschack, B. Pieber, K. Gilmore and P. H. Seeberger, *Chem Rev*, 2017, **117**, 11796–11893.

241 V. Hessel, D. Kralisch, N. Kockmann, T. No, Q. Wang and P. Helmut Ringsdorf, *ChemSusChem*, 2013, **6**, 746–789.

242 A. Bonner, A. Loftus, A. C. Padgham and M. Baumann, *Org. Biomol. Chem*, 2021, **19**, 7737.

243 T. Razzaq, T. N. Glasnov and C. O. Kappe, *European J Org Chem*, 2009, 1321–1325.

244 C. R. Sagandira, S. Nqeketo, K. Mhlana, T. Sonti, S. Gaqa and P. Watts, *Cite this: React. Chem. Eng*, 2022, **7**, 214.

245 S. V. Ley, Y. Chen, A. Robinson, B. Otter, E. Godineau and C. Battilocchio, *Org Process Res Dev*, 2021, **25**, 713–720.

246 M. Christensen, L. P. E. Yunker, P. Shiri, T. Zepel, P. L. Prieto, S. Grunert, F. Bork and J. E. Hein, *Chem Sci*, 2021, **12**, 15473.

247 L. Rogers and K. F. Jensen, *Green Chem*, 2019, **21**, 3481–3498.

248 J. Christopher McWilliams, A. D. Allian, S. M. Opalka, S. A. May, M. Journet and T. M. Braden, *Org Process Res Dev*, 2018, **22**, 1143–1166.

249 S. Krishnadasan, R. J. C. Brown, A. J. DeMello and J. C. DeMello, *Lab Chip*, 2007, **7**, 1434–1441.

250 J. P. McMullen, M. T. Stone, S. L. Buchwald and K. F. Jensen, *Angew. Chem. In. Ed.*, 2010, **49**, 7076–7080.

251 J. P. McMullen and K. F. Jensen, *Org Process Res Dev*, 2011, **15**, 398–407.

252 J. S. Moore and K. F. Jensen, *Org Process Res Dev*, 2012, **16**, 1409–1415.

253 R. A. Bourne, R. A. Skilton, A. J. Parrott, D. J. Irvine and M. Poliakoff, *Org Process Res Dev*, 2011, **15**, 932–938.

254 D. N. Jumbam, R. A. Skilton, A. J. Parrott, R. A. Bourne and M. Poliakoff, *J Flow Chem*, 2012, **2**, 24–27.

255 A. J. Parrott, R. A. Bourne, G. R. Akien, D. J. Irvine and M. Poliakoff, *Angew. Chem. Int. Ed.*, 2011, **50**, 3788–3792.

256 D. R. Pilipauskas, in *Process Chemistry in the Pharmaceutical Industry*, CRC Press, 1st edn., 1999.

257 R. Carlson and J. E. Carlson, *Org Process Res Dev*, 2005, **9**, 680–689.

258 S. A. Weissman and N. G. Anderson, *Org Process Res Dev*, 2014, **19**, 1605–1633.

259 A. D. Clayton, PhD Thesis, The University of Leeds, 2020.

260 R. Leardi, *Anal Chim Acta*, 2009, **652**, 161–172.

261 A. Rehorek and A. Plum, *Anal Bioanal Chem*, 2006, **384**, 1123–1128.

262 L. Zhu, R. G. Brereton, D. R. Thompson, P. L. Hopkins and R. E. A. Escott, *Anal Chim Acta*, 2007, **584**, 370–378.

263 J. P. McMullen, M. T. Stone, S. L. Buchwald, K. F. Jensen, J. P. McMullen, K. F. Jensen, M. T. Stone and S. L. Buchwald, *Angew. Chem. Int. Ed.*, 2010, **49**, 7076–7080.

264 J. Ke, C. Gao, A. A. Folgueiras-Amador, K. E. Jolley, O. de Frutos, C. Mateos, J. A. Rincón, R. C. D. Brown, M. Poliakoff and M. W. George, *Appl Spectrosc*, 2019, **2022**, 38–50.

265 J. G. Stevens, R. A. Bourne, M. V. Twigg and M. Poliakoff, *Angew. Chem. Int. Ed.*, 2010, **49**, 8856–8859.

266 J. G. Stevens, R. A. Bourne and M. Poliakoff, *Green Chemistry*, 2009, **11**, 409–416.

267 B. Walsh, J. R. Hyde, P. Licence and M. Poliakoff, *Green Chemistry*, 2005, **7**, 456–463.

268 Z. Qian, I. R. Baxendale and S. V Ley, *Chem. Eur. J.*, 2010, **16**, 12342–12348.

269 S. Hübner, U. Bentrup, U. Budde, K. Lovis, T. Dietrich, A. Freitag, L. Küpper and K. Jähnisch, *Org Process Res Dev*, 2009, **13**, 952–960.

270 R. Herzig-Marx, K. T. Queeney, R. J. Jackman, M. A. Schmidt and K. F. Jensen, *Anal Chem*, 2004, **76**, 6476–6483.

271 S. Mozharov, A. Nordon, D. Littlejohn, C. Wiles, P. Watts, P. Dallin, J. M. Girkin and ^ † Westchem, *J. Am. Chem. Soc*, 2011, **133**, 3601–3608.

272 A. Echtermeyer, Y. Amar, J. Zakrzewski and A. Lapkin, *Beilstein J. Org. Chem*, 2017, **13**, 150–163.

273 H. Wensink, F. Benito-Lopez, D. C. Hermes, W. Verboom, H. J. G. E. Gardeniers, D. N. Reinhoudt and A. van den Berg, *Lab Chip*, 2005, **5**, 280–284.

274 B. Musio, E. Gala and S. V Ley, *ACS Sustain Chem Eng*, 2018, **6**, 1489–1495.

275 M. V. Gomez, H. H. J. Verputten, A. Diaz-Ortiz, A. Moreno, A. De La Hoz and A. H. Velders, *Chem. Commun.*, 2010, **46**, 4514–4516.

276 S. E. Hamilton, F. Mattrey, X. Bu, D. Murray, B. Mccullough and C. J. Welch, *Org Process Res Dev*, 2014, **18**, 103–108.

277 D. L. Browne, S. Wright, B. J. Deadman, S. Dunnage, I. R. Baxendale, R. M. Turner and S. V Ley, *Rapid Commun. Mass Spectrom.*, 2012, **26**, 1999–2010.

278 G. A. Price, D. Mallik and M. G. Organ, *J Flow Chem*, 2017, **7**, 82–86.

279 M. A. Morin, W. Zhang, D. Mallik and M. G. Organ, *Angew. Chem. Int. Ed.*, 2021, **60**, 20606–20626.

280 N. Holmes, G. R. Akien, R. J. D. Savage, C. Stanetty, I. R. Baxendale, A. J. Blacker, B. A. Taylor, R. L. Woodward, R. E. Meadows and R. A. Bourne, *React Chem Eng*, 2016, **1**, 96–100.

281 K. Somerville, M. Tilley, G. Li, D. Mallik and M. G. Organ, *Org Process Res Dev*, 2014, **18**, 1315–1320.

282 V. Sans, L. Porwol, V. Dragone and L. Cronin, *Chem Sci*, 2015, **6**, 1258–1264.

283 H. J. Woerdenbag, N. Pras, R. Bos, J. F. Visser, H. Hendriks and T. M. Malingré, *Phytochemical Analysis*, 1991, **2**, 215–219.

284 A. T. Sipahimalani, D. P. Fulzele and M. R. Heble, *J Chromatogr A*, 1991, **538**, 452–455.

285 J. F. S. Ferreira, D. J. Charles, K. Wood, J. Janick and J. E. Simon, *Phytochemical Analysis*, 1994, **5**, 116–120.

286 S. S. Zhao and M. Y. Zeng, *Planta Med*, 1985, **3**, 233–237.

287 J. F. S. Ferreira and J. M. Gonzalez, *Phytochemical Analysis*, 2009, **20**, 91–97.

288 N. Acton, D. L. Klayman and I. J. Rollman, *Planta Med*, 1985, **NO. 5**, 445–446.

289 V. Melendez, J. O. Peggins, T. G. Brewer and A. D. Theoharides, *J Pharm Sci*, 1991, **80**, 132–138.

290 P. Christen and J. L. Veuthey, *Curr Med Chem*, 2012, **8**, 1827–1839.

291 M. Kohler, W. Haerdi, P. Christen and J.-L. Veuthey, *Phytochem. Anal*, 1997, **8**, 223–227.

292 B. A. Avery, K. K. Venkatesh and M. A. Avery, *J Chromatogr B Biomed Sci Appl*, 1999, **730**, 71–80.

293 C. Z. Liu, H. Y. Zhou and Y. Zhao, *Anal Chim Acta*, 2007, **581**, 298–302.

294 C. A. Peng, J. F. S. Ferreira and A. J. Wood, *J Chromatogr A*, 2006, **1133**, 254–258.

295 A. A. Lapkin, A. Walker, N. Sullivan, B. Khambay, B. Mlambo and S. Chemat, *J Pharm Biomed Anal*, 2009, **49**, 908–915.

296 C. G. Thomas, S. A. Ward and G. Edwards, *J Chromatogr B Biomed Sci Appl*, 1992, **583**, 131–136.

297 D. Harris, *Quantitative Chemical Analysis*, W.H. Freeman and Co., 6th edn., 2002.

298 K. Robards, P. R. Haddad and P. E. Jackson, *Principles and Practice of Modern Chromatographic Methods*, Academic Press, London, 1994.

299 W. T. Cooper, *Normal-Phase Liquid Chromatography*, John Wiley & Sons, Ltd, 2006.

300 T. Vehovec and A. Obreza, *J Chromatogr A*, 2010, **1217**, 1549–1556.

301 L. G. Angelini, E. Campeol, S. Tozzi, K. G. Gilbert, D. T. Cooke and P. John, *Biotechnol Prog*, 2003, **19**, 1792–1797.

302 B. Schuhn, *Performance Characteristics of the Agilent 1290 Infinity Evaporative Light Scattering Detector*, Agilent Technologies, 2013.

303 Z. Cobb, P. N. Shaw, L. L. Lloyd, N. Wrench and D. A. Barrett, *J. Microcolumn Separations*, 2001, **13**, 169–175.

304 A. Stolyhwo, H. Colin and G. Guiochon, *J Chromatogr A*, 1983, **265**, 1–18.

305 D. A. Yurek, D. L. Branch and M. S. Kuo, *J Comb Chem*, 2002, **4**, 138–148.

306 N. Tian, J. Li, S. Liu, J. Huang, X. Li and Z. Liu, *Biomed. Chromatogr.*, 2012, **26**, 708–713.

307 R. K. Haynes, S. C. Vonwiller, M. Jung, W. S. Zhou, X. X. Xu, D. L. Klayman, E. v Geldre, A. Vergauwe, S. S. Zhao, M. Y. Zeng, N. Acton, I. J. Rollman, M. S. R. Nair, D. V. J. Basile, A. Nat, Ranasinghe, J. D. Sweatlock, R. G. Cooks, J. F. S. Ferreira, J. Janicks and K. P. Madhusudanan, *Anal Chem*, 1997, **30**, 3084–3087.

308 W. Zeng, D. G. Musson, A. L. Fisher and A. Q. Wang, *Rapid Commun Mass Spectrom*, 2006, **20**, 635–640.

309 T. J. Bruno and P. D. N. Svoronos, *CRC Handbook of Basic Tables for Chemical Analysis*, CRC Press, 2nd edn., 2003.

310 C. J. Taylor, A. Baker, M. R. Chapman, W. R. Reynolds, K. E. Jolley, G. Clemens, G. E. Smith, A. J. Blacker, T. W. Chamberlain, S. D. R. Christie, B. A. Taylor and R. A. Bourne, *J Flow Chem*, 2021, **11**, 75–86.

311 F. E. Grubbs, *Technometrics*, 1969, **11**, 1.

312 F. Malz and H. Jancke, *J Pharm Biomed Anal*, 2005, **38**, 813–823.

313 T. Schoenberger, *Validation of Quantitative NMR Methods*, Bundeskriminalamt, 2012.

314 X. Ma, H. Dang, J. A. Rose, P. Rablen and S. B. Herzon, *J Am Chem Soc*, 2017, **139**, 5998–6007.

315 C. H. Tung, L. Z. Wu, L. P. Zhang, H. R. Li, X. Y. Yi, K. Song, M. Xu, Z. Y. Yuan, J. Q. Guan, H. W. Wang, Y. M. Ying and X. H. Xu, *Pure Appl. Chem.*, 2000, **72**, 2289–2298.

316 E. K. Lumley, C. E. Dyer, N. Pamme and R. W. Boyle, *Org Lett*, 2012, **14**, 5724–5727.

317 T. E. Wallaart, W. Van Uden, H. G. M. Lubberink, H. J. Woerdenbag, N. Pras and W. J. Quax, *J Nat Prod*, 1999, **62**, 430–433.

318 G. Cleaver, *Agilent Technologies Application Note*, 2013.

319 N. C. Megoulas and M. A. Koupparis, *J Pharm Biomed Anal*, 2004, **36**, 73–79.

320 W. Li and J. F. Fitzloff, *J Pharm Biomed Anal*, 2002, **30**, 67–75.

321 A. Shrivastava and V. Gupta, *Chronicles of Young Scientists*, 2011, **2**, 21.

322 M. Dong, *HPLC and UHPLC for Practicing Scientists*, Wiley, 2019.

323 Koichi. Saitoh, Masaru. Kobayashi and Nobuo. Suzuki, *Anal Chem*, 1981, **53**, 2309–2313.

324 E. Bravi, G. Perretti and L. Montanari, *J Chromatogr A*, 2006, **1134**, 210–214.

325 E. P. Serjeant and B. Dempsey, *Ionisation Constants of Organic Acids in Aqueous Solution*, Pergamon Press, Inc., New York, 1979.

326 M. Miyazawa, K. Yokote and H. Kameoka, *Phytochemistry*, 1995, **39**, 85–89.

327 E. Havinga and R. J. F. Nivard, *Recueil des Travaux Chimiques des Pays-Bas*, 1948, **67**, 846–854.

328 Holger Knapp, Markus Straubinger, Selenia Fornari, Noriaki Oka, Naoharu Watanabe and Peter Winterhalter, *J Agric Food Chem*, 1998, **46**, 1966–1970.

329 R. Alonso and T. Bach, *Angew. Chem. Int. Ed.*, 2014, **53**, 4368–4371.

330 C. Müller, A. Bauer and T. Bach, *Angew. Chem. Int. Ed.*, 2009, **48**, 6640–6642.

331 D. Cambié, C. Bottecchia, N. J. W. Straathof, V. Hessel and T. Noël, *Chem Rev.*, 2016, **116**, 10276–10341.

332 A. M. Schweidtmann, A. D. Clayton, N. Holmes, E. Bradford, R. A. Bourne and A. A. Lapkin, *Chem. Eng. J.*, 2018, **352**, 277–282.

333 A. Bauer, F. Westkämper, S. Grimme and T. Bach, *Nature*, 2005, **436**, 1139–1140.

334 T. A. Ford and M. Falk, *Can J Chem.*, 1968, **46**, 3579–3586.